Dynamics of Blast Wave and Cellular H_2-Air Flame Interaction in a Hele-Shaw Cell

by

Maxime La Flèche

Thesis submitted to the
Faculty of Graduate and Postdoctoral Studies
In partial fulfillment of the requirements
For the M.A.Sc. degree in
Mechanical Engineering

Ottawa-Carleton Institute for Mechanical and Aerospace Engineering
Faculty of Engineering
University of Ottawa

Abstract

The present thesis investigates the interaction of a shock wave with a cellular flame and the ensuing mechanisms on the dynamics of the subsequent flame deformation. The interaction is known to disrupt the flame surface through the Richtmyer-Meshkov instability, hence potentially enhancing the local combustion rates. This study aims to clarify the evolution of a flame when perturbed head-on by a shock wave. Two novel series of experiments were conducted in a vertically-oriented Hele-Shaw cell, which could successfully isolate a quasi-bidimensional cellular flame structure at ambient conditions. In the first configuration, the passage of the shock wave arising in the burned products of a deflagration wave was investigated, while both waves propagated in the same outward direction. In the other configuration, the shock wave centrally emerged in the unburned gases and collided with a cellular flame front traveling in the opposite direction. The event was captured using a Z-type Schlieren imaging system to visualize the growth of the flame cells.

Shock characterization was determined in the Hele-Shaw apparatus to estimate the strength of the blast wave generated by energy deposition using a high-voltage igniter or by decoupled detonation from a detonation tube. A combustion study was also performed to determine the laminar flame speed in a mixture of hydrogen-air according to different equivalence ratios in the apparatus. The experiments revealed that inherent cellular flame instabilities are well developed in the observation scale of the Hele-Shaw geometry. The shock-flame complex was therefore analyzed experimentally for selected mixtures. As the shock wave traversed the interface separating the burned and unburned gases, the flame became more corrugated. Following the interaction, the flame cusps were stretched and/or flattened. At later times, the wrinkled interface was reversed and developed finer scales. A time scale analysis was performed to identify the contribution of the competing effects of Richtmyer-Meshkov and Rayleigh-Taylor instabilities on the flame interface deformation. For the case of a shock wave traversing the flame interface from the unburned to the burned side, the early perturbations were mainly governed by the Richtmyer-Meshkov instability. Finally, Rayleigh-Taylor instability resulted from the decaying pressure profile of the blast wave and tended to stabilize the perturbed interface to eventually reverse the cellular structure. Experimental and inert numerical results on the flame cell's amplitude growth were found to be in good agreement.

Résumé

Le présent travail porte sur l'interaction d'une onde de choc avec une flamme cellulaire et les mécanismes de déformation qui s'ensuivent. L'interaction est reconnue pour entraîner d'importantes perturbations sur la surface de la flamme par l'entremise des instabilités de Richtmyer-Meshkov, ce qui potentiellement augmente le taux de combustion localement. Cette étude vise à mettre en lumière l'évolution d'une flamme cellulaire suivant sa collision avec une onde de choc qui décroit. Le problème est abordé initialement de manière expérimentale; deux nouvelles séries d'expériences furent menées dans une cellule verticale de type Hele-Shaw afin d'isoler une flamme cellulaire de manière quasi bidimensionelle. Le premier dispositif expérimental a permis d'investiguer le passage de l'onde de choc émanant du côté des gaz brulés de la flamme au travers de l'interface. À l'opposé, la deuxième géométrie est composée de multiples points d'allumage afin d'étudier le passage d'une onde de choc au travers d'une flamme qui se propage dans la direction opposée; la collision frontale se manifeste des gaz frais aux gaz brûlés. L'évolution des celllules de la flamme issue du complexe choc-flamme fût captée à l'aide d'un système de visualisation strioscopique à haute vitesse.

La caractérisation de l'onde de choc fût d'abord réalisée dans le dispositif de Hele-Shaw, afin d'estimer la force du choc généré à partir de la déposition d'énergie à l'aide d'un allumeur à haute tension ou par un tube à détonation. Ensuite, différents mélanges d'hydrogène-air ont été testés afin de déterminer la vitesse laminaire de flamme dans la cellule de Hele-Shaw. Les expériences ont révélé que les instabilités intrinsèques de la déflagration se développent bien selon l'échelle d'observation. L'interaction choc-flamme a donc été réalisée expérimentalement pour des mélanges réactifs sélectionnés. Alors que l'onde de choc a traversé l'interface de la flamme, les ondulations cellulaires se sont amplifiées. Ainsi, les cellules de la flamme se sont étirées et/ou aplaties suivant l'interaction avec l'onde de choc. Ultérieurement, la surface de la flamme s'est retrouvée inversée et comportant de plus petites échelles. À partir d'une analyse d'échelles de temps et d'observations expérimentales, il fût démontré que la déformation de l'interface de la flamme est influencée par les effets concurrentiels des instabilités de Richtmyer-Meshkov et de Rayleigh-Taylor. L'instabilité de Richtmyer-Meshkov contrôle d'abord les premiers instants suite au passage de l'onde de choc des gaz brûlés aux gaz frais de l'interface de la flamme. Toutefois, dû au profil décroissant de l'onde de choc, les instabilités de Rayleigh-Taylor ont un apport considérable subséquemment et contribuent à renverser l'interface de la flamme. Les résultats expérimentaux ainsi que les simulations numériques inertes se sont avérés en accord en ce qui a trait à l'évolution de l'amplitude d'une cellule de la flamme.

Acknowledgements

First and foremost, I would like to thank my supervisor, Dr. Matei Radulescu, for his insightful discussions and guidance throughout the development of this thesis. I am deeply grateful for his devotion and mentorship which allowed me to experience many opportunities over the five years as part of his research group.

I would also like to thank the staff from the Mechanical Engineering machine shop for their help, and everyone involved in the Detonation and Reactive Dynamics Laboratory (DRDL) at the University of Ottawa for their academic help and their friendship.

Special thanks are conveyed to Hongxia Yang for her valued assistance and contribution with this work. I would like to thank my lab mates and friends Qiang Xiao and Willstrong Rakotoarison for their help in the experiments and the good times we have spent together.

Finally, I must express my very profound gratitude to my parents, to my grandmothers, to my sister and to my friends for providing me with endless support, love and continuous encouragement throughout my years of study. Their presence ensured that the fire kept burning throughout this journey; this accomplishment would not have been possible without them.

Table of Contents

List of Tables

List of Figures

Nomenclature

Latin Letters

a	Acceleration
At	Atwood number
c	Sound speed
C	Capacitance
D	Shock velocity
E	Energy
$\mathcal{K}$	Curvature
k	Wave number
l	Thickness
Le	Lewis number
L	Level of refinement
M	Mach number
MW	Molecular weight
p	pressure
R	Radius
r	Radius
R_c	Critical radius for onset of instability
S_u	Laminar flame speed
T	Temperature
t	Time

V	Voltage or Volume
w	Width
x	Position

Greek Letters

α	Density ratio
γ	Ratio of specific heats
δ	Computational cell length
ζ	Ratio of unsteadiness to curvature
λ	Wavelength
ρ	Density
$\dot{\sigma}$	Thermicity
σ	Growth rate
τ	Characteristic time scale
ϕ	Equivalence ratio
ψ	Sonic parameter
ω	Vorticity

Abbreviations

2RSW	Secondary reflected shock wave
BP	Burned products
CEA	Chemical equilibrium application
CJ	Chapman-Jouguet
DDT	Deflagration to detonation transition
fps	Frames per second
HVI	High-voltage igniter
ISW	Incident shock wave

RM	Richtmyer-Meshkov
RSW	Reflected shock wave
RT	Rayleigh-Taylor
F	Flame
SW	Shock wave
TSW	Transmitted shock wave
TTL	Transistor-transistor logic

Subscripts

0	Initial/reference
ad	Adiabatic
b	Burned gas (reacted mixture)
c	Chemical reactions
e	Electrodes
f	Flame
hs	Hele-Shaw
H	Hugoniot
H	Heavy
in	Inside
L	Light
max	Maximum
obs	Observation
out	Outside
s	Shock
u	Unburned gas (fresh mixture)

Chapter 1

Introduction

1.1 Problem definition

Consider a shock wave, i.e., a wave characterized by an abrupt pressure change, passing through a flame front consisting of a density interface supported by exothermic reactions which travels at subsonic speed as shown in Fig. 1.1. The problem of shocks interacting with flames has long been recognized as of prime importance in most reactive compressible flows. It is central to practical problems such as deflagration to detonation transition (DDT) [1]. In fact, accidental releases of highly combustible mixtures may result in strong explosion scenarios; for a given reactive mixture, the interaction can lead to ignition, flame acceleration to a supersonic speed and ultimately a transition from a deflagration to a detonation. On the other hand, the interaction of shock waves with flames has been proposed to promote fuel/oxidizer mixing for supersonic propulsion applications [2].

It is known that the interaction strongly disrupts the flame surface through shock-induced Rayleigh-Taylor (RT) instability, or Richtmyer-Meshkov (RM) instability, hence enhancing turbulent mixing and amplifying local combustion rates. However, it is still not clear how the interface distortion occurs for a flame perturbed by a shock wave. The shock-flame complex is comprised of multiple phenomena on different time scales, ranging from combustion time scales to flow instabilities which develop rapidly. In spite of its fundamental importance, previous experimental studies could not isolate the interaction in

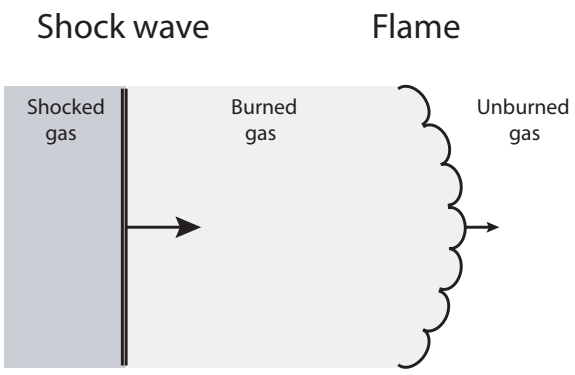

Figure 1.1: Problem investigated: a shock wave interacting with a flame front.

a canonical configuration devoid of secondary effects. This work seeks to better understand how a flame front evolves following a perturbation caused by a shock wave at early times.

1.2 Background information

Since the pioneering work of Markstein [3], the problem of the interaction between shocks and flames has been investigated experimentally and numerically. Markstein [4] studied the distortion of flames after the interaction with shock waves of different pressure ratios in shock-tubes and combustion chambers. Figure 1.2 shows the classical results of a shock-flame interaction in a shock tube obtained by Markstein. These tests were conducted in butane-air mixtures at stoichiometry and ambient pressure conditions. The first frame (top left) shows the downward-propagating shock wave and a curved flame initiated from the bottom of the shock tube. The following frames highlight the interaction of the incident shock wave with the smooth flame front, causing its folding and corrugation. A second interaction occurs eventually as the reflected shock perturbs the flame interface. The latter lead to a highly turbulent flow comprised of fine scale structures on the flame surface which complicates the observation of the shock-flame complex. In Figure 1.3, one can discern the elongation of an unburned gas funnel as a result of the initial interaction of the incident shock with the curved surface of the flame. The penetration of this unburned gas funnel in the burned gas is a characteristic of shock-flame interactions and will be discussed in Section 1.3.2. From this result, Markstein observed the reversal of the original flame shape

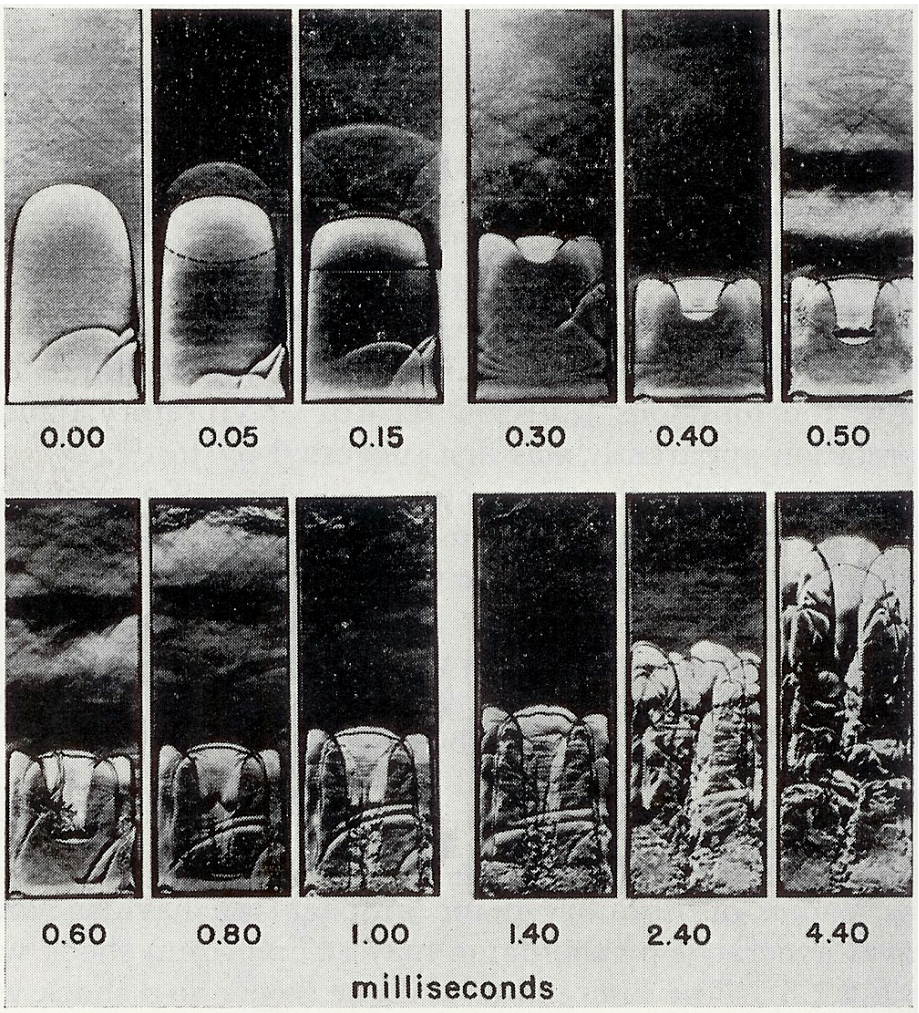

Figure 1.2: Sequence of spark photographs taken from Markstein [4] of the interaction between a stoichiometric butane-air flame and a shock wave highlighting flame acceleration throughout the process.

owing to the conditions of his experiments for a head-on colliding shock wave.

Rudinger [5] performed similar experiments of a shock wave interaction with a nearly spherical flame, as shown in Fig. 1.4. On the third frame, the funnel of unburned gas punctures the flame and later evolves as a vortex ring. A turbulent flame brush appears as a result of the subsequent interaction with the reflected shock. At this point, it becomes difficult to distinguish the three-dimensional flame surface.

Thomas *et al.* [6] examined the macroscale deformation of a spherical flame bubble with a side-on incident shock wave, leading to flame folding and the transition to detonation. Figure 1.5 illustrates the result for an experiment in a mixture of ethylene-oxygen with 50%

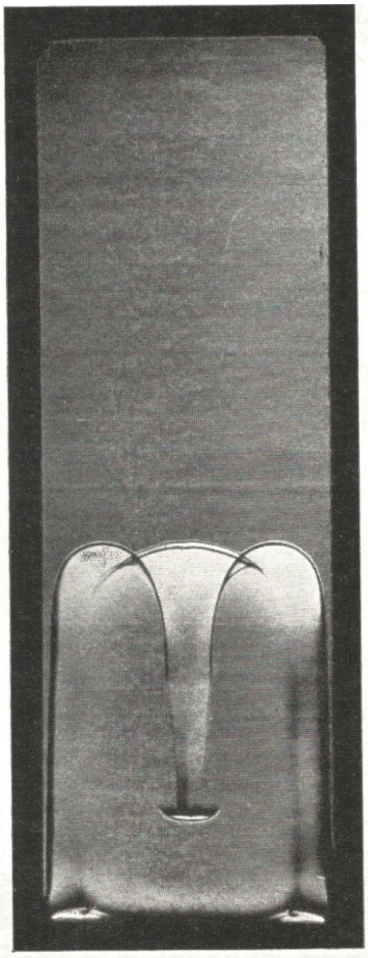

Figure 1.3: Selected spark photograph from Markstein [4] showing the formation of flame funnel following the passage of a weak shock wave on a butane-air flame front.

of nitrogen at 13.33 kPa. From the first frame, the incident shock is noticeable from the left side and a spheroidal flame devoid of irregularities is ignited through a set of electrodes. As the shock interacts with the flame, the interface separating the burned and unburned gases gets flatten significantly and reverses through the course of time in the next frames after the incident shock traverses the flame entirely. In the left-hand column, a second interaction occurs with the distorted flame kernel upon reflection of the transmitted shock on the end wall of the tube. Thomas and his colleagues were able to observe the same visual characteristics for the flame deformation and the reversal of the surface in a canonical configuration.

In these studies, the interaction generally lead to complex flow. The event became

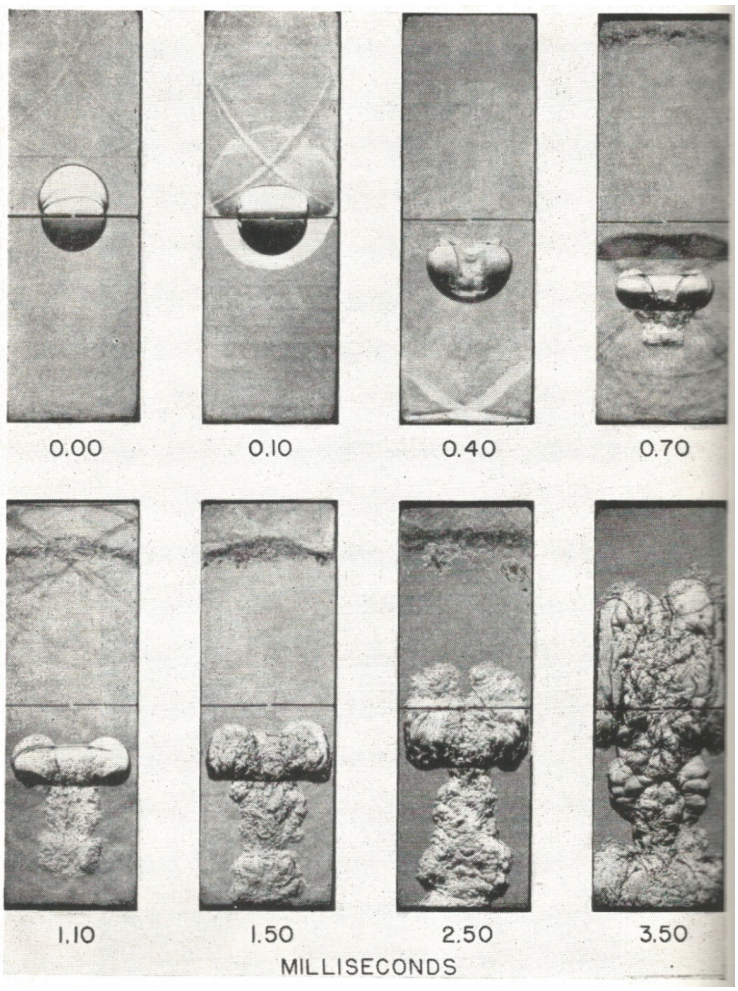

Figure 1.4: Schlieren images of a weak shock wave interacting with a spherical flame of butane-air at stoichiometry in a combustion chamber [5]. The initial smooth flame was ignited at the center of the apparatus. Taken from Rudinger.

difficult to monitor due to large deformations of the flame bubble, rapid folding of the flame surface, secondary interactions and three-dimensional effects.

Numerical studies have mostly dealt with a shock-bubble configuration [7, 8] and the chemically reacting RM instabilities on the flame cusps [9, 10, 11, 12] which is responsible for the flame distortion. Picone and Boris showed the roll-up feature of the interface caused by the generation of vorticity from the passage of the shock wave [8]. Khokhlov *et al.* [9] identified the RM-driven instability as the main mechanism for the flame distortion. Although a single interaction caused the mixing of unburned and burned gases, significant enhancement of the burning rate and acceleration of the flame are achievable only by the

passage of multiple shocks through a flame as noted by Khokhlov *et al.* [9]. Numerical results from Massa and Jha [10] showed that smaller scales were damped by chemical reactions and may have affected the growth on the flame interface. Attal *et al.* [11] recognized that the non-linearity and Rayleigh-Taylor flow are expected to influence the growth of perturbations on the interface. Jiang *et al.* reported the competitive effects of combustion and flow time scales on the evolution [12] at late times. Although previous investigators were able to address the problem of shock-flame interactions numerically, it is of interest to isolate experimentally the shock-flame complex where both the shock and flame are flat and parallel, and the interaction is along the normal direction, i.e., head-on.

In practice, flames are almost always subjected to hydrodynamic and thermal diffusive instabilities by nature and take on a cellular structure [13], as shown in Fig. 1.6. This work will thus focus on the shock-flame interaction for flames developing a cellular front, which in turn provide the seeds for RT and/or RM instabilities. In an attempt to overcome limitations of three-dimensional effects on the shock-flame interaction, the Hele-Shaw geometry has proven to be an efficient type of apparatus to isolate the cellular structure of a flame in a two-dimensional fashion to study flame instabilities in the past. The experimental rig consists of two closely separated surfaces forming a narrow channel, allowing for quasi-two dimensional evolution of the flow. For example, Sharif *et al.* [14] analyzed the thermal expansion and the buoyancy effects of a flame propagating in a Hele-Shaw cell. More recently, Almarcha *et al.* [15] studied the transition of a flat to a wrinkled flame propagation in a vertically-oriented Hele-Shaw cell consisting of two closely separated parallel plates. Fig. 1.7 shows their striking result where a self-luminous propane-air flame develops a cellular structure over time, giving birth to flame cells on its front and merging cusps. In order to visualize the cellular structure of the flames, the Hele-Shaw geometry consisting of a thin channel is thus adopted in the present work. This technique allows for the study of the cellular instabilities on the flame front in a quasi-bidimensional fashion.

In real life situations, steady shocks with vanishing pressure and velocity gradients and uniform properties are rarely present in accidental scenarios. Shock waves are rather formed as blast wave due to boundary conditions. A blast wave is driven by the rapid

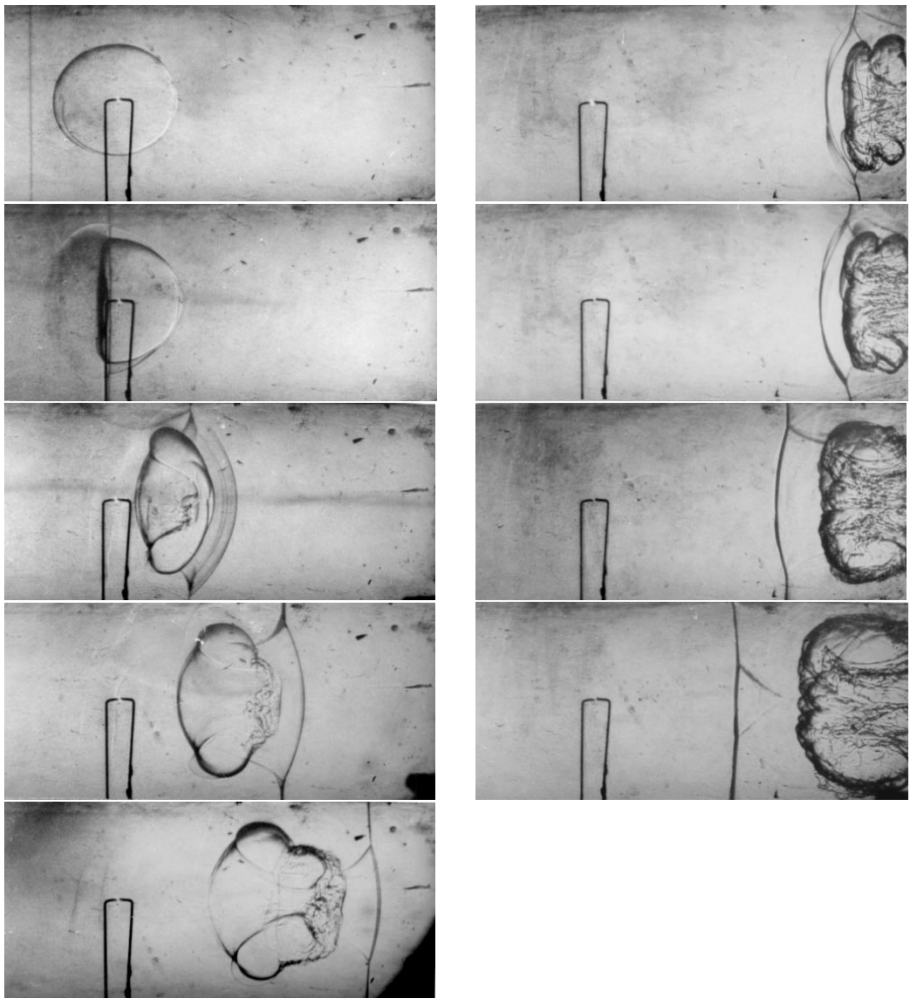

Figure 1.5: Sequence of Schlieren frames for the initial distortion of a flame bubble by a $M_s = 1.7$ shock wave taken from Thomas *et al.* [6]. Mixture of C_2H_4+$3O_2$+$4N_2$. Frame interval of 50 μs. The left column shows the interaction of the incoming incident shock, while the right column depicts the subsequent interaction of the distorted flame bubble with the reflected shock.

expansion of gasses as some energy is instantaneously released in a medium. Such an unsteady shock typically consists of a rising discontinuity at the leading front followed by a decaying phase, in which the pressure and particle velocity decrease give rise to expansion waves behind the leading front. Eventually, the overpressure decays to reach the ambient pressure. Currently, studies describing the interaction of blast waves with cellular flames currently do not exist to the best of the author's knowledge. Therefore, this work addresses the problem of a blast wave interaction on a cellular flame.

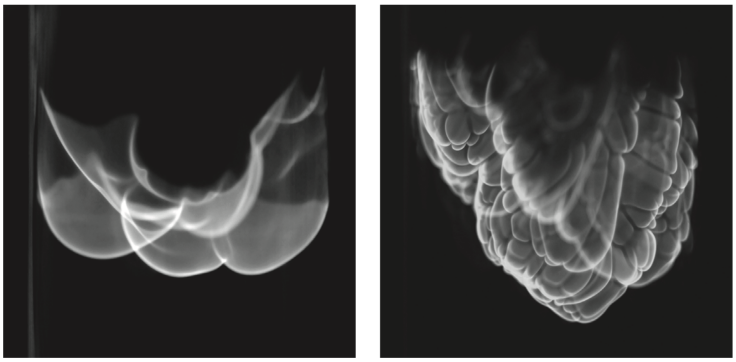

Figure 1.6: Cellular structure of laminar premixed flames of propane-air [16].

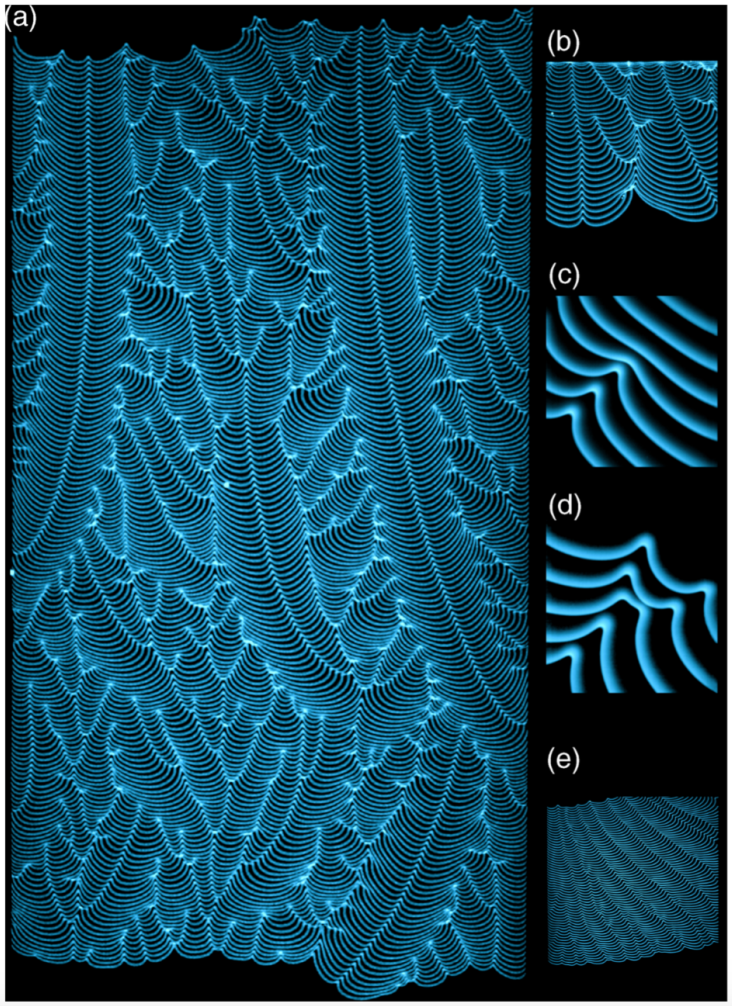

Figure 1.7: Superimposed frames of the time evolution of a premixed propane-air flame at stoichiometry in a Hele-Shaw cell. The initial cellular flame front travels from top to bottom [15].

1.3 Flow instabilities

Previous experimental and numerical studies in the literature have determined that the Richtmyer-Meshkov instability is responsible for the distortion of the flame after its interaction with a shock wave. It was also suggested that two instabilities mainly deform the interface separating the gases of different densities, namely the Rayleigh-Taylor and the Richtmyer-Meshkov instabilities [17, 16].

1.3.1 Rayleigh-Taylor instability

Two layers of heavy and light fluids as shown in Fig. 1.8a are initially at rest and separated by a slightly sinusoidal interface. The Rayleigh-Taylor instability occurs when the heavier fluid on top is accelerated into the light one lying at the bottom. The interface first deforms with an exponential growth by vorticity generation by the baroclinic torque mechanism of misaligned pressure gradient and density gradient as illustrated in Fig. 1.8b. Neglecting the viscous effects and external forces, the baroclinic production term $\vec{\nabla}\rho \times \vec{\nabla}p$ appears in the simplified vorticity equation for a compressible fluid $\dfrac{\mathrm{D}\vec{\omega}}{\mathrm{D}t} = \frac{\partial\vec{\omega}}{\partial t} + (\vec{u}\cdot\vec{\nabla})\vec{\omega} = (\vec{\omega}\cdot\vec{\nabla})\vec{u} - \vec{\omega}(\vec{\nabla}\vec{u}) + \dfrac{1}{\rho^2}\vec{\nabla}\rho \times \vec{\nabla}p$, where $\vec{u}$, ρ and p are the local flow velocity, density and pressure, respectively. Therefore, the heavy fluid penetrates into the light fluid, while the light fluid rises in the heavier material. It should be noted that the interface is only unstable if the heavy fluid is accelerated into the light fluid; for the opposite acceleration direction, the interface is stable and may oscillate if perturbed.

Sharp [18] divided the growth of Rayleigh-Taylor instability according to four different stages. The first stage is characterized by an exponential growth and can be determined using linear stability theory. The early time growth rate of the instability derived by Taylor [19] is

$$\sigma_{\mathrm{RT}} = \sqrt{k\ At\ a} \tag{1.1}$$

where $k = \frac{2\pi}{\lambda}$ is the perturbed wave number, λ is the wavelength, $At = \frac{\rho_{\mathrm{H}}-\rho_{\mathrm{L}}}{\rho_{\mathrm{H}}+\rho_{\mathrm{L}}}$ is the

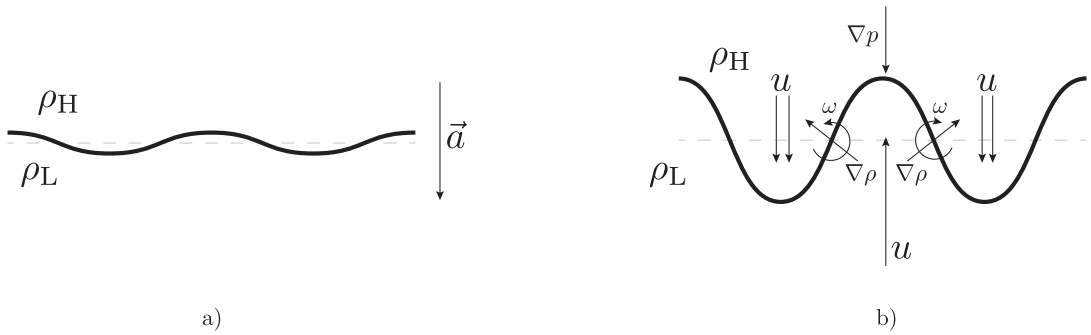

Figure 1.8: Development of Rayleigh-Taylor instability for an accelerated density interface by vorticity generation.

Atwood number and a is the acceleration. The second stage gives rise to non-linear effects and the perturbed interface starts to be influenced by three-dimensional effects. During the third stage, shear layers develop along the contact surface of the spike of light fluid. Kelvin-Helmoltz instability starts to grow owing to the difference in velocity between the two sides of the interface. This stage is also characterized by the formation of rolled-up features forming a "mushroom" shape. Ultimately, the interface develops fine structures and deforms significantly through turbulent mixing.

1.3.2 Richtmyer-Meshkov instability

The shock-induced Rayleigh-Taylor instability arises when a density interface is impulsively accelerated by a shock discontinuity, and is referred as the Richtmyer-Meshkov instability. The mechanism of distortion is similar to the Rayleigh-Taylor instability, i.e., by baroclinic torque caused by the misalignment of the pressure gradient of the shock wave and density gradient across the interface between two fluids of different densities. The passage of the shock wave across the density interface deposits vorticity, allowing the interface to deform linearly with the formation of spikes of heavy fluid, and bubbles of light fluid at early times (see Fig. 1.9a-c). The growth rate of the instability [20] derived from linear perturbation theory is defined such that

$$\sigma_{\mathrm{RM}} = k\ At\ [u] \tag{1.2}$$

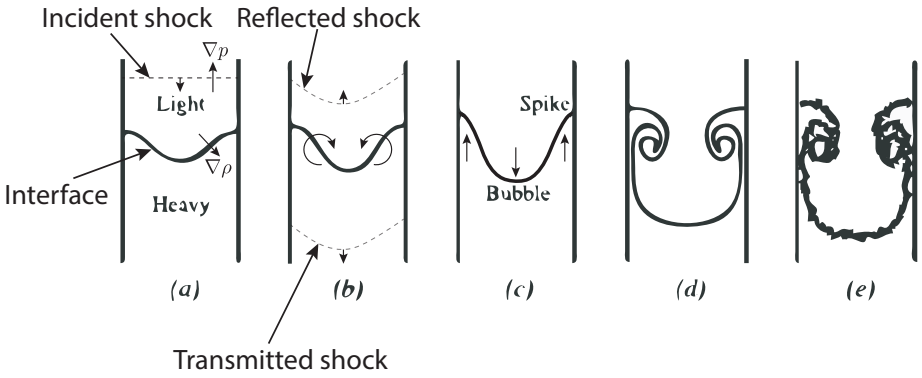

Figure 1.9: Time evolution of Richtmyer-Meshkov instability on a density interface. Adapted from Brouillette [20].

where $k = \frac{2\pi}{\lambda}$ is the perturbed wave number, λ is the wavelength, $At = \frac{\rho_H - \rho_L}{\rho_H + \rho_L}$ is the Atwood number and $[u]$ is the velocity of the interface imparted by the passage of the shock wave. As the amplification of the perturbations progresses, vortices start to develop at the tip of the spikes and the evolution shifts in the non-linear phase as shown in Fig. 1.9d. Finally, the interface mixes with turbulent motions. The Richtmyer-Meshkov environment is always unstable and does not rely on the direction of propagation of the shock.

1.4 Motivation and objectives

With the advent of a hydrogen industry deployment, the combustion behaviour of hydrogen-air mixtures is of interest in the case of accidental scenarios in industrial explosions and/or propulsion systems. Additionally, the low flammability limit for hydrogen fuel mixed with air are a concern for safer combustion environments. Hydrogen-air flames are propitious to develop a cellular structure at a small critical radius ($R_c \sim$ few centimeters) compared to other reactive mixtures, such as propane-air mixtures [21]. Thus, the sensitivity of this mixture allows for small scale visualization, which does not require large scale apparatus or high pressure to achieve the desired cellular flame structure.

In the present study, two novel Hele-Shaw geometries, whereby a cellular flame of

(a) Interaction from the light to heavy gas. (b) Interaction from the heavy to light gas.

Figure 1.10: Schematics of the problem definition.

hydrogen-air interacts with a blast wave head-on, are proposed. The passage of the decaying shock wave in both directions is investigated: from the burned to the unburned side, and *vice-versa*, as illustrated in Figs. 1.10a and 1.10b, respectively. The goal of the study is to monitor the flame deformation subsequent to the interaction on flame time scales and the ensuing lengthening of the flame sheet to elucidate the physical mechanisms that control the dynamics.

1.5 Thesis outline

The present thesis is organized as follows. The details of the experimental procedure for isolating the shock-flame interaction are described in Chapter 2, along with the visualization system used and the shock characterization. The visualization of hydrogen-air deflagrations in the the Hele-Shaw cell is reported in Chapter 3 without the interaction with a blast wave. In Chapter 4, experiments are presented involving the interaction of a blast wave emerging in the burned (light) gases with a cellular flame, while varying the hydrogen content concentration. Preliminary results for the interaction of a blast wave with a cellular flame with the shock wave developing in the unburned (heavy) gases are outlined in Chapter 5. Chapter 6 presents the comparison of experimental results with numerical calculations to give insight into the controlling instability mechanisms. Finally, Chapter 7 summarizes the current study and suggests potential avenues for future investigations.

Chapter 2

Experimental method

The present chapter provides an overview of the experimental procedure to study the quasi-bidimensional interactions between a blast wave and a cellular flame. The implementation of the apparatus and its limitations are described along with the optical visualization system. Shock dynamics in the experimental set-up are also presented.

2.1 Hele-Shaw cell

The experiments were undertaken in a vertically oriented Hele-Shaw cell. The vessel consisted of two optically clear acrylic plates with a diameter of 280 mm and a thickness of 17.5 mm to allow for the observations of the combustion event and the subsequent interaction with the shock wave. The gap width was achieved by inserting eight spacers having a thickness of 5 mm along the circumference of the apparatus. The size of the gap was chosen to avoid the development of flame cells in the third dimension. The distance also insured that premixed flames would not quench as they propagated in the vessel. The Hele-Shaw apparatus was equipped with a 0.15-mm thick cylindrical latex sheet on its circumference to allow for sealing and for a nearly constant-pressure evolution as the sheet deforms with the expansion of the burned gas. The sealing was provided by compressing the latex sheet and an o-ring into a groove with worm gear clamps. An inlet port was machined on the back plate to empty the cell of any gases, to fill the reactive mixture

and to evacuate the remaining products after the experiment. The front plate also had a port at the center point to mount the equipment to generate the shock wave. The vessel was positioned on the optical table and was kept in place by using aluminum 6061 L-shape brackets. The experiments were performed at ambient conditions, i.e., atmospheric pressure and temperature.

The experiments were conducted according to two different configurations using a single spark ignition for the light to heavy gas interaction, and with multiple ignition points to reproduce the interaction from the heavy to light gas side.

2.1.1 Single spark ignition

Fig. 2.1 shows the Hele-Shaw cell with a single point ignition. This configuration aimed to reproduce a head-on interaction of the flame with the shock wave propagating from the burned gases to the unburned. A pair of thin copper strips were attached inside the vessel, and connected to a trigger module (EG&G Trigger Module - Model TM-11). The ignition was triggered by a transistor-transistor logic (TTL) signal from a pulse generator (Berkeley Nucleonics - Model 575 Digital Delay) to control time intervals for synchronization with the visualization system. The electrodes ignited the reactive mixture with a weak spark at the center point of the vessel and a shock wave was initiated subsequently from the same location. Both the flame and the shock propagated in the same outward direction. When the flame reached close to the boundary of the Hele-Shaw cell, the latex sheet expanded noticeably and ruptured on some occasions.

2.1.2 Multiple sparks ignition

A second configuration was built to study the interaction of the flame following the passage of the shock wave through its interface from the unburned gases to the burned gases as shown in Figure 2.2. The ignition plate was embedded with eight ignition points along the edge of the circular acrylic plate in a symmetric fashion. The sets of electrodes were connected individually to their own spark gap igniter and the arrangement was powered

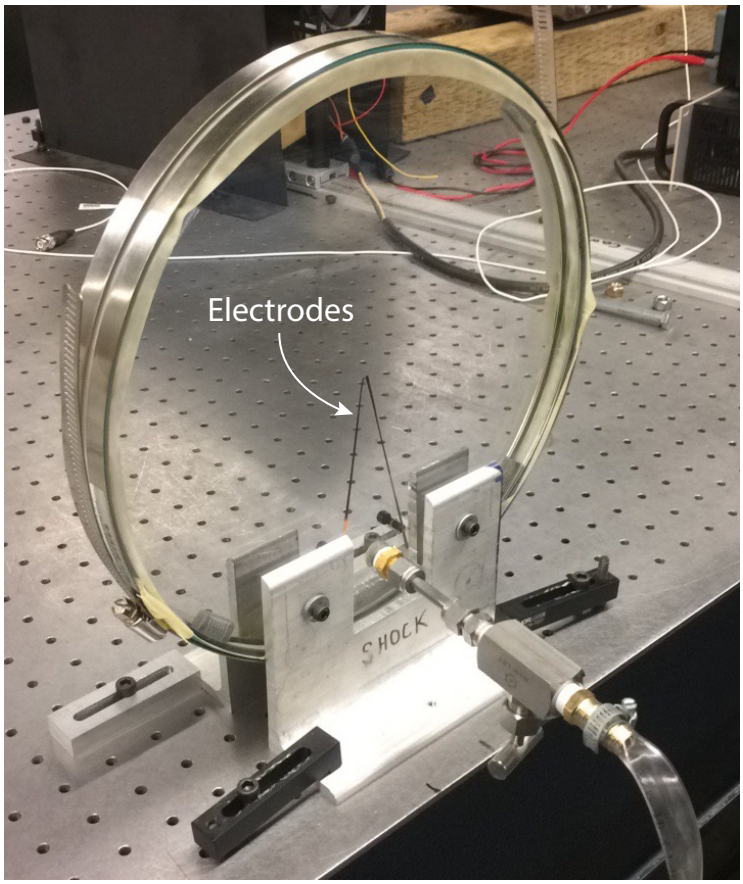

Figure 2.1: Hele-Shaw apparatus with a single point ignition.

by a 6-V 12-AH sealed lead acid battery capable of high current discharge. The ignition was triggered by a TTL signal from the pulse generator unit with a 30 ms pulse width. The electrodes ignited the reactive mixture with a set of weak sparks along the vessel's edge, allowing the flame to propagate towards the center of the Hele-Shaw cell. When the flame had traveled sufficiently, a shock wave was generated from the center point of the Hele-Shaw, and the interaction occurred in the opposite direction.

2.1.3 Gas mixture preparation and handling

Four different compositions of H_2-air mixtures at $\phi = 1$, $\phi = 0.6$, $\phi = 0.3$ and $\phi = 0.18$ were tested in the Hele-Shaw cell. The reactive gas mixture was prepared using the partial pressure method upon determining the composition. Hydrogen, nitrogen and oxygen from high pressure cylinders were respectively introduced in a 45-L mixing tank at 2 bar using

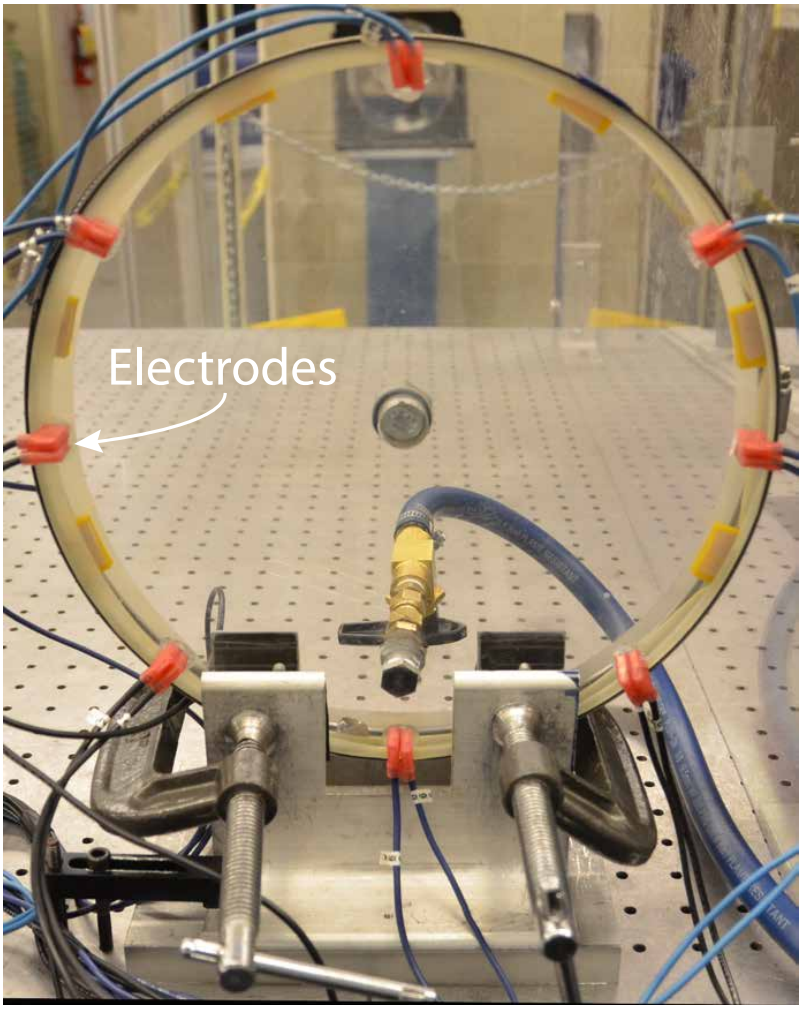

Figure 2.2: Hele-Shaw apparatus with eight ignition points.

a manifold. After filling the components, the mixture was left to diffuse for a day. When conducting experiments, the vessel was first evacuated to a pressure of 80 Pa. Then, the reactive mixture from the mixing tank was filled in the cell at ambient pressure. After conducting the experiment, combustion products in the Hele-Shaw cell were emptied before the fresh reactive mixture was introduced for the next test. Experiments were conducted with time intervals of around half an hour.

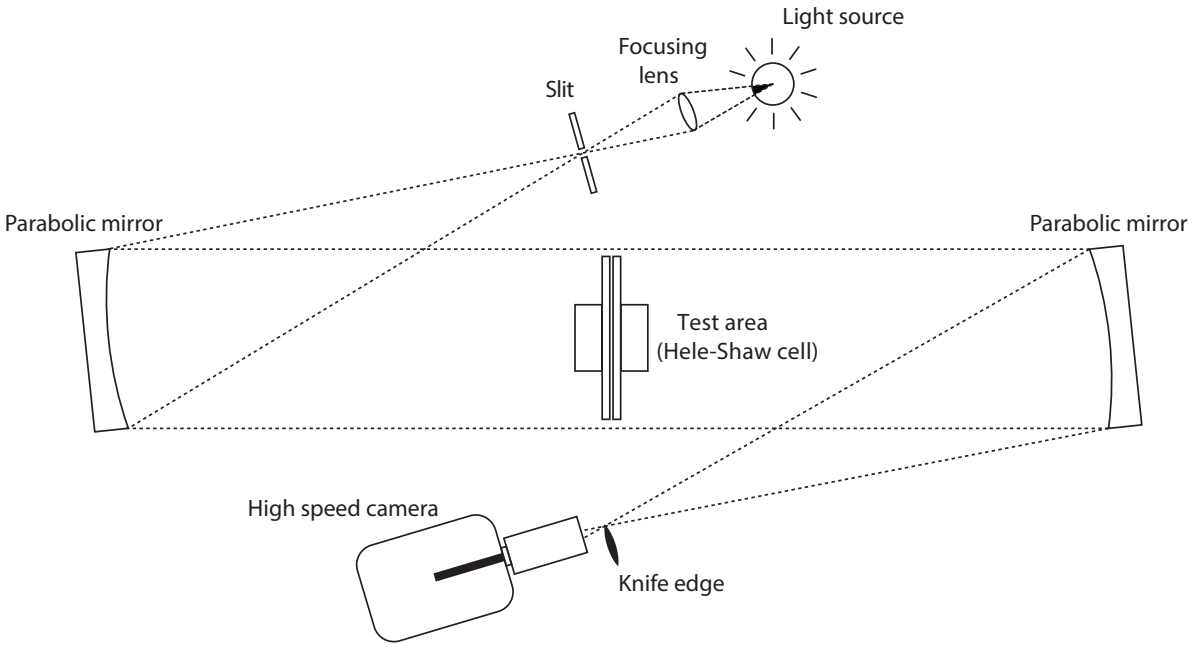

Figure 2.3: Schematic of the Z-type Schlieren optical system.

2.2 Visualization

To visualize the event, a Z-type Schlieren system [22] was implemented to capture the horizontal density gradients and the image sequence was recorded using a high speed camera (Phantom v1210) as shown in Fig. 2.3. The light emitted from a 360-watt light bulb was focused through a slit at the focal point of the first parabolic mirror. The parallel beam of light was then oriented to the second parabolic mirror while traversing the test area. The second mirror condensed back to the focal point using a knife edge positioned at the focal point of the mirror to cut half of the image. Finally, the light was further expanded to the high speed camera sensor. The camera lens was focused to infinity with a $f/2.8$ aperture. The frame rate was varied from 3,000 to 104,918 frames per second (fps) with a resolution from 256 $\times$ 256 pixels to 1280 $\times$ 800 pixels. The exposure time was set to 0.468 μs and the field of view of the $\lambda/8$ parabolic mirrors was 317.5 mm.

2.3 Shock dynamics

In order to study the shock-flame complex, a decaying shock wave was initiated in the center of the Hele-Shaw vessel and propagated outward in all cases. Two different methods were implemented to produce the decaying shock wave, i.e., a high-voltage igniter and a detonation tube.

2.3.1 High voltage igniter

The high voltage igniter (HVI) is primarily comprised of a capacitor bank and a spark gap. The discharge characteristics have been well documented elsewhere [23, 24]. The unit, which had a total nominal energy of $E = \frac{CV^2}{2} = 400$ J, was triggered to release 5 J of energy in less than 2 μs through a set of copper electrodes separated by a 3-mm gap thus creating a shock wave from the center of the Hele-Shaw vessel. A series of tests were conducted to determine the strength of the shock before its passage through the flame interface. The characterization was done for a cylindrical shock between the parallel plates. Fig. 2.4 shows the shock generated by the discharge of the HVI between two parallel plates separated by a 5-mm gap. In the first frame, the capacitors were discharged and the energy was deposited through the set of electrodes in air at ambient conditions. In the subsequent frames, the outwardly expanding blast wave was noticeable through the end of the image sequence.

2.3.2 Detonation tube

However, the HVI's electrodes emitted a bright amount of light during the discharge and altered the Schlieren visualization in the early stages of the interaction with the flame interface when the radius was sufficiently small. Thus, a small detonation tube was also designed to overcome this drawback.

The detonation tube arrangement was built from 316/316L stainless steel tubing with an internal diameter of 3 mm. The total length of the tube assembly is 1.16 m. The end

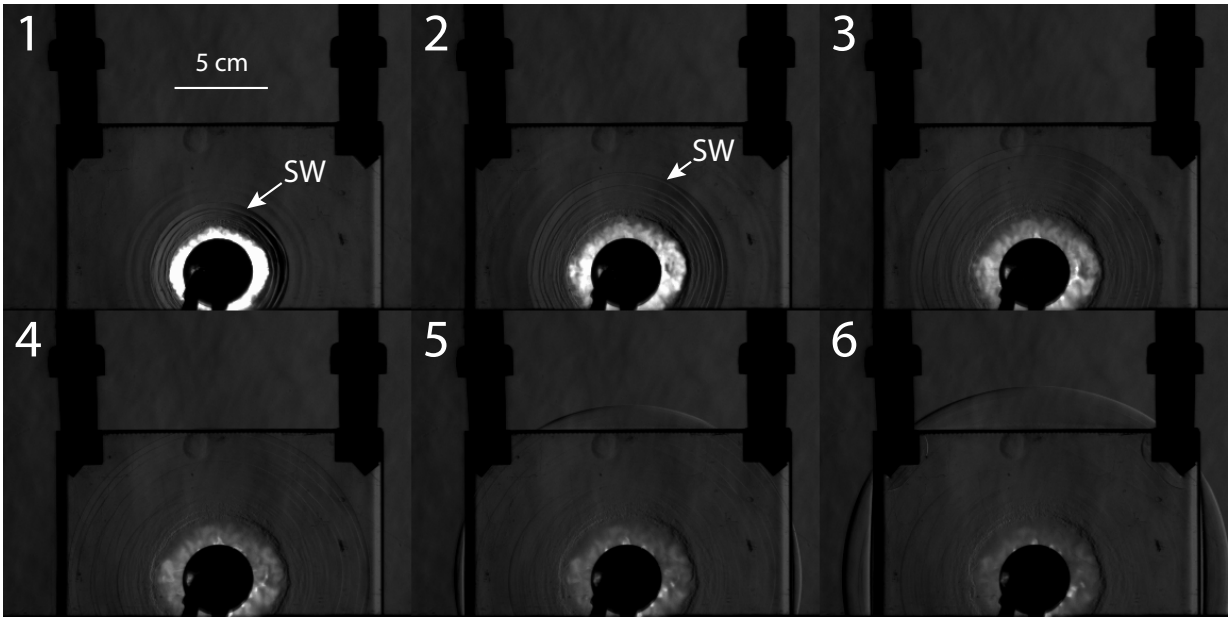

Figure 2.4: Sequence of Schlieren images of a cylindrical shock wave between two separated parallel plates. The gap width is 5 mm. The video was recorded at 77,481 fps, with an exposure time of 0.468 μs and a resolution of 324 $\times$ 288 pixels. The time interval is 25.8 μs. The averaged Mach number is 1.95.

of the detonation tube was isolated with a thin aluminum diaphragm and attached to the Hele-Shaw vessel. The diaphragm acted as a seal to contain the reactive mixture inside the detonation tube. Figure 2.5 shows the detonation tube arrangement with the Hele-Shaw vessel. The shock wave which emanated from the outlet of the tube was driven by a detonation wave consuming the reactive mixture inside the tube. First, the tube was evacuated to a pressure below 80 Pa and filled with a stoichiometric mixture of ethylene-oxygen at atmospheric pressure. An automotive spark plug ignited the highly reactive mixture and a combustion wave propagated through a Shchelkin spiral with a 44% blockage ratio. The wire spiral had the purpose to enhance the deflagration transition to a detonation wave. Then, the detonation traveled throughout last portion of the tube towards the outlet section as it consumed the fresh detonable mixture. Upon breaking the aluminum diaphragm, the detonation wave diffracted and the shock wave was decoupled from the reaction zone. The generated shock finally propagated in the Hele-Shaw cell radially from the center to the edge of the vessel.

Two piezoelectrical pins (Dynasen - Time-of-arrival pins CA-1135) were positioned in

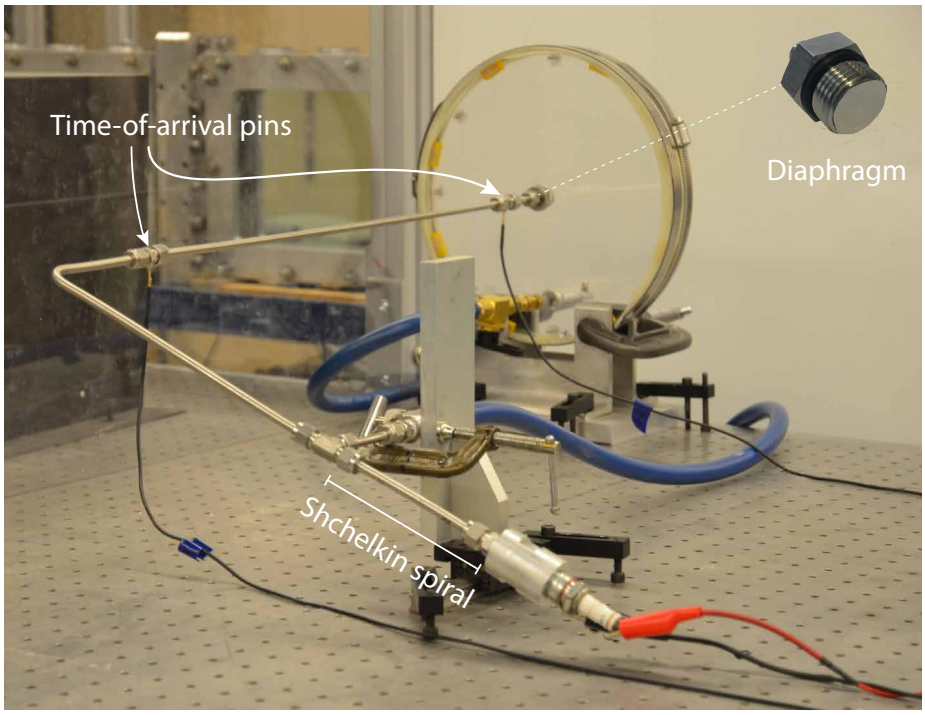

Figure 2.5: Small detonation tube assembly with Hele-Shaw cell.

the last section of the detonation tube to measure the time-of-arrival of the wave (see Fig. 2.5). The characterization of the wave velocity was done using an oscilloscope (LeCroy - WaveSurfer 24Xs-A) at a sampling frequency of 250 MHz. The detonation wave velocity was determined by measuring the displacement of the wave over two distinct time stamps on a short period of time after ignition of the reactive mixture in the tube. Additionally, the velocity of the decoupled shock was measured using optical visualization after the detonation diffracted in ambient air. Table 2.1 outlines the overall results of the measurements for the velocity of the waves for the detonation tube attached to the Hele-Shaw cell. The velocity of the wave propagating inside the detonation tube was found to be in good agreement with the calculated Chapman-Jouguet (CJ) condition for a detonation using NASA Chemical Equilibrium Application Program (CEA) [25]. Therefore, the formation of a detonation within the tube provided a reproducible method to generate a shock wave. Figures 2.6 and 2.7 show the results of the blast wave propagation for the unconfined and confined geometries, respectively. The decoupled shock wave (SW) and burned products (BP) from the detonation products were discernible throughout both image sequences. Results showed that while the detonation wave propagated at $M \approx 7$ inside the tube, the

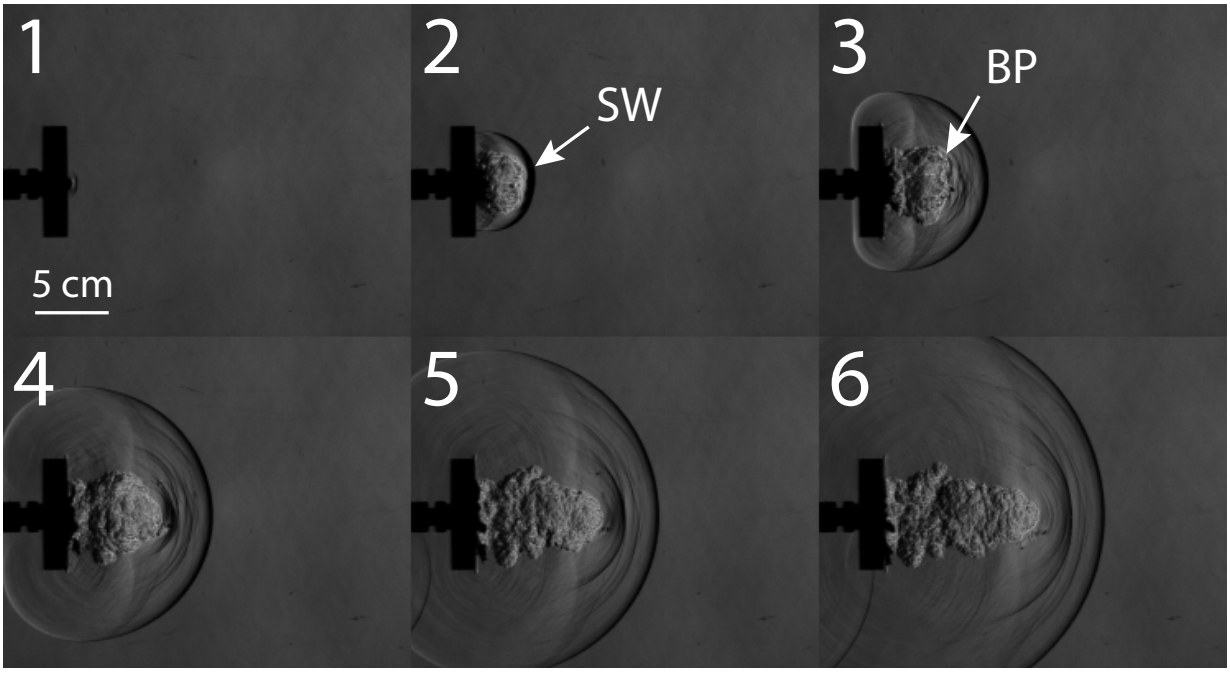

Figure 2.6: Schlieren images of shock wave from the detonation tube into the air. The reactive mixture is C_2H_4 + $3O_2$ at p_{in} = 1 atm. The video was recorded at 77,481 fps, with an exposure time of 0.468 μs and a resolution of 324 × 288 pixels. The inter-frame time is 51.6 μs. The resulting Mach number is 1.67.

decoupled shock wave traveled at $M \approx 2$ in air at ambient temperature and pressure after breaking the diaphragm.

Table 2.1: Velocity measurements for detonation and decoupled shock in the Hele-Shaw cell filled with air

Test ID	Date	p_0 (kPa)	T_0 (K)	D_{in} (m/s)	D_{CJ} (CEA) (m/s)	Error %	M_{in}	M_{out}
exp17	28/08/17	101.02	293	2662	2375	12.1%	8.2	2.2
exp18	28/08/17	101.08	293	2631	2375	10.8%	8.1	2.1
20170831-S1	31/08/17	101.08	294	2294	2375	3.4%	7.1	1.8
20170831-S2	31/08/17	101.42	294	2321	2375	2.3%	7.1	2.0
20170831-S4	31/08/17	101.28	294	2305	2375	2.9%	7.1	2.0
20171007-S1	07/10/17	101.08	294	2161	2375	9.0%	6.7	1.6

2.3.3 Numerical model for generating a shock wave

In an effort to compare the experiment using numerical simulations, the series of experiments for a shock wave in air was modeled using the energy release from hot products to drive a blast wave in the Hele-Shaw cell. The purpose of these simulations was to estimate

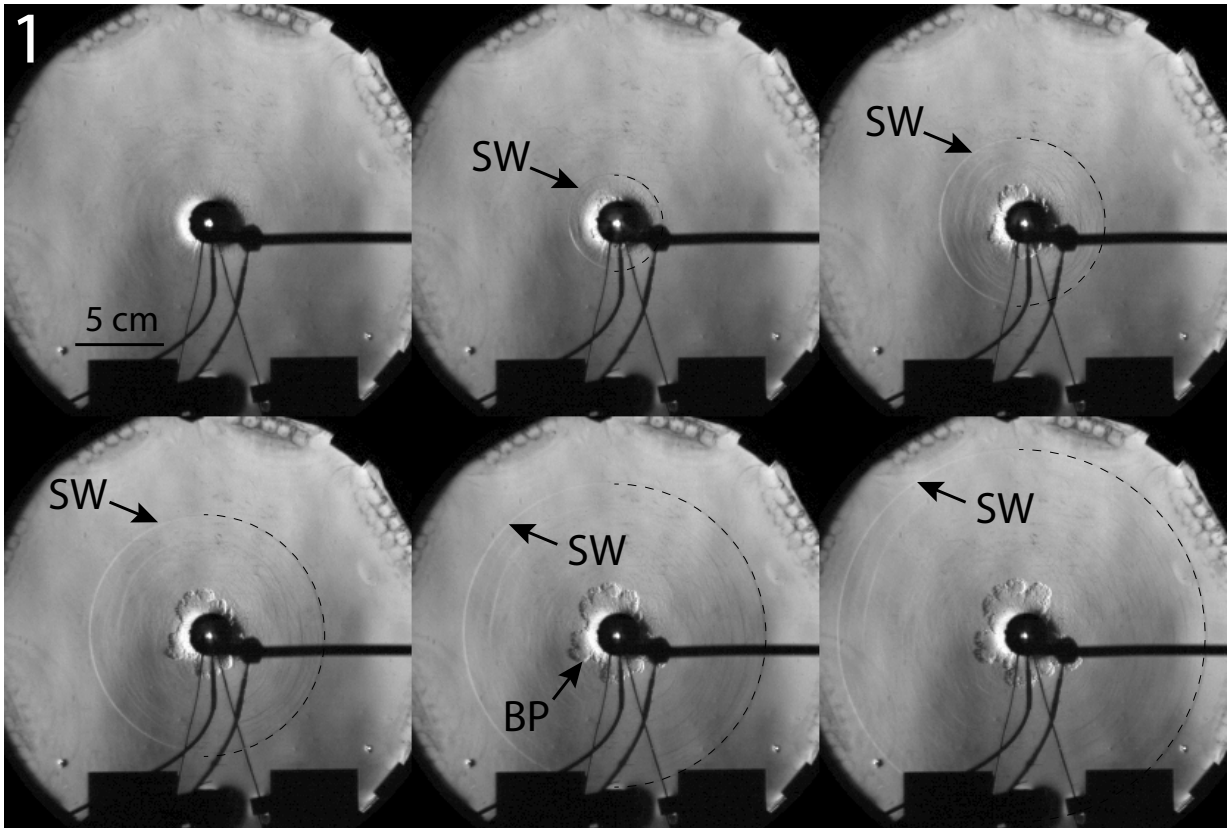

Figure 2.7: Schlieren images of shock wave (SW) from the detonation tube into the Hele-Shaw cell. The reactive mixture is $C_2H_4 + 3O_2$ at $p_{in} = 1$ atm. The video was recorded at 77,481 fps, with an exposure time of 0.468 μs and a resolution of 324 $\times$ 288 pixels. The inter-frame time is 51.6 μs. The resulting Mach number is 1.6.

the equivalent energy deposition in the system by fitting the shock decay obtained through calculation with experimental results. The energy release of the source by the expansion of hot products for a cylindrical slab of gas is given by the internal energy such that

$$E = \frac{p\,V}{\gamma - 1} \tag{2.1}$$

where p is the gas pressure, V is the volume of the cylindrical region of energy deposition and γ is the ratio of specific heats. The cylindrical volume is taken as $V = \pi {r_e}^2 w_{hs}$, where $r_e = 1.5$ mm is chosen as the half distance between the electrodes of the HVI or the diameter of the detonation tube, and $w_{hs} = 5$ mm is the thickness of the Hele-Shaw cell.

One-dimensional axisymmetric numerical simulations were conducted by varying the energy deposition, and thus the initial pressure in a small volume of the domain, to obtain

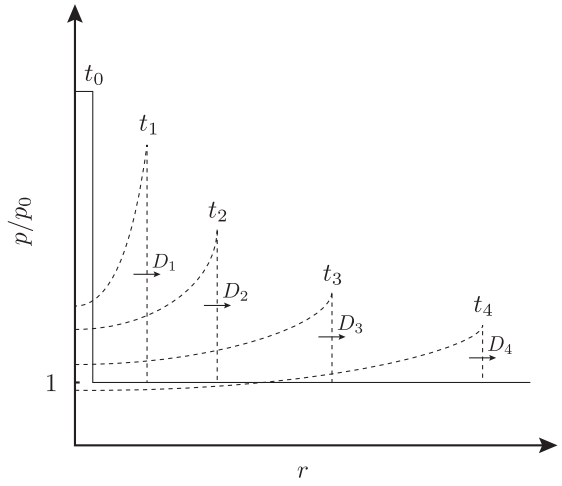

Figure 2.8: Cartoon of the over-pressure decay following an energy deposition using top hat pressure.

the shock decay along the radius of the Hele-Shaw in air. The Euler equations were solved using the MG code developed by Mantis Ltd. [26], a hydrodynamic code using a second-order accurate Godunov-type solver with adaptive mesh refinement. The problem was set up by initializing a top hat pressure region in the numerical domain ($p/p_0 \gg 1.0$), while keeping the density constant and the gas at rest. The remaining gas in the domain was initialized at ambient pressure ($p/p_0 = 1.0$). Thus, the high pressure was sufficient to drive a shock wave which decayed over time as shown in Fig. 2.8. The shock position was captured from the pressure peak profile emplacement to compute the shock velocity over time from numerical simulations.

Figure 2.9 shows experimental data points for the shock velocity decay in the Hele-Shaw filled with air at atmospheric pressure obtained for both the HVI and the detonation tube. The curves were computed from 1D numerical simulations using the model of energy release from a source from hot products in cylindrical polar coordinates. The error bars represent the uncertainty of the measurement using image velocimetry. The uncertainty of the shock velocity was determined using the propagation of error in space and in time. Since the inter-frame time of the camera is very small when capturing the event, the time uncertainty can be neglected when determining the uncertainty of the velocity, such that $\delta D_s = D_s \left(\frac{x_{\text{error}}}{\Delta x} \right)$, where δD_s is the uncertainty of the shock velocity, D_s is the calculated

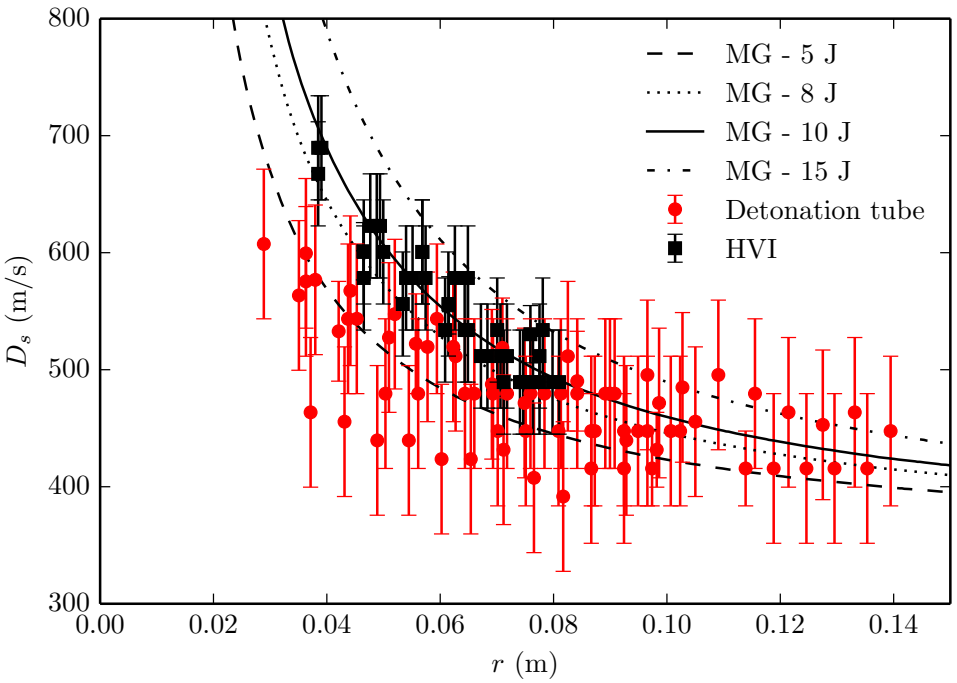

Figure 2.9: Cylindrical shock decay in air as a function of distance in the Hele-Shaw cell configuration.

shock velocity in the experiments, x_{error} is the position measurement uncertainty and Δx is the measured position of the shock. From this graph, an initial energy deposition of 10 J, represented by the solid curve, is in good agreement with experiments with the HVI. Alternatively, for experiments with the detonation tube, the same energy release model was used to fit an equivalent energy of 5 J.

The analysis of the shock dynamics indicated good control of the shock strength in the Hele-Shaw cell from both methods for generating the desired blast wave. The equivalent energies from 1D simulations were adopted to set up initial conditions for the forthcoming numerical simulations in two-dimensions. In the following, the term shock wave is referred to as blast wave to describe the interaction with a cellular flame.

Chapter 3

Flame dynamics

This chapter presents the results obtained for a cellular flame propagating in the Hele-Shaw cell. The equivalence ratio was varied to visualize the evolution of partially confined deflagrations and the development of their cellular structure with time.

3.1 Velocity measurements

A combustion study was first achieved to quantify the laminar flame speed of the flame from the videos in the Hele-Shaw cell without a shock wave. Consider a cylindrical flame expanding in a reactive mixture, as shown in Fig. 3.1a, at a velocity $\dot{R}_\mathrm{f}$ with burned gases at rest ($u_\mathrm{b} = 0$). In the frame of reference of the flame, the interface consumes the unburned mixture ahead. Thus, the conservation of mass flux across the flame requires that $\rho_\mathrm{b}\dot{R}_\mathrm{f} = \rho_\mathrm{u}S_\mathrm{u}$. The laminar flame speed is then

$$S_\mathrm{u} = \frac{\rho_\mathrm{b}}{\rho_\mathrm{u}}\dot{R}_\mathrm{f} \tag{3.1}$$

where S_u is the unburned gas velocity, ρ_b and ρ_u are the densities in the burned and unburned gases, respectively, and $\dot{R}_\mathrm{f}$ is the burned gas velocity. The velocity $\dot{R}_\mathrm{f}$ was measured by image velocimetry from the high speed videos using the ImageJ software for image processing. Spatial calibration was achieved by measuring a reference length on the

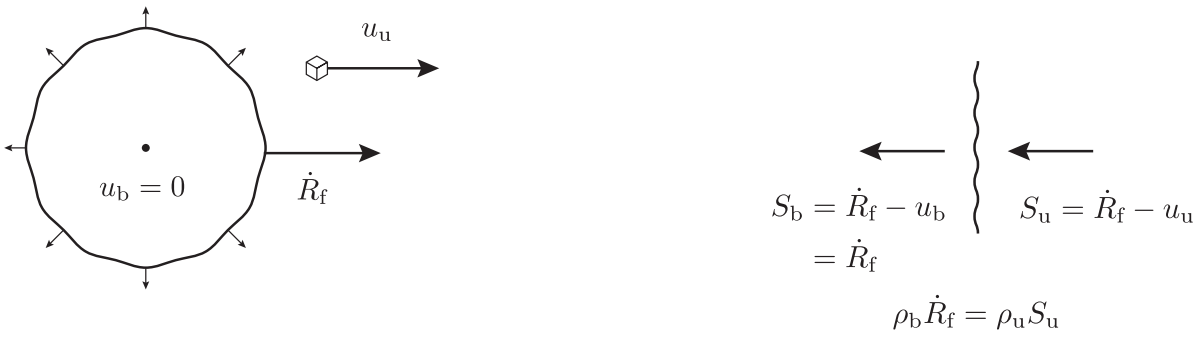

(a) Lab frame reference.

(b) Flame reference.

Figure 3.1: Flame speed schematics.

videos. The position of the flame surface was tracked from the image sequence, while the time interval between the frames was known *a priori* from the sample rate of the high speed camera. The displacement was thus taken as the slope from the $x - t$ curve to determine $\dot{R}_f$. The density ratio ρ_b/ρ_u was obtained from the Cantera package by solving the equilibrium state of the H_2-air mixture at constant pressure and enthalpy using the Li mechanism [27]. The laminar flame speed S_u was then computed using Eq. 3.1.

Figure 3.2 depicts the flame dynamics of a stoichiometric hydrogen-air mixture at ambient pressure and temperature conditions. In the early stages (frames 1 & 2), the flame surface remained nearly smooth and circular. Additionally, the flame propagated in a symmetrical fashion. In the third frame, cracks were noticeable on the wrinkled flame surface structure. Eventually, the deflagration wave took on a cellular structure as it consumed the fresh mixture ahead (frames 3 – 8). When the deflagration reached the edge of the circular plates, the latex sheet expanded due to the expansion of the burned products. The shape of the flame front was quasi two-dimensional, provided having a thin gap between the closely separated plates. The laminar flame speed extracted from the video was $S_u = 2.7$ m/s and remained nearly constant across the field of view. The flame speed from experiments was about 17% larger than the predicted value from Cantera's free flame calculation using the mixture-averaged transport model. The discrepancy can be explained by the confined geometry in two-dimensions of the experiment; the narrow channel will cause the curvature of the flame front to be larger locally, which translates into a greater velocity for flames

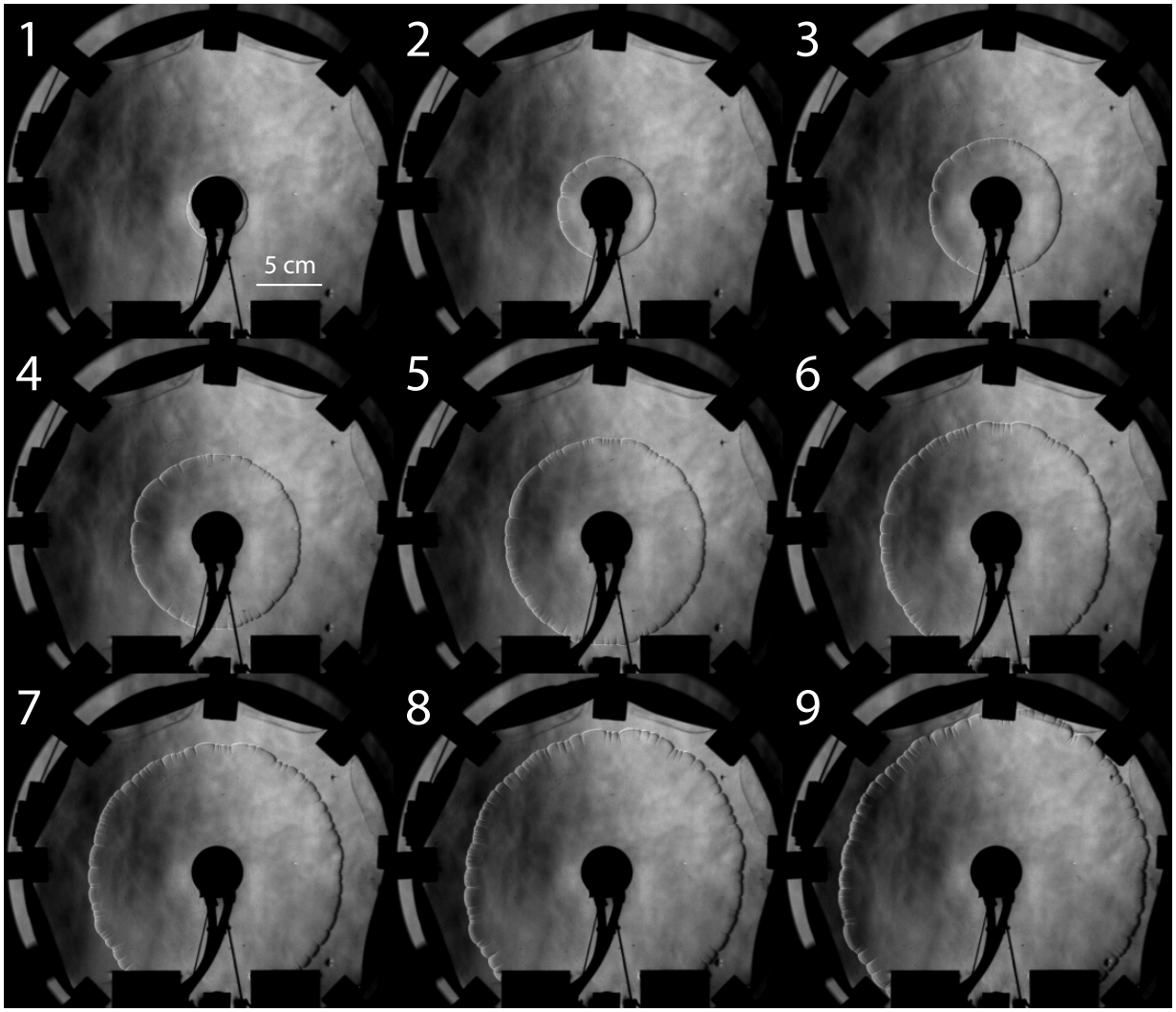

Figure 3.2: Schlieren images of a flame propagation in a H_2-air mixture at $\phi = 1.0$ in the Hele-Shaw cell. The video was recorded at 77,481 fps with an exposure time of 0.468 μs. The time interval between frames is 0.47 ms. The resolution is 324 $\times$ 288 pixels. The mixture was ignited at the center point of the vessel.

characterized by $Le < 1$.

3.2 Effect of the equivalence ratio

One approach to increase the cell size on the flame front is to reduce the hydrogen concentration to a lean mixture as the flame cellular size varies as a function of the flame thickness. Lean hydrogen-air premixed flames are also more prone to grow instabilities at

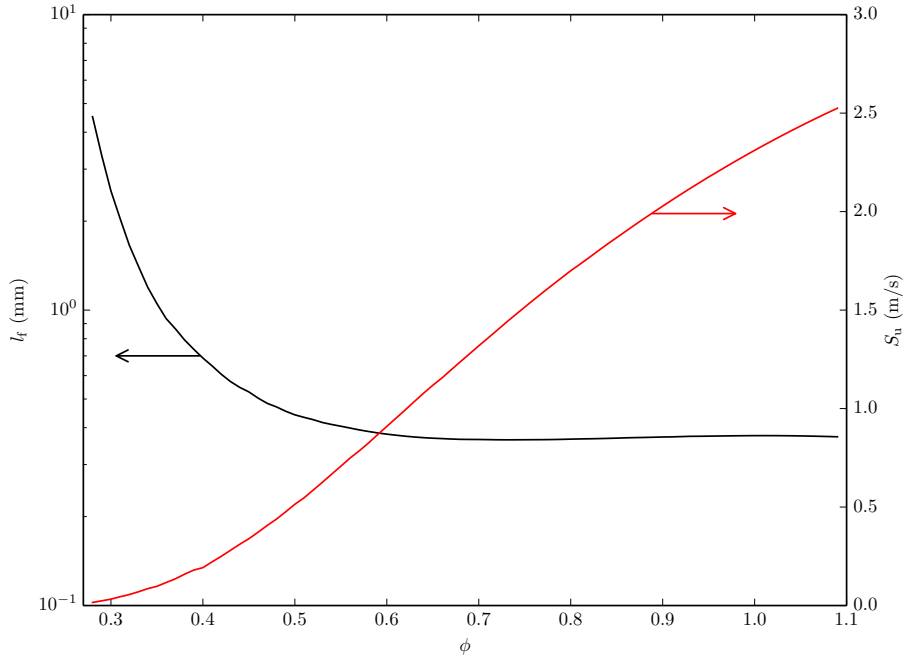

Figure 3.3: Flame thickness (black) and laminar flame speed (red) as a function of the equivalence ratio for hydrogen-air mixtures at $p_0 = 1$ atm and $T_0 = 300$ K using Cantera with Li mechanism [27].

a smaller observable scale as a result of the decrease in Markstein length at the prescribed atmospheric pressure. Those lean flames are characterized by $Le < 1$ which translates into a greater effect from thermo-diffusive instabilities on their surface. Thus, the flame thickness was evaluated for different equivalence ratios from Cantera calculations from the temperature gradient based on the profile of the flame structure, such that

$$l_\mathrm{f} = \frac{T_\mathrm{ad} - T_0}{\left(\mathrm{d}T/\mathrm{d}x\right)_\mathrm{max}} \tag{3.2}$$

where T_ad is the adiabatic flame temperature, T_0 is the initial temperature and $\left(\mathrm{d}T/\mathrm{d}x\right)_\mathrm{max}$ is the maximum temperature gradient obtained from the flame temperature profile. Figure 3.3 depicts the variation of the flame thickness according to the equivalence ratio of the hydrogen-air mixture. From this figure, one can observe that the flame thickness increases significantly towards the lean side when $\phi < 0.6$.

Therefore, three lean hydrogen-air mixtures were tested to observe the early onset of flame instabilities in the Hele-Shaw cell. The evolution of a deflagration wave in a mixture

of hydrogen-air at $\phi = 0.6$ is presented in Fig. 3.4. From the first frames (1–2 of the image sequence), the flame surface grew relatively smoothly. In the sixth frame, one can discern the emergence of a collection of cells forming larger cusps. The following frames illustrate a more wrinkled flame than the previous result for $\phi = 1.0$ as expected. In this experiment, the flame propagated at 2.1 m/s and was found to be 133% larger than the laminar flame speed predicted by Cantera.

Figure 3.5 shows the result for a flame propagating in a lean hydrogen-air mixture with an equivalence ratio of $\phi = 0.3$ at ambient pressure. Similarly, the flame surface remained smooth and circular in the early stages. The laminar flame speed in this case was much slower than that for the stoichiometric mixture with a value of 0.31 m/s. The experimental value deviated notably from the Cantera calculation with a laminar flame speed 9.1 times larger. From the second frame, a cellular structure appeared rapidly at a smaller radius compared to the previous mixture. Larger cusps also formed on the flame surface and gave rise to a flower shape. A fractal pattern of the structure demonstrated a flame front incorporating multiple wavelengths. Later on, one can see that the buoyancy started to play a role as the top of the flame propagated faster than the bottom part (see frame 6). In the end, this mixture was promising for visualizing the interaction of a shock wave on large cusps.

The reduction in fuel concentration also allowed for the visualization of buoyancy-affected flames. Figure 3.6 shows selected frames for the propagation of a deflagration in a mixture of H_2-air at $\phi = 0.18$ in the Hele-Shaw cell. The experiment revealed that buoyancy started to have a considerable effect in the early stage of the combustion after ignition as shown in the two first frames. In the second frame, the flame kernel had already started to rise from the center of the apparatus. In the subsequent frames, the flame folded on itself with the characteristic "bean shape". A smooth surface devoid of a cellular structure is also observed to diffuse throughout the observable area. The flame rises faster than it could burn the surrounding fresh mixture, leaving unreacted mixture in the Hele-Shaw cell. The laminar flame speed was measured as 0.26 m/s by extracting the position of the flame front initially at small radius in the first few frames, where it is

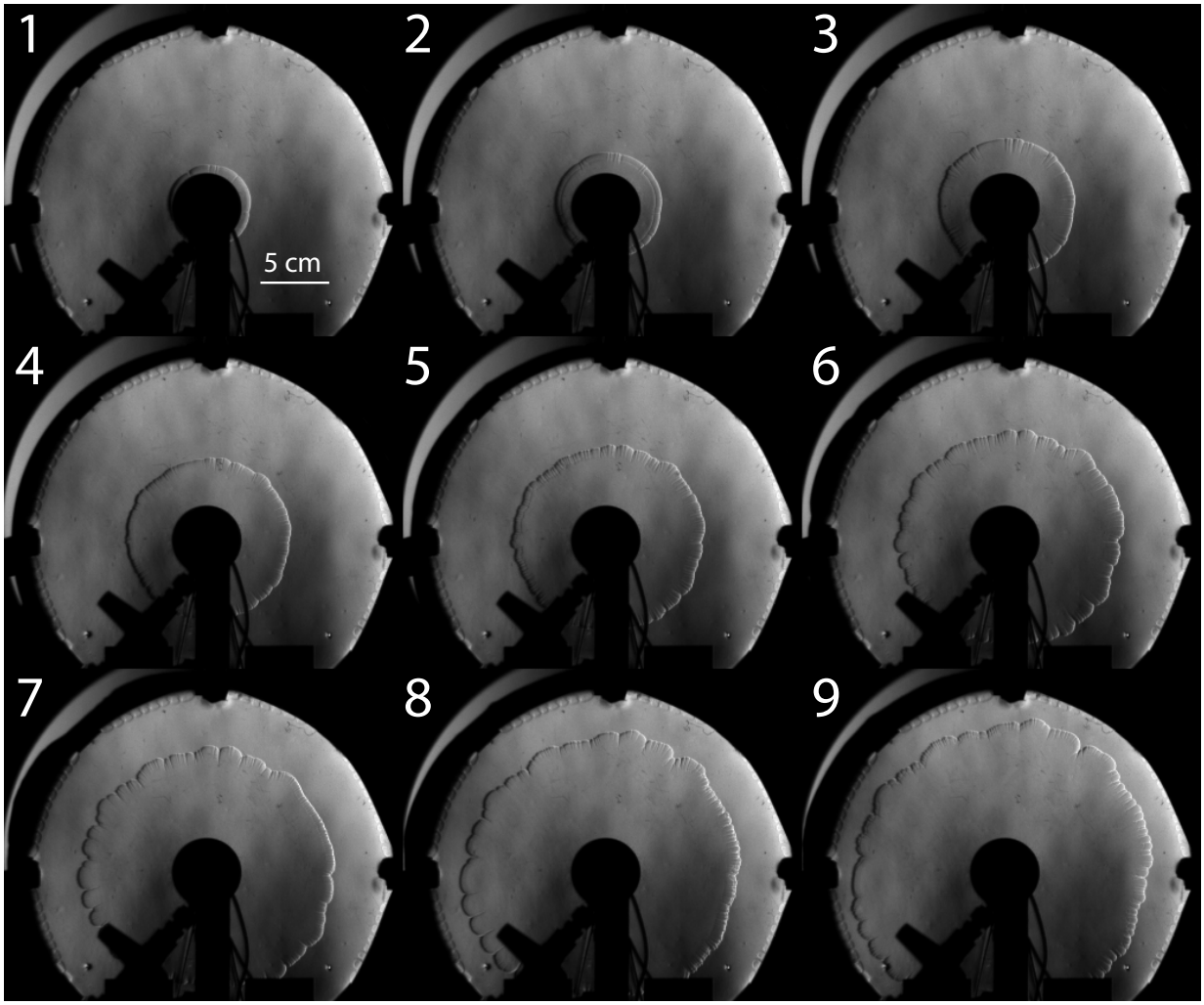

Figure 3.4: Image sequence of a flame propagation in a H_2-air mixture at $\phi = 0.6$ in the Hele-Shaw cell. The video was recorded at 77,481 fps with an exposure time of 0.468 μs. The time interval between frames is 0.90 ms. The resolution is 324 $\times$ 288 pixels. The mixture was ignited at the center point of the vessel.

not affected by buoyancy. By taking the above into consideration, this particular mixture is not suitable for the analysis of cellular flames perturbed by a blast wave.

Figure 3.7 illustrates the superimposed frames of the time evolution of the flame front according to the different mixtures of H_2-air. The flame was ignited from the center by the electrodes and propagated in the outward direction. From the figures, the appearance of cells clearly occurred at a smaller radius as the equivalence ratio was decreased. Large cusps bifurcated into smaller cells as shown by the creation of radial lines, while small cells also agglomerated through merging lines. Local cell curvature became more pronounced

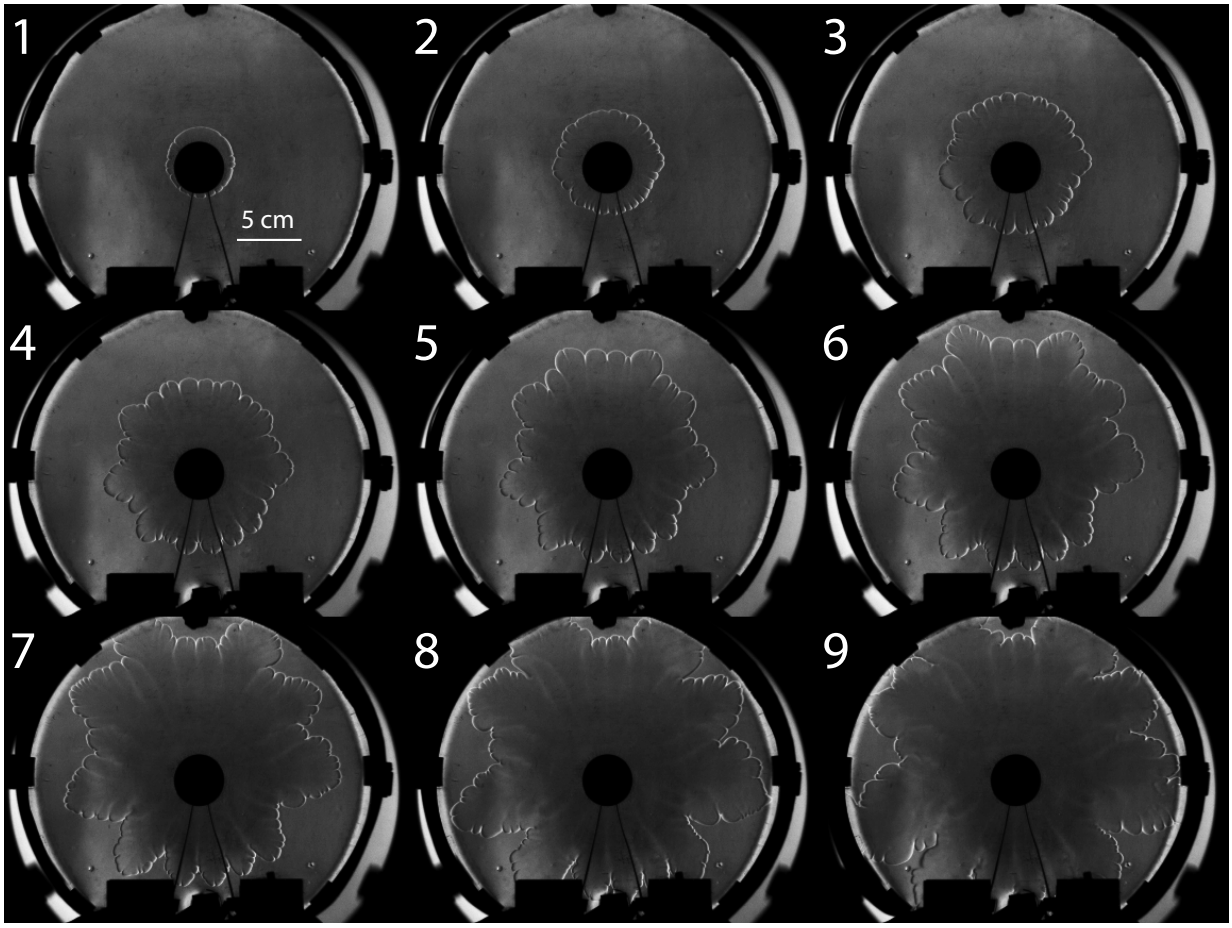

Figure 3.5: Selected frames for a flame in a H_2-air mixture at $\phi = 0.3$ in the Hele-Shaw cell. The video was recorded at 77,481 fps with an exposure time of 0.468 μs. The time interval between frames is 1.39 ms. The resolution is 324 $\times$ 288 pixels. The mixture was ignited at the center point of the vessel.

at large radius of the flame.

From the results in this chapter, the Hele-Shaw geometry has proven to successfully isolate the cellular structure of flames for a certain range of equivalence ratios. Intrinsic instabilities of the flames were well observed from the high-speed videos. Three mixtures were chosen accordingly to study the shock-flame interactions on various flame cell sizes, i.e. for $\phi = 1.0,\ 0.6$ and 0.3.

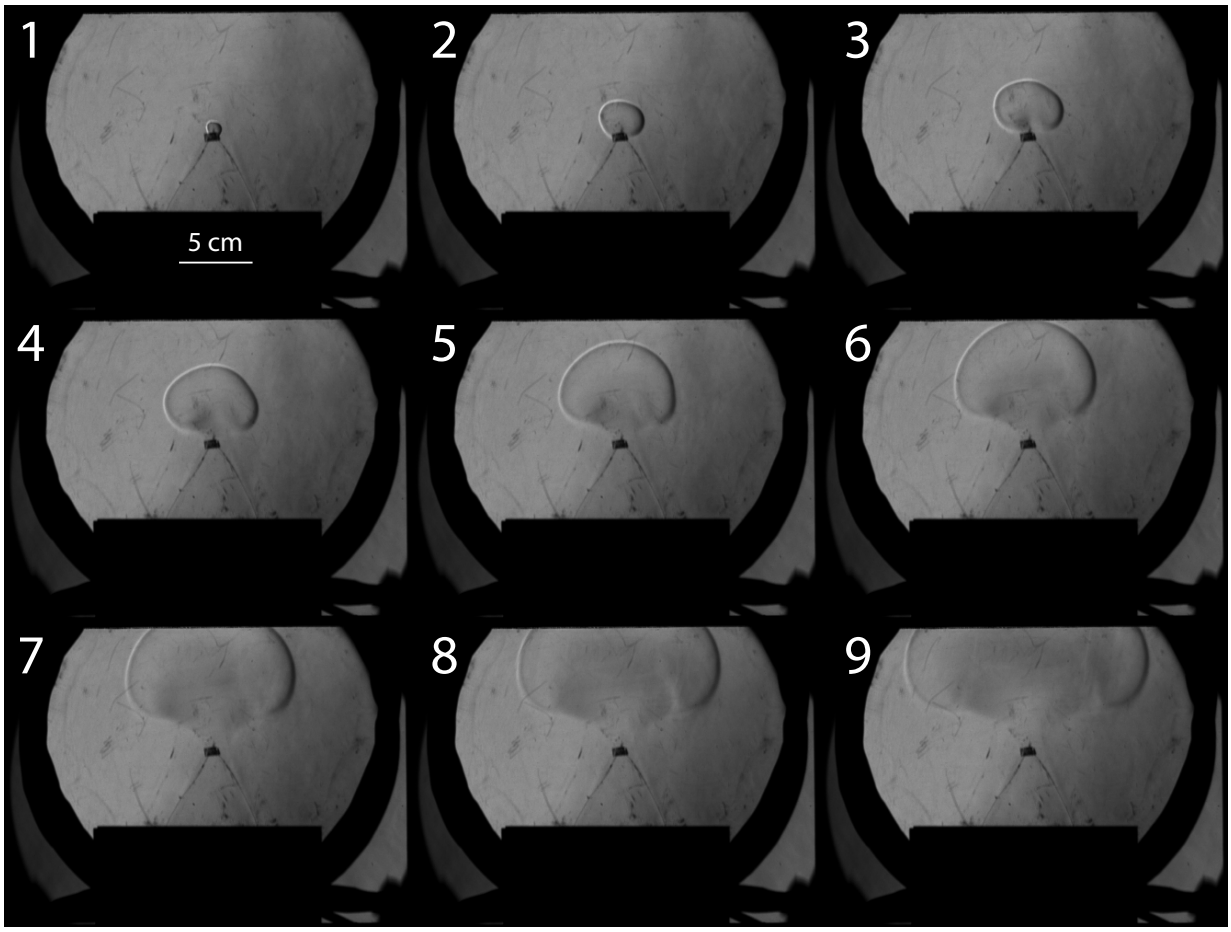

Figure 3.6: Image sequence of a flame propagation in a H_2-air mixture at $\phi = 0.18$ in the Hele-Shaw cell. The sample rate was set to 3,000 fps with an exposure time of 0.468 μs. The time interval between frames is 50 ms. The resolution is 512 $\times$ 384 pixels. The mixture was ignited at the center point of the vessel.

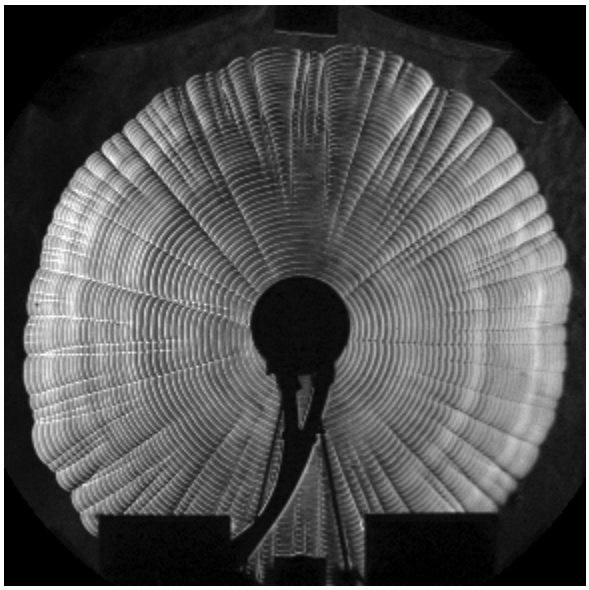

(a) $\phi = 1.0$

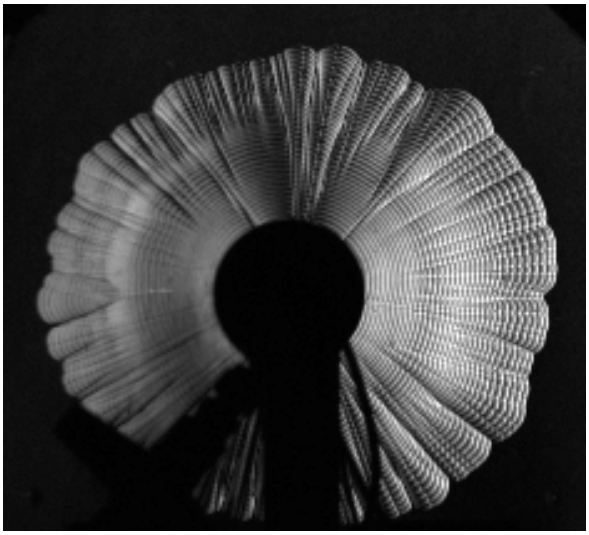

(b) $\phi = 0.6$

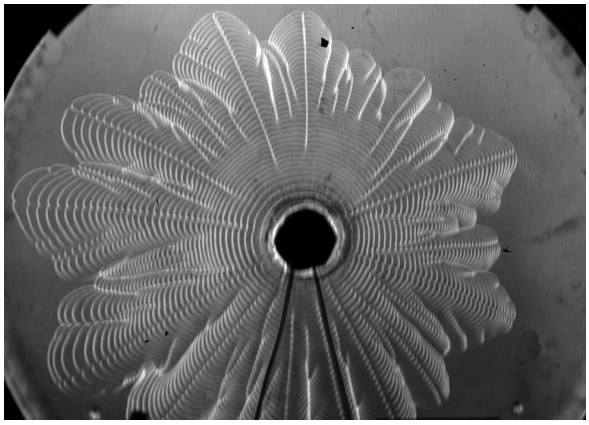

(c) $\phi = 0.3$

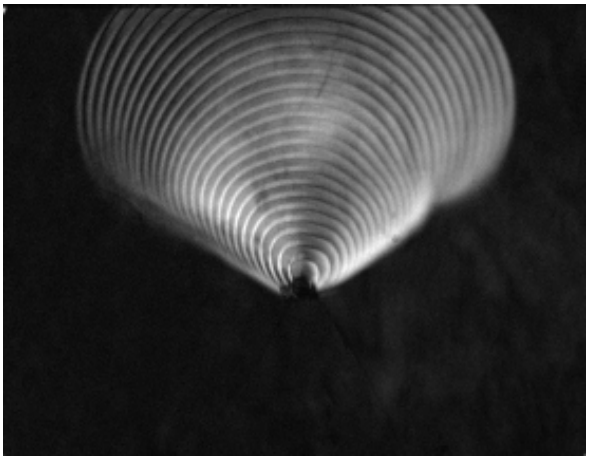

(d) $\phi = 0.18$

Figure 3.7: Superimposed frames of an outward propagating flame of hydrogen-air in the Hele-Shaw cell. The initial flame front is located at the center.

Chapter 4

Shock-Flame interactions – Light to heavy

This chapter presents the results for the shock-flame interactions for the configuration where a shock originating in the burned products overtakes the flame interface.

4.1 Stoichiometric mixture

Figure 4.1 shows the interaction of a $M = 1.2$ shock wave with a flame front (F) in the Hele-Shaw cell. The tests conditions were not varied and remained at ambient pressure and temperature. Similarly, the flame remained nearly cylindrical with a smooth surface at the initial stages (see frames 1 and 2). In the third frame, flame cusps were distinguished on the surface. After the flame had sufficiently propagated, the HVI was synchronized to be discharged and to create a cylindrical shock wave centrally. An incident shock wave (ISW) was driven in the burned products by depositing the amount of energy in a short period of time with the HVI. In the fourth frame, the shock traveled in the combustion products to reach the flame interface. The passage of the shock wave across the interface gave rise to a transmitted shock (TSW), which expanded in the unburned material. Following the passage of the shock, the flame interface was accelerated and flame cells were stretched. One can discern the acceleration of the flame front after the interaction. Moreover, funnels

of unburned gases, as illustrated in Fig. 4.2b, elongated along the circumference of the interface and penetrated in the burned gases as shown from the sixth frame. In the seventh frame, the stretched cells then tended to flatten and the interface became less wrinkled. This characteristic feature can be seen in Fig. 4.2c. From the eighth frame, the folding of the interface was discernible before a second shock interacted with the perturbed flame surface. In the tenth image, a second shock wave was transmitted into the unburned gases. At this point, the flame front appeared to be fully inverted and more corrugated as highlighted in Fig. 4.2d. Shock reflections on the spacers moved back towards the interface and in turn caused multiple interactions until the end of the image sequence. Although this study only focused on the initial interaction, the multiple interactions seemed to greatly enhance the combustion of the unreacted mixture. The cellular structure had been distorted when compared to its initial state. The increase of flame surface area caused by the stretching of the cells translated into an increase of the flame speed. Enhanced mixing is also expected to promote the combustion in the funnels and on the surface of the roughened deflagration wave.

The second transmitted shock wave which, appears in the tenth frame of Fig. 4.1 is believed to come from the initial interaction of the incident shock with the interface. One-dimensional axisymmetric inert numerical simulations were accomplished to confirm the provenance of the secondary shock. Figure 4.3 shows numerical results for the interaction of a shock wave on an inert density interface to get insight into the flow field in the Hele-Shaw cell, especially in the burned gases where experimental observation is made difficult by the gases at high temperature. From the $r-t$ diagrams, the energy deposited drives the incident blast wave, which progresses towards the density interface at rest. The densities are equivalent to the combustion event in a mixture at stoichiometry and normalized with the burned state. Upon reaching the interface separating the light and heavy gases, the wave gets transmitted, but also reflects to travel back in the light gases towards the center. The reflected wave is indeed a shock, as opposed to a rarefaction wave, due to large impedance from the unburned side ($\rho_{\mathrm{u}} c_{\mathrm{u}} > \rho_{\mathrm{b}} c_{\mathrm{b}}$). Since the shocked region behind the interface is characterized by a higher temperature, the reflected wave travels faster than the transmitted wave, especially near the initial location where there is a contact

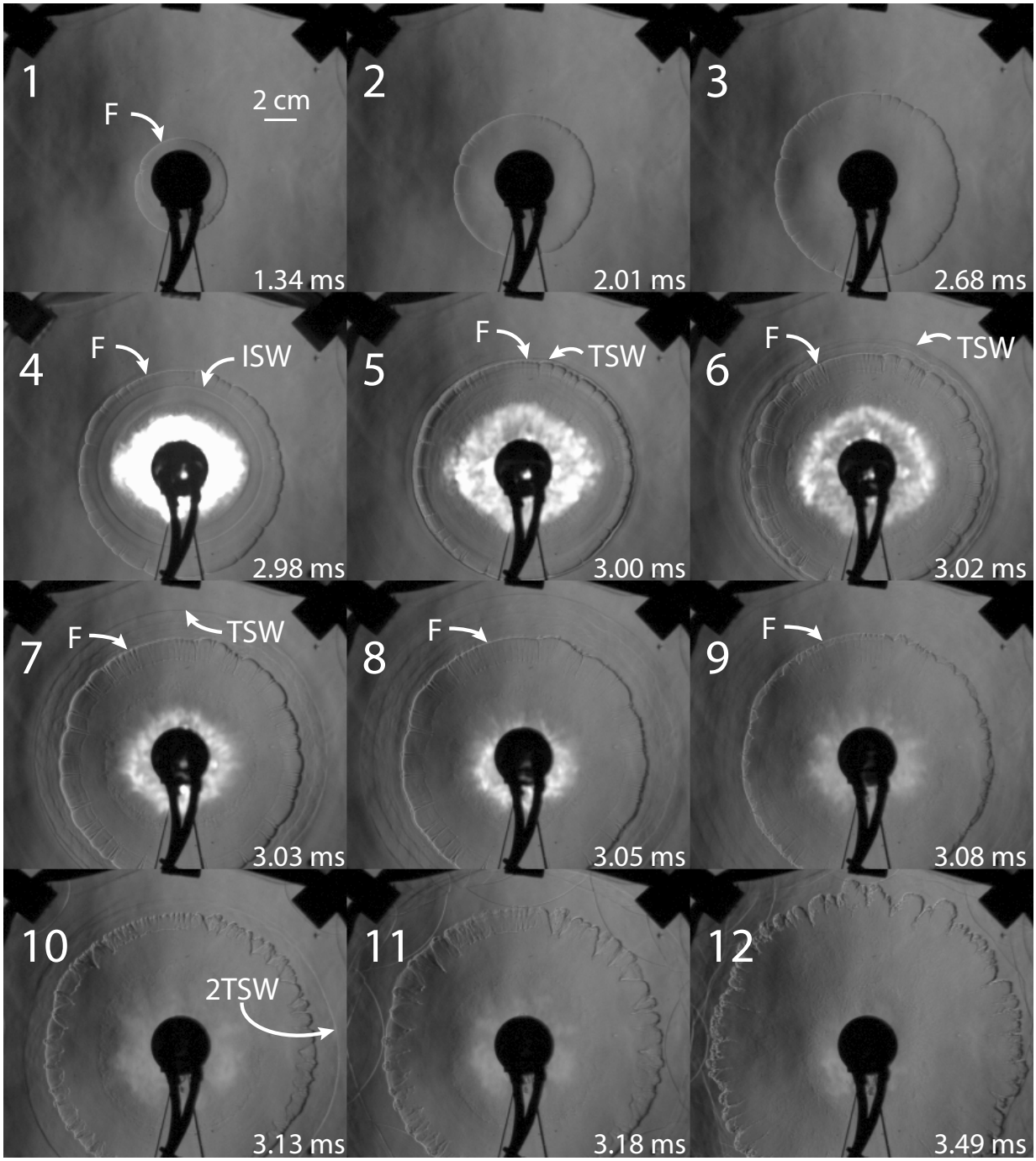

Figure 4.1: Schlieren images of the interaction of a shock wave (SW) with a cylindrical flame (F) in a hydrogen-air mixture at stoichiometry propagating in the Hele-Shaw cell. Initial pressure of 1 atm. Recorded at 59,590 fps.

surface of high pressure, i.e., near the center at $r/R < 0.1$. Once it has reflected at the center, the shock propagates back in the direction of the unstable interface to cause the second interaction. This qualitative behaviour was found to be in good agreement with

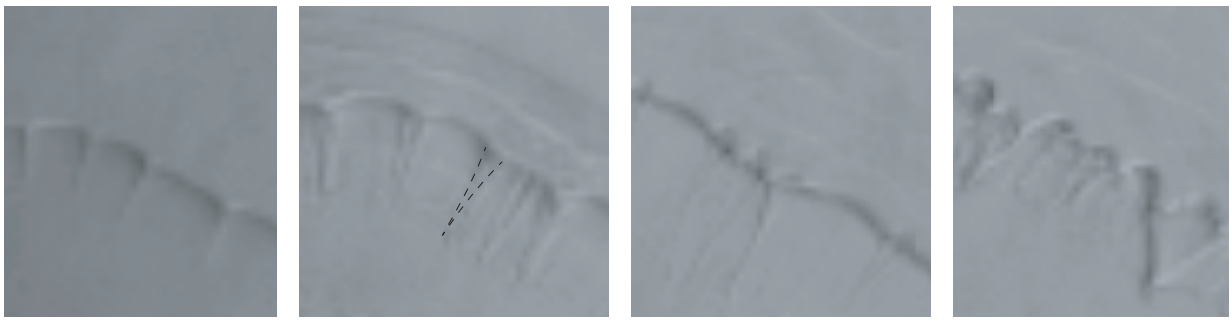

a) b) c) d)

Figure 4.2: Flame interface deformation features caused by its interaction with a blast wave.

the experiment.

To investigate the shock-flame complex on larger cells, the equivalence ratio was varied to observe the evolution of the perturbed interface at early times and spatial scales.

4.2 Lean mixtures

Figure 4.4 illustrates the results for an HVI-initiated shock interacting with a lean flame of hydrogen-air at $\phi = 0.6$ at ambient conditions. In this case, the perturbation occurred

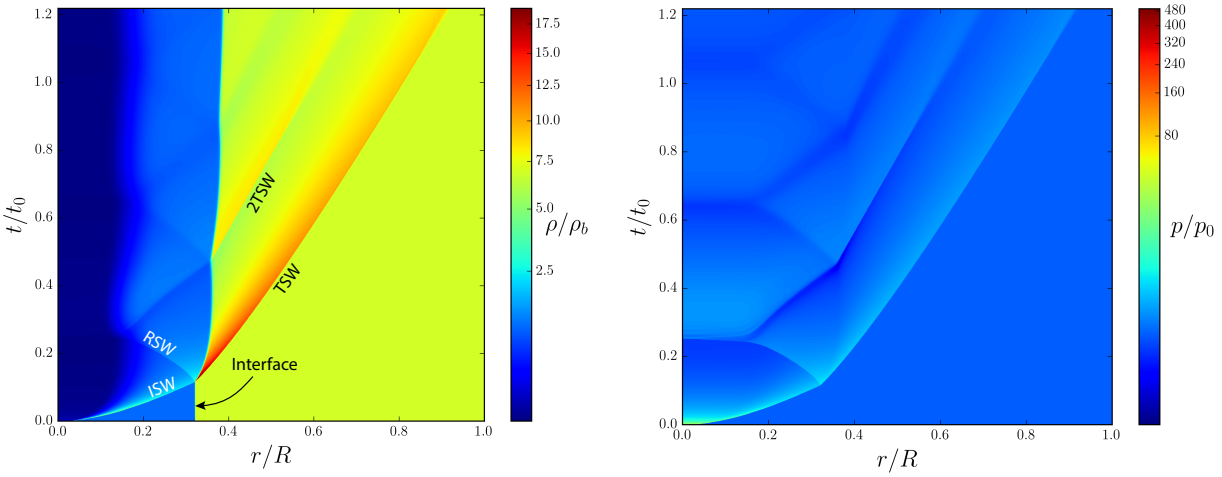

(a) Density (b) Pressure

Figure 4.3: $r-t$ diagrams of the interaction of a blast wave with an inert density interface in 1D axisymmetric. The density ratio across the interface is $\alpha = 6.86$.

earlier, when the mean radius of the flame was smaller. The shock wave propagated in the light gases as shown in the third frame. In the fourth frame, the transmitted shock grew in the unburned gases while the perturbed cellular flame got amplified as a consequence from the interaction with the shock wave. Funnels of unburned mixture were extended in the hot products of the flame. The interface elongation is clearly apparent when compared with its initial structure illustrated in the second frame. The top part of the flame was comprised of an interesting feature for analysis. The indentation separating two distinct cusps developed over time to catch up with the cellular front. On the other hand, the wrinkled flame front unfolded on itself and developed a nascent finer structure as shown in the sixth and seventh frames. However, the flame had still not reversed at this point. The reversal was only noticeable once the second shock interaction arose in the eighth frame; the reflected shock passed through the already unstable interface and caused the indent to become a peak. The late reversal can be owed to the shorter displacement of the initial flame front when the shock wave is generated. The time allowed to observe the flame folding and turnaround before the arrival of the reflected shock was not sufficient, as the acoustic time for the shock to travel in the light gases was smaller. In the latest frame, shock wave reflections were about to perturb the interface from the opposite direction due to the geometry of the apparatus. The same features were found after multiple interactions and were thus not represented in the figure.

By further varying the equivalence ratio towards the lean side, the head-on interaction of the blast wave with the flame took place on a wider range of flame cell size with larger cusps. Figure 4.5 depicts the interaction in a mixture of H_2-air mixture at $\phi = 0.3$. For this experiment, the blast wave was generated by the detonation-driven shock tube. The cellular structure appeared early as shown in the second frame. After the flame front had traveled sufficiently in the radial direction, the detonation was triggered to generate the incident shock (ISW) in the combustion products. As it passed through the flame, the shock wave compressed the interface in the beginning as illustrated in the fourth frame. Afterwards, flame cells got stretched and eventually retrieved a flat shape in the fifth frame. Moreover, small cells appeared on the flame surface here and there where cracks were initially located between cells. This characteristic was more noticeable in the seventh

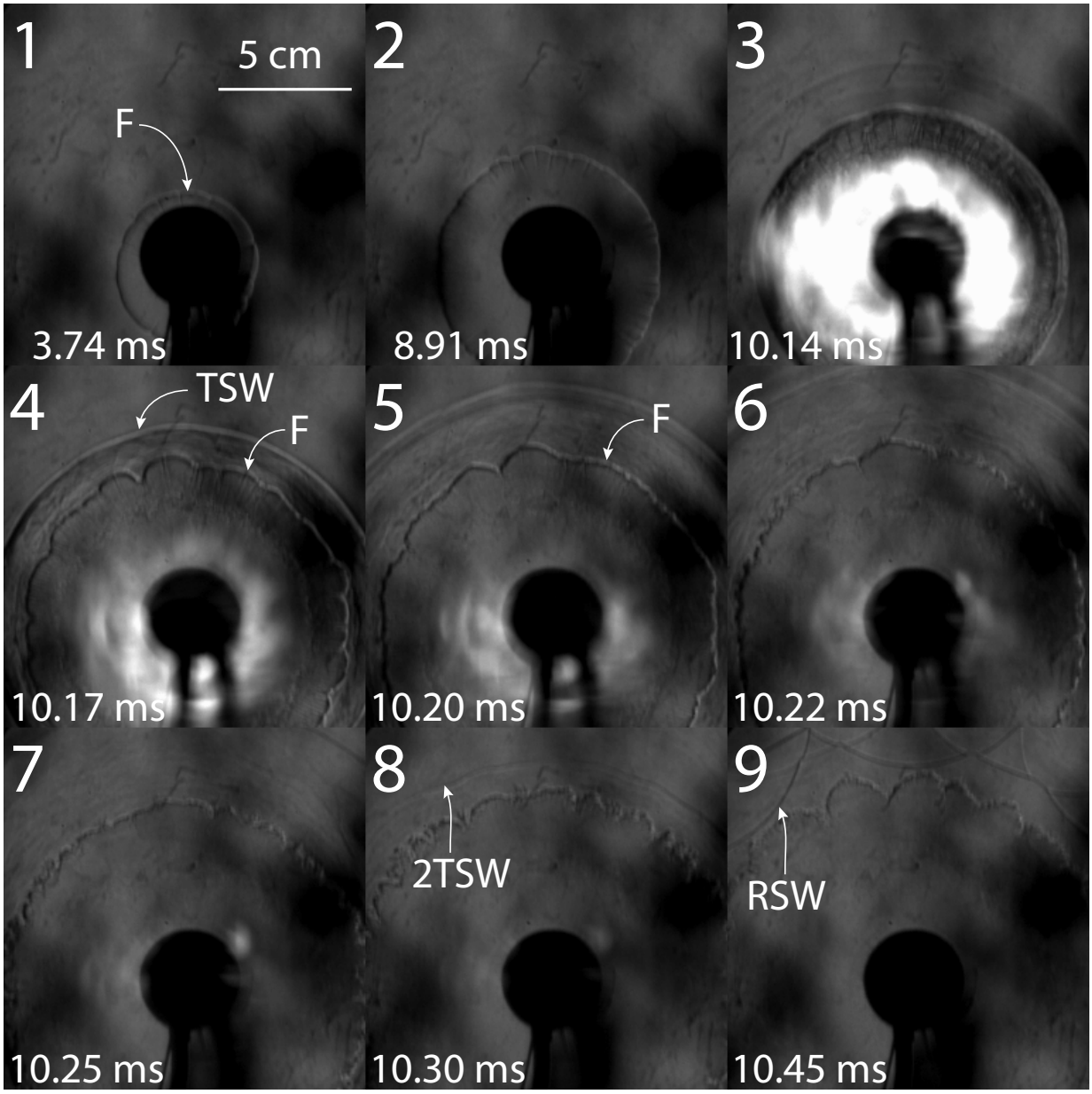

Figure 4.4: Sequence of Schlieren images of the interaction of a shock wave (SW) with a flame (F) in a hydrogen-air mixture at $\phi = 0.6$ propagating in the Hele-Shaw cell. Initial pressure of 1 atm. Recorded at 104,918 fps.

frame upon the arrival of the reflected shock. The appearance of such fingers could illustrate a partial reversal of the flame structure, although the cells or cusps were not fully folded by the end of the image sequence. In this experiment, the resulting flame surface was highly corrugated due to its interaction with the blast wave. In the last frame, the original smooth interface had transitioned to a distorted surface endowed with a rough texture,

highlighting the transition of a smooth laminar flame to a turbulent-like structure.

Results in the present configuration have shown similar key features with previous experimental evidences in the literature for the interaction of a shock parallel with a flame density interface [3, 6]. Apart from the advent of burned products from the detonation wave inside the Hele-Shaw cell, no significant difference has been monitored by using the detonation tube or the HVI to generate the blast wave in the vessel. To further investigate the effect of the direction of the shock on the combustion front, experiments were conducted with multiple igniters to initiate the flame on the contour of the Hele-Shaw cell. In this case, the shock wave originated from the center and traversed the flame interface from the opposite direction, i.e., from the unburned to the burned gas.

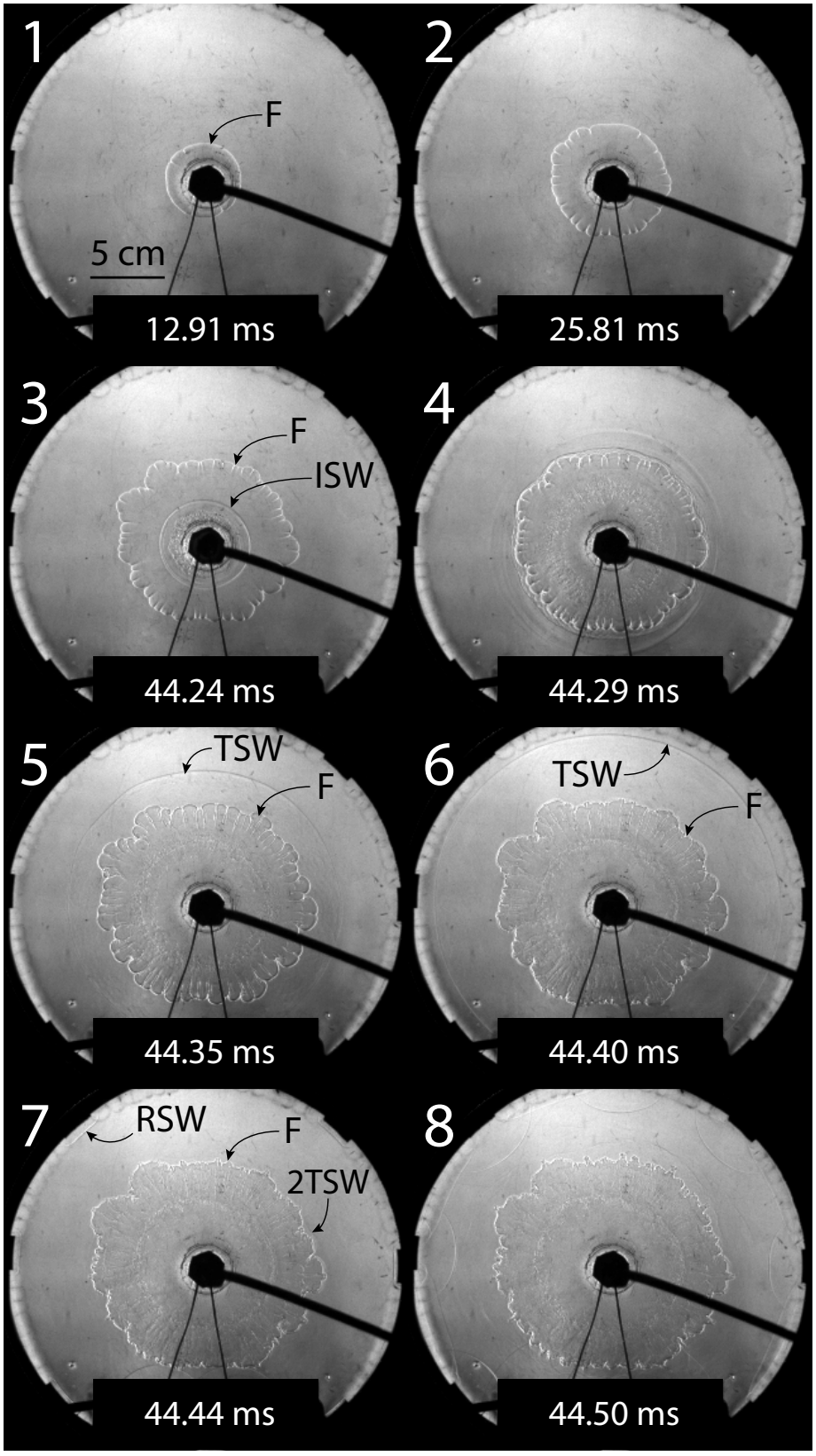

Figure 4.5: Sequence of Schlieren images of the interaction of a shock wave (SW) with a flame (F) in a hydrogen-air mixture at $\phi = 0.3$ propagating in the Hele-Shaw cell. Initial pressure of 1 atm. Recorded at 77,481 fps.

Chapter 5

Shock-flame interactions – Heavy to light

This chapter reports preliminary results for the head-on interaction of a blast wave with a cellular flame front when the shock originates in the unburned gases and collides on the flame interface propagating in the opposite direction.

5.1 Lean mixtures

Figure 5.1 presents the results for the passage of a blast wave through a flame traveling in the opposite direction with $\phi = 0.6$ at ambient conditions. From the series of initial frames (1 – 3), ignition was well synchronized on the contour of the Hele-Shaw cell allowing the flame kernels to burn in a quasi-symmetric fashion. In the third frame, the mixture inside the detonation tube was ignited and the incident shock wave (ISW) propagated in the heavy unreacted gases from the center of the Hele-Shaw cell. Burned products (BP) from the detonation wave were trailing behind the blast wave as shown in the fourth frame. When the incident shock reached the interface, part of the shock was transmitted, and the other was reflected. For the case of a shock encountering the cellular interface in the opposite direction, the interaction was more disruptive; the initial interface got flattened immediately after the passing of the shock. In this configuration, the Richtmyer-Meshkov

instability is expected to have an initially stabilizing effect on the initial perturbed density interface and will tend to smooth out the cells. On the other hand, the direction of the acceleration from the heavy to light gases would amplify the growth of cells' amplitude through the Rayleigh-Taylor instability. Eventually, the cellular structure was fully reversed, with funnels of unburned gases penetrating in the flame kernels as shown in the eighth frame. Shock reflections (RSW) coming from the sealing latex balloon and the spacers were also noticeable; they eventually caused multiple interactions with the cellular flame kernels at later times. In the latest frame, microscales developed as the surface got more corrugated and the tail of the funnels were consumed by the combustion process.

Experiments on the interaction of a blast wave on a cellular flame front using multiple igniters were also carried out for a lean mixture of H_2-air at with an equivalence ratio of $\phi = 0.3$. Figure 5.2 shows the evolution of the flame following its interaction with a blast wave initiated with the detonation tube. The reactive mixture filled at ambient conditions was first ignited by the set of eight electrodes in the Hele-Shaw cell (see frame 1). After some time of development, the flame kernels developed in a quasi-symmetrical fashion. The flame, characterized by a low flame speed, manifested its cellular structure comprised of large cusps which possessed smaller cells. In the second frame of the image sequence, the initial cores of the flames merged altogether to create a common cellular front consuming the fresh mixture towards the center of the vessel. From the fourth image, the detonation tube was triggered to generate an incident shock wave (ISW) in the unburned mixture which travels in the opposite direction. The passage of the blast wave through the bottom cusp rapidly deformed the interface in the fifth frame. The strong deformation yielded a full structure reversal with the appearance of funnels in the burned mixture. Moreover, the transmitted wave (TSW) propagated on the burned side of the interface (see frame 6). At this point, the head-on interaction caused the flame front to remain stationary for a short period of time before the extended fingers would amplify in size. These characteristic features are a signature of Richtmyer-Meshkov and Rayleigh-Taylor instabilities acting on the interface to cause its distortion. From the last frames of the sequence, these funnels on the flame surface were displayed throughout the circumference of the initial flame front. Similar results were observed in previous studies involving the same configuration, i.e. for a

head-on collision [28, 29]. Ultimately, the transmitted shock was reflected off the boundary of the cylindrical chamber where the spacers are located as can be seen in the ninth frame. After $t = 149.63$ ms, the interaction of the flame front with the successive reflected shocks created a highly turbulent flame brush that kept oscillating position due to the incoming shock waves from different directions.

Preliminary results offered good visualization of the shock-flame complex in the case of a head-on interaction with an inward propagating cellular flame front with a shock wave originating from the inverse direction. The present results were analyzed qualitatively due to the breakup of the initial cellular front which lead to a complex flow after the interaction with the blast wave. The events for the light-to-heavy configuration for $\phi = 1.0$, $\phi = 0.6$ and $\phi = 0.3$ were further investigated in the next chapter to get the controlling dynamics on the interface occurring subsequent to the incoming precursor blast wave.

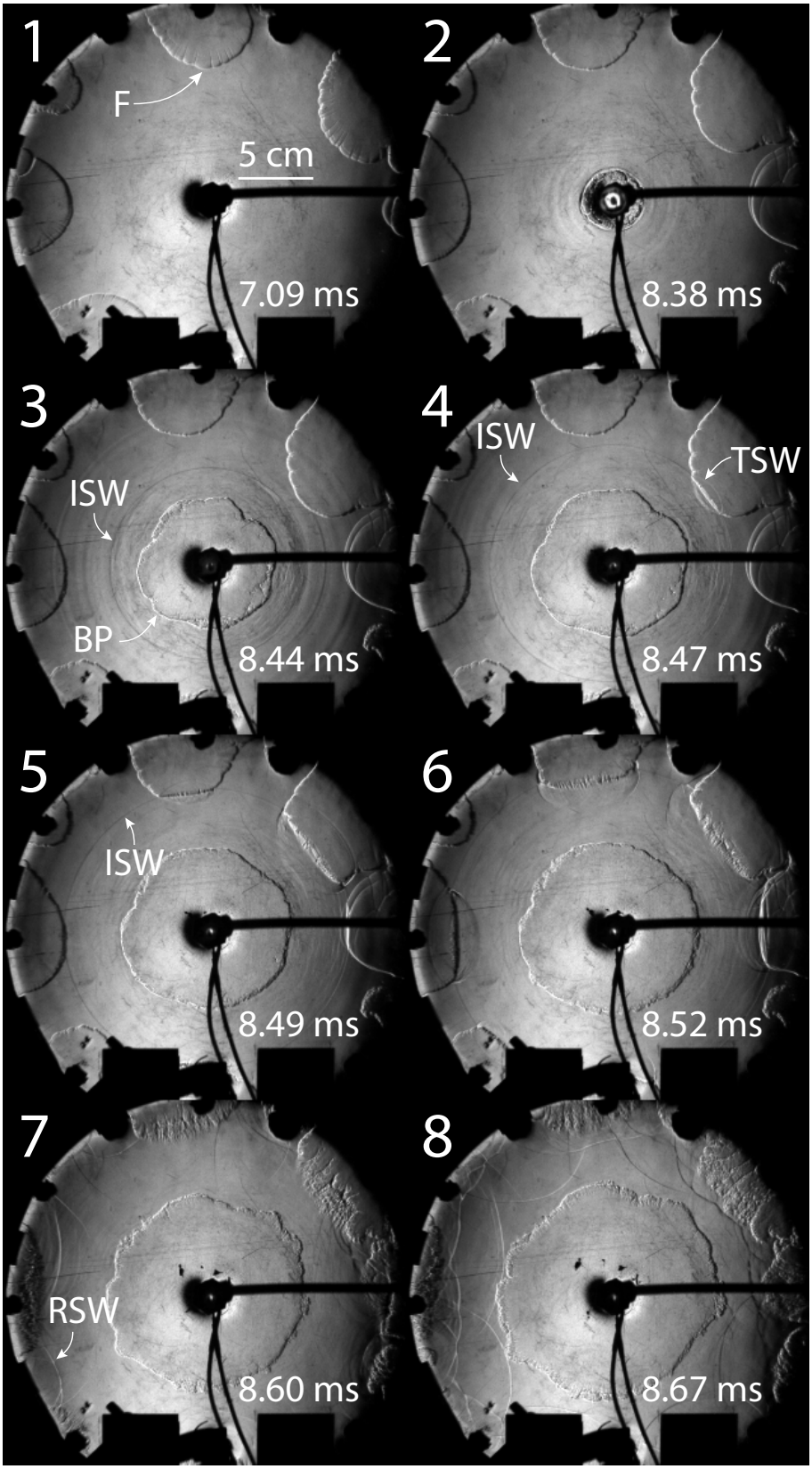

Figure 5.1: Sequence of Schlieren images of the interaction of a shock wave (SW) with a flame (F) in a hydrogen-air mixture at $\phi = 0.6$ propagating in the Hele-Shaw cell. Initial pressure of 1 atm. Recorded at 77,481 fps.

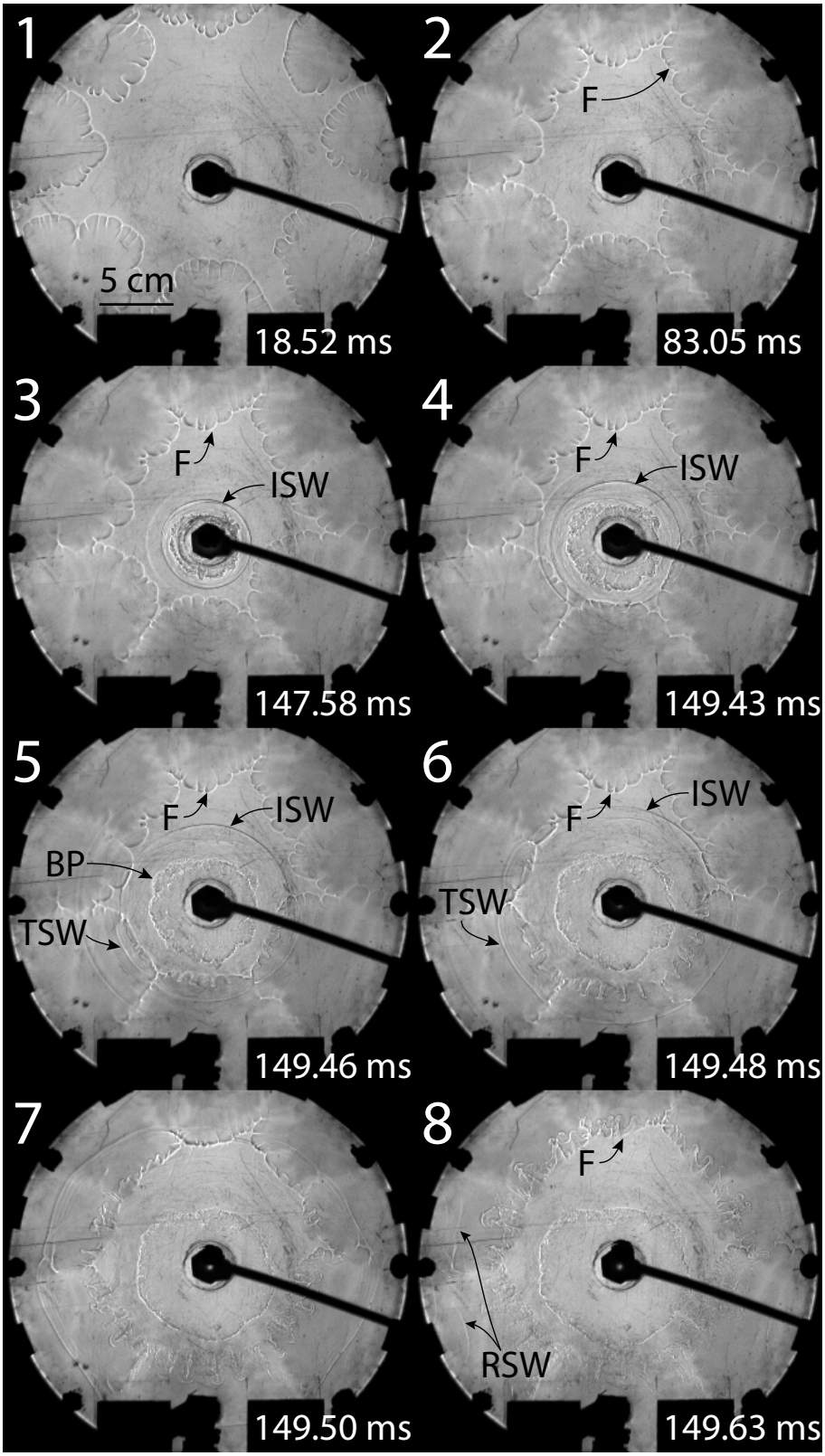

Figure 5.2: Selected photographs of the interaction of a shock wave (SW) with a flame (F) in a hydrogen-air mixture at $\phi = 0.3$ propagating in the Hele-Shaw cell using multiple ignition points. Initial pressure of 1 atm. Recorded at 77,481 fps with an exposure time of 0.468 μs.

Chapter 6

Dynamics of the interaction

This chapter discusses the relative roles of the instabilities in the deformation of the flame interface deduced from the experimental results presented in Chap. 4. A temporal analysis together with numerical simulations provide some insights on the evolution of instabilities throughout the shock-flame interaction.

6.1 Time scale analysis

The analysis was first conducted based on the results for the interaction of a shock wave with a cellular flame at stoichiometry. A time scale analysis was done to compare the time for flame and flow instabilities to affect the deformation of the density interface of the perturbed flame. The characteristic time scale for combustion is defined as

$$\tau_{\mathrm{c}} = \frac{l_{\mathrm{f}}}{S_{\mathrm{u}}} \tag{6.1}$$

On the other hand, the time scale for the Richtmyer-Meshkov instability to influence the distortion of the interface is defined as

$$\tau_{\mathrm{RM}} = \frac{1}{\sigma_{\mathrm{RM}}} \tag{6.2}$$

The Rayleigh-Taylor instability arises from the transient profile behind the shock front. After the passage of the leading front through the interface, the latter is subjected to a pressure gradient, which decays over time and causes the flow field to decelerate. The characteristic time scale for Rayleigh-Taylor instability in the linear regime is defined as

$$\tau_{\mathrm{RT}} = \frac{1}{\sigma_{\mathrm{RT}}} \tag{6.3}$$

For instance, the characteristic reaction time of the laminar flame for a concentration of $\phi = 1.0$ is found as 1.4×10^{-4} s. The laminar flame thickness l_{f} was calculated using the Cantera as stated previously, while the laminar flame speed S_{u} was measured experimentally from the high speed videos for the given mixture. Similarly, the flame propagation timescales for $\phi = 0.6$ and $\phi = 0.3$ were found as 2.5×10^{-3} s and 9.6×10^{-4} s, respectively. To verify the controlling mechanism of shock induced flame acceleration, time scales of RM instability and RT instability were also calculated and compared with τ_{c}. The linear RM instability time scale has a value of 9.3×10^{-6} s, and the time scale for RT instability is 3.0×10^{-5} s for $\phi = 1.0$. In these equations, σ_{RM} is the growth rate from the theory of RM instability (see Eq. 1.2) and σ_{RT} is the growth rate of the amplitude for RT instability in Eq. 1.1. The acceleration for the flow behind the shock wave found in Eq. 1.1 was derived from the shock change equations in the limit of strong shocks. More details on the derivation can be found in Appendix C. As shown in Fig. 6.1, λ is the wavelength of the chosen cell (C) for the analysis. Here, the amplitude refers to the perpendicular distance from the top of a cell to the line linking the intersection point of the cell with the adjacent cells without considering the funnels extended to the burned gas. The parameters $[u]$, a and λ were measured experimentally.

Figure 6.2 illustrates the time scales of flame propagation and flow instabilities according to different H_2-air mixtures. For the experiment at $\phi = 1.0$, the time interval between the first and second shock-flame interaction is $\tau_{\mathrm{obs}} = 1.2 \times 10^{-4}$ s. Both time scales of RM and RT are found to be smaller than the observation time of the experiment, signifying that both phenomena may play an important role. Here, the observation time is the time between the first passage of the incident shock on the interface and the re-shock. Omitting

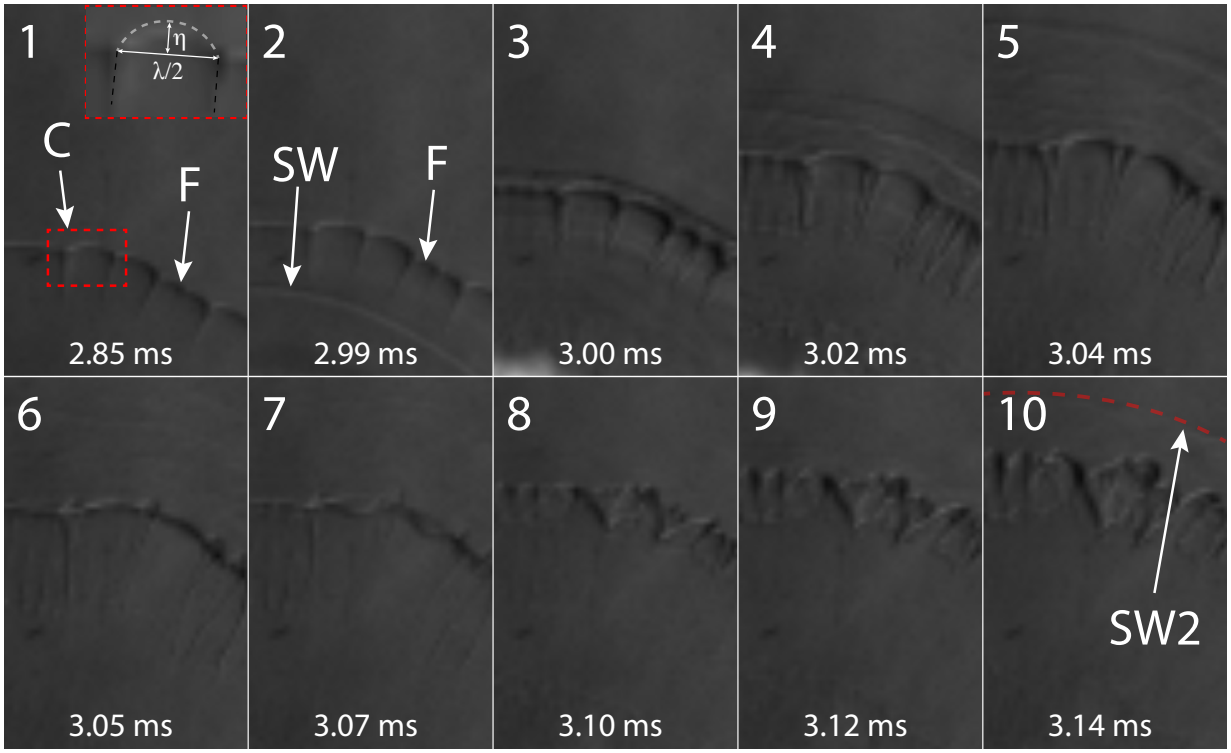

Figure 6.1: Selected zoomed images of the interaction of a shock wave (S) with a cylindrical flame (F) in hydrogen-air mixture at stoichiometry propagating in a the Hele-Shaw cell. Initial pressure of 1 atm. Recorded at 59,590 fps.

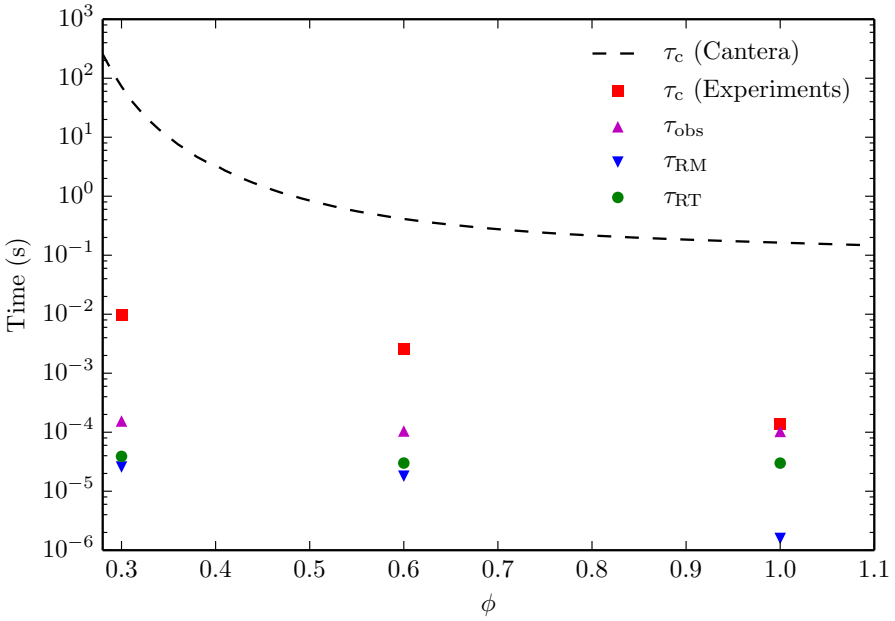

Figure 6.2: Relative time scales of instabilities and observation times with respect to the equivalence ratio of H_2-air mixtures.

the flame dynamics is acceptable for analyzing the relative role of each instability on the dynamics, since the time for the shock to traverse the density interface is shorter than the time scale of combustion. The same assumption is also applicable for the lean mixtures, which typically have a larger flame thickness and a lower flame speed. It those cases, the characteristic time scale for a flame to evolve was found to be in the order of 10^{-3} s and above the time scale for observation of the first interaction with the blast wave. For all cases, it was found that $\tau_{\mathrm{RM}} < \tau_{\mathrm{RT}} < \tau_{\mathrm{c}}$.

Integrating the growth rates of the instabilities, one can seek the cell's amplitude solutions from the linear theory of Richtmyer-Meshkov and Rayleigh-Taylor such that

$$\eta'(t)_{\mathrm{RT}} = -\sigma_{\mathrm{RT}}\ \eta(t) \tag{6.4}$$

$$\eta'(t)_{\mathrm{RM}} = \sigma_{\mathrm{RM}}\ \eta_0 \tag{6.5}$$

$$\eta'(t)_{\mathrm{RMRT}} = -\sigma_{\mathrm{RT}}\ \eta(t) + \sigma_{\mathrm{RM}}\ \eta_0 \tag{6.6}$$

where $\eta(t)$ is the amplitude of a cell at a given time and η_0 is the initial amplitude of a perturbed cell. Equation 6.6 denotes the linear superposition of both instabilities. Figure 6.3 shows the evolution of the cell's amplitude from linear theory predictions and for the experiment. Due to the resolution of the high speed camera and the small scale of the cellular structure of the flame, the typical uncertainty corresponding to the measurement of the amplitude from the experiment was approximately 50%. For the case of a shock emerging in the burned gases and traversing the flame interface from the light to the heavy gases, the Rayleigh-Taylor instability is expected to have a stabilizing effect on the initially perturbed interface as plotted in Fig. 6.3. Thus, it takes on a negative growth rate in Equations 6.4 and 6.6. Otherwise, the acceleration in the case of a colliding shock-flame interaction will cause the interface to be Rayleigh-Taylor unstable and the associated growth rate would be positive. From this figure, one can notice that the growth of the amplitude from experiments does not relate with the linear theory predictions. Temporal resolution of the experiment does not permit to measure the very early growth of the cell's

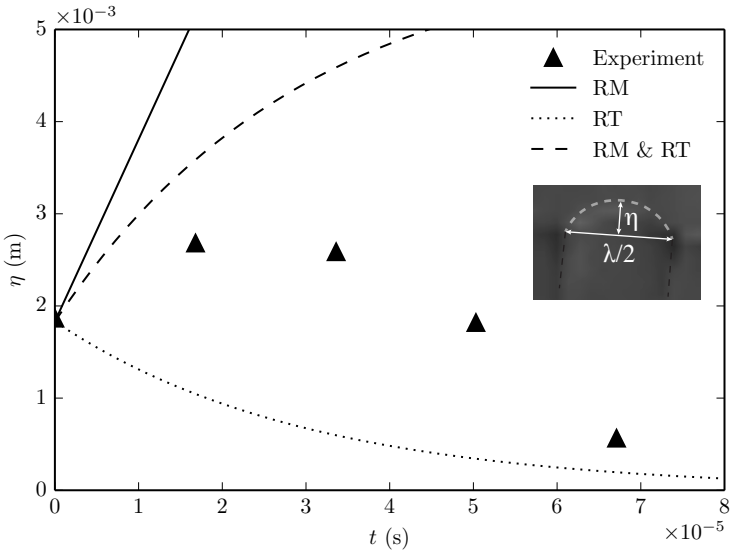

Figure 6.3: Prediction of cell amplitude growth for a stoichiometric H_2-air mixture from linear stability theories of RM, RT and their superposition (RM & RT).

amplitude. Therefore, the transition to a non-linear regime is believed to play a role in the growth of perturbations.

6.2 Numerical analysis

In order to help in the interpretation of the experimental results, numerical simulations were also performed in two-dimensions for a shock wave incident on a density interface with the shape of a wrinkled flame composed with cells dispersed in a symmetrical manner. The purpose of the following numerical analysis is to get a quantitative insight of the non-linear phase of the evolution in the flow field. The numerical solutions to the Euler equations in 2D were obtained using a hydro-code using a second-order accurate Godunov-type solver [26] with adaptive mesh refinement. The numerical problem is restricted to an inert density interface devoid of chemical reactions. The variables were non-dimensionalized as follows

$$
\begin{aligned}
&\text{for } x: && x = R\bar{x} \\
&\text{for } p: && p = p_0\bar{p} \\
&\text{for } \rho: && \rho = \rho_\mathrm{b}\bar{\rho} \\
&\text{for } T: && T = T_*\bar{T} \text{ where } T_* = \frac{p_0}{\rho_\mathrm{b}\ {}^{R_\mathrm{u}}/_{MW}} \\
&\text{for } c: && c = c_*\bar{c} \text{ where } c_* = \sqrt{\frac{p_0}{\rho_\mathrm{b}}} \\
&\text{for } t: && t = t_*\bar{t} \text{ where } t_* = \frac{R}{c_*} = {}^{R}/_{\sqrt{\frac{p_0}{\rho_\mathrm{b}}}}
\end{aligned}
$$

where $R = 0.14$ m is the radius of the Hele-Shaw cell, p_0 is the atmospheric pressure at which the mixture is initially filled in the vessel, ρ_b is the density of the burned gas, R_u is the universal gas constant and MW is the molecular weight of the mixture. The problem is set up in Cartesian coordinates in the positive quadrant. Figure 6.4 illustrates the initialization of the numerical problem. The planar domain has a square aspect ratio of dimensions $R \times R$ associated to the physical dimensions of the Hele-Shaw cell. The reflective boundary conditions are used to mimic the symmetrical behaviour of the event on the bottom and left sides ($x = 0$ and $y = 0$), while the right and top sides ($x = R$ and $y = R$) have free-type outflow boundary conditions assuming a zero normal gradient for flow variables. Initially, a non-reactive interface corresponding to the flame interface in the experiment is implemented to separate the reacted and fresh mixture having different densities. The cell parameters were taken from the experiment results as illustrated in Fig. 6.1 to mimic the cellular structure. For simplicity, the interface is set with a single mode having the same wavelength instead of multiple wavelengths. The flame interface velocity with respect to the stationary fresh mixture being small compared to the shock wave velocity, it was thus neglected when establishing the initial conditions of the simulation. The gases initially at rest have the same atmospheric pressure $p_0 = 1$ atm. However, a contact surface is established near the origin with a top hat pressure on an area covering the distance between the centrally located electrodes in the Hele-Shaw, or the exit diameter of the detonation tube. The high pressure is determined at first glance using the model of

energy release for the source as described previously in Section 2.3.3. The ratio of specific heats at equilibrium is representative of the burned state such that $\gamma = \gamma_b$ and calculated using NASA-CEA software. The constant value of γ_b is taken to reproduce the dynamics of the blast wave accordingly in the burned state, where the gases are lighter than on the unburned side of the interface. The numerical solutions were solved in the laboratory frame of reference.

For the set of numerical simulations in a quadrant, the number of computational cells in the domain was kept constant in each direction (100×100) for the base grid. Adaptive mesh refinement was used in regions of interest, e.g., the shock and the density discontinuities. The number of grid refinement levels was varied for the same base grid size to investigate the convergence of the interface position. As shown in Fig. 6.5, the computational grid is refined in and around regions of large density gradients, while keeping a coarser grid size elsewhere. In the simulations, the grid levels have a grid spacing of $\delta/2^{L-1}$, where δ is the computational cell size and L is the level of refinement. For example, a coarse cell using 4 grid levels (L = 5) would be refined by a factor of 16. Figure 6.6 depicts the interface position for three different levels of refinement and this at three instants. As shown in red, the coarsest refinement does not converge properly over time as the interface moves after the passage of the shock wave. On the other hand, the blue and green curves appear to converge to the same position while the interface deforms and propagates subsequent to the interaction. The level of refinement L = 5 was hence adopted for the mesh size of the remaining numerical simulations, since it sufficiently resolves the shock waves and the density interface while maintaining relatively low computer resources. For the chosen resolution, the most refined cell yielded a dimension of 8.75×10^{-5} m.

Figure 6.7 shows the time evolution of an inert interface (I) of density ratio 6.85 representative of the deformation of the flame cusps after the shock-flame interaction. The characteristic amplitude and wavelength were measured from a single as shown in Fig. 6.1. The decaying shock (SW) was developed by using a contact surface with a top hat pressure distribution to deposit an equivalent energy of 10 J obtained from the shock strength analysis. As in the experiments, the density interface was rippled when the shock passed

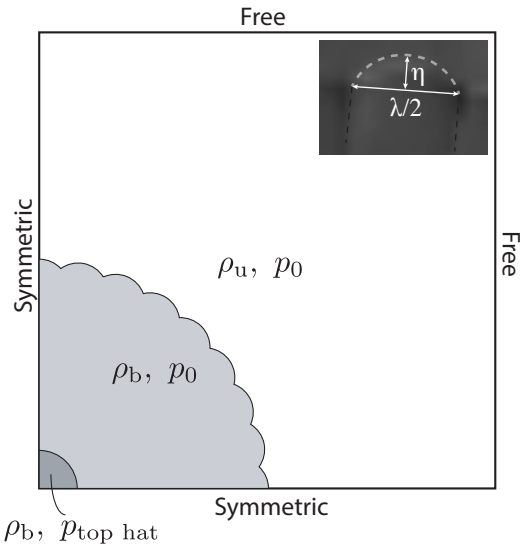

Figure 6.4: Schematic of the two-dimensional numerical domain with boundary and initial conditions for simulating the inert interaction in a quadrant of the Hele-Shaw cell.

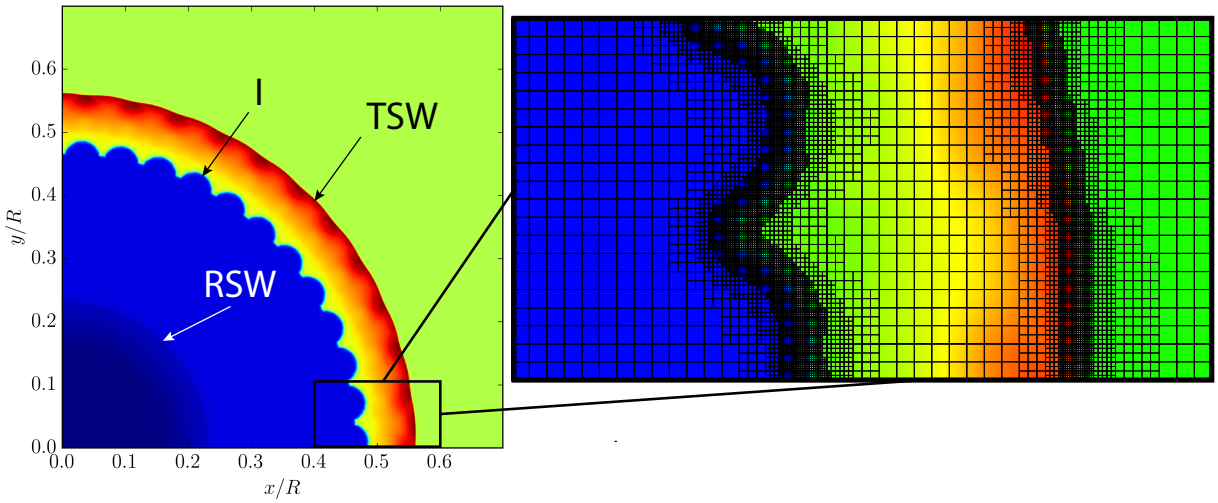

Figure 6.5: Density plot of the interface (I) deformation after the passing of the blast wave (TSW). On the right, the resulting grid is illustrated using the adaptive mesh refinement with 4 grid levels.

across the interface. At $t/t_0 = 0.220$, the reflected wave (RSW) traveled inward and the transmitted shock continued to expand in the heavier gas. The passage of the shock over the non-flat density surface deposited vorticity by the baroclinic torque mechanism of misaligned pressure gradients and density gradients. Then, as the transmitted decaying shock moved forward, both the shock and cusps interface tended to flatten. Small cells also ex-

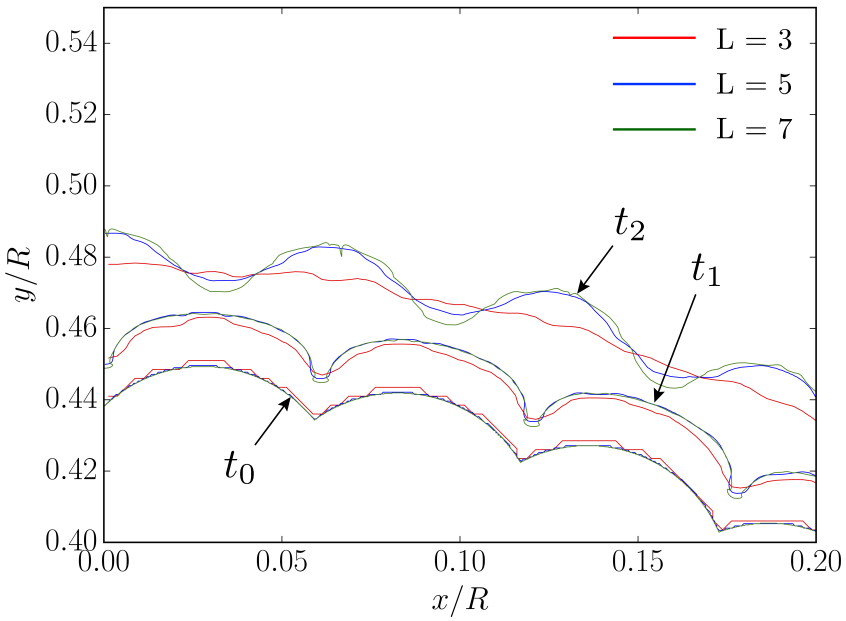

Figure 6.6: Interface density contours at three different instances for numerical grid verification study.

tended between every adjacent cusp. Eventually, the density interface folded, while still traveling in the outward direction.

One can also measure the amplitude perturbation solutions for the cellular structure with initial amplitude corresponding to the characteristic cell (C) as shown in the red box in Fig. 6.1 to compare with the linear prediction from Eqs. 6.4–6.6. To isolate the dynamics of a shock interacting with a flame, we only considered the perturbation caused by the arrival of the first incoming shock. Figure 6.8 illustrates the amplitude growth of the characteristic cell from theoretical analysis (black lines), experimental result (black triangles) and numerical solution (red circles). In the very beginning, the interface experiences a compression due to its initial wrinkled surface.

The growth rate of amplitude decreases as the shock decays, while it still shows a good agreement with the RM instability before it reaches its maximum value at $t = 2.5 \times 10^{-5}$ s. The initial growth rate of the simulation was fitted to the three initial points after compression and compared well to the linear model of RM theory (see Fig. 6.8). Afterwards, as it reaches the time scale of RT instability, the amplitude starts to decrease

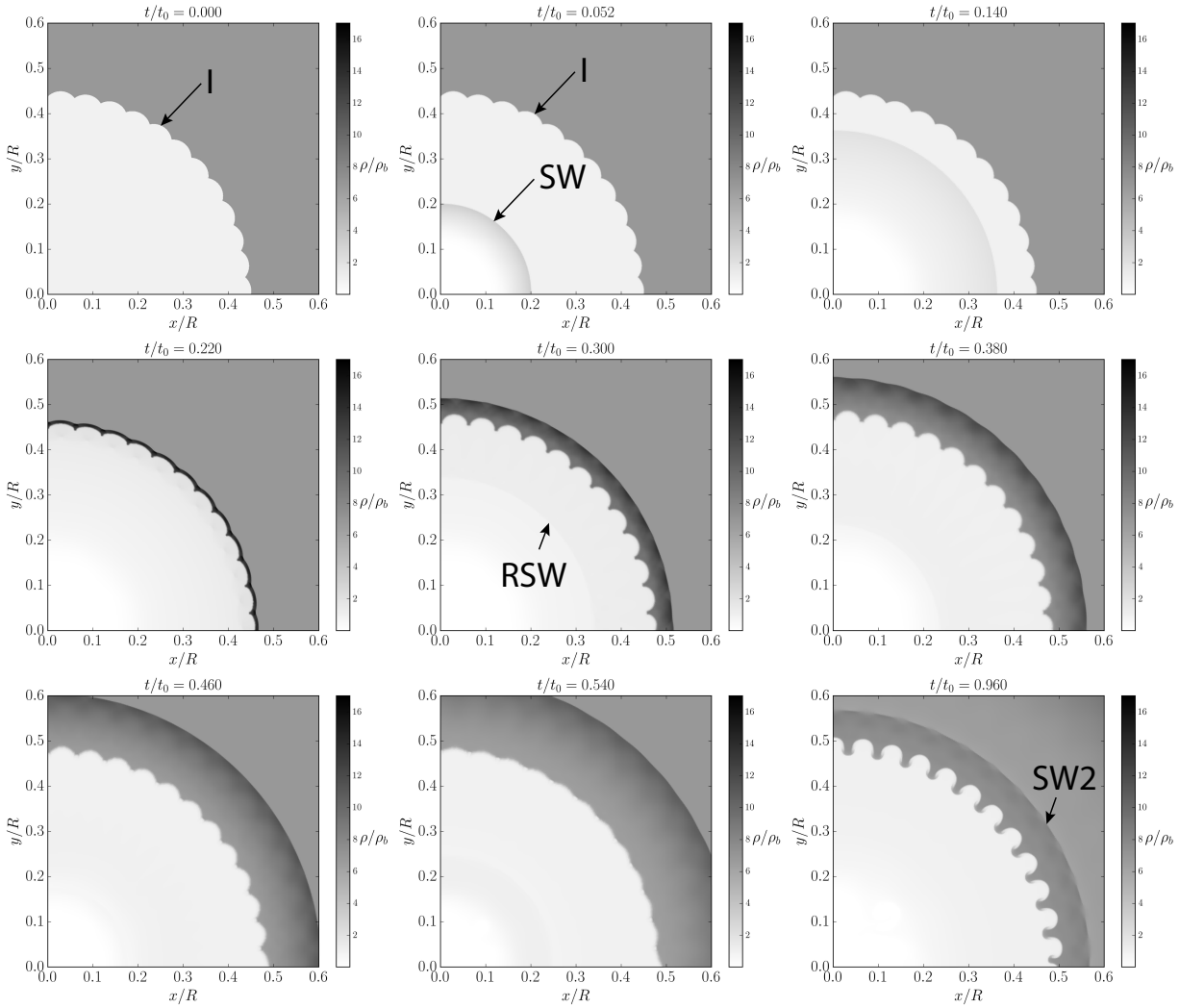

Figure 6.7: Density plots of the interaction of a shock wave (SW) coming from the origin with a density interface (I). The latest frame highlights the arrival of the reflected shock (SW2) resulting from the initial interaction.

due to the opposite acceleration caused by the expansion wave behind the shock. The time for the cusps to flatten is smaller in the simulation than in the experiment. Figures 6.9 and 6.10 depict the growth of the amplitude for the lean mixtures. The same trends can be observed: the interface gets compressed initially as represented by the numerical data points, then the amplitude of the cell enlarges until it reaches a maximum value and finally decays. The numerical solutions and the experimental data points are found to be in fairly good agreement. Besides the transient profile of the decaying shock that has a time-varying acceleration, other sources may explain the slight deviation from the linear

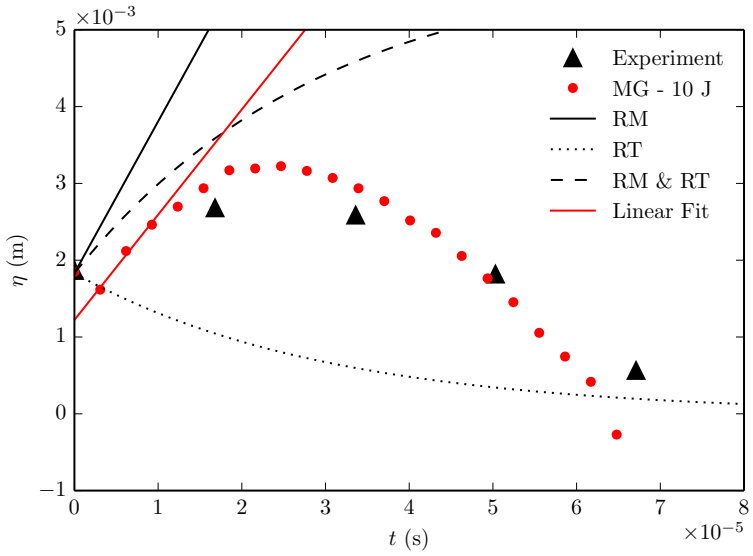

Figure 6.8: Time evolution of cell amplitude from experiment in stoichiometric H_2-air and from corresponding numerical simulation on a density interface. The curves indicate the prediction from linear models of RM, RT and their superposition (RM & RT).

prediction of RM at early times. As the amplitude increases, funnels of heavier gas would extend into the light density side and would later become shear layers, with nascent finer scale mixing. This phase exhibits secondary effects such as a Kelvin–Helmholtz instability and the deformation of the interface may transition into the non-linear regime.

6.3 Richtmyer-Meshkov instability at early times and the effect of expansion wave

To determine the relative roles of RM and RT instabilities on the flame deformation, a series of simulations of RM instability and RT instability were run in a rectangular tube with a single sinusoidal density interface separating light and heavy gases. For this case, the conditions for the experiment at $\phi = 1.0$ were investigated, using the same Mach number of 1.2 and acceleration of 3.0×10^6 $^{m}/_{s^2}$ measured from the experiment. Again, the wavelength and the initial amplitude were the same as the characteristic cell in Fig. 6.1. The computation domain was refined using adaptive mesh refinement with similar criteria as stated in Section 6.2. Shock jump conditions were used to initialize a steady shock in

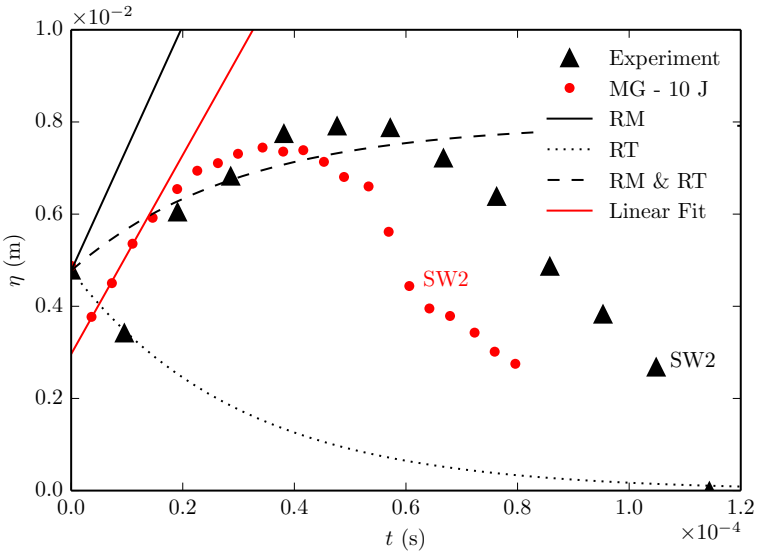

Figure 6.9: Time evolution of cell amplitude from experiment in H_2-air at $\phi = 0.6$ and from corresponding numerical simulation on a density interface. The curves indicate the prediction from linear models of RM, RT and their superposition (RM & RT). The arrival of the second shock wave (SW2) is highlighted for each set of data points.

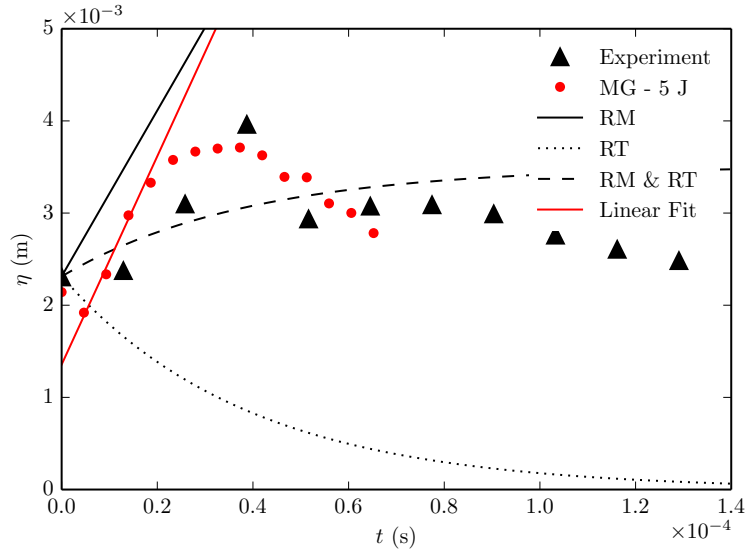

Figure 6.10: Time evolution of cell amplitude from experiment in H_2-air at $\phi = 0.3$ and from corresponding numerical simulation on a density interface. The curves indicate the prediction from linear models of RM, RT and their superposition (RM & RT).

the light gas near the density interface for the RM case. Symmetric boundary conditions at $y = 0$ and $y = \lambda$ were used, while free-type conditions were set for x boundaries. For the case of RT, a constant acceleration corresponding to a was added to the equations

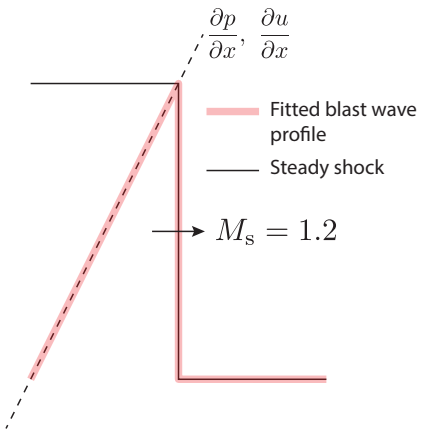

Figure 6.11: Fitted blast wave profile with decaying pressure and velocity gradient behind the leading shock front.

of motion. The acceleration was also counteracted by a hydrostatic pressure gradient. Boundary conditions were all reflective for the rectangular channel. A fitted blast wave profile was used to initiate a simulation from the superposition of a shock wave with $M_s = 1.2$ with constant pressure and velocity profiles ($\partial p/\partial x$ and $\partial u/\partial x$) behind the leading shock as illustrated in Fig. 6.11. The decaying profile of $\partial p/\partial x$ and $\partial u/\partial x$ were calculated from shock change equations using the parameters obtained from the experiments. The results of amplitude evolution are shown in Fig. 6.12. It is clear that when the shock travels from the light to heavy gases, the RM instability tends to elongate the perturbed interface and the RT instability contributes to stabilize the interface. In the case where a decaying shock interacts with the perturbed interface, the RM instability initially controls the elongation of the cusps, as the time scale for RT is three times larger than for RM. The vorticity drives the surface deformation in early times, and leads to flame stretching. Furthermore, the shock strength decreases over time, allowing the RT instability to play an important role and to eventually cause the phase reversal of the density interface to its original shape. Since the pressure gradient $\vec{\nabla} p$ is different behind the precursor shock, the vorticity changes direction due to the baroclinic term. In this optic, the reversal of the cusps has shown good qualitative agreement with the results of Collins [30], in which the expansion wave caused the perturbed interface to reverse.

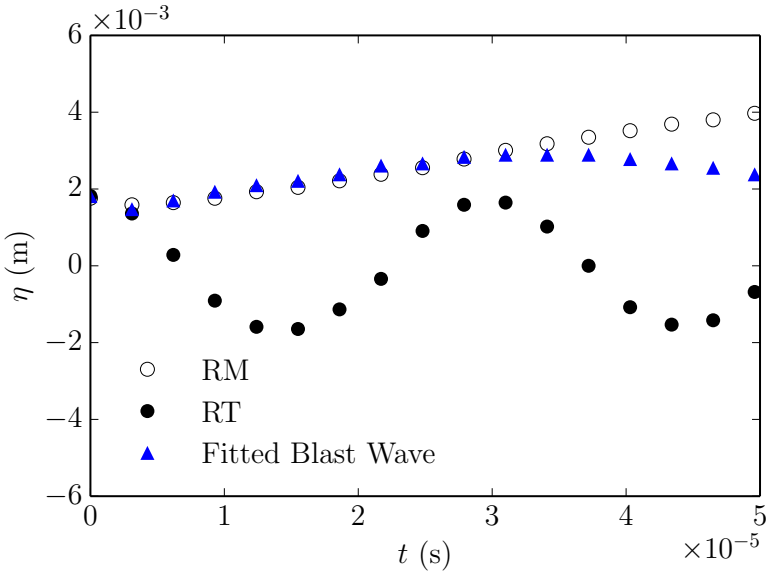

Figure 6.12: Time evolution of the amplitude of an isolated cell subjected to RM, RT and the combination of RM & RT, independently.

6.4 Multiple interactions

Although the analysis has predominantly dealt with the initial interaction of a cellular flame in the same direction with a blast wave originating in the light gases, or reacted products of the combustion wave, the reshocked interface constitutes an important phase of the shock-flame complex in the Hele-Shaw vessel. In fact, the interface is already unstable and would accelerate a second time after the passage of the reflected shock. Subsequently, the shock-induced acceleration is accompanied by a complete phase reversal of the interface. A second interaction causes the surface to become more corrugated. Thus, the contact area of the flame increases accordingly and could translate to an increase of the burning rate. Multiple interactions from the reflected shocks on the boundary of the Hele-Shaw cell dominate the late-time deformation on the flame density interface. The distortion is thus characterized by secondary effects and significant mixing enhancement is observed. Combustion of the unburned mixture may potentially play a role as time develops.

Chapter 7

Conclusion

7.1 Contribution of the present study

The problem of the interaction of a blast wave with a cellular flame was addressed experimentally in a Hele-Shaw cell with a hydrogen-air mixture and numerically for a non-reactive case. The implementation of a Hele-Shaw cell technique provided two novel geometries to monitor head-on shock-flame interactions for a shock wave parallel with the cellular flame interface. The experimental apparatus successfully isolated the flame propagation in a quasi-two dimensional manner. The first geometry allowed to study the passage of shock wave through the flame where both the blast wave and the interface grew outwardly from the same ignition location. The second geometry, which was comprised of multiple ignition points for the deflagration, provided a way to investigate the colliding shock-flame interaction by allowing a centrally generated blast wave to traverse the cellular flame front propagating inwards. For the light-to-heavy shock-flame interaction, experimental evidence revealed that the reversal of the density interface separating the burned and unburned gases is caused by the expansion waves associated with the time-varying decaying profile of the shock wave. Competing effects of flow instabilities affect the distortion of the flame. A time scale analysis was performed to help in the interpretation of the contribution of RM and RT instabilities on the flame interface. The combustion process of the H_2-air mixtures in the present study is not expected to influence the deformation of the interface, since

the time scales for combustion were an order of magnitude or greater than the observation time of the evolution of the perturbations. Numerical simulations on an inert density interface, which mimicked the flame cusps shape, have shown that a RM instability acts in the first place at early times for the light-to-heavy case and tends to elongate the flame cusps. After some time of development, a RT instability starts to play a significant role by overturning the vorticity generated by the shock-excited RM instability. This phenomenon lead to reverse the cellular front. In this aspect, experiments and inert numerical results were found to be in good agreement. For the case of a blast wave propagating from the heavy-to-light gases, the distortion was much more disruptive, causing the reversal of the flame front in the initial instants after the interaction with the shock wave.

7.2 Recommendations

The present thesis has mainly focused on the analysis of a shock wave interacting with a cellular flame front in the same outward propagation direction, and this, for H_2-air mixtures at stoichiometry and leaner concentrations. Based on the work performed, the following ideas could be addressed in the scope of shock-flame interactions using the implemented apparatus:

- The analysis of the deformation has been performed on a single cell for one experiment for the three equivalence ratios. In fact, as shown in the experimental records, cellular flames are composed of multiple wavelengths with different cell sizes. Multiple cells should be taken into consideration for the measurement of the average of cells' amplitude for an experiment;
- In terms of the interaction for the heavy-to-light case, the passage of the shock from the heavy density side renders the interface unstable to both RM & RT. Quantitative measurements should be devoted to clarifying the early deformation of the latter. Initially, RM would have a stabilizing effect. After the reversal, RT would take over and amplify the amplitude deformation;

– The present study dealt with the combustion of a mixture of hydrogen-air at ambient pressure. The experiment setup can be further improved or installed in other chambers, where the pressure and reactive mixture compositions could be varied to observe the development of cellular flame structures perturbed by a blast wave. More reactive mixtures could eventually lead to a fast flame regime or DDT;

– By knowing the shock profile, one could predict the ensuing time for the reversal of the flame structure based on its interaction with the blast wave. In this optic, future work should be addressed to develop analytical models for blast wave interactions with a cellular flame front;

– A larger test vessel with the same characteristics of the present Hele-Shaw cell system could be implemented to have more time to observe the development of instabilities on the interface, and especially for the case of an interaction from the heavy-to-light gases using multiple igniters;

– Numerical simulations in this work were performed for an inert interface corresponding to the density ratio separating the burned and unburned gases devoid of chemical reactions. Numerical simulations with a reactive configuration should be achieved to better compare with experiments; combustion may substantially affect the early deformation of the interface for more reactive mixtures, e.g., hydrogen-oxygen.

APPENDICES

Appendix A

Technical Drawings

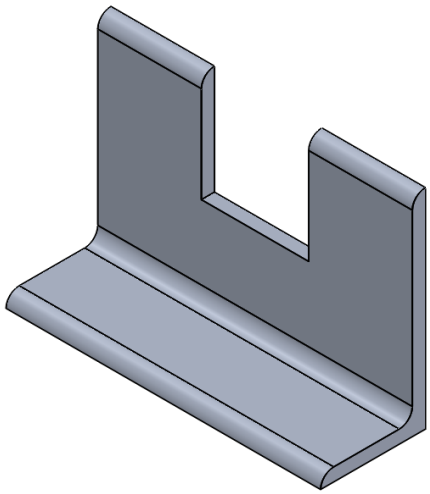

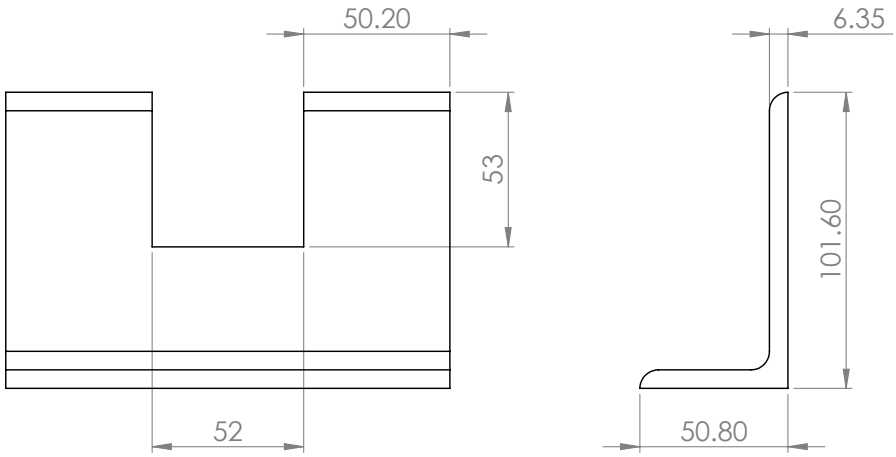

UNLESS OTHERWISE SPECIFIED: DIMENSIONS ARE IN MILLIMETERS SURFACE FINISH: TOLERANCES: LINEAR: ANGULAR:		FINISH:			DEBUR AND BREAK SHARP EDGES	DO NOT SCALE DRAWING	REVISION
	NAME	SIGNATURE	DATE			TITLE:	
DRAWN							
CHK'D							
APPV'D							
MFG							
Q.A				MATERIAL: 6061 Al		DWG NO. bracket_shock	A4
				WEIGHT:		SCALE:1:2	SHEET 1 OF 1

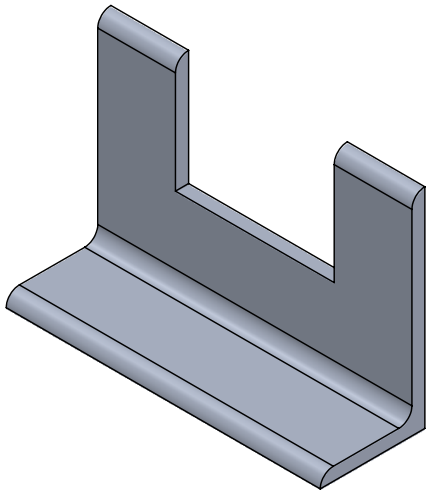

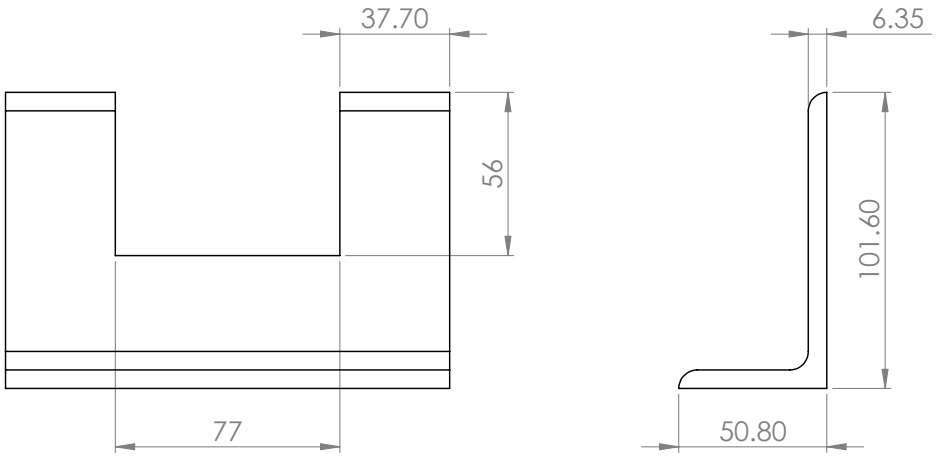

UNLESS OTHERWISE SPECIFIED: DIMENSIONS ARE IN MILLIMETERS SURFACE FINISH: TOLERANCES: LINEAR: ANGULAR:		FINISH:			DEBUR AND BREAK SHARP EDGES	DO NOT SCALE DRAWING	REVISION
	NAME	SIGNATURE	DATE			TITLE:	
DRAWN							
CHK'D							
APPV'D							
MFG							
Q.A				MATERIAL: 6061 Al		DWG NO. bracket_spark	A4
				WEIGHT:		SCALE:1:2	SHEET 1 OF 1

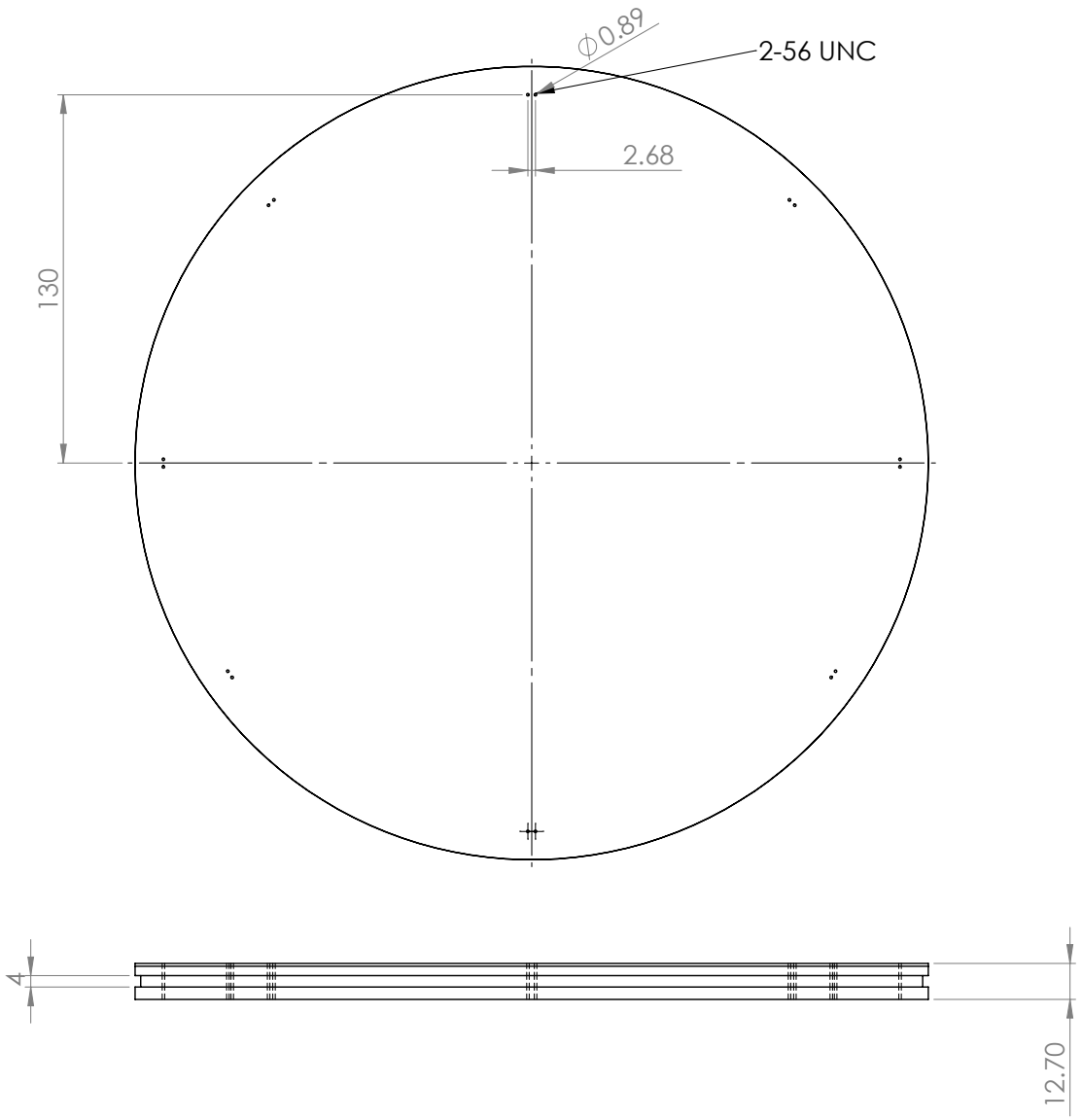

UNLESS OTHERWISE SPECIFIED: DIMENSIONS ARE IN MILLIMETERS SURFACE FINISH: TOLERANCES: LINEAR: ANGULAR:	FINISH:		DEBUR AND BREAK SHARP EDGES			DO NOT SCALE DRAWING	REVISION
	NAME	SIGNATURE	DATE			TITLE:	
DRAWN							
CHK'D							
APPV'D							
MFG							
Q.A				MATERIAL: Acrylic		DWG NO. plate_mult_spark	A4
				WEIGHT:		SCALE:1:2	SHEET 1 OF 1

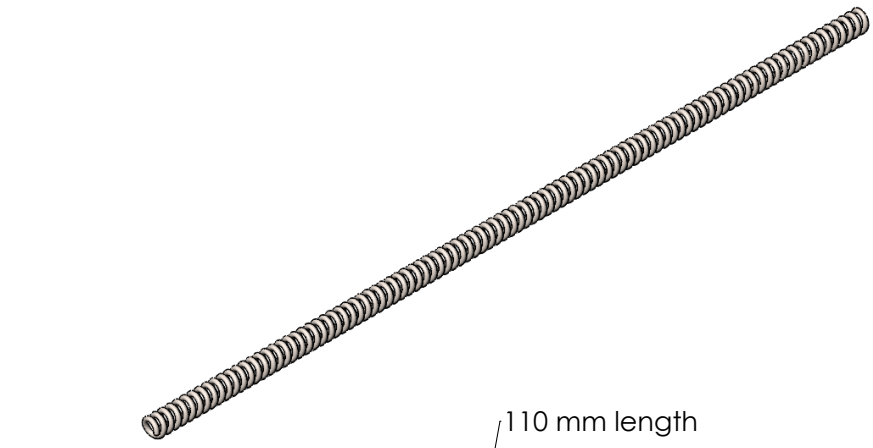

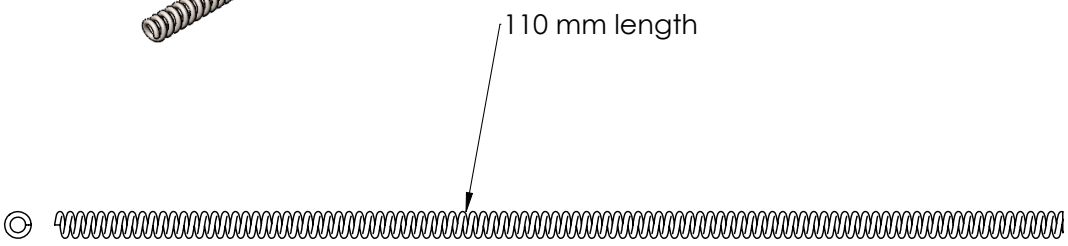

UNLESS OTHERWISE SPECIFIED: DIMENSIONS ARE IN MILLIMETERS SURFACE FINISH: TOLERANCES: LINEAR: ANGULAR:		FINISH:			DEBUR AND BREAK SHARP EDGES	DO NOT SCALE DRAWING	REVISION
	NAME	SIGNATURE	DATE			TITLE:	
DRAWN							
CHK'D							
APPV'D							
MFG							
Q.A				MATERIAL: Music Wire		DWG NO. Shchelkin spiral	A4
				WEIGHT:		SCALE:1.5:1	SHEET 1 OF 1

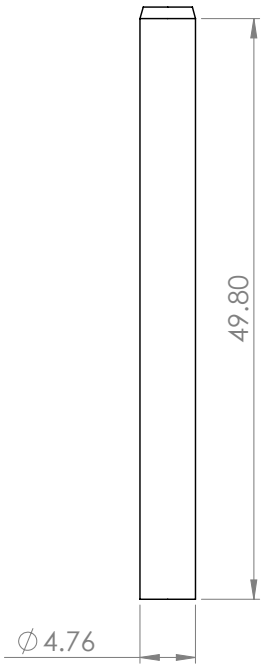

UNLESS OTHERWISE SPECIFIED: DIMENSIONS ARE IN MILLIMETERS SURFACE FINISH: TOLERANCES: LINEAR: ANGULAR:		FINISH:			DEBUR AND BREAK SHARP EDGES	DO NOT SCALE DRAWING	REVISION
	NAME	SIGNATURE	DATE			TITLE:	
DRAWN							
CHK'D							
APPV'D							
MFG							
Q.A				MATERIAL: Copper		DWG NO. copper_electrode	A4
				WEIGHT:		SCALE:2:1	SHEET 1 OF 1

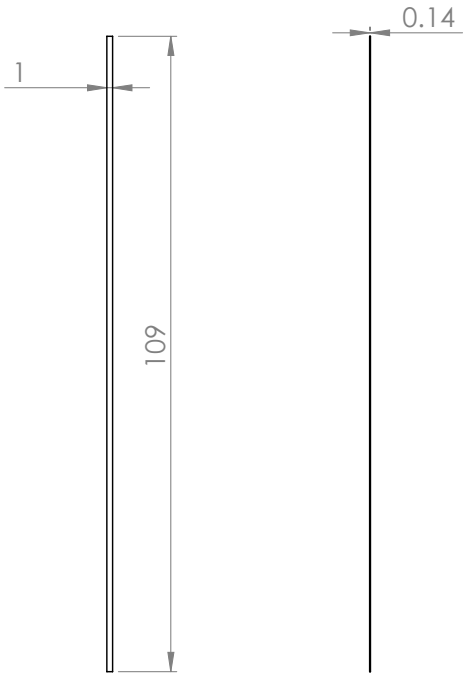

UNLESS OTHERWISE SPECIFIED: DIMENSIONS ARE IN MILLIMETERS SURFACE FINISH: TOLERANCES: LINEAR: ANGULAR:		FINISH:			DEBUR AND BREAK SHARP EDGES	DO NOT SCALE DRAWING	REVISION
	NAME	SIGNATURE	DATE			TITLE:	
DRAWN							
CHK'D							
APPV'D							
MFG							
Q.A				MATERIAL: Copper		DWG NO. copper_strip	A4
				WEIGHT:		SCALE:1:1	SHEET 1 OF 1

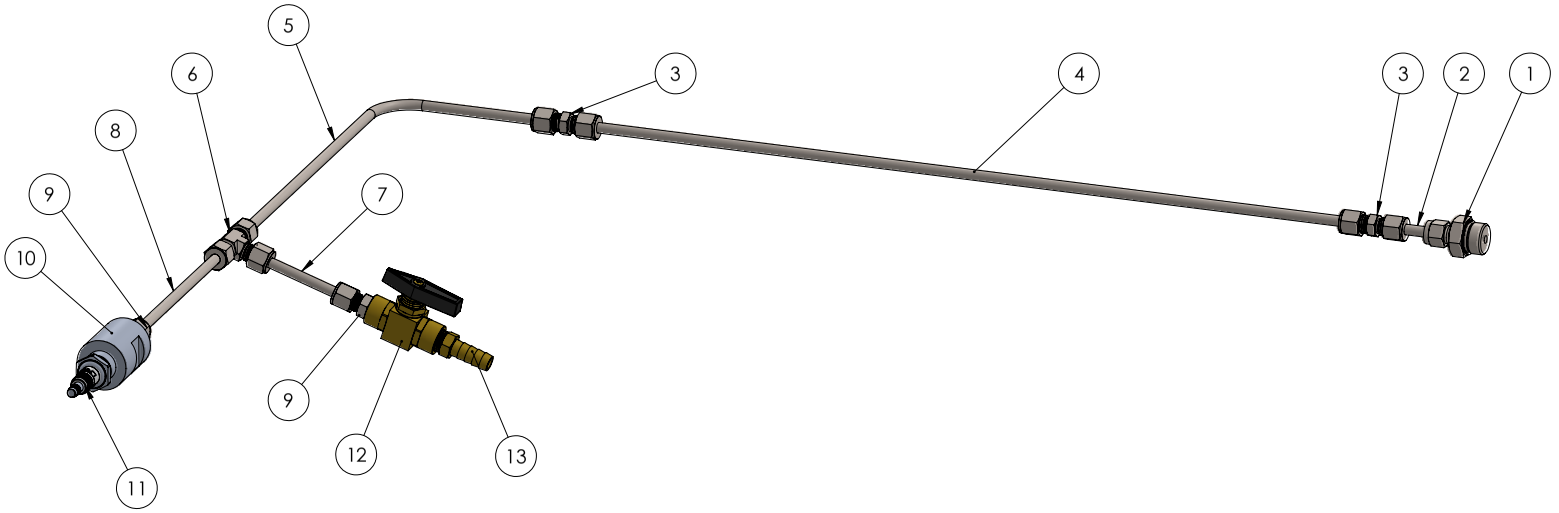

ITEM NUMBER	DESCRIPTION
1	3/4-16 UNF to 1/4 OD Swagelok fitting
2	1/4 OD (2.72 mm ID) 316 SS tube
3	1/4 Swagelok straight connector
4	1/4 OD (2.72 mm ID) 316 SS tube
5	1/4 OD (2.72 mm ID) 316 SS tube
6	1/4 Swagelok tee fitting
7	1/4 OD (2.72 mm ID) 316 SS tube
8	1/4 OD (2.72 mm ID) 316 SS tube with Shchelkin spiral
9	1/4 Swagelok to 1/4 NPT male fitting
10	Spark plug port
11	Spark plug (Champion L78C)
12	Quarter-turn ball valve 1/4 NPT female
13	1/4 NPT to 3/8 barbed hose fitting

UNLESS OTHERWISE SPECIFIED: DIMENSIONS ARE IN MILLIMETERS SURFACE FINISH: TOLERANCES: LINEAR: ANGULAR:		FINISH:				DEBUR AND BREAK SHARP EDGES	DO NOT SCALE DRAWING	REVISION
	NAME	SIGNATURE	DATE				TITLE:	
DRAWN								
CHK'D								
APP'V'D								
MFG								
Q.A				MATERIAL:			DWG NO. detonation_tube_assembly	A3
				WEIGHT:			SCALE:1:2.5	SHEET 1 OF 1

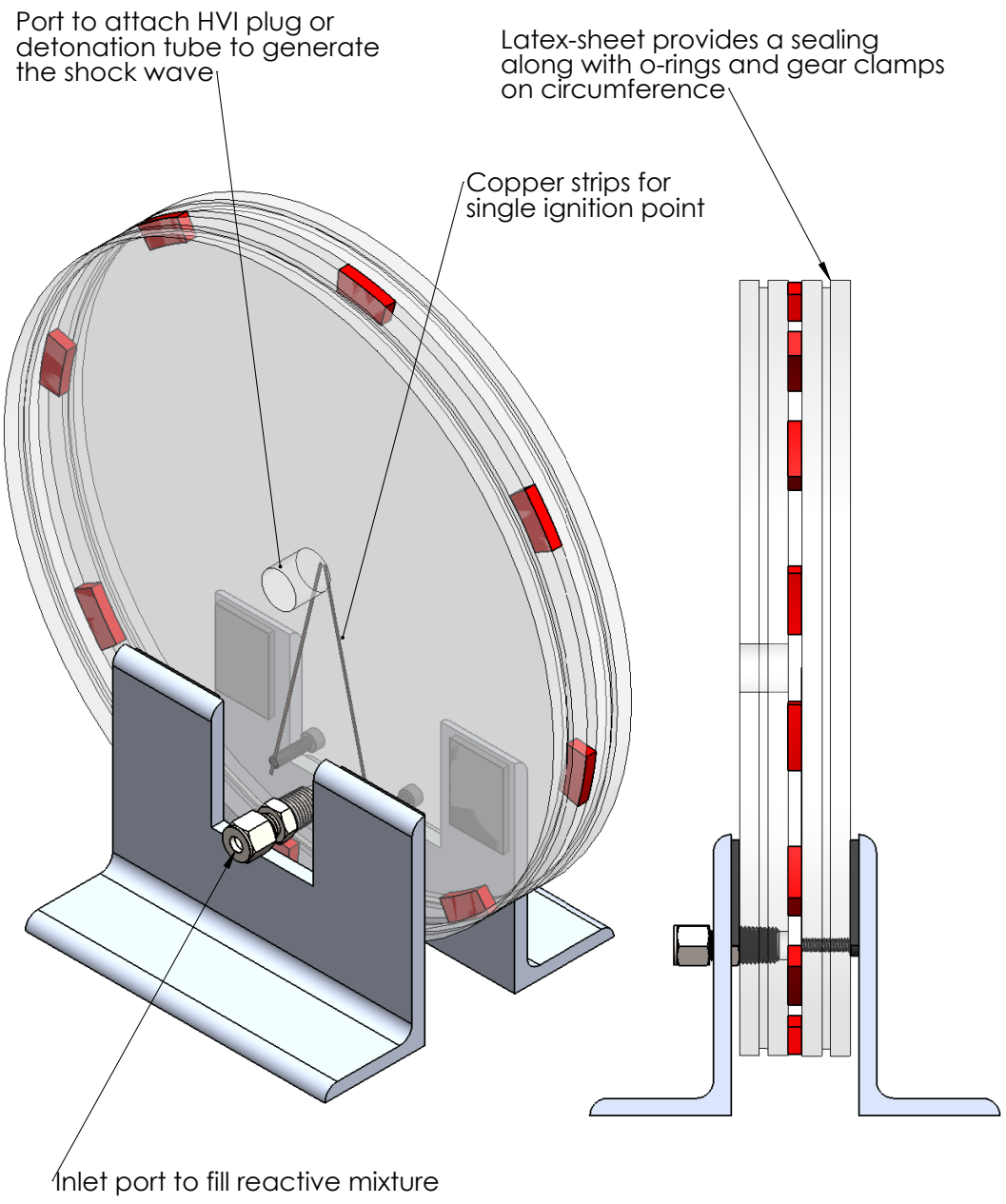

UNLESS OTHERWISE SPECIFIED: DIMENSIONS ARE IN MILLIMETERS SURFACE FINISH: TOLERANCES: LINEAR: ANGULAR:	FINISH:		DEBUR AND BREAK SHARP EDGES		DO NOT SCALE DRAWING	REVISION
	NAME	SIGNATURE	DATE			TITLE:
DRAWN						
CHK'D						
APPV'D						
MFG						
Q.A				MATERIAL:	DWG NO. hele_shaw_cell_assembly	A4
				WEIGHT:	SCALE:1:2	SHEET 1 OF 1

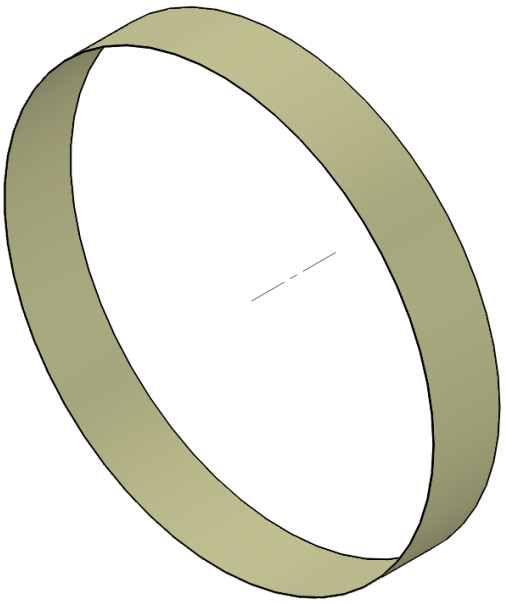

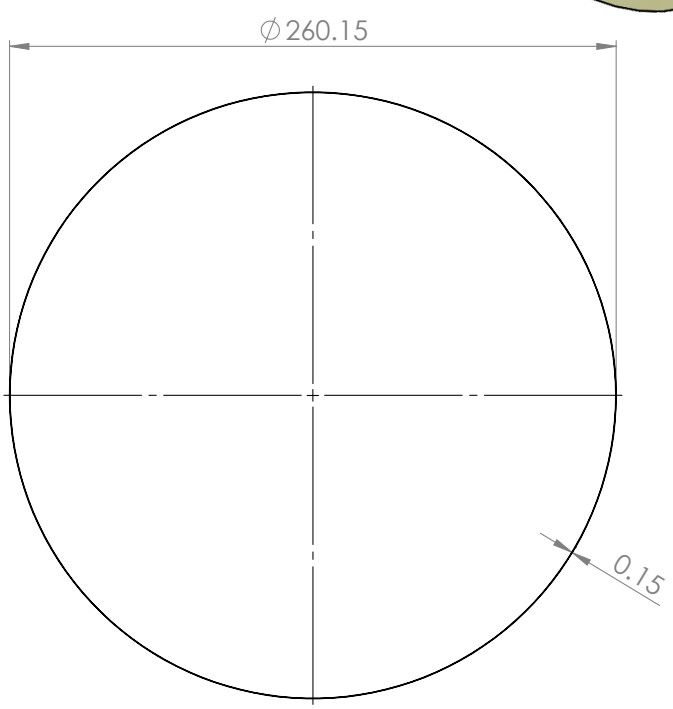

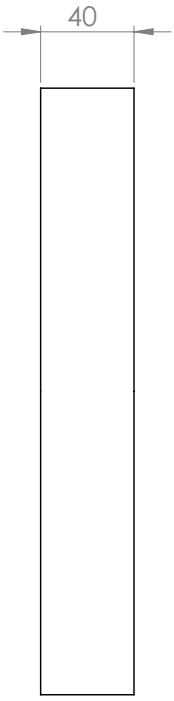

UNLESS OTHERWISE SPECIFIED: DIMENSIONS ARE IN MILLIMETERS SURFACE FINISH: TOLERANCES: LINEAR: ANGULAR:	FINISH:		DEBUR AND BREAK SHARP EDGES		DO NOT SCALE DRAWING	REVISION
	NAME	SIGNATURE	DATE			TITLE:
DRAWN						
CHK'D						
APPV'D						
MFG						
Q.A				MATERIAL: Natural rubber	DWG NO. latex_sheet	A4
				WEIGHT:	SCALE:1:2.5	SHEET 1 OF 1

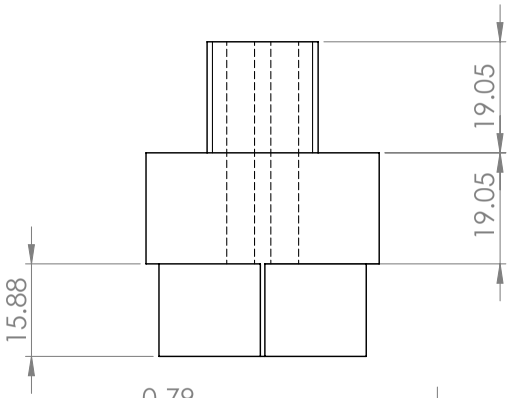

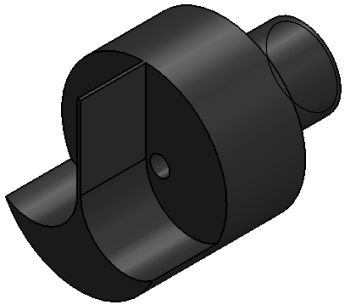

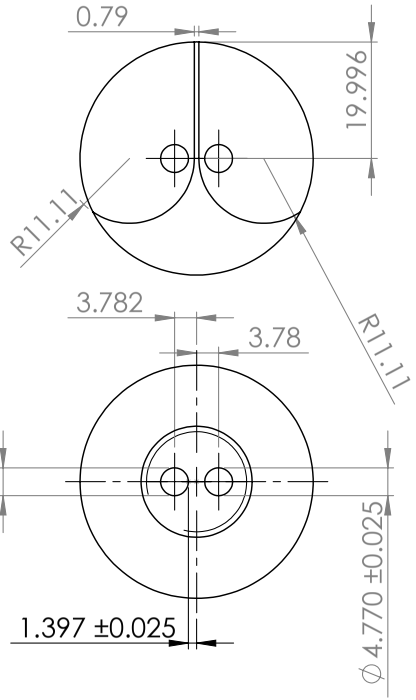

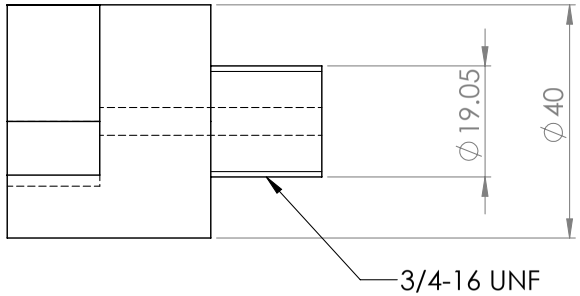

UNLESS OTHERWISE SPECIFIED: DIMENSIONS ARE IN MILLIMETERS SURFACE FINISH: TOLERANCES: LINEAR: ANGULAR:		FINISH:			DEBUR AND BREAK SHARP EDGES		DO NOT SCALE DRAWING	REVISION
	NAME	SIGNATURE	DATE				TITLE:	
DRAWN								
CHK'D								
APPV'D								
MFG								
Q.A				MATERIAL:			DWG NO.	A4
				ABS			HVI_plug	
				WEIGHT:			SCALE:1:1	SHEET 1 OF 1

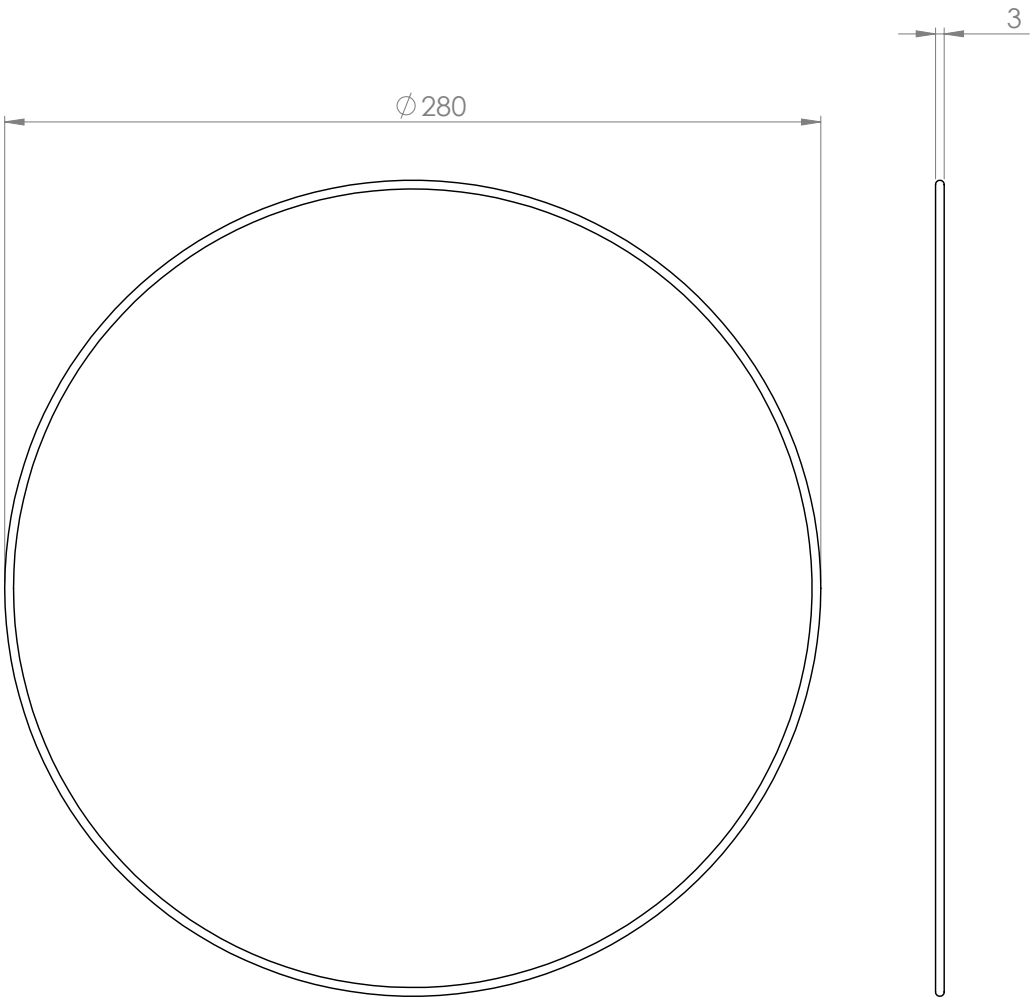

UNLESS OTHERWISE SPECIFIED: DIMENSIONS ARE IN MILLIMETERS SURFACE FINISH: TOLERANCES: LINEAR: ANGULAR:		FINISH:			DEBUR AND BREAK SHARP EDGES	DO NOT SCALE DRAWING	REVISION
	NAME	SIGNATURE	DATE			TITLE:	
DRAWN							
CHK'D							
APPV'D							
MFG							
Q.A				MATERIAL: Buna-N		DWG NO. o-ring	A4
				WEIGHT:		SCALE:1:2	SHEET 1 OF 1

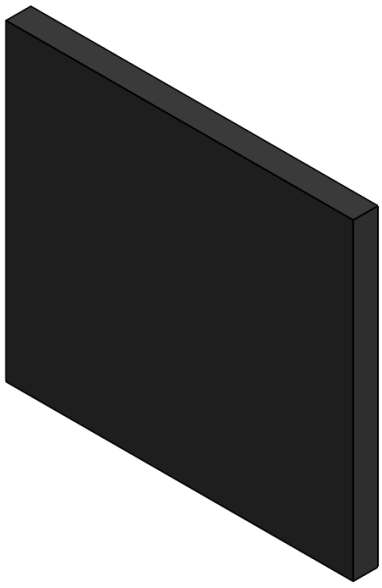

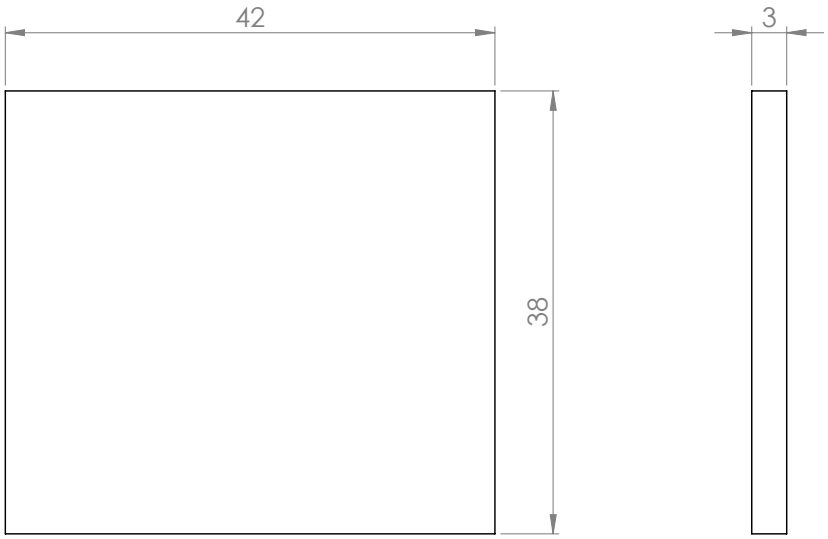

UNLESS OTHERWISE SPECIFIED: DIMENSIONS ARE IN MILLIMETERS SURFACE FINISH: TOLERANCES: LINEAR: ANGULAR:	FINISH:		DEBUR AND BREAK SHARP EDGES	DO NOT SCALE DRAWING	REVISION	
	NAME	SIGNATURE	DATE	TITLE:		
DRAWN						
CHK'D						
APPV'D						
MFG						
Q.A				MATERIAL: Neoprene	DWG NO. pad_bracket_shock	A4
				WEIGHT:	SCALE:2:1	SHEET 1 OF 1

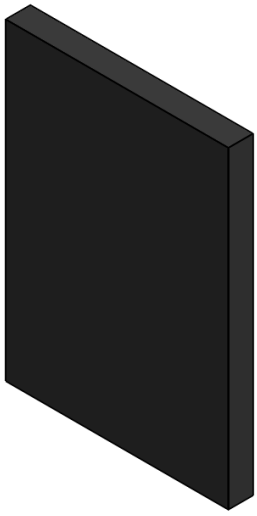

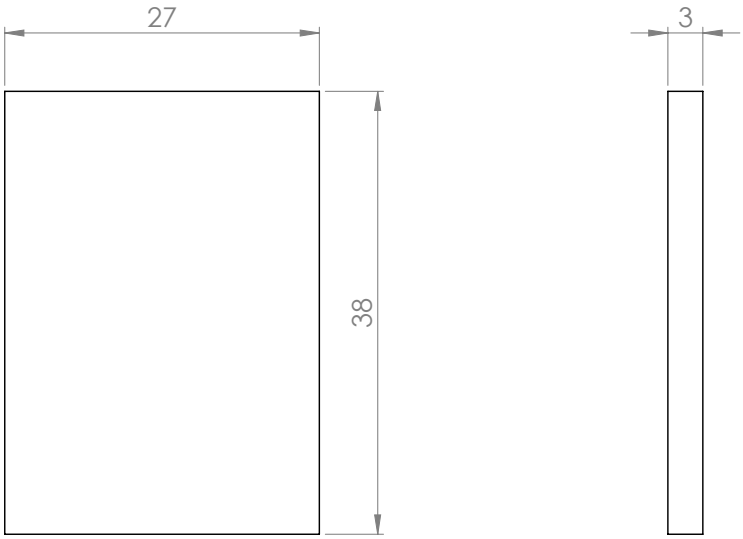

UNLESS OTHERWISE SPECIFIED: DIMENSIONS ARE IN MILLIMETERS SURFACE FINISH: TOLERANCES: LINEAR: ANGULAR:	FINISH:		DEBUR AND BREAK SHARP EDGES	DO NOT SCALE DRAWING	REVISION	
	NAME	SIGNATURE	DATE	TITLE:		
DRAWN						
CHK'D						
APPV'D						
MFG						
Q.A				MATERIAL: Neoprene	DWG NO. pad_bracket_spark	A4
				WEIGHT:	SCALE:2:1	SHEET 1 OF 1

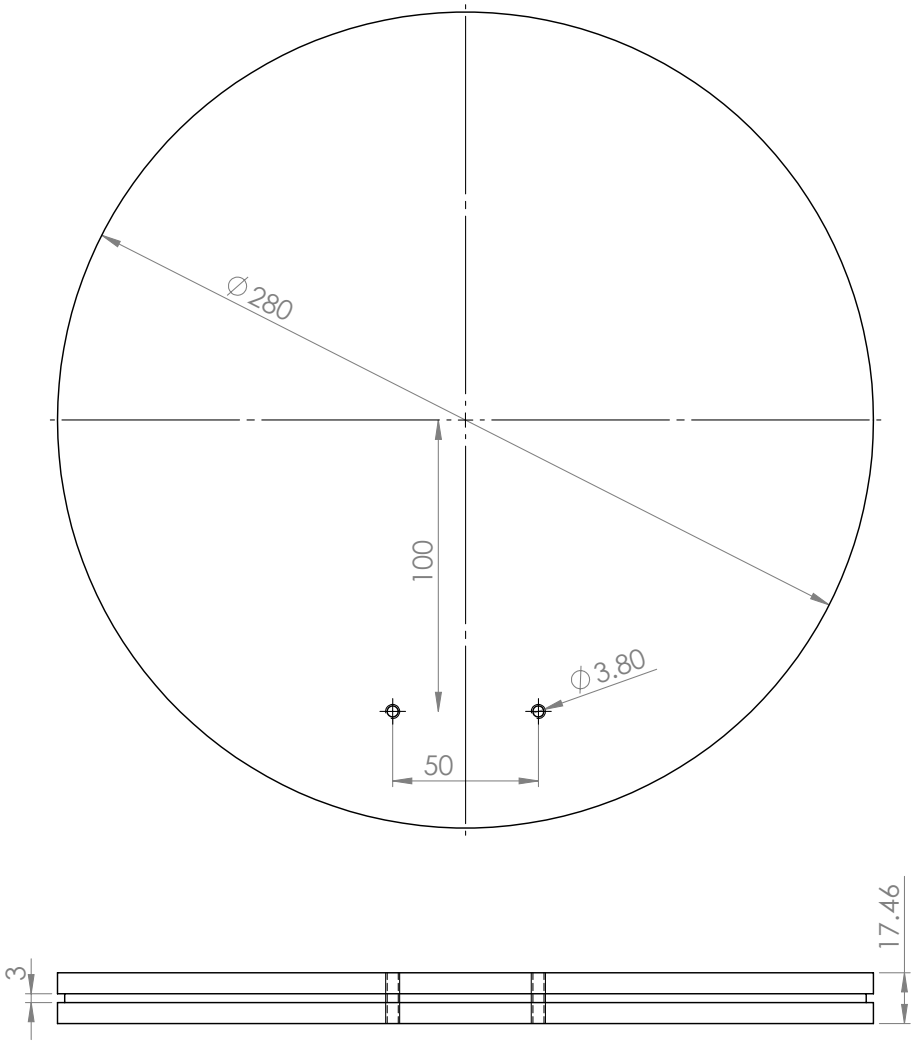

UNLESS OTHERWISE SPECIFIED: DIMENSIONS ARE IN MILLIMETERS SURFACE FINISH: TOLERANCES: LINEAR: ANGULAR:		FINISH:			DEBUR AND BREAK SHARP EDGES	DO NOT SCALE DRAWING	REVISION
	NAME	SIGNATURE	DATE			TITLE:	
DRAWN							
CHK'D							
APPV'D							
MFG							
Q.A				MATERIAL: Acrylic		DWG NO. plate_single_spark	A4
				WEIGHT:		SCALE:1:2	SHEET 1 OF 1

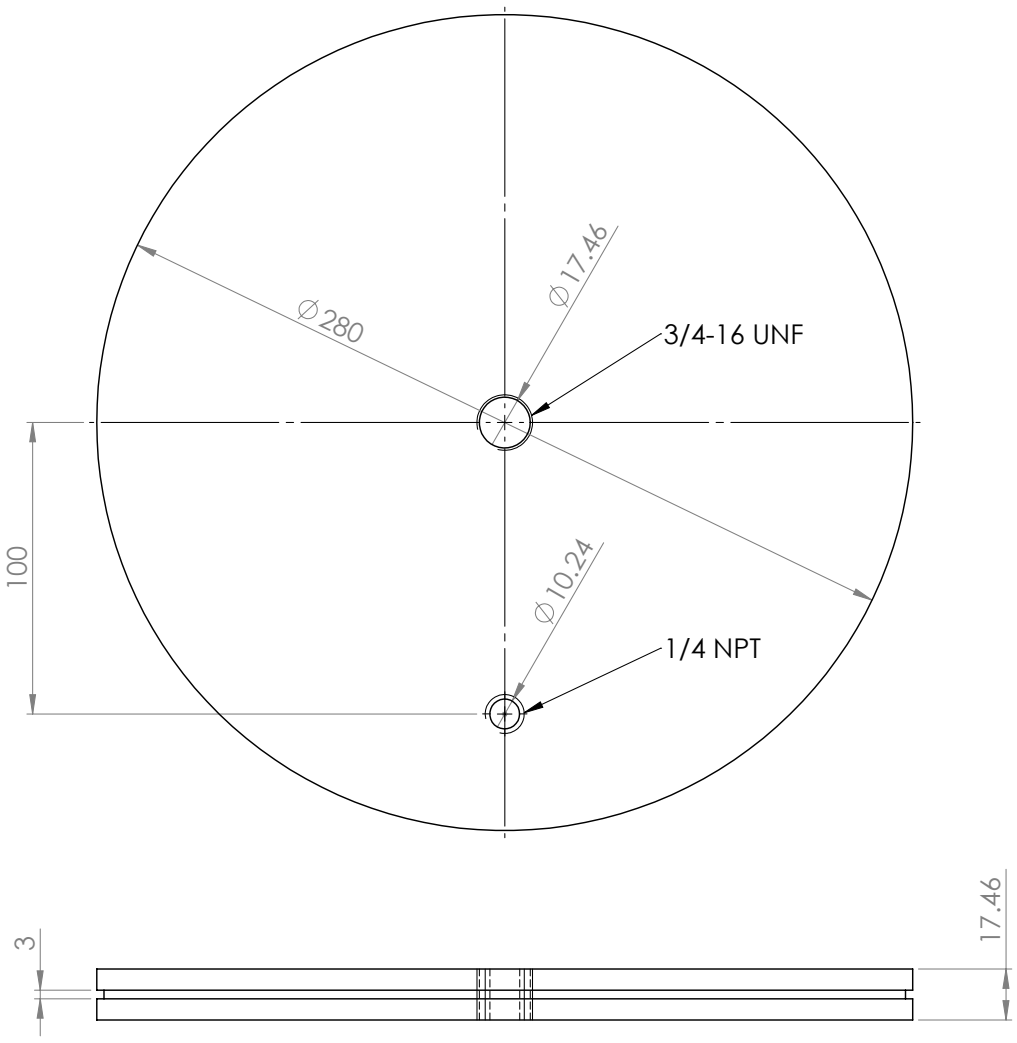

UNLESS OTHERWISE SPECIFIED: DIMENSIONS ARE IN MILLIMETERS SURFACE FINISH: TOLERANCES: LINEAR: ANGULAR:		FINISH:			DEBUR AND BREAK SHARP EDGES	DO NOT SCALE DRAWING	REVISION
	NAME	SIGNATURE	DATE			TITLE:	
DRAWN							
CHK'D							
APPV'D							
MFG							
Q.A				MATERIAL: Acrylic		DWG NO. plate_shock_inlet	A4
				WEIGHT:		SCALE:1:2	SHEET 1 OF 1

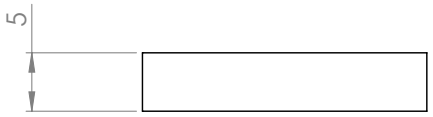

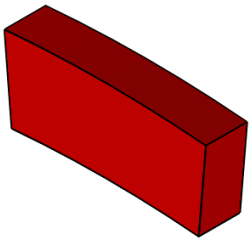

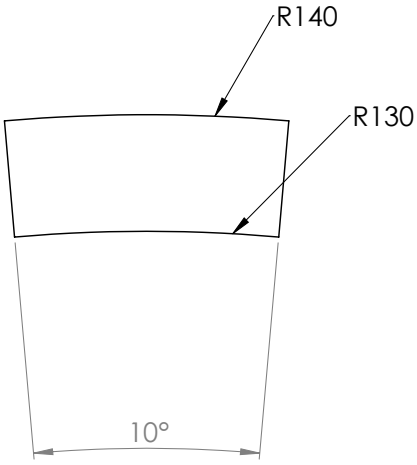

UNLESS OTHERWISE SPECIFIED: DIMENSIONS ARE IN MILLIMETERS SURFACE FINISH: TOLERANCES: LINEAR: ANGULAR:	FINISH:		DEBUR AND BREAK SHARP EDGES	DO NOT SCALE DRAWING	REVISION	
	NAME	SIGNATURE	DATE			TITLE:
DRAWN						
CHK'D						
APPV'D						
MFG						
Q.A				MATERIAL: PLA	DWG NO. spacer	A4
				WEIGHT:	SCALE:2:1	SHEET 1 OF 1

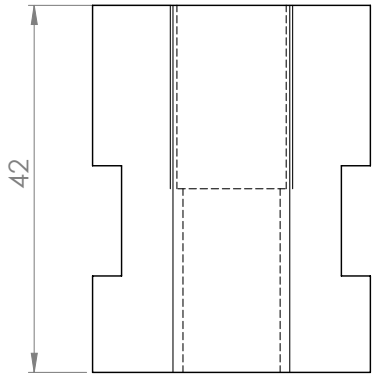

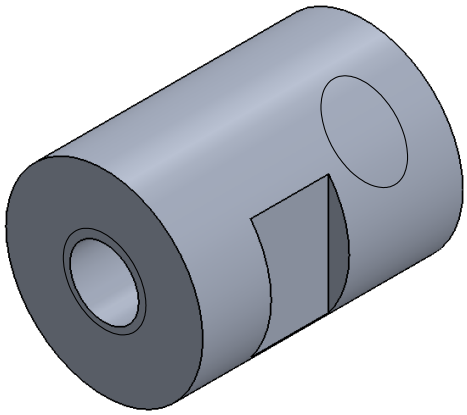

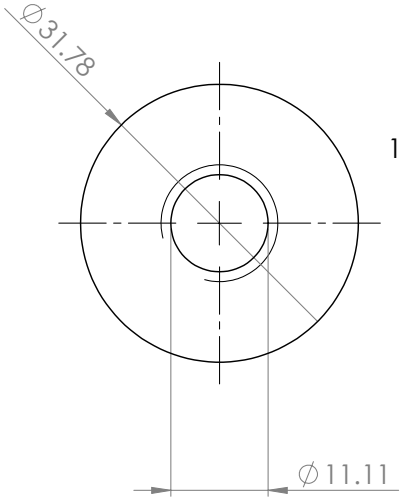

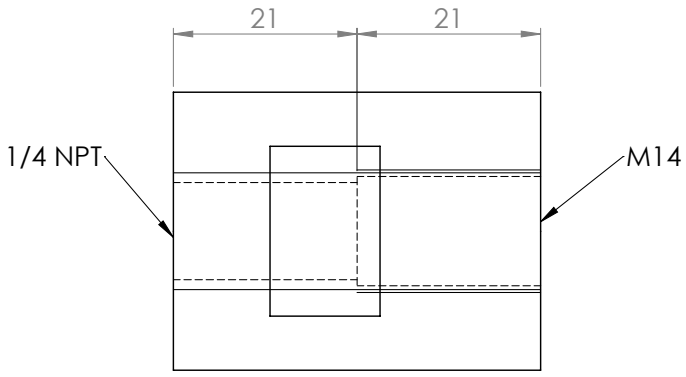

UNLESS OTHERWISE SPECIFIED: DIMENSIONS ARE IN MILLIMETERS SURFACE FINISH: TOLERANCES: LINEAR: ANGULAR:		FINISH:			DEBUR AND BREAK SHARP EDGES	DO NOT SCALE DRAWING	REVISION
	NAME	SIGNATURE	DATE			TITLE:	
DRAWN							
CHK'D							
APPV'D							
MFG							
Q.A				MATERIAL: 6061 Al		DWG NO. spark_plug_port	A4
				WEIGHT:		SCALE:1.5:1	SHEET 1 OF 1

Appendix B

Video Details

Table B.1: Hydrogen-air flame experiments in the Hele-Shaw cell.

Date	Test ID	p_0 (psi)	T_0 (°C)	Equivalence ratio	Configuration	Exposure time (μs)	Sample rate (fps)	Resolution (px)	Note
2016/07/26	2016-07-26-HS1	14.40	19	0.18	Single ignition	0.468	3,000	512 x 384	Selected for flame speed measurement
2016/12/29	2016-12-29-2H2+AIR-flame1-14.39psi	14.39	20	1.0	Single ignition	0.468	59,590	512 × 320	
2016/12/29	2016-12-29-2H2+AIR-flame2-14.00psi	14.00	20	1.0	Single ignition	0.468	59,590	512 × 320	
2016/12/29	2016-12-29-2H2+AIR-flame3-14.39psi	14.39	20	1.0	Single ignition	0.468	59,590	512 × 320	
2016/12/29	2016-12-29-2H2+AIR-flame4-14.39psi	14.39	20	1.0	Single ignition	0.468	59,590	512 × 320	
2016/12/30	2016-12-30-2H2+AIR-flame1-14.56psi	14.56	20	1.0	Single ignition	0.468	59,590	512 × 320	
2016/12/30	2016-12-30-2H2+AIR-flame1-14.70psi	14.70	20	1.0	Single ignition	0.468	59,590	512 × 320	
2017/01/02	2017-01-02-2H2+AIR-flame1-14.4psi	14.40	20	1.0	Single ignition	0.468	59,590	512 × 320	
2017/01/02	2017-01-02-2H2+AIR-flame1-14.36psi	14.36	20	1.0	Single ignition	0.468	59,590	512 × 320	
2017/01/02	2017-01-02-2H2+AIR-flame1-14.43psi	14.43	20	1.0	Single ignition	0.468	59,590	512 × 320	
2017/01/02	2017-01-02-2H2+AIR-flame1-14.46psi	14.46	20	1.0	Single ignition	0.468	59,590	512 × 320	
2017/01/02	2017-01-02-2H2+AIR-flame1-14.51psi	14.51	20	1.0	Single ignition	0.468	59,590	512 × 320	
2017/01/10	2017-01-10-2H2+AIR-flame1-14.67psi	14.67	20	1.0	Single ignition	0.468	59,590	512 × 320	Selected for flame speed measurement
2017/01/10	2017-01-10-2H2+AIR-flame1-14.68psi	14.68	20	1.0	Single ignition	0.468	59,590	512 × 320	
2017/02/02	2017-02-02-20%H2+AIR-flame1-14.6psi	14.60	21	0.6	Single ignition	0.468	77,481	384 × 288	Double flame kernels
2017/02/08	2017-02-08-20%H2+AIR-flame1-14.52psi	14.52	20	0.6	Single ignition	0.468	77,481	384 × 288	Oscillations of the flame / bad Schlieren
2017/02/08	2017-02-08-20%H2+AIR-flame2-14.52psi	14.52	20	0.6	Single ignition	0.468	77,481	384 × 288	Oscillations of the flame / bad Schlieren
2017/03/09	09-03-2017-14.6psi-flame1	14.60	21	0.6	Single ignition	0.468	77,481	384 × 288	
2017/07/25	2017-07-25_20%_flame1	14.50	21	0.6	Single ignition	0.468	77,481	384 × 288	Selected for flame speed measurement
2017/09/21	2017-09-21_8sparks_20H2-air_flame1	14.46	20	0.6	Multiple ignitions	0.468	77,481	384 × 288	Flame moves a lot
2017/09/22	2017-09-22_8sparks_20H2-air_flame1	14.50	20	0.6	Multiple ignitions	0.468	77,481	384 × 288	Not symmetrical
2017/09/25	2017-09-25_8sparks_20H2-air_flame1	14.49	21	0.6	Multiple ignitions	0.468	77,481	384 × 288	Not symmetrical, but still good
2017/09/26	2017-09-26_20H2-air_flame1	14.50	21	0.6	Multiple ignitions	0.468	77,481	384 × 288	Not symmetrical, but still good
2017/09/27	2017-09-27_20H2-air_flame1	14.52	19	0.6	Multiple ignitions	0.468	77,481	384 × 288	Not symmetrical
2017/09/27	2017-09-27_20H2-air_flame2	14.52	19	0.6	Multiple ignitions	0.468	77,481	384 × 288	Not symmetrical
2017/09/27	2017-09-27_20H2-air_flame3	14.52	19	0.6	Multiple ignitions	0.468	77,481	384 × 288	Not symmetrical
2017/10/05	2017-10-05_20H2-air_flame1	14.60	19	0.6	Multiple ignitions	0.468	77,481	384 × 288	Not symmetrical
2017/10/05	2017-10-05_20H2-air_flame2	14.60	19	0.6	Multiple ignitions	0.468	77,481	384 × 288	Not symmetrical
2017/10/07	2017-10-07_flame1	14.52	19	0.6	Single ignition	0.468	77,481	384 × 288	
2017/10/17	2017-10-17_flame1	14.50	19	0.3	Single ignition	0.468	77,481	384 × 288	Selected for flame speed measurement
2017/10/17	2017-10-17_flame2	14.50	19	0.3	Single ignition	0.468	77,481	384 × 288	
2017/10/17	2017-10-17_flame3	14.50	19	0.3	Single ignition	0.468	77,481	384 × 288	
2017/10/17	2017-10-17_flame4	14.50	19	0.3	Single ignition	0.468	77,481	384 × 288	
2018/01/24	2018-01-24-flame1	14.50	21	0.3	Single ignition	0.468	77,481	384 × 288	
2018/01/24	flame_high_resolution2	14.50	21	0.3	Single ignition	0.468	12,713	1280 × 800	High resolution with new lens
2018/01/26	2018-01-26-flame1.mp4	14.52	20	0.3	Multiple ignitions	0.468	77,481	384 × 288	

Table B.2: Shock-flame experiments in hydrogen-air in the Hele-Shaw cell – Light-to-heavy configuration.

Date	Test ID	p_0 (psi)	T_0 (°C)	Equivalence ratio	Shock source	Exposure time (μs)	Sample rate (fps)	Resolution (px)	Note
2017/01/10	2017-01-10-2H2+AIR-shockflame1-14.68psi-21.3kV	14.68	20	1.00	HVI	0.468	59,590	512 × 320	Selected for cell's amplitude measurement
2017/03/16	16-03-2017-14.6psi-flame1	14.60	21	0.6	HVI	0.468	77,481	384 × 288	Bad timing/schlieren quality
2017/03/16	16-03-2017-14.6psi-flame2	14.60	21	0.6	HVI	0.468	77,481	384 × 288	Bad timing/schlieren quality
2017/03/16	16-03-2017-14.6psi-flame3	14.60	21	0.6	HVI	0.468	77,481	384 × 288	Bad Schlieren quality
2017/03/16	16-03-2017-14.6psi-flame4	14.60	21	0.6	HVI	0.468	77,481	384 × 288	Bad Schlieren quality
2017/03/16	16-03-2017-14.6psi-flame5	14.60	21	0.6	HVI	0.468	104,918	256 × 256	Bad Schlieren quality / Selected for cell's amplitude measurement
2017/07/27	2017-07-27_20%_shockflame1	14.50	20	0.6	Det. tube	0.468	77,481	384 × 288	
2017/08/30	2017-08-30_20%H2-air_shockflame1	14.50	21	0.6	Det. tube	0.468	77,481	384 × 288	
2017/08/31	2017-08-31_shock3_14.69psi_20H2_14.66psi	14.66	21	0.6	Det. tube	0.468	77,481	384 × 288	Shock wave too early
2017/09/05	2017-09-05_14.48psiHS_14.61DT_shockflame1	14.48	22	0.6	Det. tube	0.468	77,481	384 × 288	
2017/09/07	2017-09-07_14.452psiHS_14.66DT_shockflame1	14.45	22	0.6	Det. tube	0.468	77481	384 × 288	
2017/10/07	2017-10-07_shockflame1	14.48	19	0.6	Det. tube	0.468	77,481	384 × 288	Problem with detonation tube
2018/01/24	2018-01-24-shockflame1	14.50	21	0.3	Det. tube	0.468	77,481	384 × 288	Shock wave too late
2018/01/24	2018-01-24-shockflame2	14.50	21	0.3	Det. tube	0.468	77,481	384 × 288	Shock wave too late
2018/01/24	2018-01-24-shockflame3	14.50	21	0.3	Det. tube	0.468	77,481	384 × 288	Shock wave too late
2018/01/24	2018-01-24-shockflame4	14.50	21	0.3	Det. tube	0.468	77,481	384 × 288	
2018/01/24	2018-01-24-shockflame5	14.50	21	0.3	Det. tube	0.468	77,481	384 × 288	
2018/01/25	2018-01-25-shockflame1	14.50	21	0.3	Det. tube	0.468	77,481	384 × 288	Shock wave too late
2018/01/25	2018-01-25-shockflame2	14.50	21	0.3	Det. tube	0.468	77,481	384 × 288	
2018/01/25	2018-01-25-shockflame3	14.50	21	0.3	Det. tube	0.468	77,481	384 × 288	
2018/01/25	2018-01-25-shockflame4	14.50	21	0.3	Det. tube	0.468	77,481	384 × 288	Selected for cell's amplitude measurement
2018/01/25	2018-01-25-shockflame5	14.50	21	0.3	Det. tube	0.468	77,481	384 × 288	

Table B.3: Shock-flame experiments in hydrogen-air in the Hele-Shaw cell – Heavy-to-light configuration.

Date	Test ID	p_0 (psi)	T_0 (°C)	Equivalence ratio	Shock source	Exposure time (μs)	Sample rate (fps)	Resolution (px)	Note
2017/10/16	2017-10-16_20H2-air_shockflame1	14.74	22	0.6	Det. tube	0.468	77,481	384 × 288	
2018/01/25	2018-01-25-shockflame5	14.50	21	0.3	Det. tube	0.468	77,481	384 × 288	
2018/01/26	2018-01-26-shockflame1	14.52	21	0.3	Det. tube	0.468	77,481	384 × 288	
2018/01/26	2018-01-26-shockflame2	14.52	21	0.3	Det. tube	0.468	77,481	384 × 288	

Table B.4: Shock wave experiments in air in the Hele-Shaw cell.

Date	Test ID	p_0 (psi)	T_0 (°C)	Shock source	Mixture in detonation tube	Exposure time (μs)	Sample rate (fps)	Resolution (px)	Note
2016/12/01	2016-12-01-5mm-17.3kV-shock1	14.66	20	HVI	N/A	0.468	77,481	384 × 288	
2016/12/01	2016-12-01-5mm-17.3kV-shock2	14.66	20	HVI	N/A	0.468	77,481	384 × 288	
2016/12/04	2016-12-04-5mm-17.3kV-shock1	14.57	20	HVI	N/A	0.468	77,481	384 × 288	Secondary shock
2016/12/04	2016-12-04-5mm-17.3kV-shock2	14.57	20	HVI	N/A	0.468	77,481	384 × 288	
2016/12/04	2016-12-04-5mm-18.9kV-shock1	14.57	20	HVI	N/A	0.468	77,481	384 × 288	
2016/12/04	2016-12-04-5mm-19.7kV-shock1	14.57	20	HVI	N/A	0.468	77,481	384 × 288	
2016/12/04	2016-12-04-5mm-20.6kV-shock1	14.57	20	HVI	N/A	0.468	77,481	384 × 288	
2016/12/04	2016-12-04-5mm-20.6kV-shock2	14.57	20	HVI	N/A	0.468	77,481	384 × 288	
2016/12/04	2016-12-04-5mm-21.7kV-shock1	14.57	20	HVI	N/A	0.468	77,481	384 × 288	
2017/10/07	2017-10-07_shock1	14.45	21	Det. tube	C_2H_4+3O_2	0.468	77,481	384 × 288	
2017/07/27	2017-07-27_14.5psi_shock1	14.50	20	Det. tube	C_2H_4+3O_2	0.468	77,481	384 × 288	
2017/08/29	exp17	14.60	19	Det. tube	C_2H_4+3O_2	0.468	77,481	384 × 288	
2017/08/29	exp18	14.60	19	Det. tube	C_2H_4+3O_2	0.468	77,481	384 × 288	
2017/08/31	2017-08-31_shock1	14.60	20	Det. tube	C_2H_4+3O_2	0.468	77,481	384 × 288	
2017/08/31	2017-08-31_shock2_14.71psi	14.71	20	Det. tube	C_2H_4+3O_2	0.468	77,481	384 × 288	
2017/08/31	2017-08-31_shock4_14.69psi	14.69	20	Det. tube	C_2H_4+3O_2	0.468	77,481	384 × 288	

Table B.5: Detonation tube experiments in laboratory ambient air.

Date	Test ID	p_0 (psi)	T_0 (°C)	Mixture in detonation tube	Exposure time (μs)	Sample rate (fps)	Resolution (px)	Note
2017/08/20	exp4	14.72	20	C_2H_4+3O_2	0.468	77,481	384 × 288	
2017/08/20	exp5	14.62	20	C_2H_4+3O_2	0.468	77,481	384 × 288	
2017/08/20	exp6	14.62	20	C_2H_4+3O_2	0.468	77,481	384 × 288	
2017/08/21	exp7	14.66	19	C_2H_4+3O_2	0.468	77,481	384 × 288	
2017/08/21	exp8	14.66	19	C_2H_4+3O_2	0.468	77,481	384 × 288	
2017/08/21	exp9	14.66	19	C_2H_4+3O_2	0.468	77,481	384 × 288	
2017/08/21	exp10	14.66	19	C_2H_4+3O_2	0.468	77,481	384 × 288	
2017/08/21	exp11	14.67	19	C_2H_4+3O_2	0.468	77,481	384 × 288	
2017/08/21	exp12	14.66	19	C_2H_4+3O_2	0.468	77,481	384 × 288	
2017/08/21	exp13	14.67	19	C_2H_4+3O_2	0.468	77,481	384 × 288	
2017/08/21	exp14	14.66	20	C_2H_4+3O_2	0.468	77,481	384 × 288	
2017/08/21	exp15	14.68	20	C_2H_4+3O_2	0.468	77,481	384 × 288	
2017/08/21	exp16	14.68	20	C_2H_4+3O_2	0.468	77,481	384 × 288	

Appendix C

Flow acceleration behind the shock wave

Due to the boundary condition in the semi-confined Hele-Shaw geometry, the generated shock wave at the center of the vessel will develop a blast wave profile with decaying properties such as pressure, density and velocity, as it evolves radially in the gas. The decay rate of the blast wave will cause the flow behind the precursor shock to decelerate if the observer is in the lab frame of reference. This acceleration can be derived from the shock change equations as follows.

Fickett and Davis [31] derived some expressions for the shock change equations in the laboratory frame of reference as follows

$$\left(\frac{\mathrm{d}p}{\mathrm{d}t}\right)_{\mathrm{s}} = \frac{\rho c^2(\dot{\sigma} - \dot{\sigma}_A - \psi u_x)}{1 + \rho_0 D\left(\frac{\mathrm{d}u}{\mathrm{d}p}\right)_H} \tag{C.1}$$

or in terms of p_x

$$\left(\frac{\mathrm{d}p}{\mathrm{d}t}\right)_{\mathrm{s}} = \frac{\rho c^2\left(\dot{\sigma} - \dot{\sigma}_A - \frac{\psi}{\rho_0 D}p_x\right)}{1 + \frac{\rho_0 D}{1-\psi}\left(\frac{\mathrm{d}u}{\mathrm{d}p}\right)_H} \tag{C.2}$$

where $\dot{\sigma}$ is the thermicity, $\dot{\sigma}_A = u\mathcal{K} = u\frac{1}{A}\frac{\mathrm{d}A}{\mathrm{d}x}$ and $\psi = 1 - \left(\frac{D-u}{c}\right)^2$ is the sonic parameter.

Equations C.1 & C.2 can be used to isolate u_x and p_x and express them in terms of the shock decay parameter $\left(\frac{\mathrm{d}p}{\mathrm{d}t}\right)_\mathrm{s} = \frac{\partial p}{\partial t} + D\frac{\partial p}{\partial x}$. From Eq. C.1,

$$\boxed{u_x = \frac{\dot{\sigma} - \dot{\sigma}_A - \frac{1}{\rho c^2}\left(\frac{\mathrm{d}p}{\mathrm{d}t}\right)_\mathrm{s}\left(1 + \rho_0 D\left(\frac{\mathrm{d}u}{\mathrm{d}p}\right)_H\right)}{\psi}} \tag{C.3}$$

From the equation for mass conservation,

$$\frac{1}{\rho}\frac{\mathrm{D}\rho}{\mathrm{D}t} = -\nabla\cdot\vec{u} = -\frac{\partial u}{\partial x} - \dot{\sigma}_A \tag{C.4}$$

$$\frac{1}{\rho}\frac{\mathrm{D}\rho}{\mathrm{D}t} = -u_x - \dot{\sigma}_A = \frac{-\dot{\sigma} + \dot{\sigma}_A + \frac{1}{\rho c^2}\left(\frac{\mathrm{d}p}{\mathrm{d}t}\right)_\mathrm{s}\left(1 + \rho_0 D\left(\frac{\mathrm{d}u}{\mathrm{d}p}\right)_H\right)}{\psi} - \frac{\dot{\sigma}_A\psi}{\psi}$$

$$\boxed{\frac{1}{\rho}\frac{\mathrm{D}\rho}{\mathrm{D}t} = \frac{-\dot{\sigma} + \dot{\sigma}_A(1-\psi) + \frac{1}{\rho c^2}\left(\frac{\mathrm{d}p}{\mathrm{d}t}\right)_\mathrm{s}\left(1 + \rho_0 D\left(\frac{\mathrm{d}u}{\mathrm{d}p}\right)_H\right)}{\psi}} \tag{C.5}$$

Similarly for Eq. C.2, we can develop p_x:

$$\frac{1}{\rho c^2}\left(\frac{\mathrm{d}p}{\mathrm{d}t}\right)_\mathrm{s}\left(1 + \frac{\rho_0 D}{1-\psi}\left(\frac{\mathrm{d}u}{\mathrm{d}p}\right)_H\right) = \dot{\sigma} - \dot{\sigma}_A - \frac{\psi}{\rho_0 D}p_x$$

$$\boxed{p_x = \frac{\rho_0 D\left[\dot{\sigma} - \dot{\sigma}_A - \frac{1}{\rho c^2}\left(\frac{\mathrm{d}p}{\mathrm{d}t}\right)_\mathrm{s}\left(1 + \frac{\rho_0 D}{1-\psi}\left(\frac{\mathrm{d}u}{\mathrm{d}p}\right)_H\right)\right]}{\psi}} \tag{C.6}$$

From the momentum equation,

$$\rho \frac{\mathrm{D}u}{\mathrm{D}t} = -\frac{\partial p}{\partial x} \tag{C.7}$$

the acceleration is given by

$$a = \frac{\mathrm{D}u}{\mathrm{D}t} = -\frac{1}{\rho}\frac{\partial p}{\partial x} \tag{C.8}$$

Using Equations C.6 & C.8, one can find an expression for the acceleration behind the shock:

$$\boxed{a = \frac{\dfrac{\rho_0 D}{\rho}\left[\dot{\sigma}_A - \dot{\sigma} + \dfrac{1}{\rho c^2}\left(\dfrac{\mathrm{d}p}{\mathrm{d}t}\right)_{\mathrm{s}}\left(1 + \dfrac{\rho_0 D}{1-\psi}\left(\dfrac{\mathrm{d}u}{\mathrm{d}p}\right)_H\right)\right]}{\psi}} \tag{C.9}$$

The expressions for Eqs. C.3, C.5, C.6 & C.9 can be further simplified for a perfect gas model, for which one can find the analytical expressions for $\left(\dfrac{\mathrm{d}p}{\mathrm{d}t}\right)_{\mathrm{s}}$, $\left(\dfrac{\mathrm{d}u}{\mathrm{d}p}\right)_H$ and the usual jump conditions for each variable. The Rankine-Hugoniot relations for a perfect gas are:

$$\frac{u - \cancelto{0}{u_0}}{c_0} = \frac{2({M_{\mathrm{s}}}^2 - 1)}{(\gamma+1)M_{\mathrm{s}}} \tag{C.10}$$

$$\frac{p - p_0}{p_0} = \frac{2\gamma({M_{\mathrm{s}}}^2 - 1)}{\gamma + 1} \tag{C.11}$$

Using *Mathematica* software to differentiate $\left(\dfrac{\mathrm{d}u}{\mathrm{d}M_{\mathrm{s}}}\right)_H$ and $\left(\dfrac{\mathrm{d}p}{\mathrm{d}M_{\mathrm{s}}}\right)_H$, one obtains

$$\left(\frac{\mathrm{d}u}{\mathrm{d}M_\mathrm{s}}\right)_H = \frac{2c_0\left({M_\mathrm{s}}^2+1\right)}{{M_\mathrm{s}}^2(\gamma+1)} \tag{C.12}$$

$$\left(\frac{\mathrm{d}p}{\mathrm{d}M_\mathrm{s}}\right)_H = \frac{4{c_0}^2 M_\mathrm{s}\rho_0}{\gamma+1} \tag{C.13}$$

Therefore,

$$\left(\frac{\mathrm{d}u}{\mathrm{d}p}\right)_H = \left(\frac{\mathrm{d}u}{\mathrm{d}M_\mathrm{s}}\right)_H \cdot \left(\frac{\mathrm{d}M_\mathrm{s}}{\mathrm{d}p}\right)_H = \frac{\left(\frac{\mathrm{d}u}{\mathrm{d}M_\mathrm{s}}\right)_H}{\left(\frac{\mathrm{d}p}{\mathrm{d}M_\mathrm{s}}\right)_H} = \frac{c_0({M_\mathrm{s}}^2+1)}{2{M_\mathrm{s}}^3\gamma p_0} \tag{C.14}$$

Similarly, the term $\left(\frac{\mathrm{d}p}{\mathrm{d}t}\right)_\mathrm{s}$ can be expressed as

$$\left(\frac{\mathrm{d}p}{\mathrm{d}t}\right)_\mathrm{s} = \left(\frac{\mathrm{d}p}{\mathrm{d}M_\mathrm{s}}\right)_H \cdot \underbrace{\left(\frac{\mathrm{d}M_\mathrm{s}}{\mathrm{d}t}\right)_\mathrm{s}}_{\equiv \dot{M}_s} = \frac{4\gamma p_0 M_\mathrm{s}}{\gamma+1}\dot{M}_s \tag{C.15}$$

The jump relation for the density is expressed as

$$\frac{\rho}{\rho_0} = \frac{(\gamma+1){M_\mathrm{s}}^2}{(\gamma-1){M_\mathrm{s}}^2+2} \tag{C.16}$$

and for the sound speed

$$c = \sqrt{\gamma\frac{p}{\rho}} \tag{C.17}$$

$$\left(\frac{c}{c_0}\right)^2 = \frac{\left(2\gamma{M_\mathrm{s}}^2-(\gamma-1)\right)\left((\gamma-1){M_\mathrm{s}}^2+2\right)}{(\gamma+1)^2{M_\mathrm{s}}^2} \tag{C.18}$$

The expression for the sonic parameter can now be re-written as

$$\psi = 1 - \left(\frac{D-u}{c}\right)^2 = 1 - \left(\frac{D-u}{D} \cdot \frac{D}{c_0} \cdot \frac{c_0}{c}\right)^2$$

From mass conservation across the shock,

$$\rho(D-u) = \rho_0 D$$
$$\frac{D-u}{D} = \frac{\rho_0}{\rho}$$

Thus,

$$\psi = 1 - \left(\frac{\rho_0}{\rho} \cdot M_\mathrm{s} \cdot \frac{c_0}{c}\right)^2 \tag{C.19}$$

which can be written in terms of M_s only with the help of C.16 & C.18, such that

$$\psi = \frac{\left({M_\mathrm{s}}^2 - 1\right)(\gamma+1)}{1+\gamma\left(2{M_\mathrm{s}}^2 - 1\right)} \tag{C.20}$$

The algebra for all substitutions can be best done with *Mathematica* in order to avoid unnecessary typos. For a non-reacting flow the thermicity terms can be neglected and the parameters become

$$\frac{1}{\rho}\frac{\mathrm{D}\rho}{\mathrm{D}t} = \frac{2\left[(3M^2+1)(\gamma+1)\dot{M} + c_0\left(M^2-1\right)\left(2+{M_\mathrm{s}}^2(\gamma-1)\right)\mathcal{K}\right]}{M_\mathrm{s}\left({M_\mathrm{s}}^2-1\right)(\gamma+1)^2} \tag{C.21}$$

$$\frac{\partial u}{\partial x} = -\frac{2\left[(3M^2+1)(\gamma+1)\dot{M} + c_0\left(M^2-1\right)\left(1+\gamma\left(2{M_\mathrm{s}}^2-1\right)\right)\mathcal{K}\right]}{M_\mathrm{s}\left({M_\mathrm{s}}^2-1\right)(\gamma+1)^2} \tag{C.22}$$

$$\frac{\partial p}{\partial x} = -\frac{2c_0\rho_0\left[\left(1-\gamma+M^2(\gamma+5)+M^4(4\gamma-2)\right)(\gamma+1)\dot{M} + c_0(M-1)(M+1)\left(2+M^2(\gamma-1)\right)\left(1+\gamma\left(2M^2-1\right)\mathcal{K}\right)\right]}{\left(M^2-1\right)\left(2+M^2(\gamma-1)\right)(\gamma+1)^2} \tag{C.23}$$

$$a = -\frac{1}{\rho}\frac{\partial \rho}{\partial x} = -\frac{2c_0\left[\left(1-\gamma+M^2(\gamma+5)+M^4(4\gamma-2)\right)(\gamma+1)\dot{M} + c_0(M-1)(M+1)\left(2+M^2(\gamma-1)\right)\left(1+\gamma\left(2M^2-1\right)\mathcal{K}\right)\right]}{M^2\left(M^2-1\right)(\gamma+1)^3} \tag{C.24}$$

One can also review the ratio between the unsteady term and curvature term in the Eq. to get

$$\zeta = \frac{(3M^2+1)(\gamma+1)\dot{M}}{c_0(M^2-1)\left(2+{M_s}^2(\gamma-1)\right)\mathcal{K}} \tag{C.25}$$

For Taylor-Sedov blast waves,

$$R \sim t^{\frac{2}{j+3}} \begin{cases} j=0 & \text{for planar} \\ j=1 & \text{for cylindrical} \\ j=2 & \text{for spherical} \end{cases} \tag{C.26}$$

Differentiate to get $D = \dot{R}$, $\dot{D} = \ddot{R}$ with $\mathcal{K} = \dfrac{j}{R}$, we get:

$$\frac{\dot{D}}{D^2\mathcal{K}} = -\frac{j+1}{2j} \begin{cases} \infty & j=0 & \text{for planar} \\ -1 & j=1 & \text{for cylindrical} \\ -\frac{3}{4} & j=2 & \text{for spherical} \end{cases} \tag{C.27}$$

We can now evaluate ζ for strong shocks, Taylor-Sedov:

$$\begin{aligned} \zeta\big|_{M\to\infty} &= \frac{3\cancel{M^2}\dot{M}(\gamma+1)}{c_0\cancel{M^2}(\gamma-1)\mathcal{K}M^2} \\ &= \frac{3}{c_0}\left(\frac{\gamma+1}{\gamma-1}\right)\frac{\dot{M}}{M^2\mathcal{K}} \\ &= \frac{3}{c_0}\left(\frac{\gamma+1}{\gamma-1}\right)\frac{{c_0}^2\frac{1}{c_0}\dot{D}}{D^2\mathcal{K}} \\ &= 3\left(\frac{\gamma+1}{\gamma-1}\right)\frac{\dot{D}}{D^2\mathcal{K}} \end{aligned} \tag{C.28}$$

which is the same result as shown by Sheperd & Eckett in their Appendix [32].

For Taylor-Sedov:

$$\zeta_{\text{Strong, Taylor-Sedov}} = -2\frac{\gamma+1}{\gamma-1}\frac{j+1}{2j}\begin{cases}\infty & \text{for planar}\\ -12 & \text{for cylindrical}\\ -9 & \text{for spherical}\end{cases} \tag{C.29}$$

This shows that for decaying shock waves of the Taylor-Sedov type, curvature effects are always an order of magnitude less important and can be neglected from the analysis. Neglecting the curvature terms ($\mathcal{K} = 0$) in the above relations, in the limit of strong shocks, we get the following simple equations for the velocity, pressure gradient and acceleration, as a function of the shock velocity decay; the latter can be extracted from experimental results using image velocimetry.

$$\frac{1}{\rho}\frac{\mathrm{D}\rho}{\mathrm{D}t} = \frac{2\left(3\cancel{M^2}\dot{M}\cancel{(\gamma+1)}\right)}{M^{\cancel{3}}(\gamma+1)^{\cancel{2}}} = \frac{6}{\gamma+1}\frac{\dot{M}}{M} = \frac{6}{\gamma+1}\frac{\dot{D}}{D} \tag{C.30}$$

$$\frac{\partial u}{\partial x} = -\frac{6}{\gamma+1}\frac{\dot{M}}{M} = \boxed{-\frac{6}{\gamma+1}\frac{\dot{D}}{D}} \tag{C.31}$$

$$\frac{\partial p}{\partial x} = -\frac{2c_0\rho_0\dot{M}\cancel{(\gamma+1)}\cancel{M^4}(4\gamma-2)}{\cancel{M^2}(\gamma-1)\cancel{M^2}(\gamma+1)^{\cancel{2}}} = -\frac{4c_0\rho_0\dot{M}(2\gamma-1)}{(\gamma+1)(\gamma-1)} = \boxed{-\frac{4\rho_0\dot{D}(2\gamma-1)}{(\gamma+1)(\gamma-1)}} \tag{C.32}$$

$$a = -\frac{1}{\rho}\frac{\partial p}{\partial x} = \frac{2c_0\dot{M}\cancel{(\gamma+1)}\left(\cancel{M^4}(4\gamma-2)\right)}{\cancel{M^4}(\gamma+1)^{\cancel{2}^{\cancel{2}}}} = \frac{4c_0\dot{M}(2\gamma-1)}{(\gamma+1)^2} = \boxed{\frac{4\dot{D}(2\gamma-1)}{(\gamma+1)^2}} \tag{C.33}$$

One can also retain the curvature terms in Eqns C.21 to C.24, but still seek the limit of strong shocks:

$$\frac{1}{\rho}\frac{\mathrm{D}\rho}{\mathrm{D}t} = \frac{6\dot{D}}{(\gamma+1)D} + \frac{2c_0 M^2 M^2(\gamma-1)\mathcal{K}}{{M_\mathrm{s}}^3(\gamma+1)^2} = \frac{6\dot{D}}{(\gamma+1)D} + 2D\mathcal{K}\frac{(\gamma-1)}{(\gamma+1)^2} \tag{C.34}$$

$$\frac{\partial u}{\partial x} = -\frac{6\dot{D}}{(\gamma+1)D} - \frac{2c_0 M^2 2\gamma M^2\mathcal{K}}{{M_\mathrm{s}}^3(\gamma+1)^2} = -\frac{6\dot{D}}{(\gamma+1)D} - \frac{4D\mathcal{K}\gamma}{(\gamma+1)^2} \tag{C.35}$$

$$\frac{\partial p}{\partial x} = -\frac{4\rho_0\dot{D}(2\gamma-1)}{(\gamma+1)(\gamma-1)} - \frac{2\rho_0 {c_0}^2 \cancel{M^2 M^2(\gamma-1)}2\gamma M^2\mathcal{K}}{\cancel{M^4(\gamma-1)}(\gamma+1)^2} = -\frac{4\rho_0\dot{D}(2\gamma-1)}{(\gamma+1)(\gamma-1)} - \frac{4\rho_0\gamma D^2\mathcal{K}}{(\gamma+1)^2} \tag{C.36}$$

$$a = \frac{4\dot{D}(2\gamma-1)}{(\gamma+1)^2} + \frac{2{c_0}^2 \cancel{M^2 M^2}(\gamma-1)\gamma 2M^2\mathcal{K}}{\cancel{M^4}(\gamma+1)^3} = \frac{4\dot{D}(2\gamma-1)}{(\gamma+1)^2} + \frac{4\gamma(\gamma-1)D^2\mathcal{K}}{(\gamma+1)^3} \tag{C.37}$$

Appendix D

Supplementary figures

This appendix presents experimental records for flame experiments and shock-flame interactions in the Hele-Shaw apparatus.

D.1 Flame

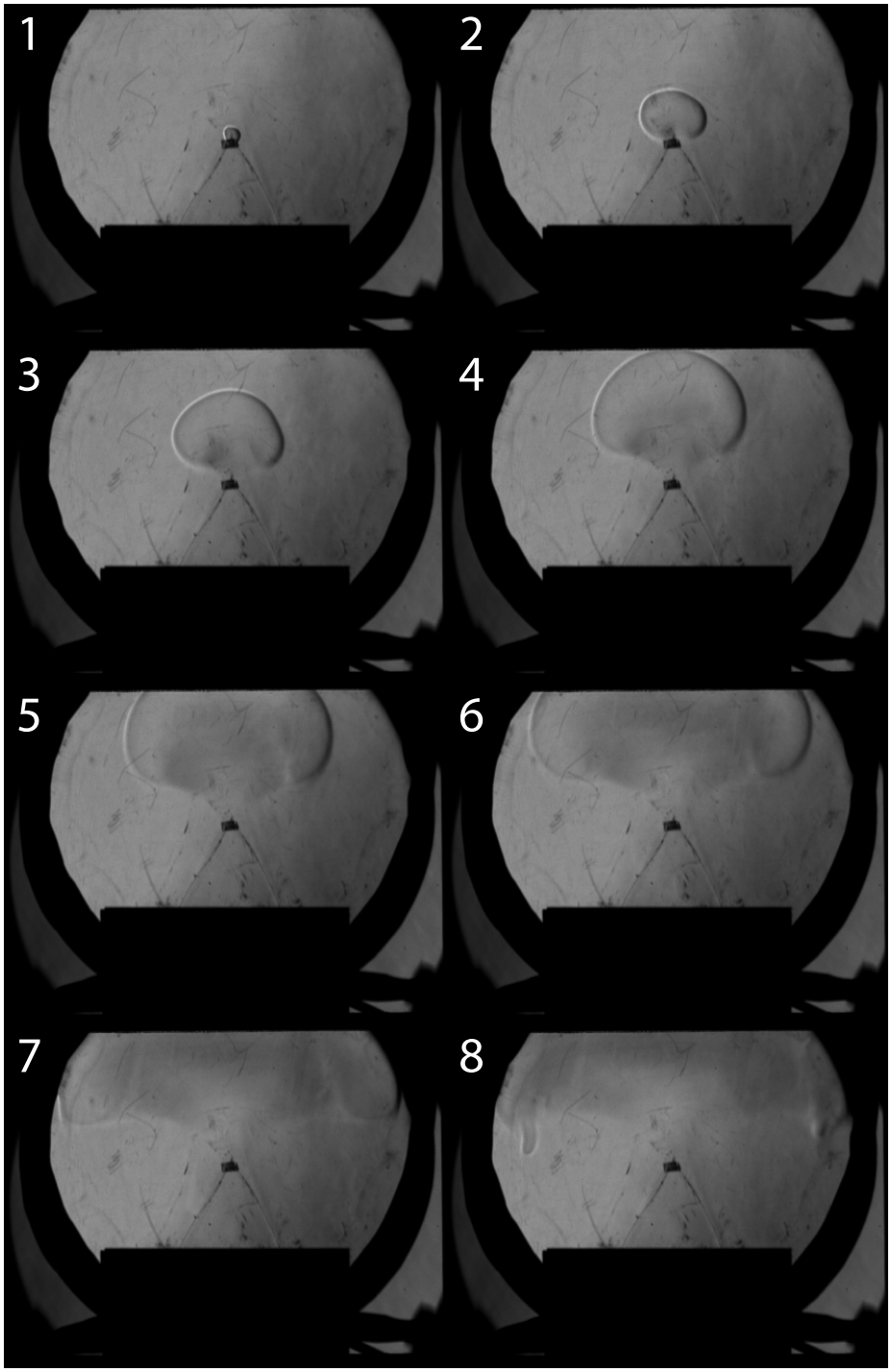

Figure D.1: Sequence of Schlieren images of a deflagration in a hydrogen-air mixture at $\phi = 0.18$ propagating in the Hele-Shaw cell. Ambient room conditions. Recorded at 3,000 fps. Inter-frame time is 83.33 ms.

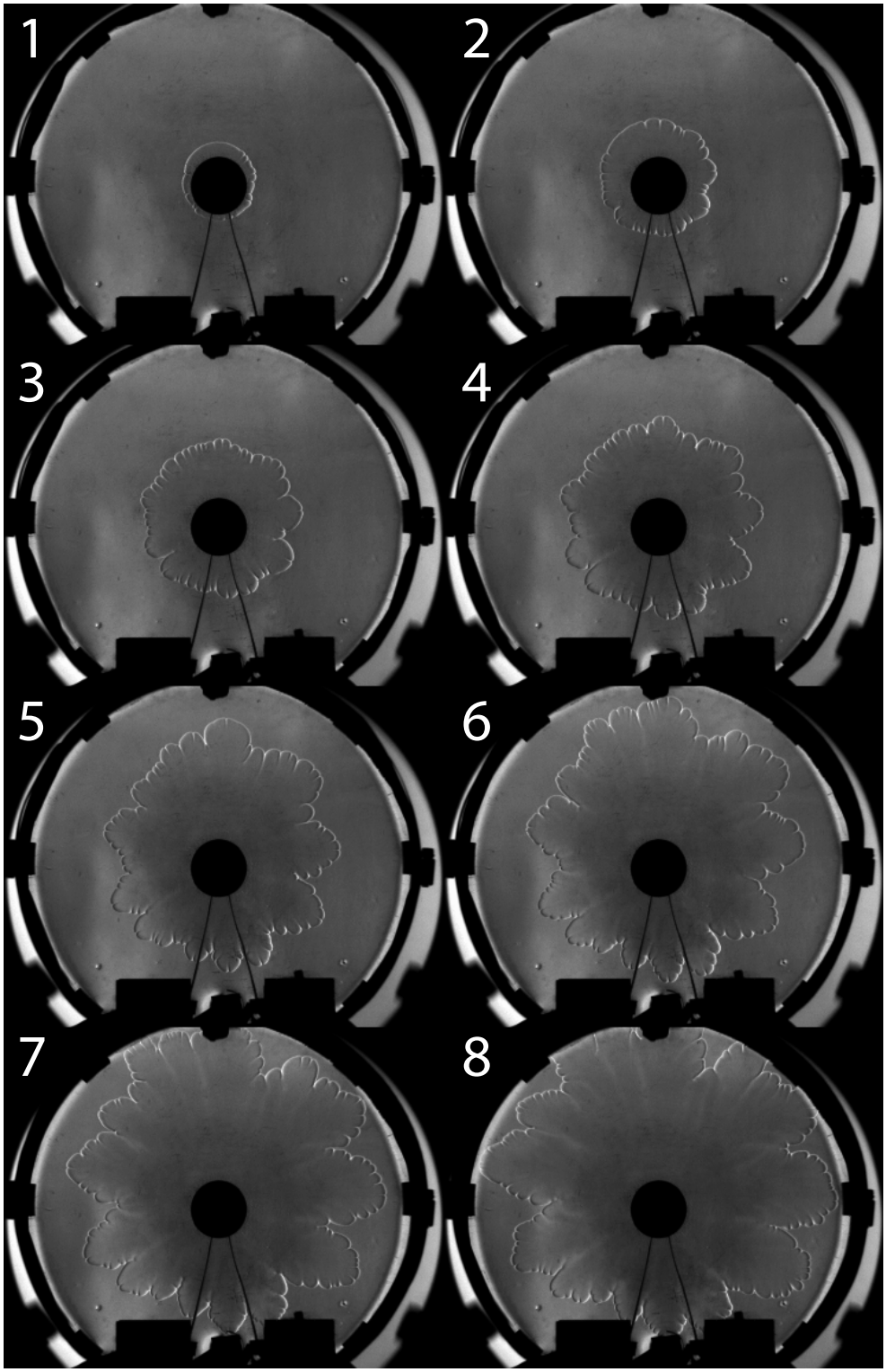

Figure D.2: Sequence of Schlieren images of a deflagration in a hydrogen-air mixture at $\phi = 0.3$ propagating in the Hele-Shaw cell. Ambient room conditions. Recorded at 77,481 fps. Inter-frame time is 14.20 ms.

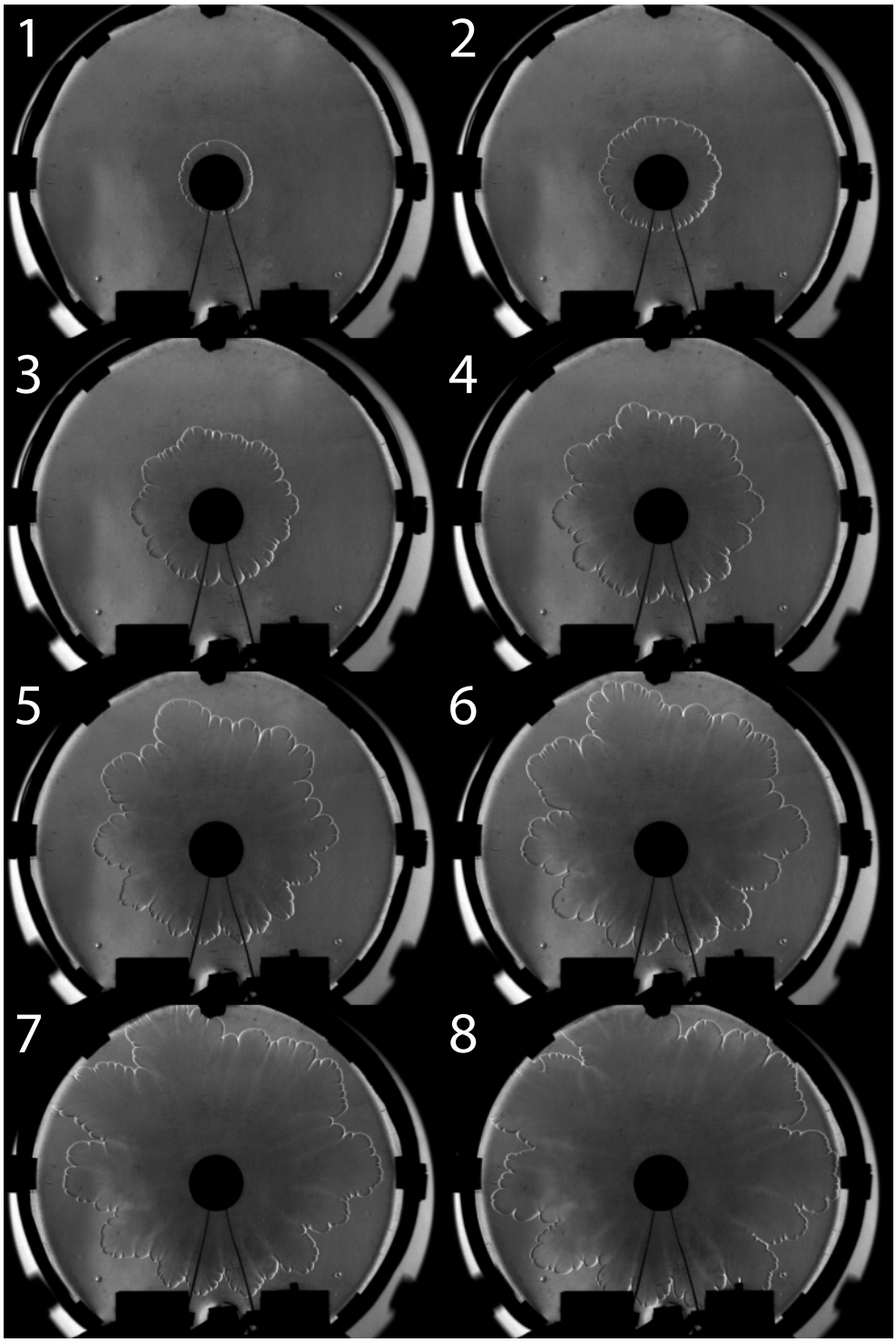

Figure D.3: Sequence of Schlieren images of a deflagration in a hydrogen-air mixture at $\phi = 0.3$ propagating in the Hele-Shaw cell. Ambient room conditions. Recorded at 77,481 fps. Inter-frame time is 14.20 ms.

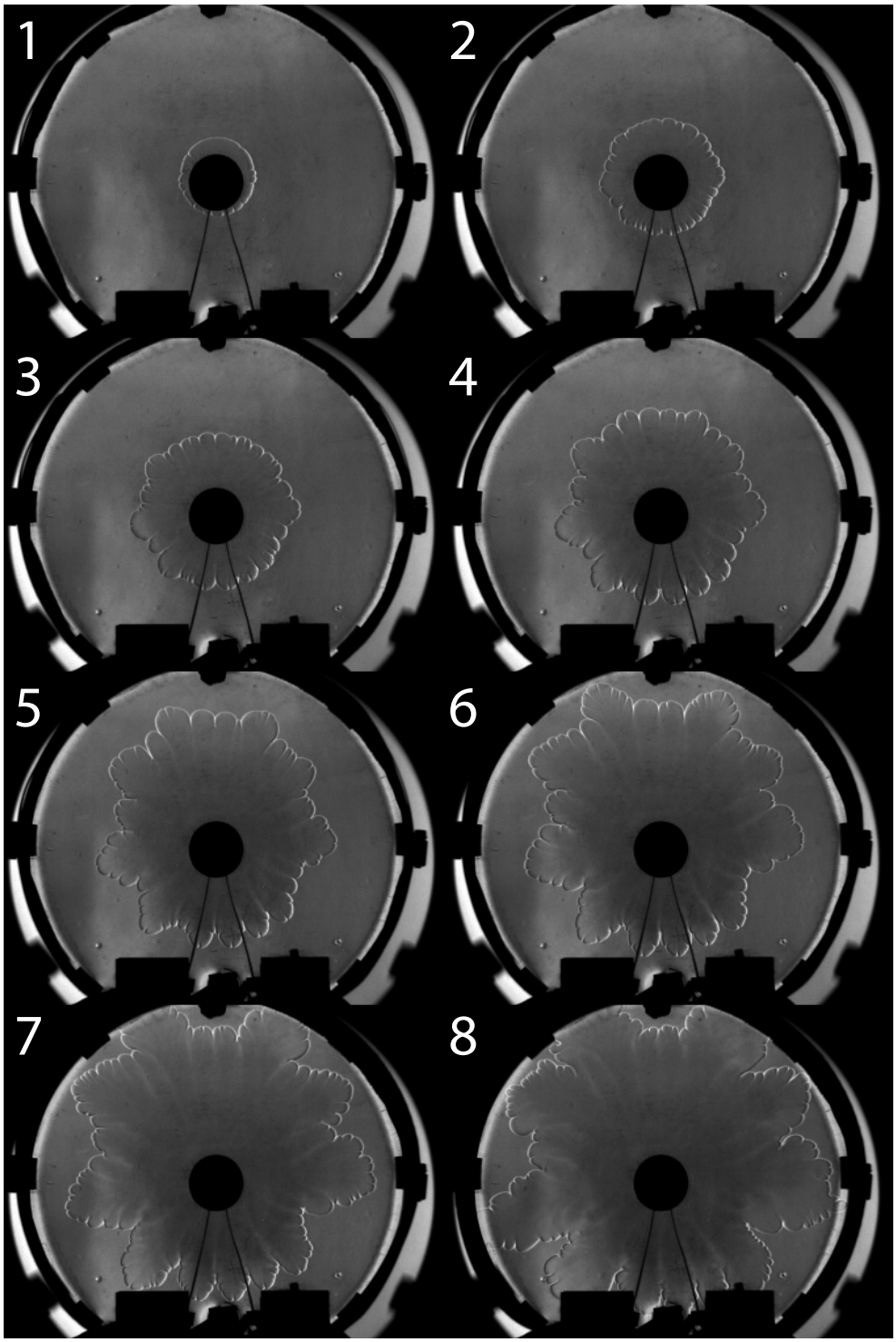

Figure D.4: Sequence of Schlieren images of a deflagration in a hydrogen-air mixture at $\phi = 0.3$ propagating in the Hele-Shaw cell. Ambient room conditions. Recorded at 77,481 fps. Inter-frame time is 14.20 ms.

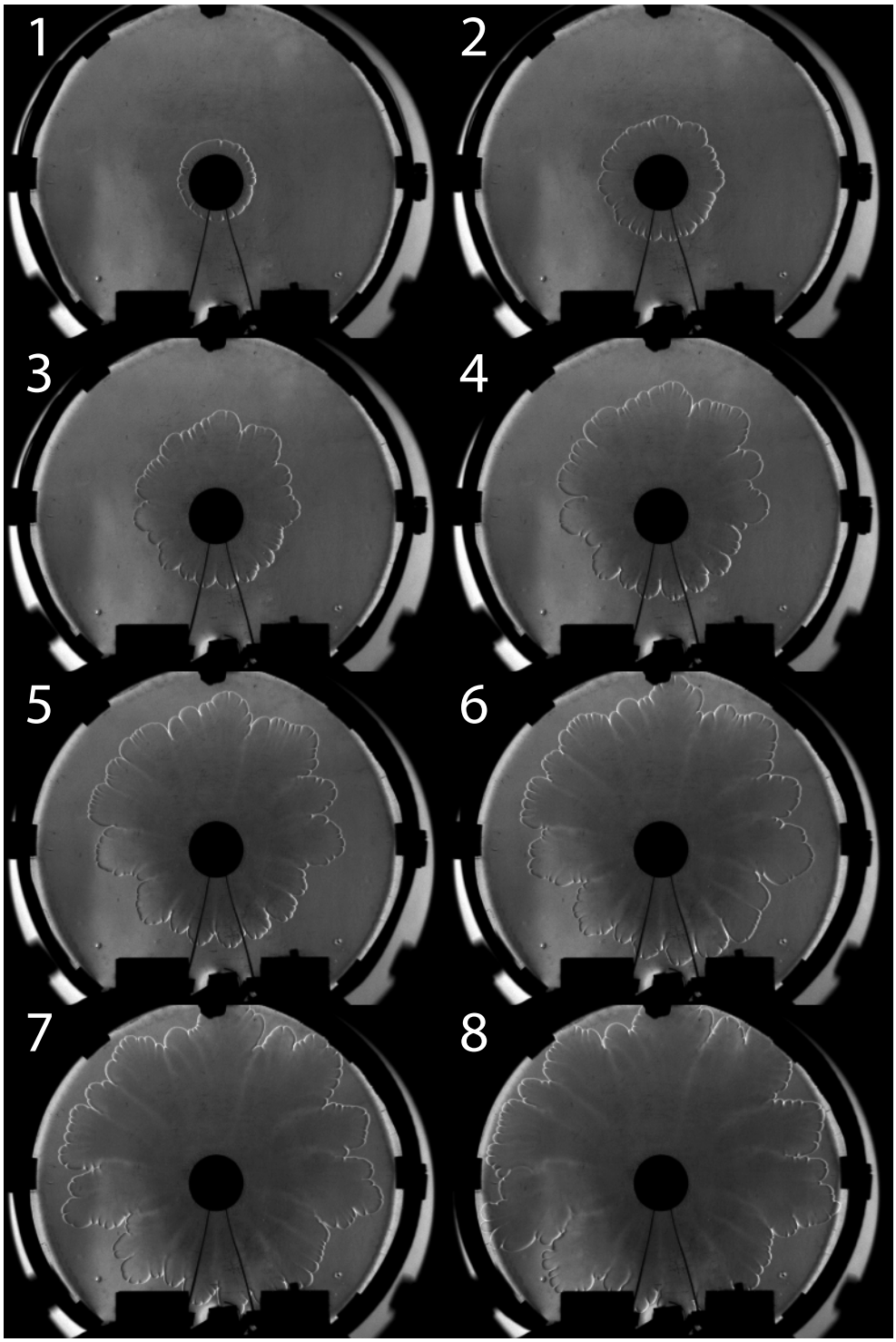

Figure D.5: Sequence of Schlieren images of a deflagration in a hydrogen-air mixture at $\phi = 0.3$ propagating in the Hele-Shaw cell. Ambient room conditions. Recorded at 77,481 fps. Inter-frame time is 14.20 ms.

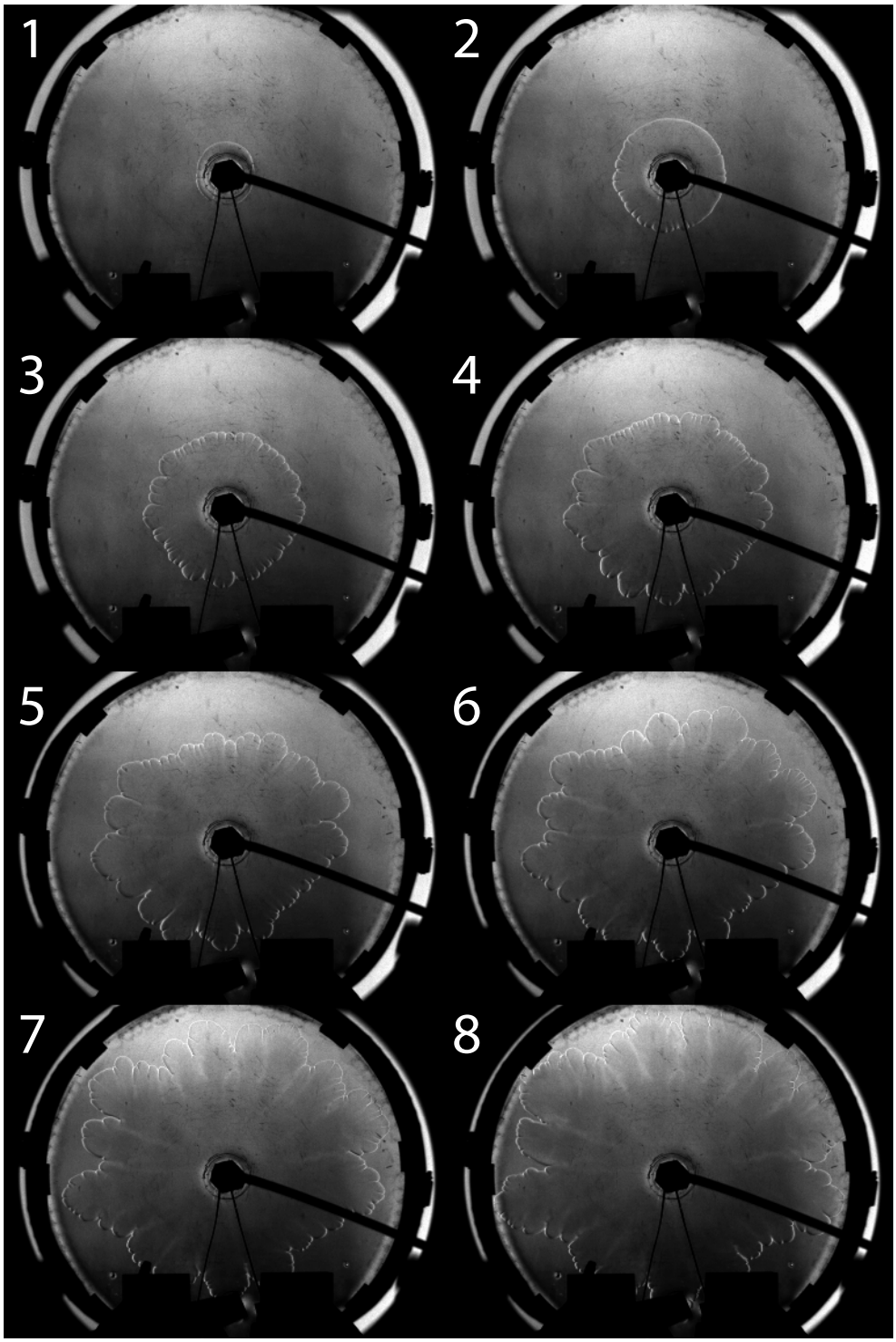

Figure D.6: Sequence of Schlieren images of a deflagration in a hydrogen-air mixture at $\phi = 0.3$ propagating in the Hele-Shaw cell. Ambient room conditions. Recorded at 77,481 fps. Inter-frame time is 12.91 ms.

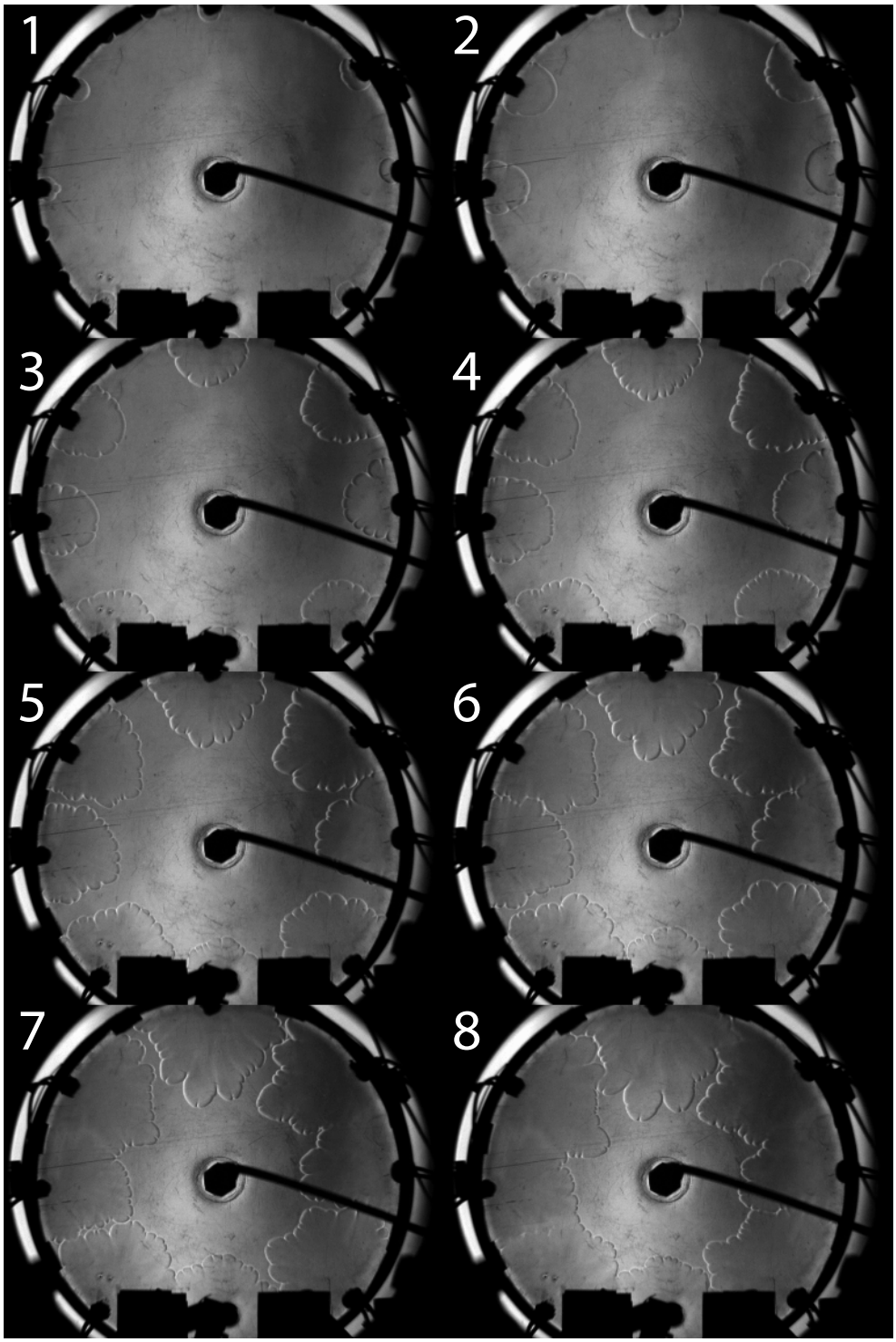

Figure D.7: Sequence of Schlieren images of a deflagration propagating inwards in a hydrogen-air mixture at $\phi = 0.3$ propagating in the Hele-Shaw cell. Ambient room conditions. Recorded at 77,481 fps. Inter-frame time is 12.91 ms.

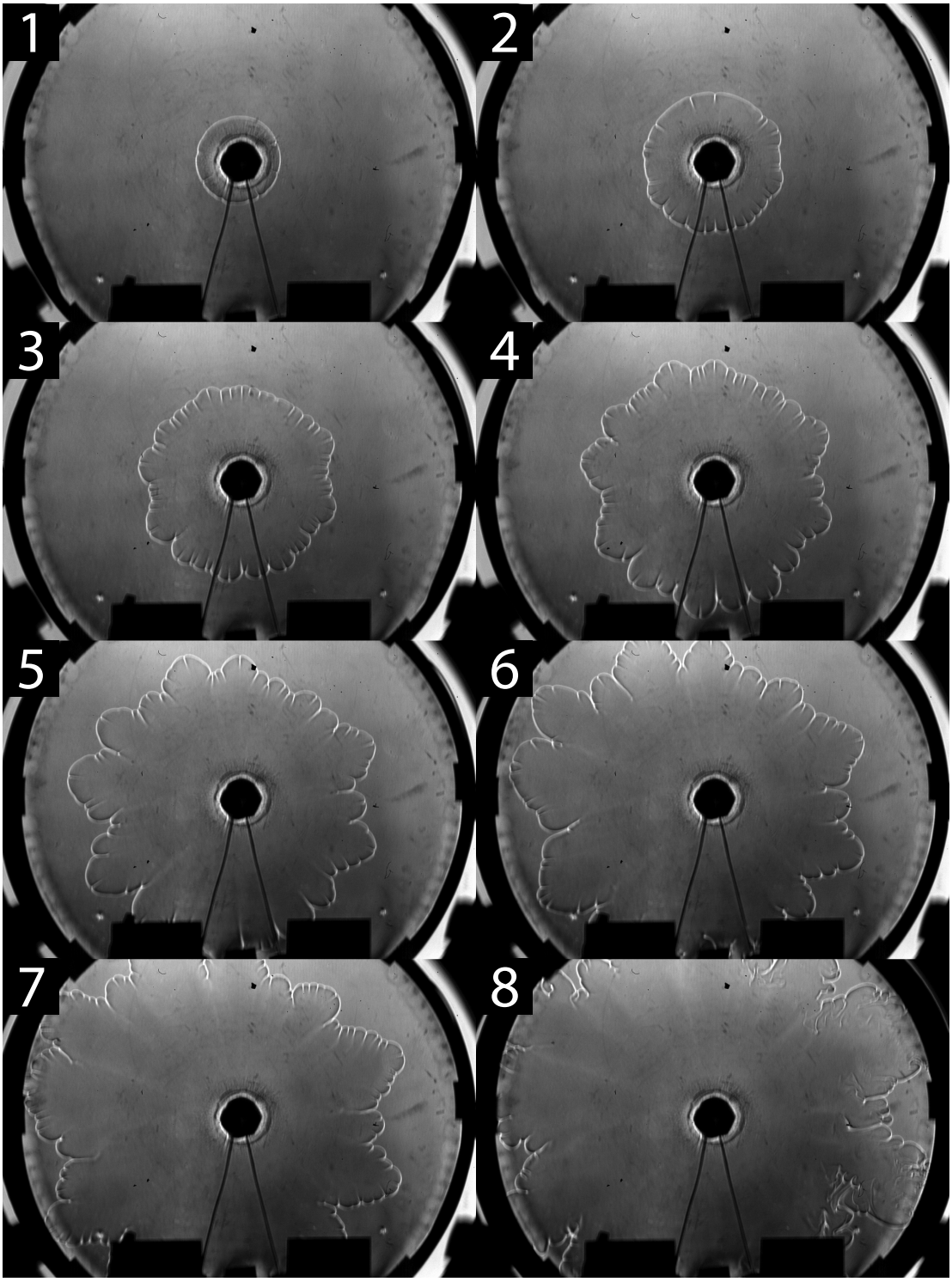

Figure D.8: Sequence of Schlieren images of a deflagration in a hydrogen-air mixture at $\phi = 0.3$ propagating in the Hele-Shaw cell. Ambient room conditions. Recorded at 77,481 fps. Inter-frame time is 11.80 ms.

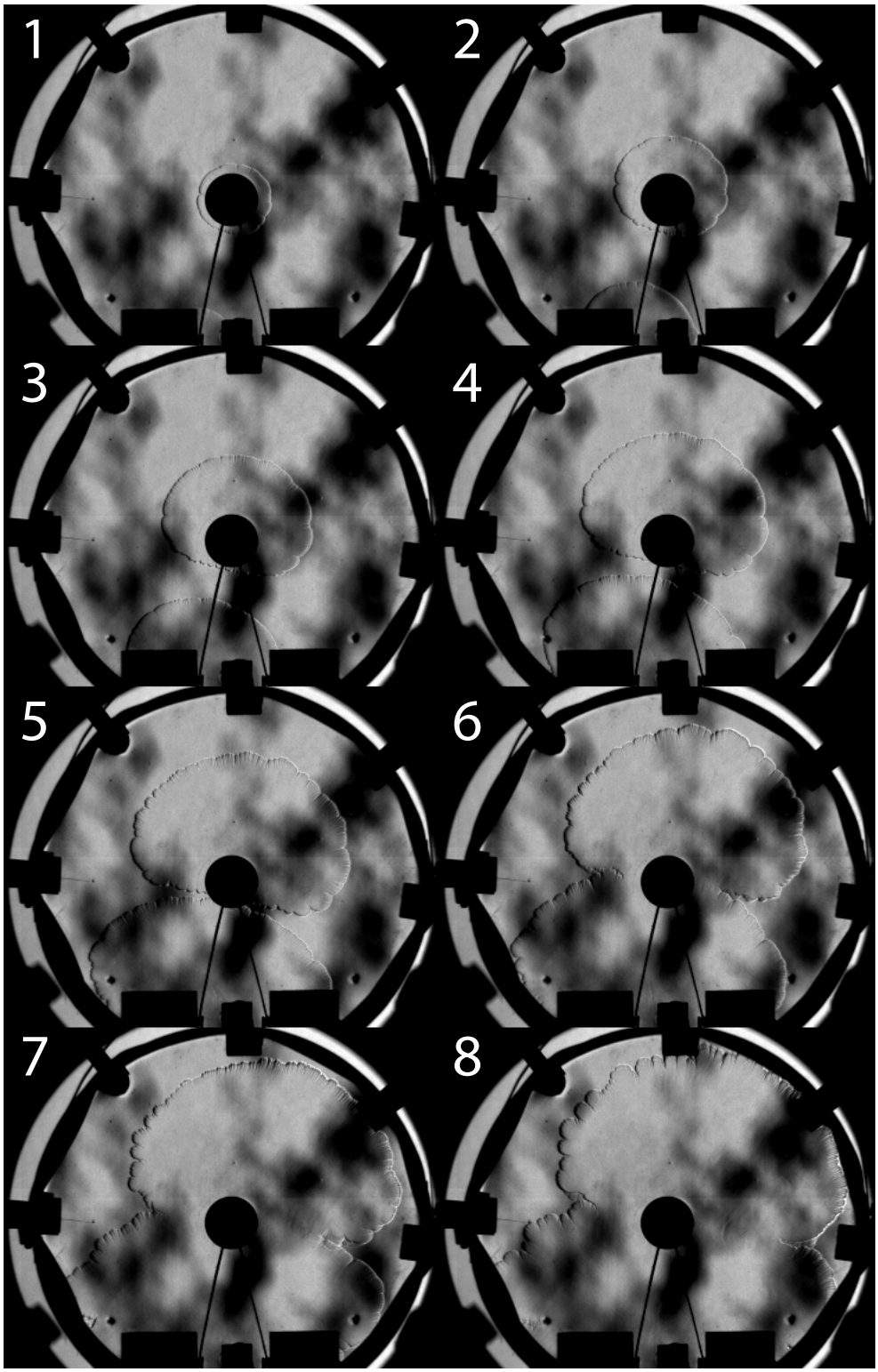

Figure D.9: Sequence of Schlieren images of a deflagration in a hydrogen-air mixture at $\phi = 0.6$ propagating in the Hele-Shaw cell. Ambient room conditions. Recorded at 77,481 fps. The time between frames is 1.81 ms.

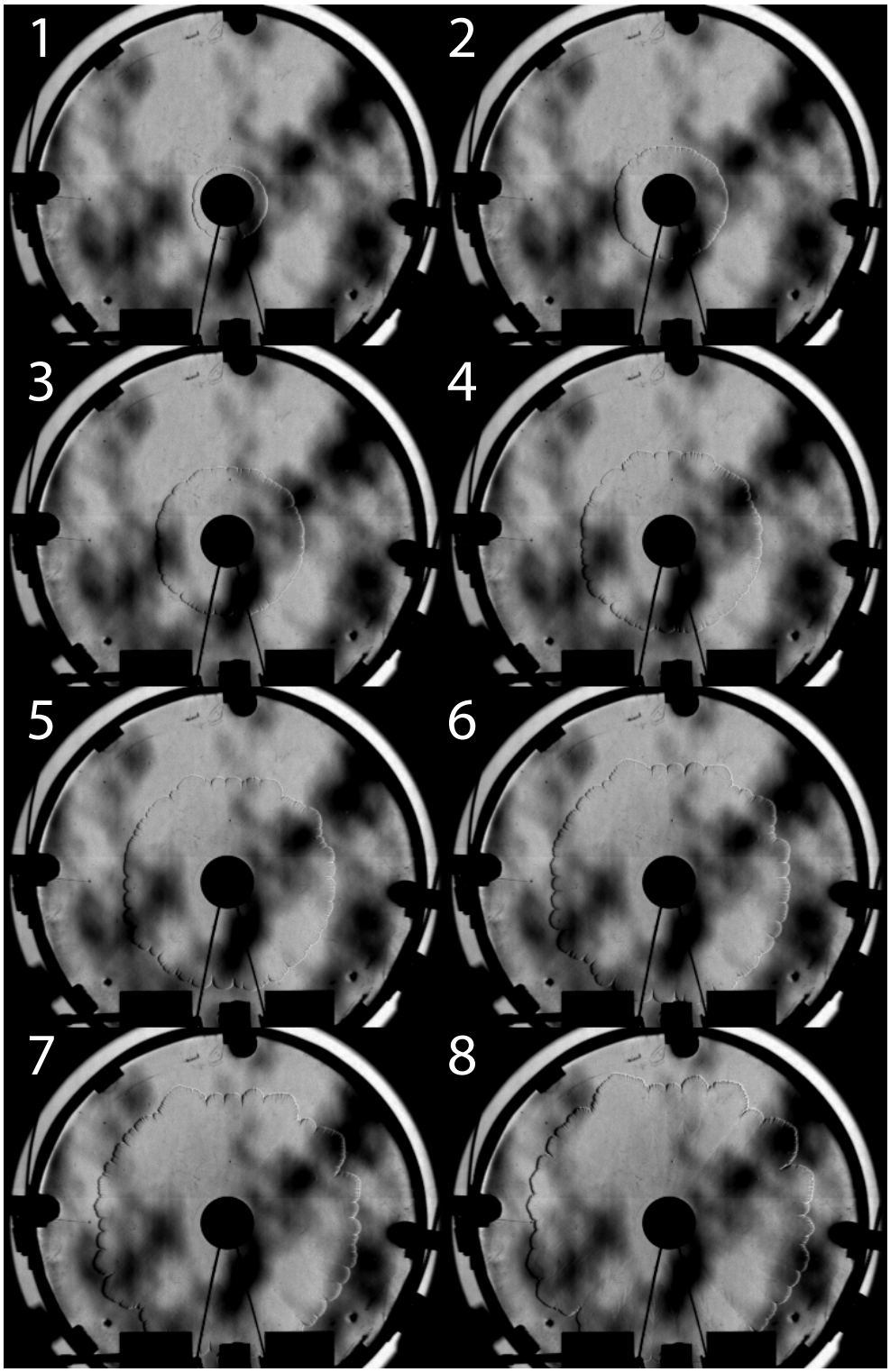

Figure D.10: Sequence of Schlieren images of a deflagration in a hydrogen-air mixture at $\phi = 0.6$ propagating in the Hele-Shaw cell. Ambient room conditions. Recorded at 77,481 fps. The time between frames is 1.81 ms.

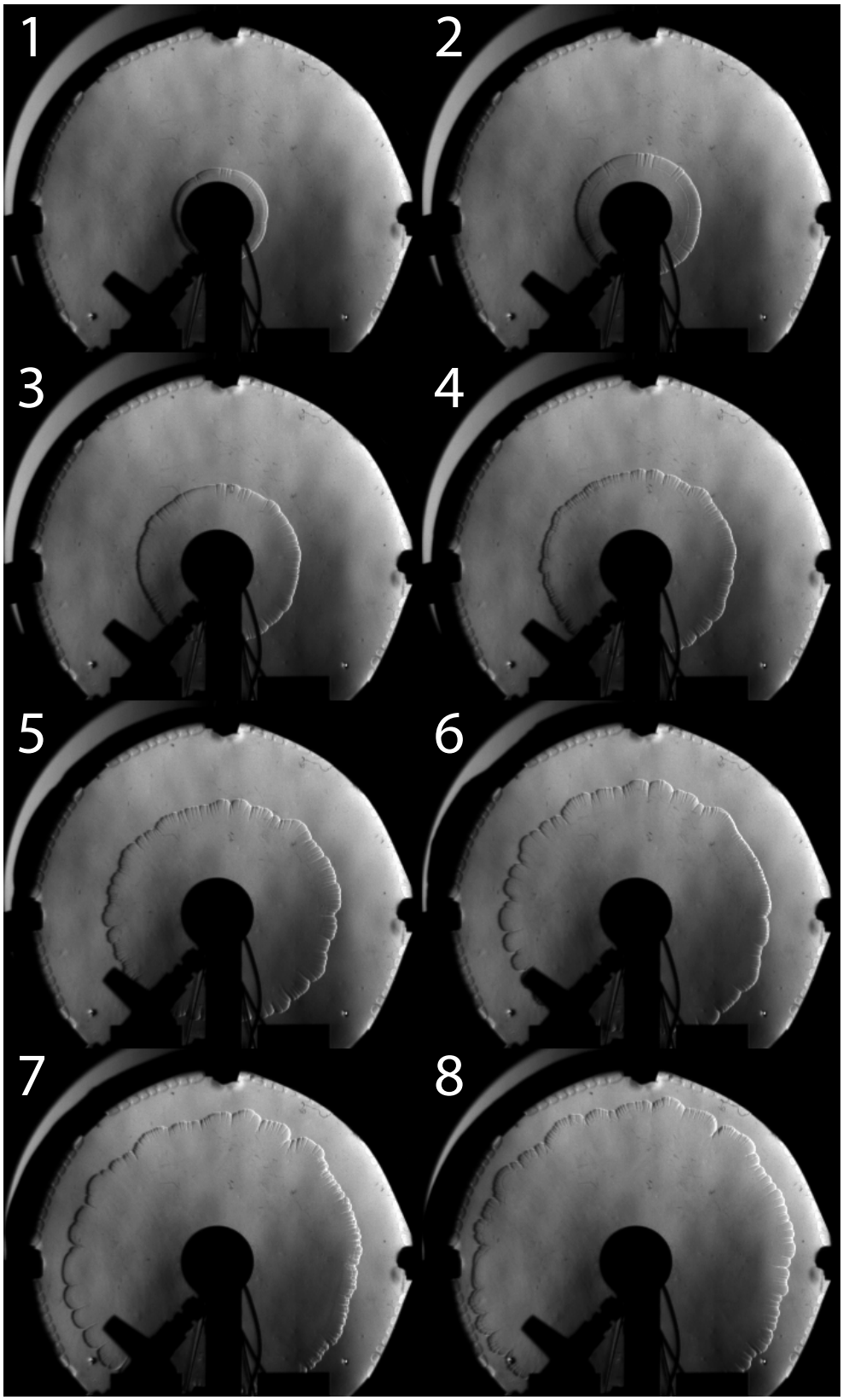

Figure D.11: Sequence of Schlieren images of a deflagration in a hydrogen-air mixture at $\phi = 0.6$ propagating in the Hele-Shaw cell. Ambient room conditions. Recorded at 77,481 fps. The time between frames is 1.03 ms.

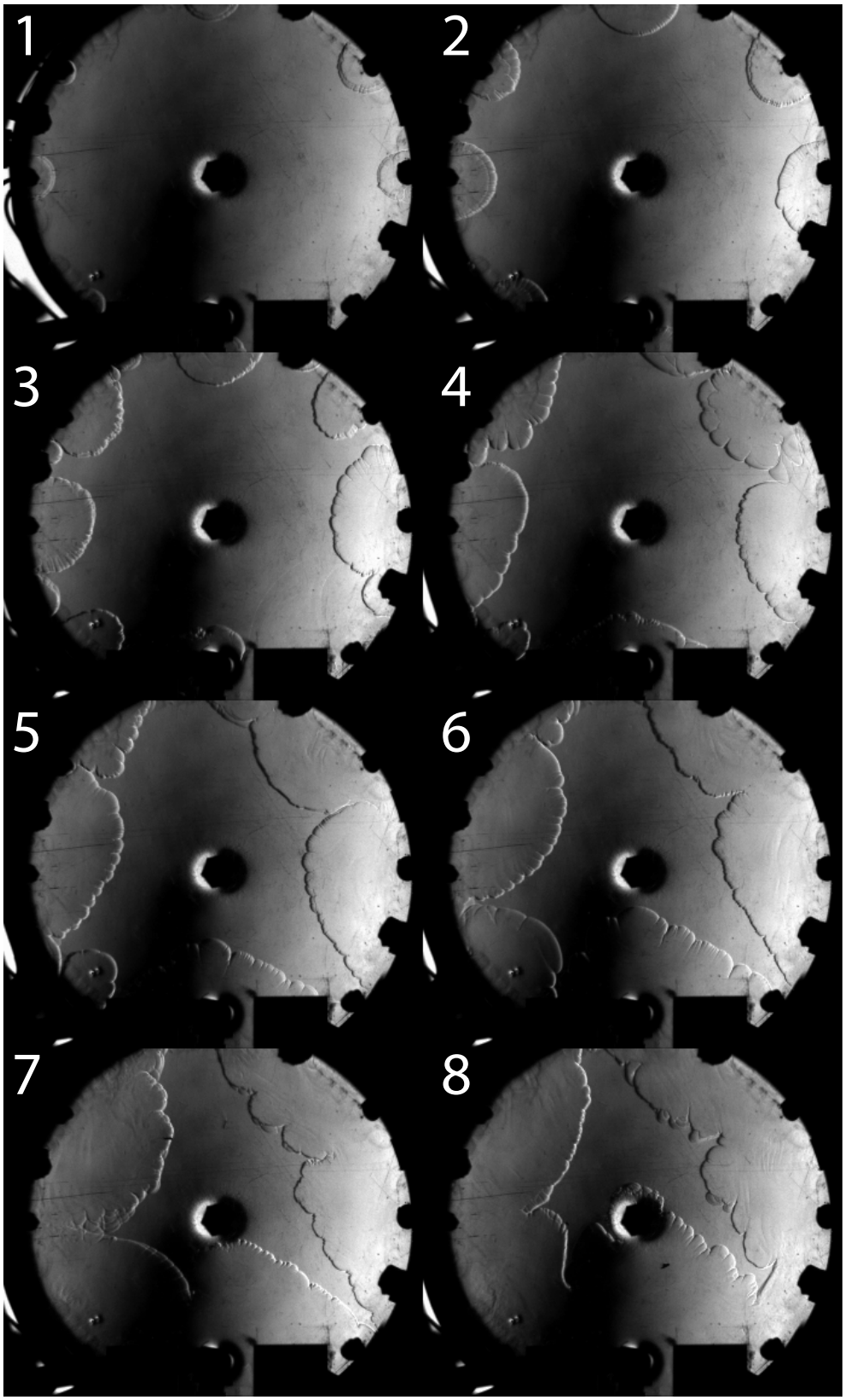

Figure D.12: Sequence of Schlieren images of a deflagration in a hydrogen-air mixture at $\phi = 0.6$ propagating in the Hele-Shaw cell with multiple ignition points. Ambient room conditions. Recorded at 77,481 fps. The time between frames is 2.26 ms.

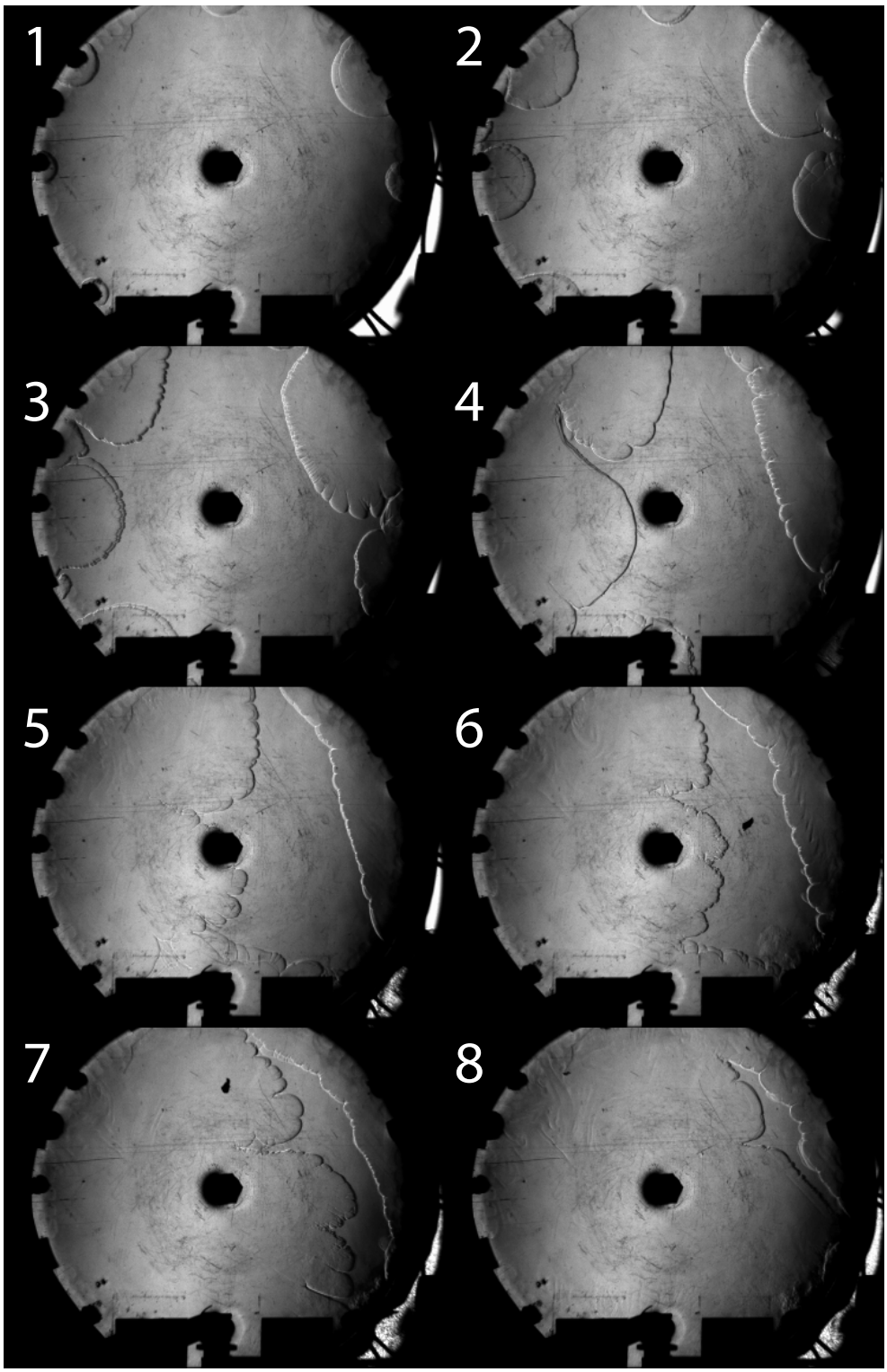

Figure D.13: Sequence of Schlieren images of an inward-propagating deflagration in a hydrogen-air mixture at $\phi = 0.6$ propagating in the Hele-Shaw cell. Ambient room conditions. Recorded at 77,481 fps. The time between frames is 1.94 ms.

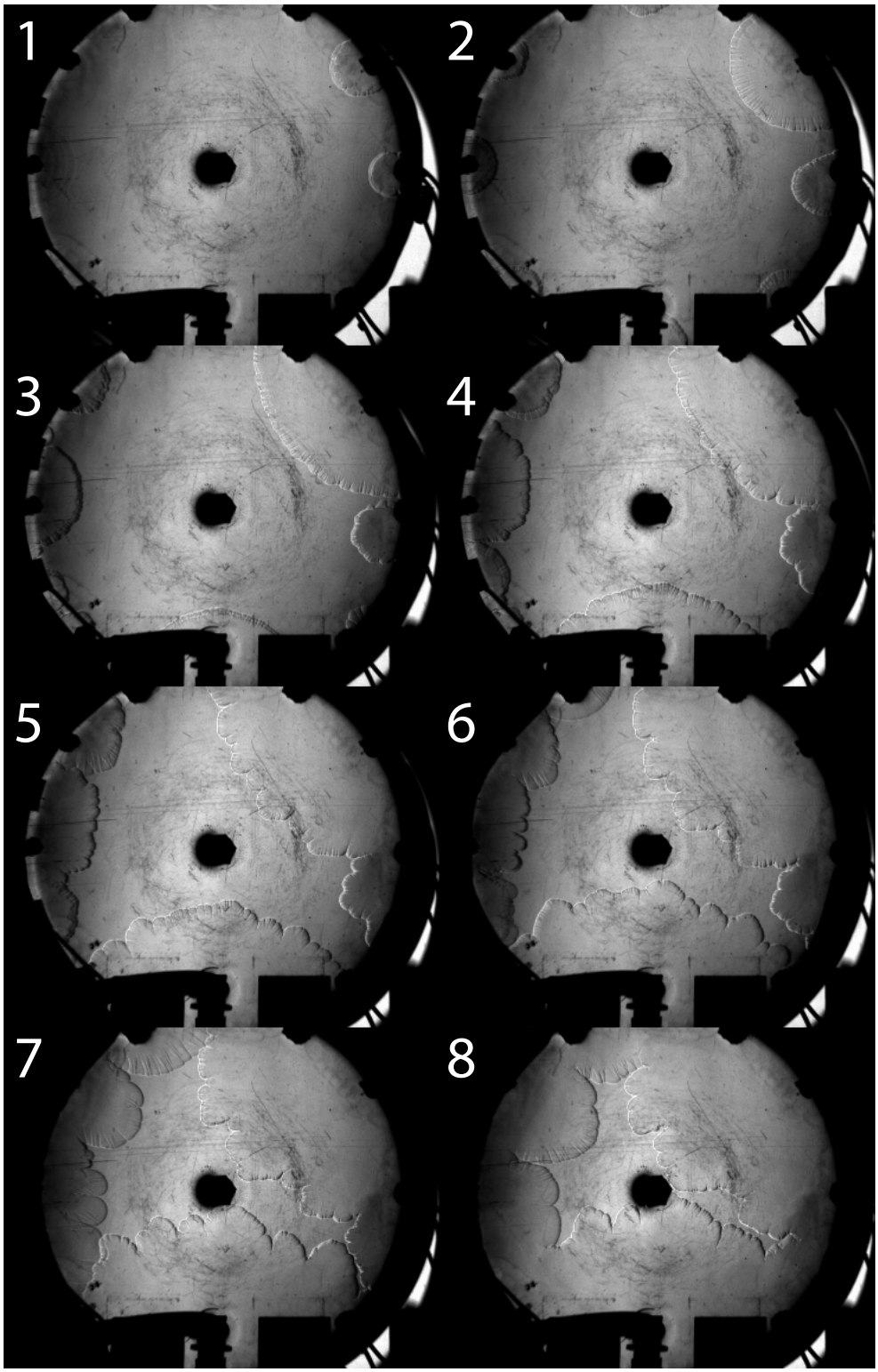

Figure D.14: Sequence of Schlieren images of a deflagration in a hydrogen-air mixture at $\phi = 0.6$ propagating in the Hele-Shaw cell with multiple ignition points. Ambient room conditions. Recorded at 77,481 fps. The time between frames is 3.23 ms.

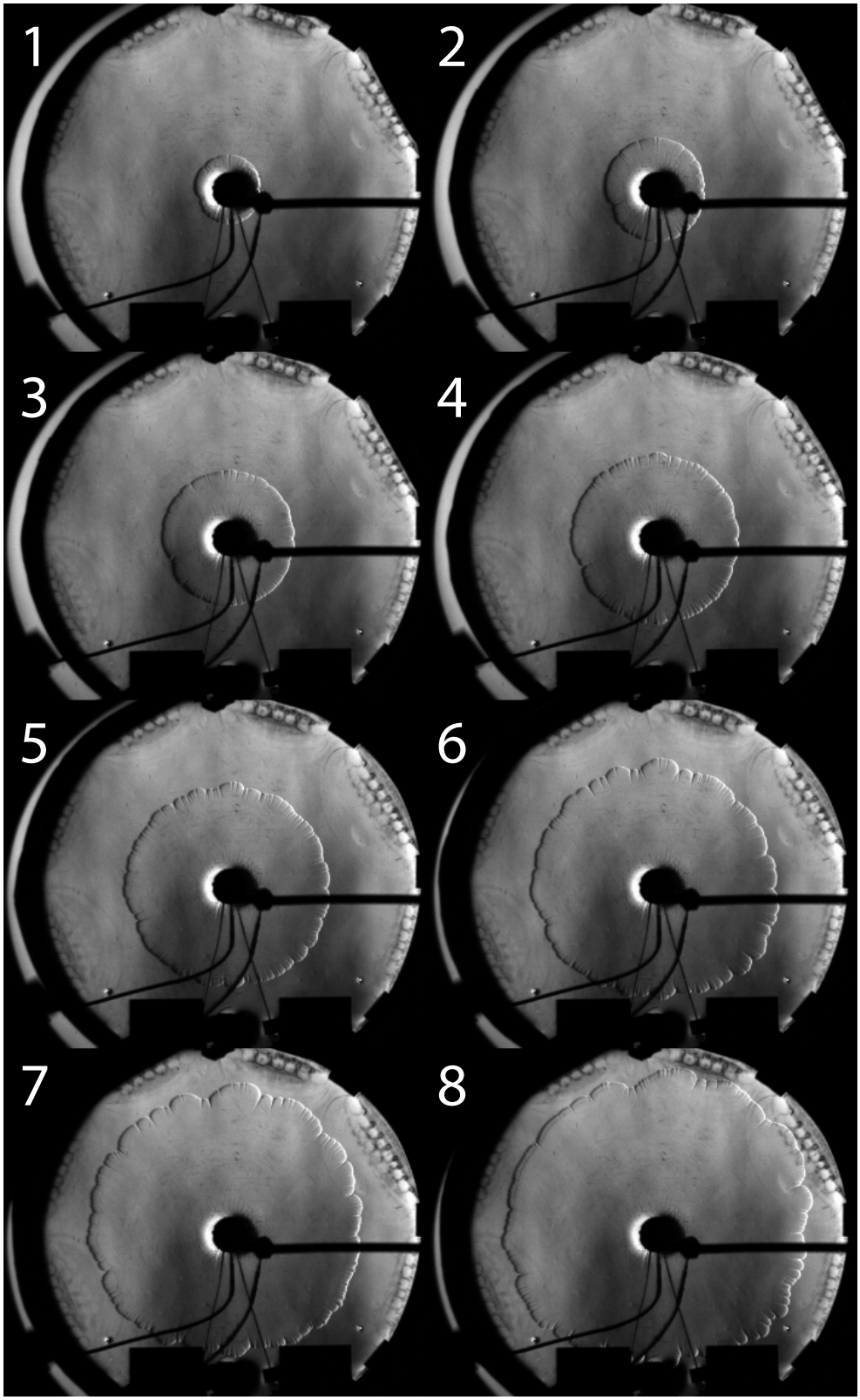

Figure D.15: Sequence of Schlieren images of a deflagration in a hydrogen-air mixture at $\phi = 0.6$ propagating in the Hele-Shaw cell. Ambient room conditions. Recorded at 77,481 fps. The time between frames is 1.29 ms.

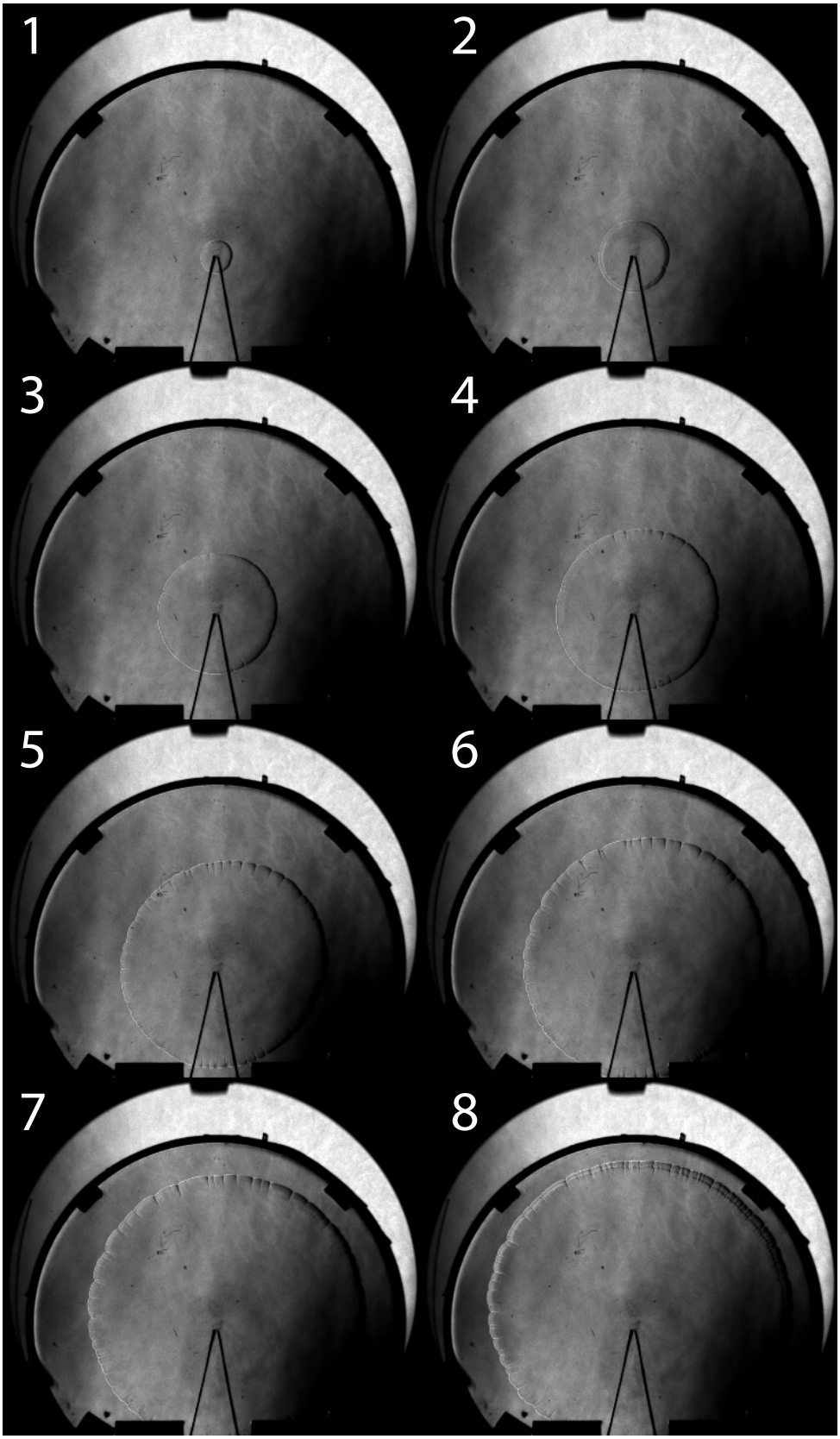

Figure D.16: Sequence of Schlieren images of a deflagration in a hydrogen-air mixture at $\phi = 1.0$ propagating in the Hele-Shaw cell. Ambient room conditions. Recorded at 59,590 fps. Inter-frame time is 0.79 ms.

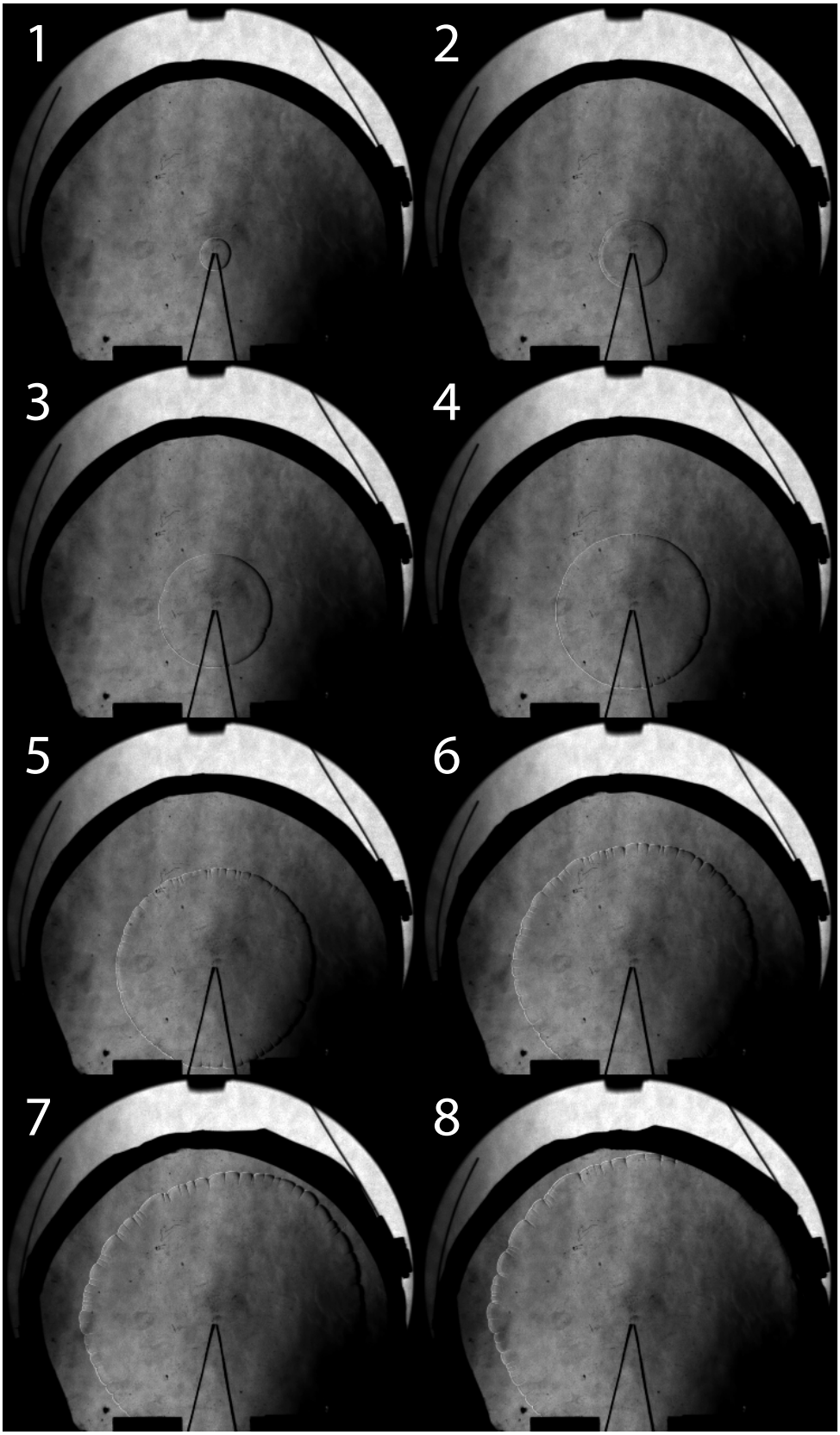

Figure D.17: Sequence of Schlieren images of a deflagration in a hydrogen-air mixture at $\phi = 1.0$ propagating in the Hele-Shaw cell. Ambient room conditions. Recorded at 59,590 fps. Inter-frame time is 0.79 ms.

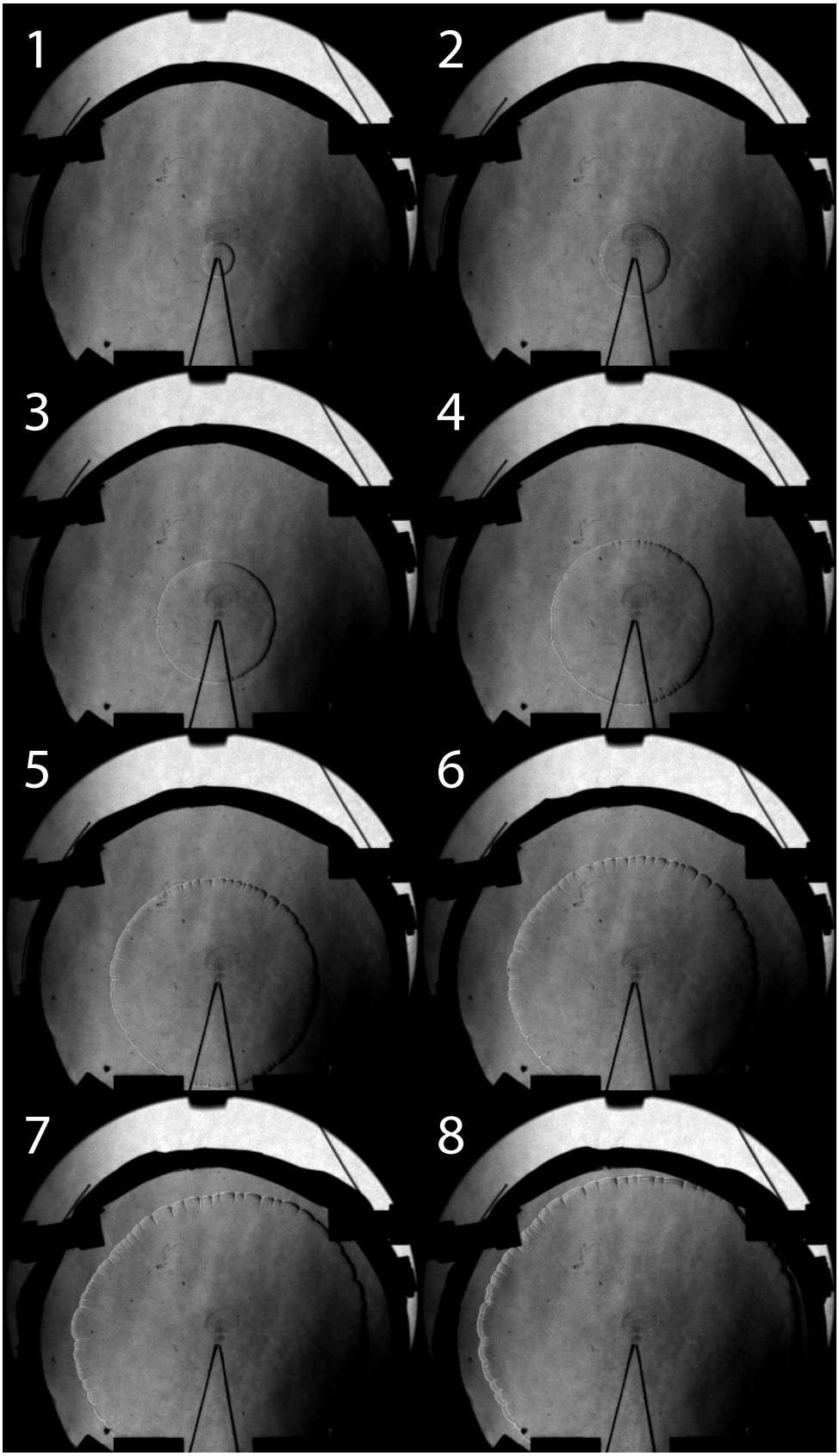

Figure D.18: Sequence of Schlieren images of a deflagration in a hydrogen-air mixture at $\phi = 1.0$ propagating in the Hele-Shaw cell. Ambient room conditions. Recorded at 59,590 fps. Inter-frame time is 0.79 ms.

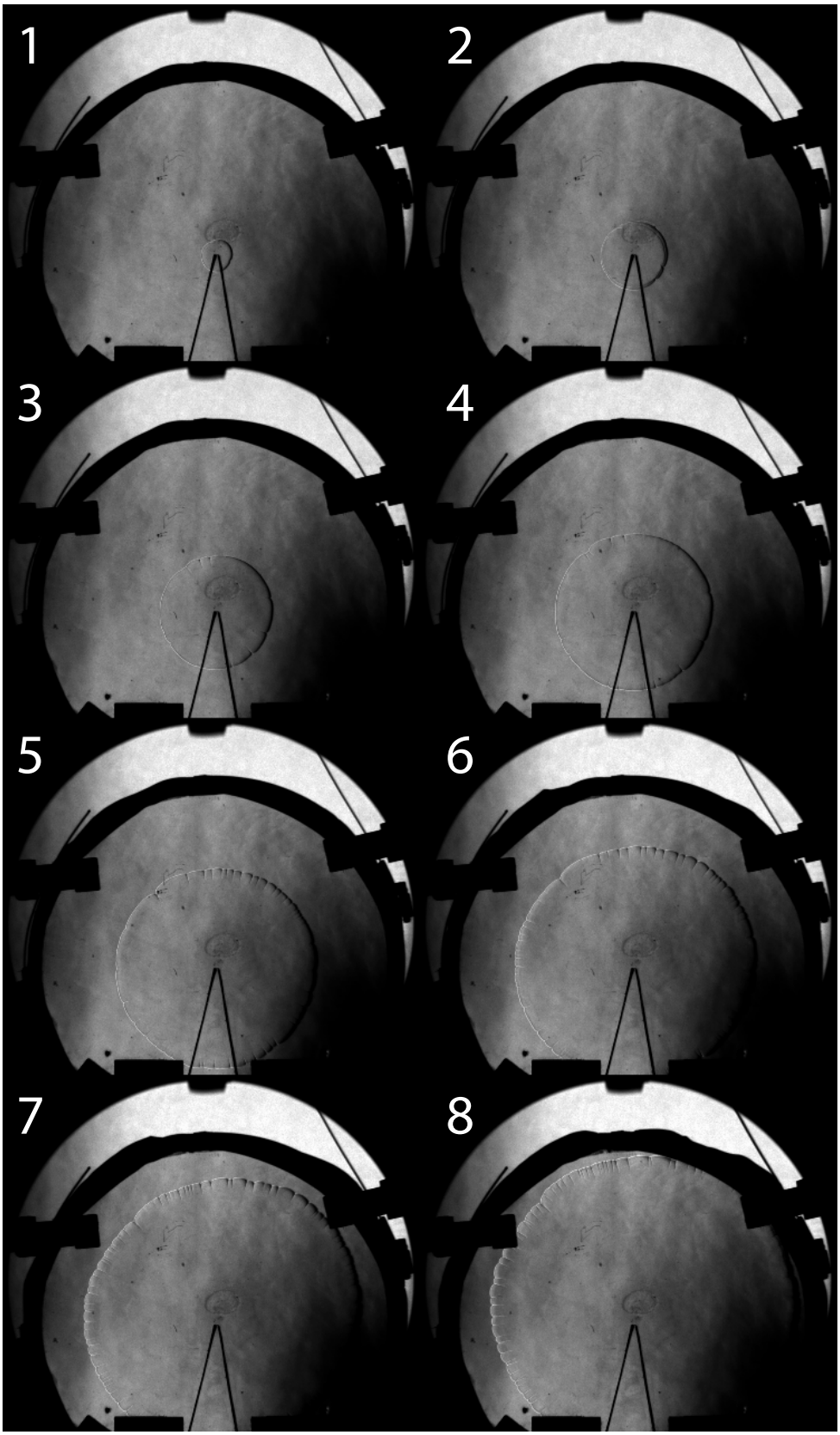

Figure D.19: Sequence of Schlieren images of a deflagration in a hydrogen-air mixture at $\phi = 1.0$ propagating in the Hele-Shaw cell. Ambient room conditions. Recorded at 59,590 fps. Inter-frame time is 0.79 ms.

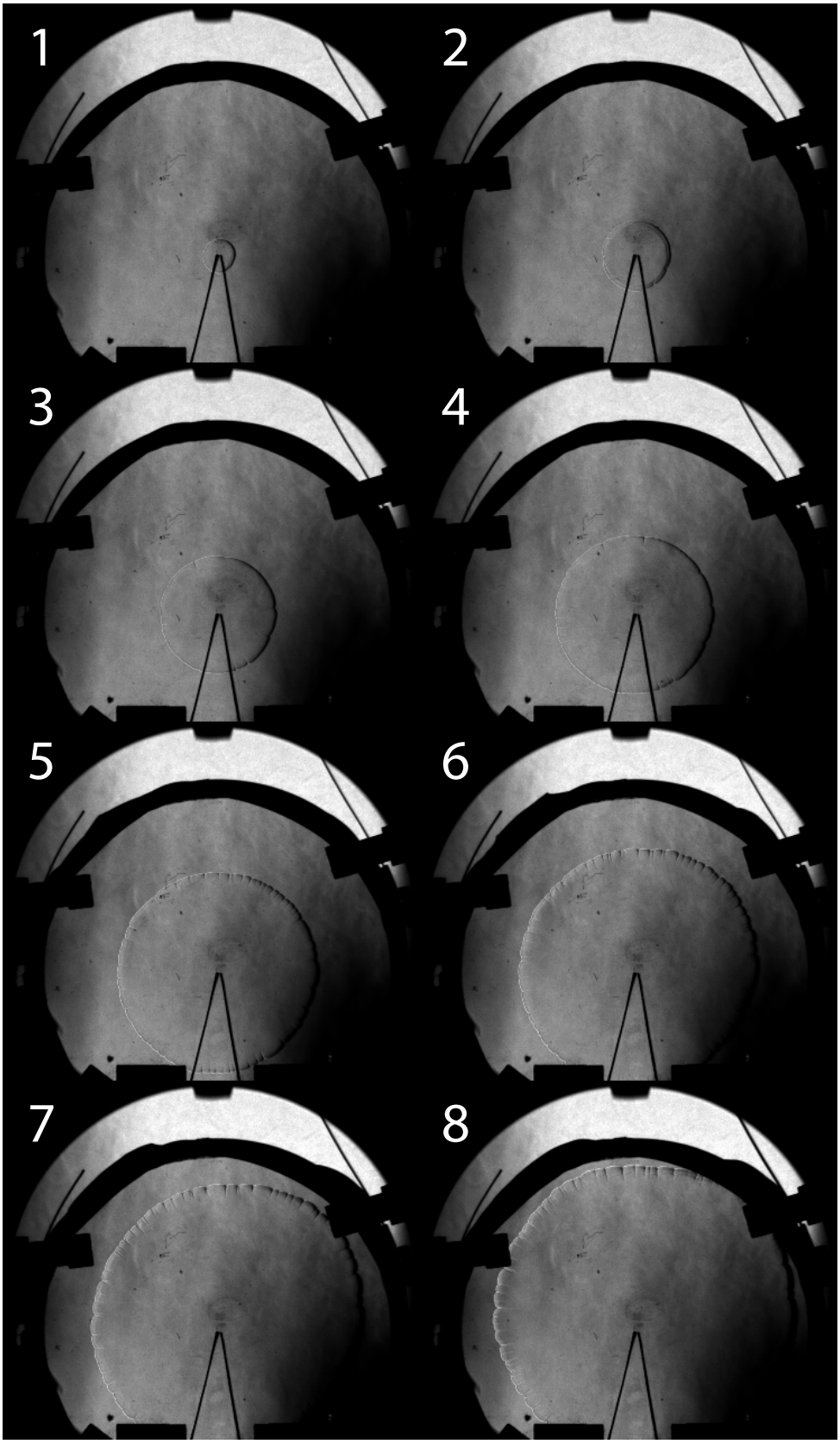

Figure D.20: Sequence of Schlieren images of a deflagration in a hydrogen-air mixture at $\phi = 1.0$ propagating in the Hele-Shaw cell. Ambient room conditions. Recorded at 59,590 fps. Inter-frame time is 0.79 ms.

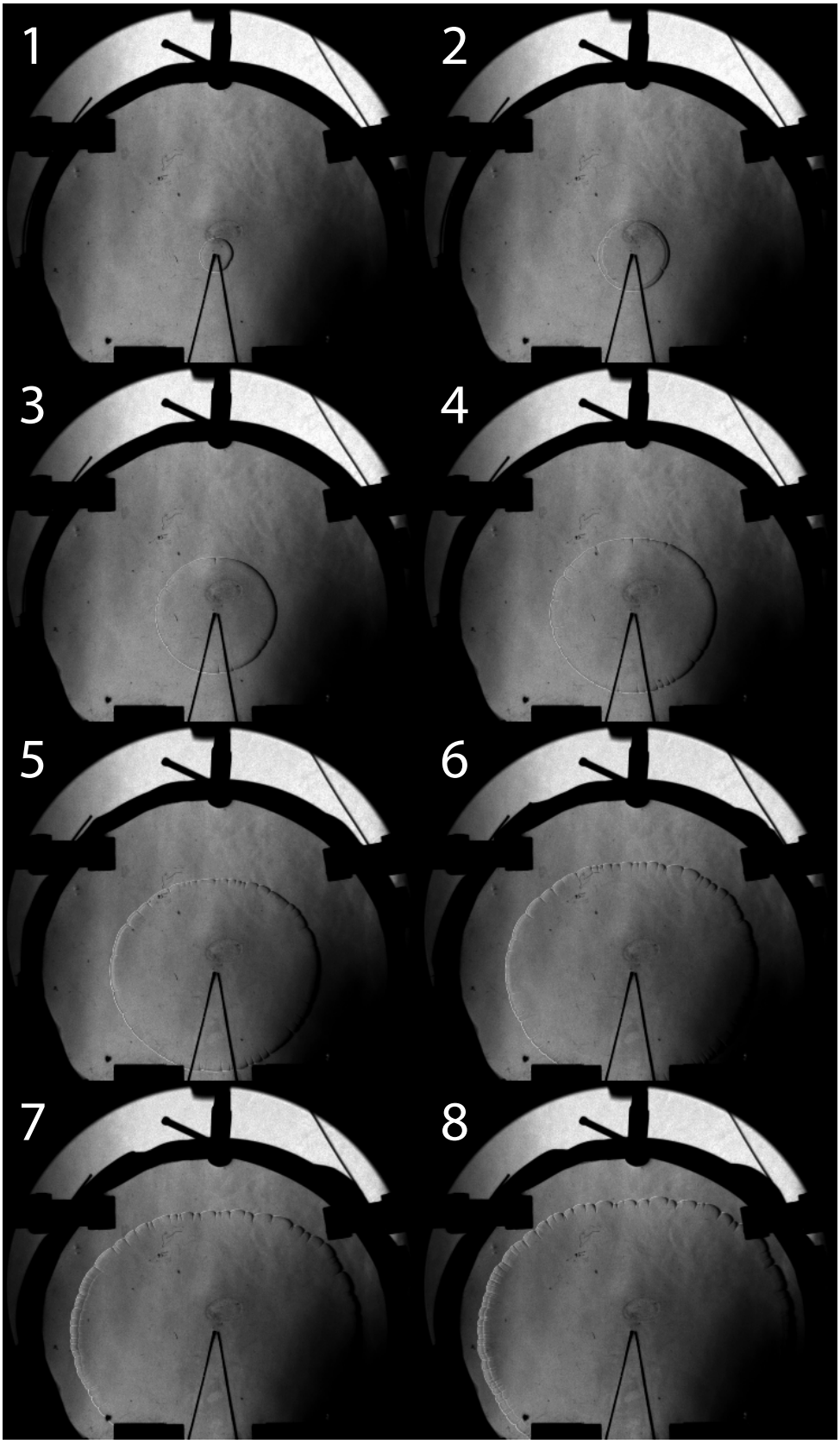

Figure D.21: Sequence of Schlieren images of a deflagration in a hydrogen-air mixture at $\phi = 1.0$ propagating in the Hele-Shaw cell. Ambient room conditions. Recorded at 59,590 fps. Inter-frame time is 0.79 ms.

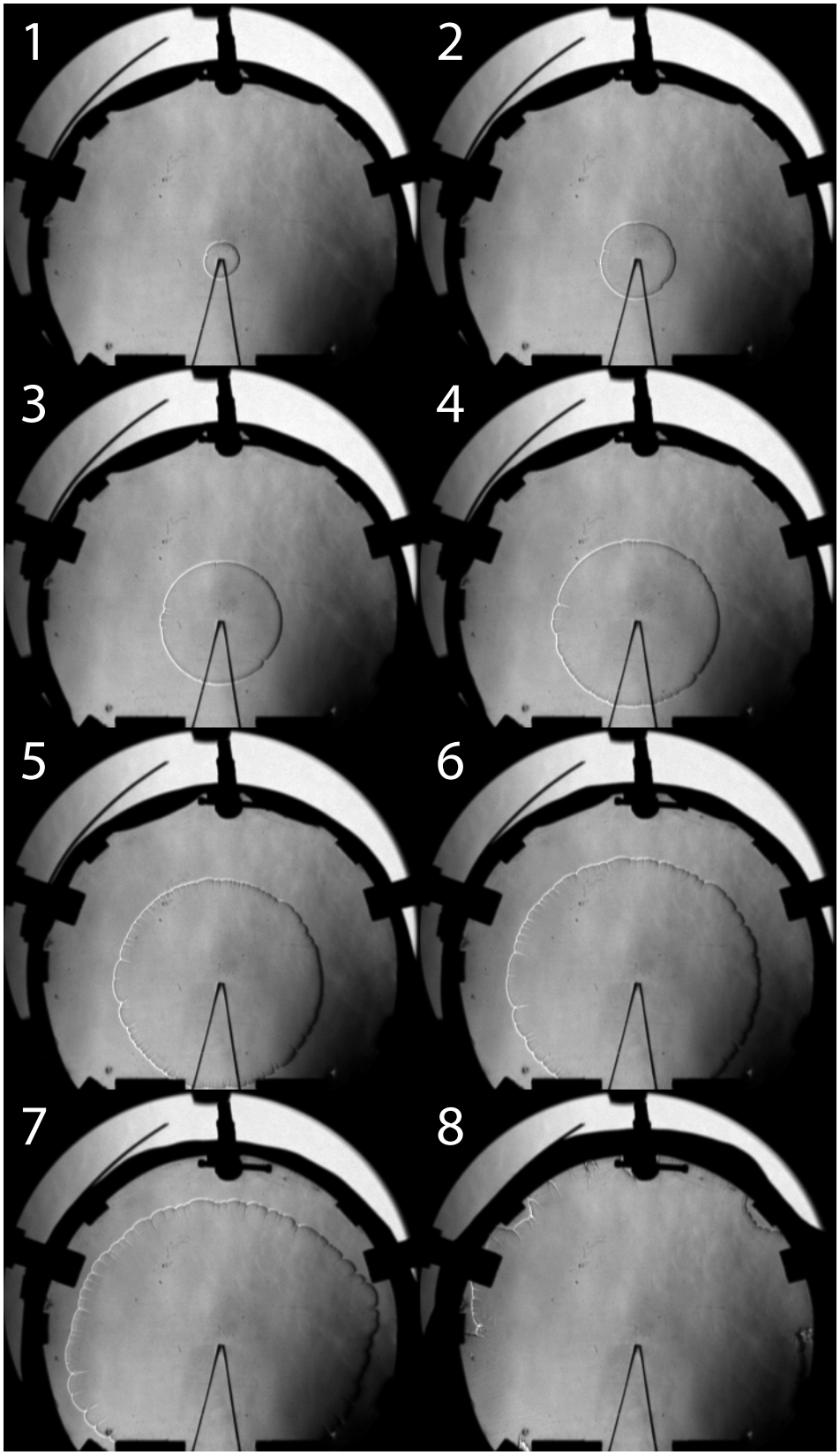

Figure D.22: Sequence of Schlieren images of a deflagration in a hydrogen-air mixture at $\phi = 1.0$ propagating in the Hele-Shaw cell. Ambient room conditions. Recorded at 59,590 fps. Inter-frame time is 0.79 ms.

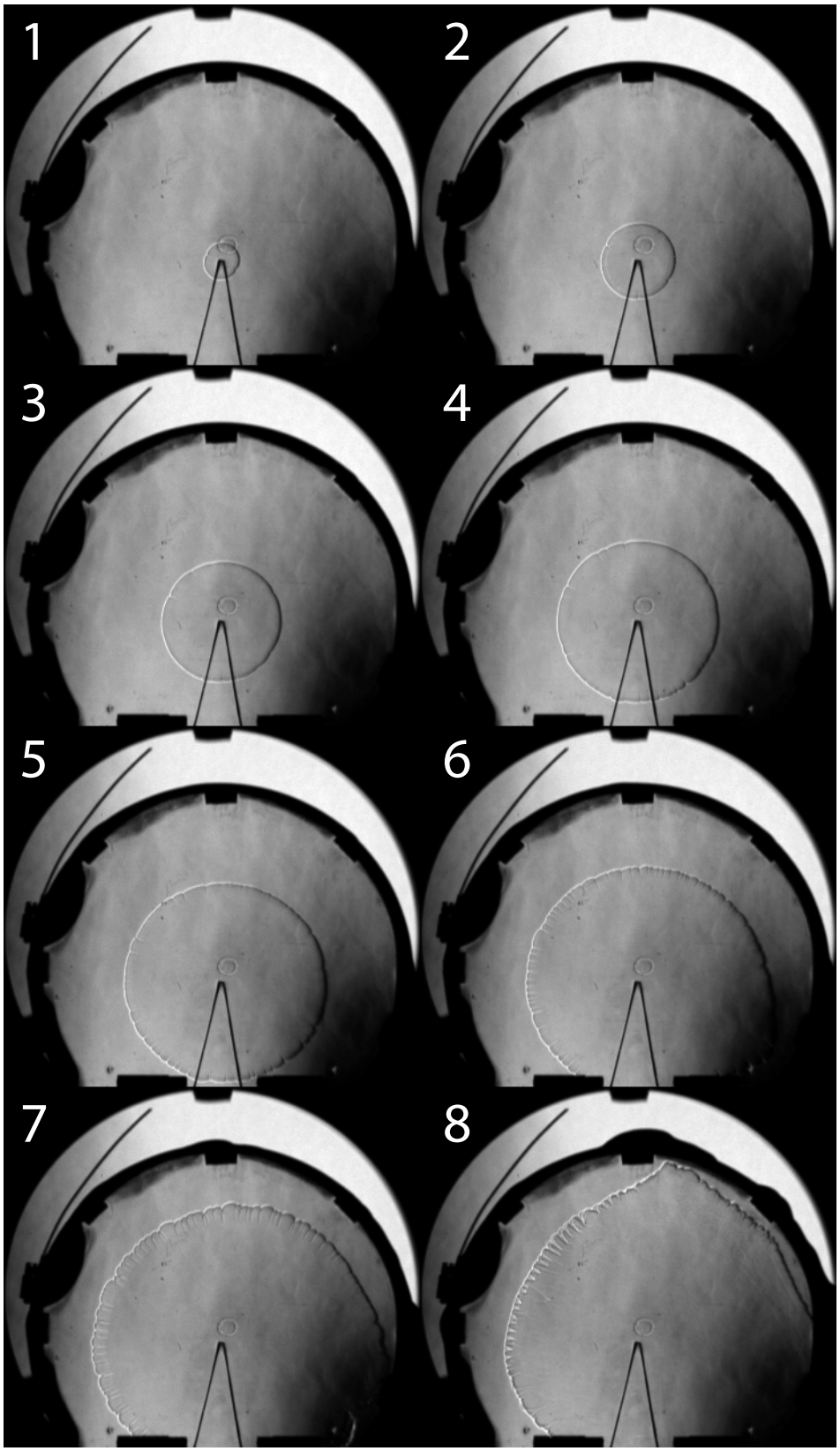

Figure D.23: Sequence of Schlieren images of a deflagration in a hydrogen-air mixture at $\phi = 1.0$ propagating in the Hele-Shaw cell. Ambient room conditions. Recorded at 59,590 fps. Inter-frame time is 0.79 ms.

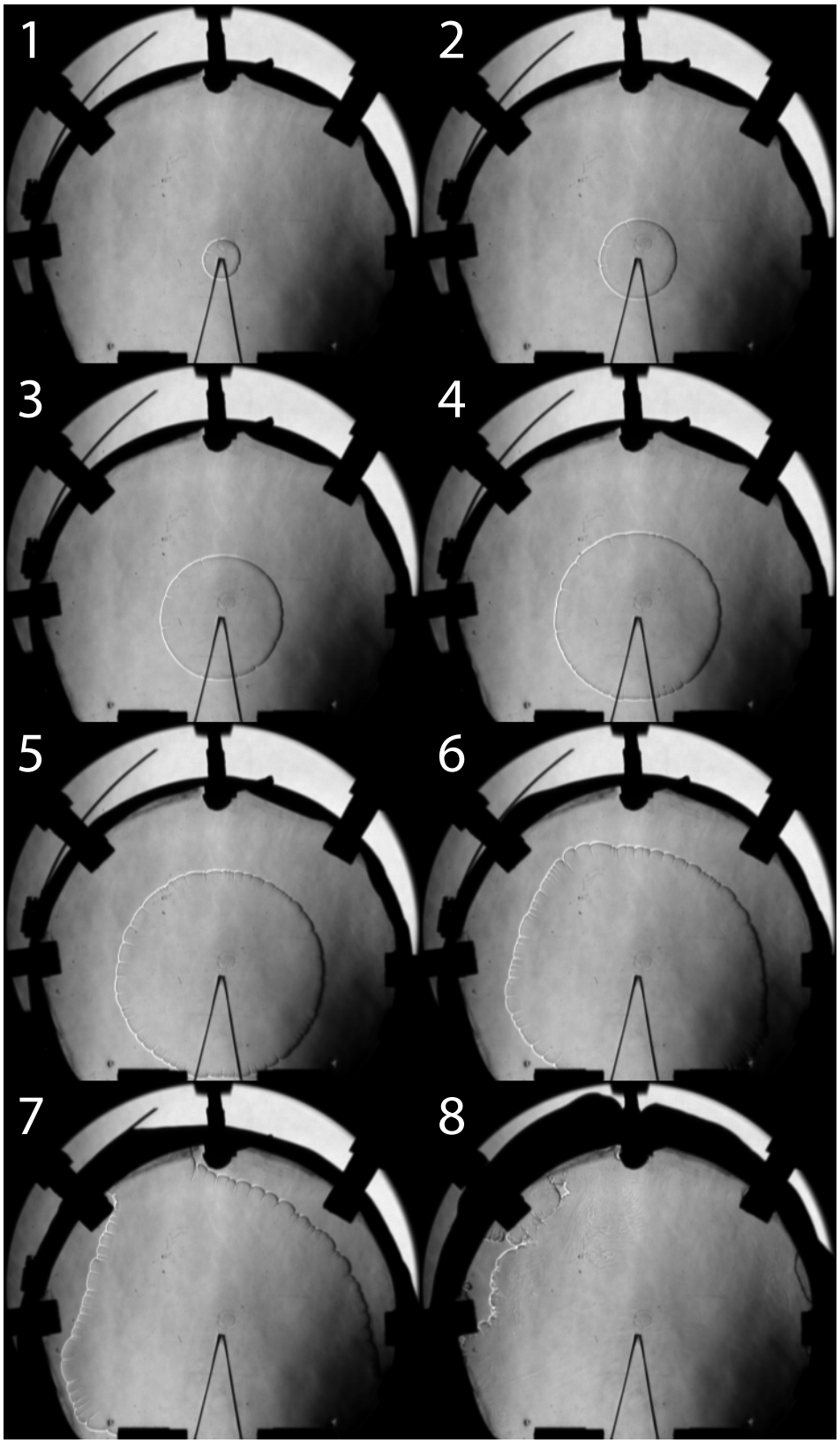

Figure D.24: Sequence of Schlieren images of a deflagration in a hydrogen-air mixture at $\phi = 1.0$ propagating in the Hele-Shaw cell. Ambient room conditions. Recorded at 59,590 fps. Inter-frame time is 0.79 ms.

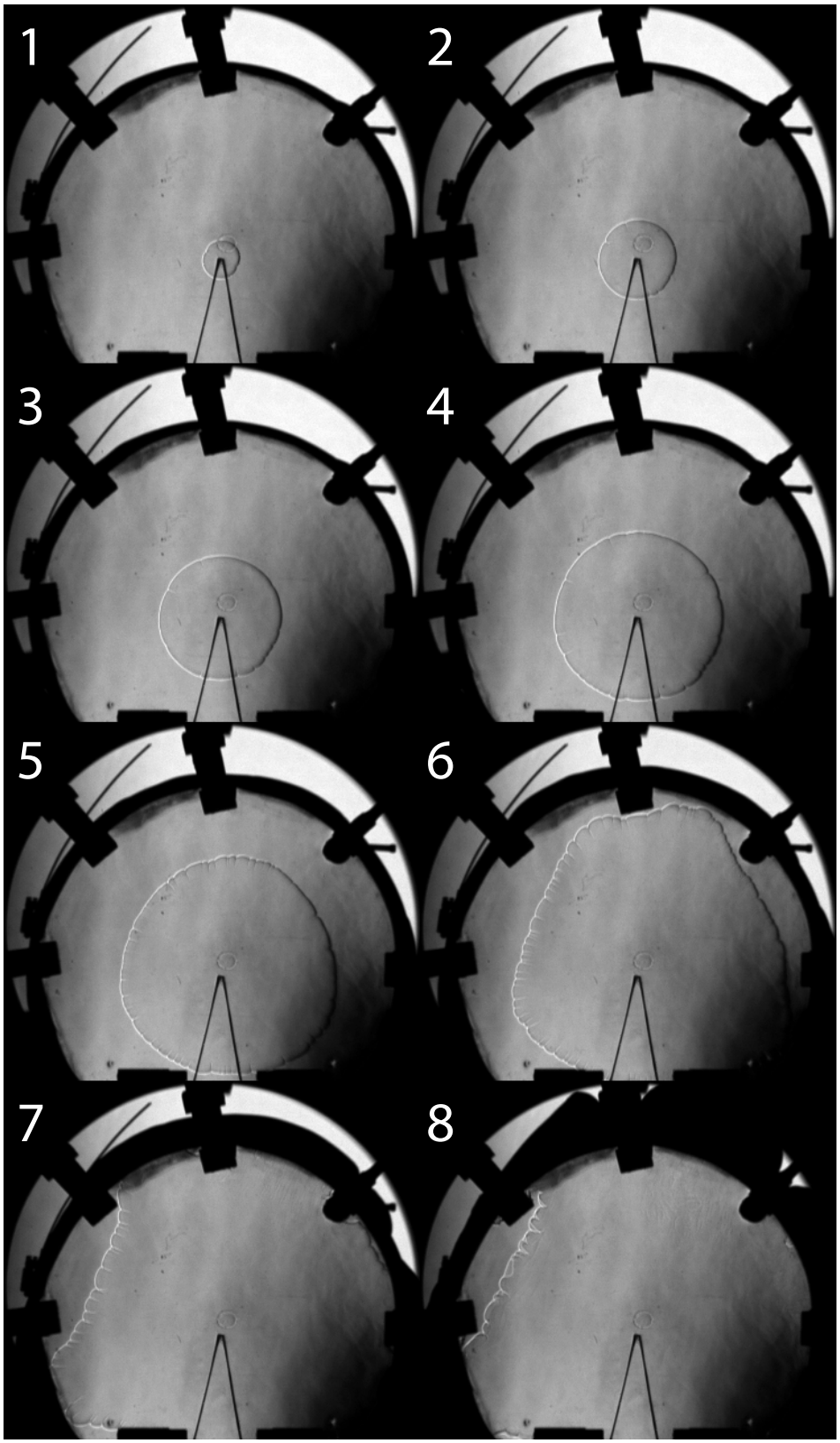

Figure D.25: Sequence of Schlieren images of a deflagration in a hydrogen-air mixture at $\phi = 1.0$ propagating in the Hele-Shaw cell. Ambient room conditions. Recorded at 59,590 fps. Inter-frame time is 0.79 ms.

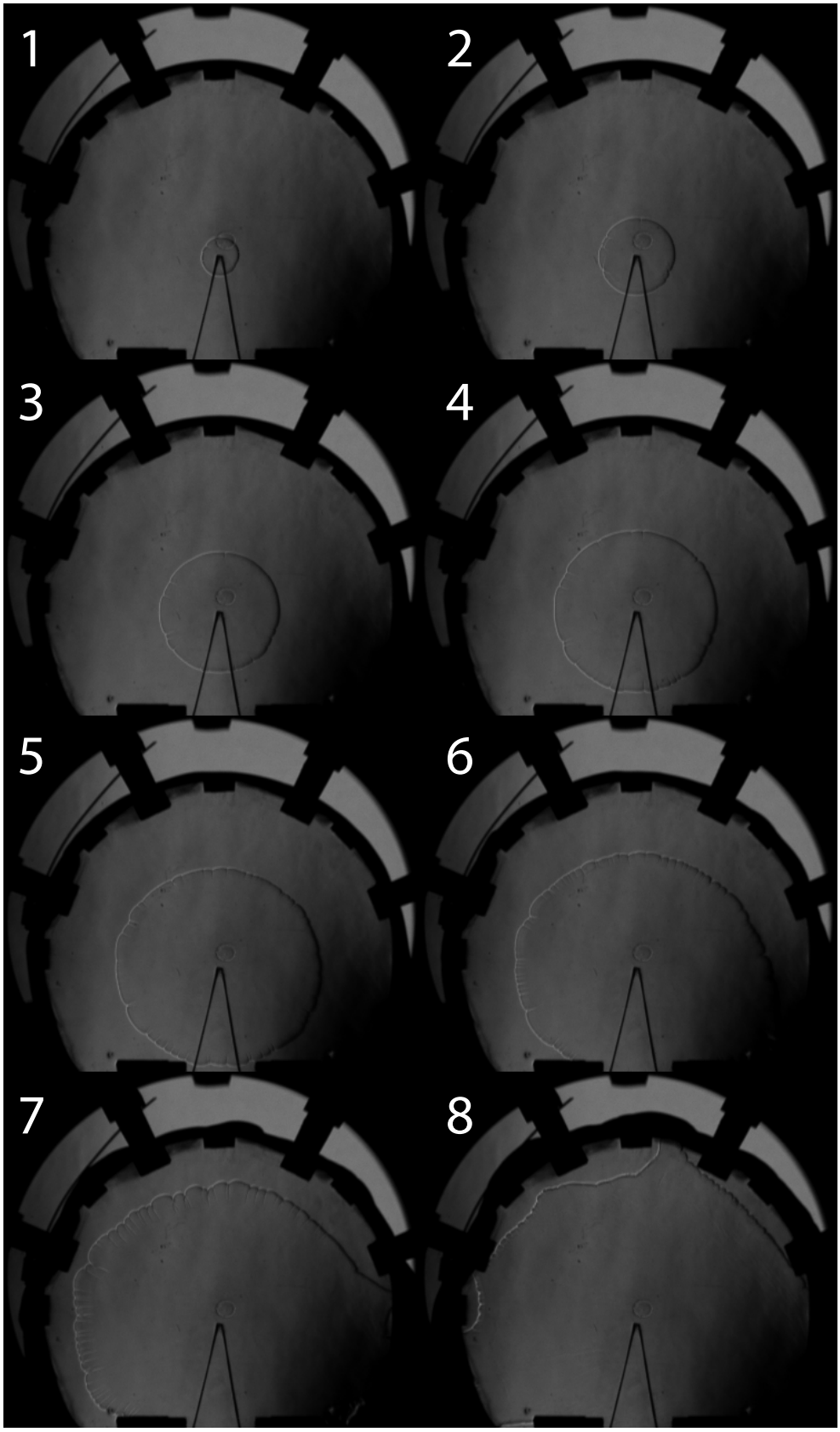

Figure D.26: Sequence of Schlieren images of a deflagration in a hydrogen-air mixture at $\phi = 1.0$ propagating in the Hele-Shaw cell. Ambient room conditions. Recorded at 59,590 fps. Inter-frame time is 0.79 ms.

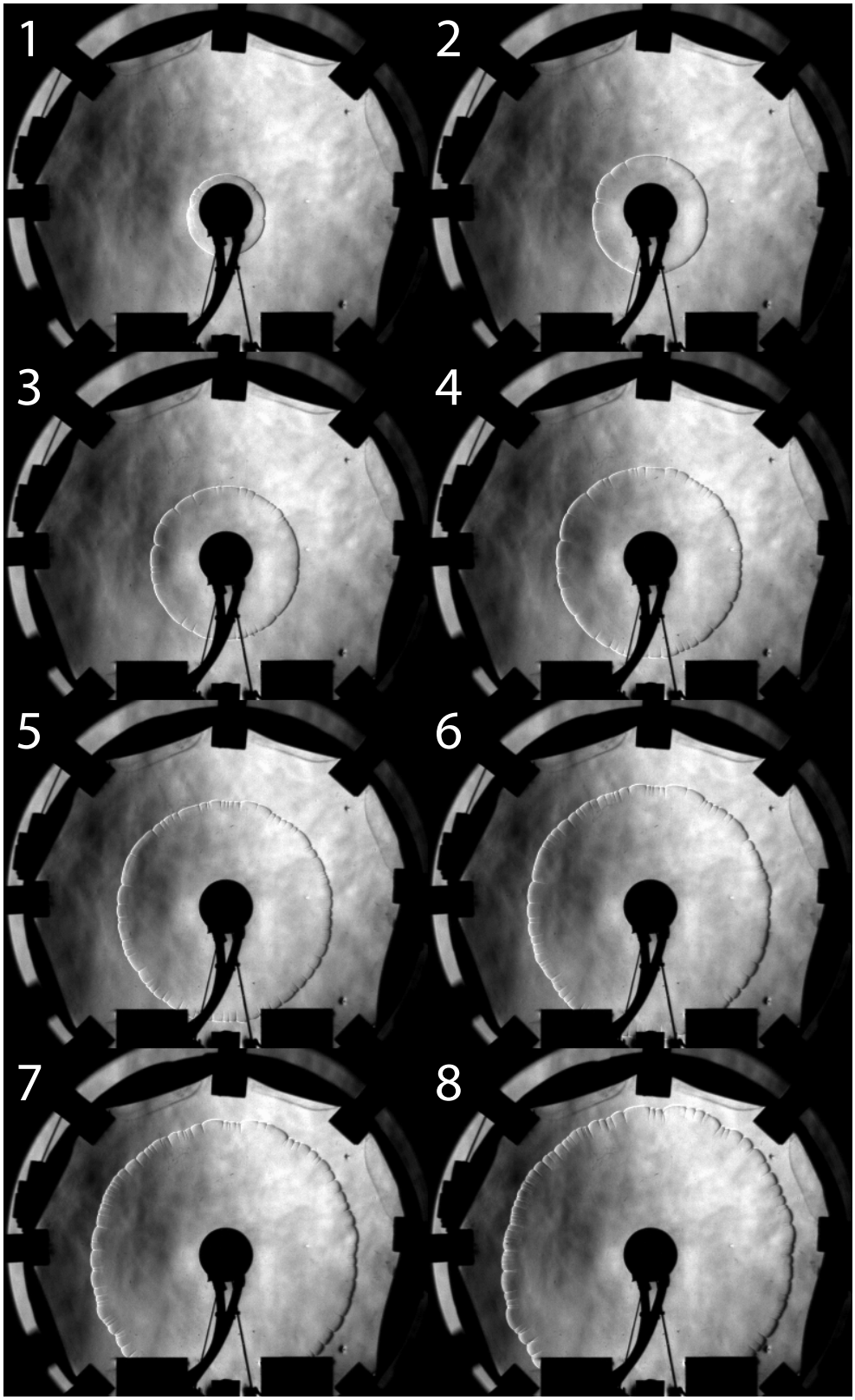

Figure D.27: Sequence of Schlieren images of a deflagration in a hydrogen-air mixture at $\phi = 1.0$ propagating in the Hele-Shaw cell. Ambient room conditions. Recorded at 59,590 fps. Inter-frame time is 0.59 ms.

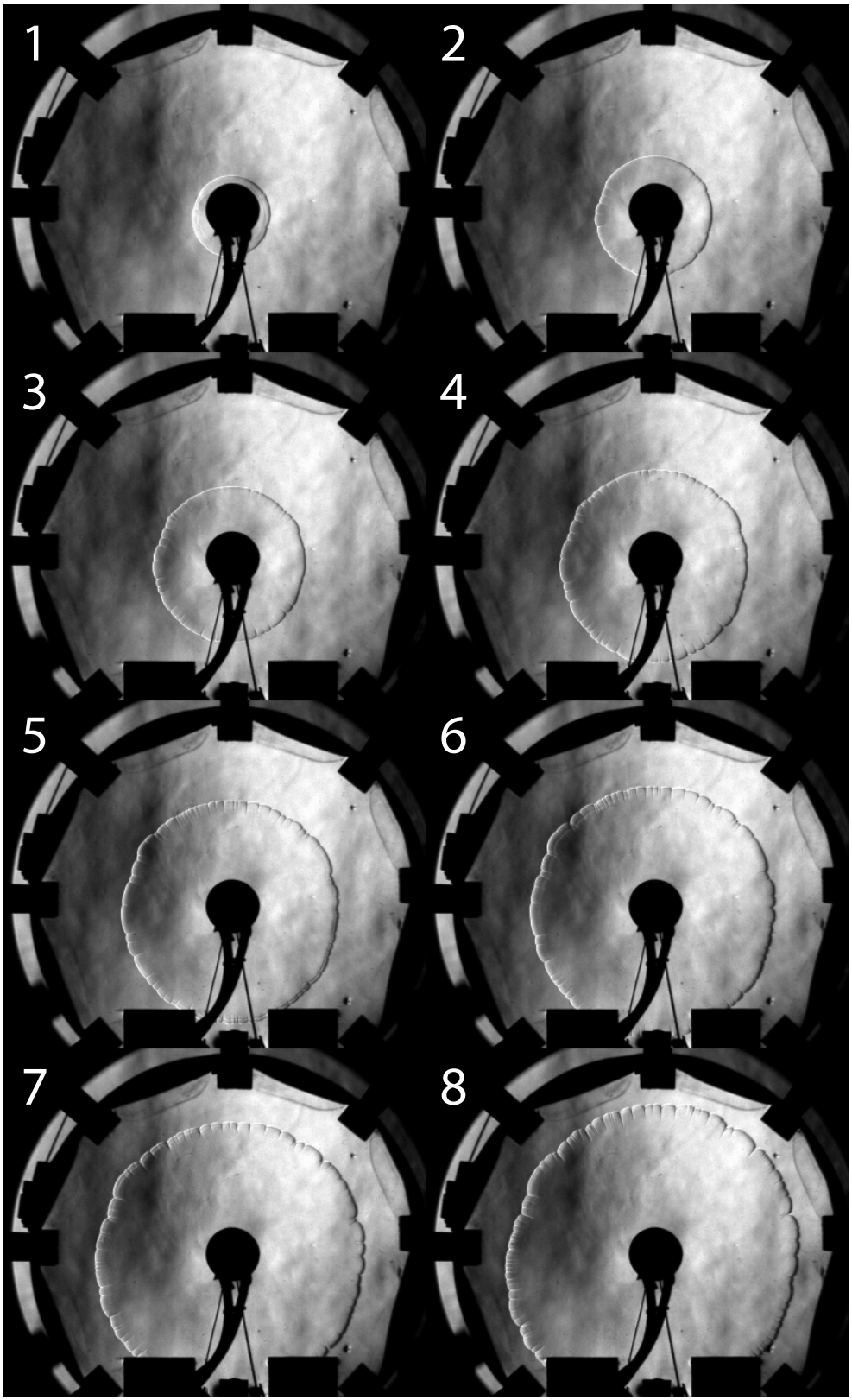

Figure D.28: Sequence of Schlieren images of a deflagration in a hydrogen-air mixture at $\phi = 1.0$ propagating in the Hele-Shaw cell. Ambient room conditions. Recorded at 59,590 fps. Inter-frame time is 0.59 ms.

D.2 Shock-Flame – Light-to-heavy

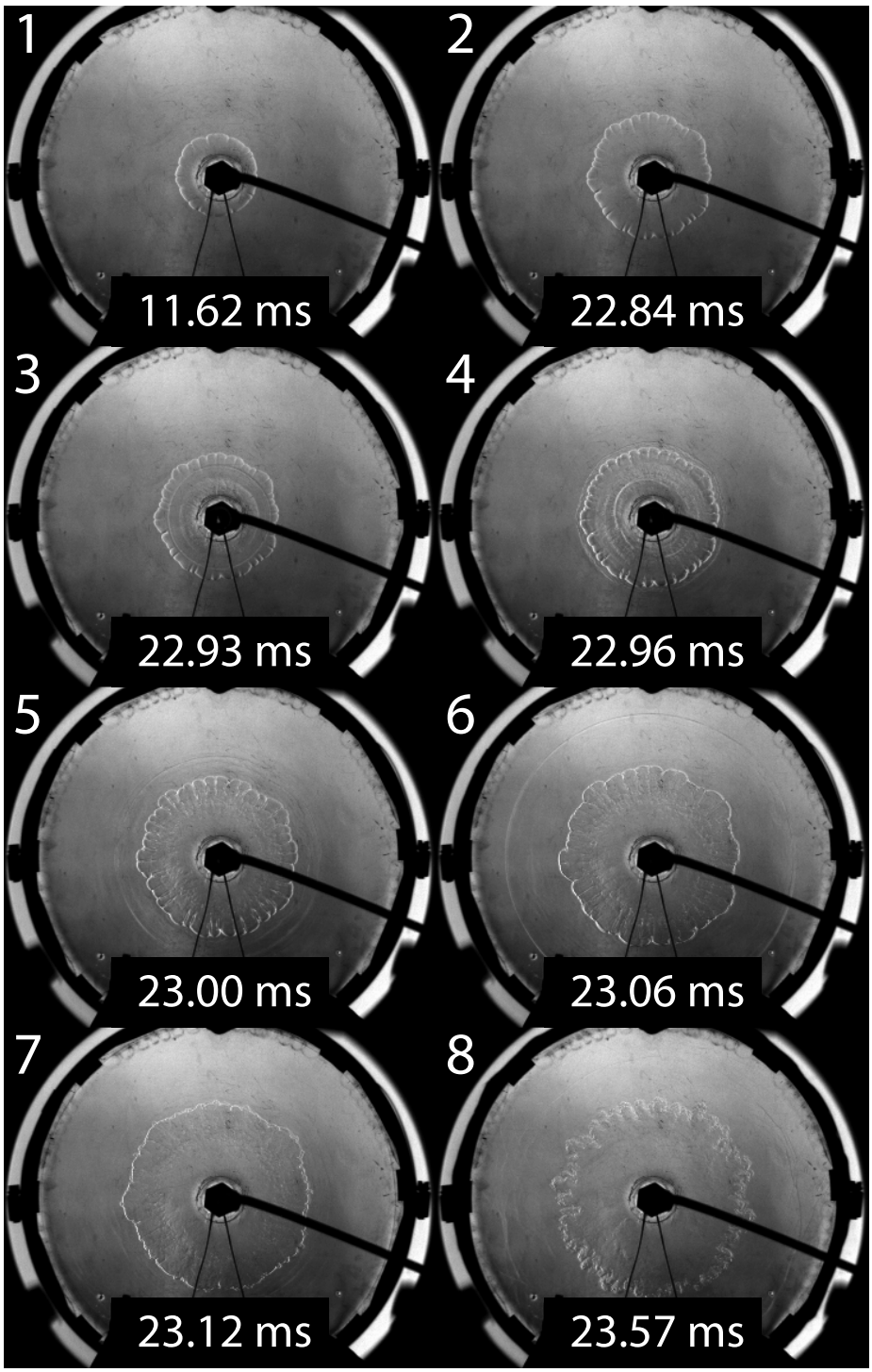

Figure D.29: Schlieren records of detonation-driven shock interacting with a flame in a hydrogen-air mixture at $\phi = 0.3$ propagating in the Hele-Shaw cell. Ambient room conditions. Recorded at 77,481 fps.

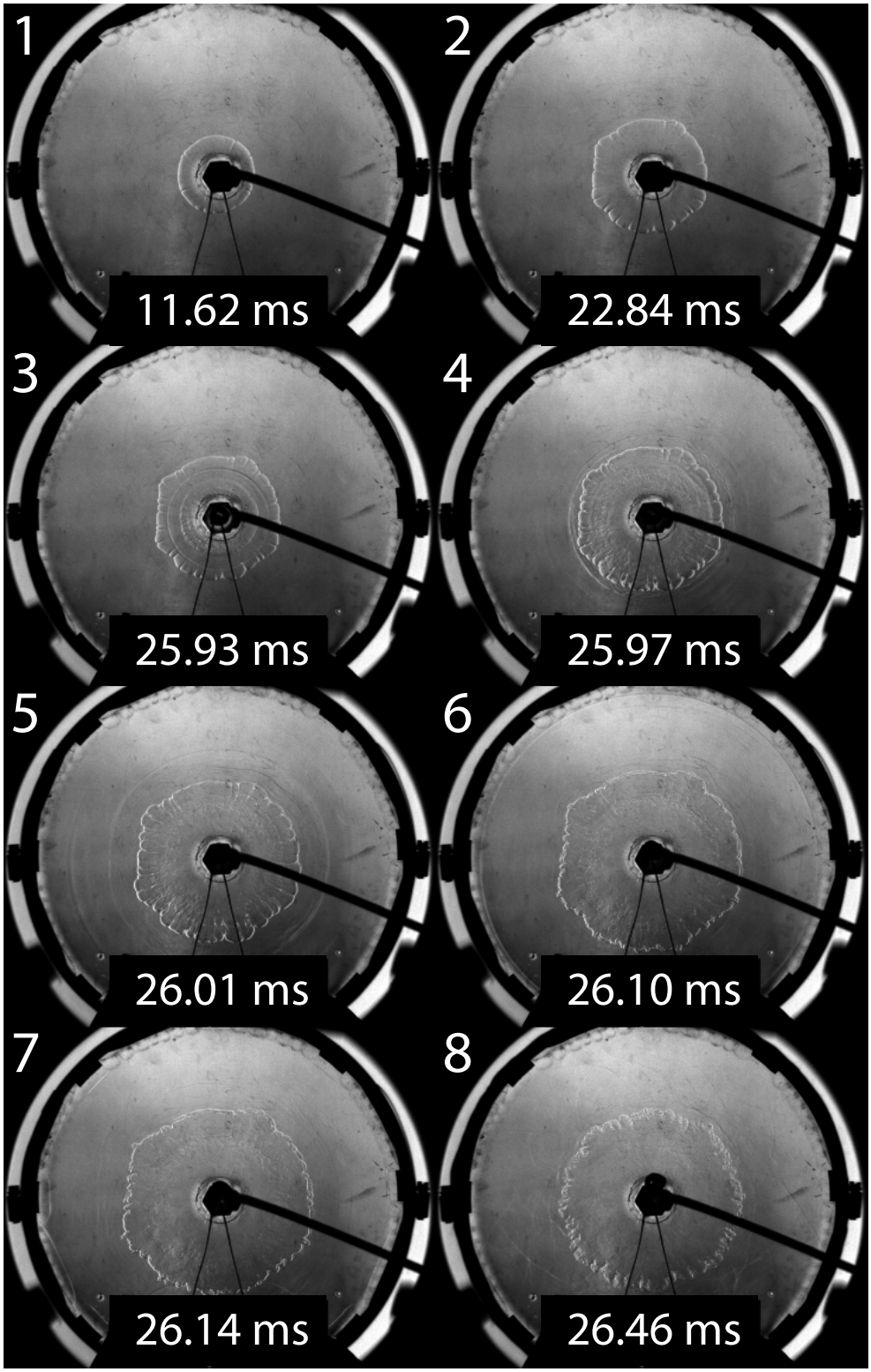

Figure D.30: Schlieren records of detonation-driven shock interacting with a flame in a hydrogen-air mixture at $\phi = 0.3$ propagating in the Hele-Shaw cell. Ambient room conditions. Recorded at 77,481 fps.

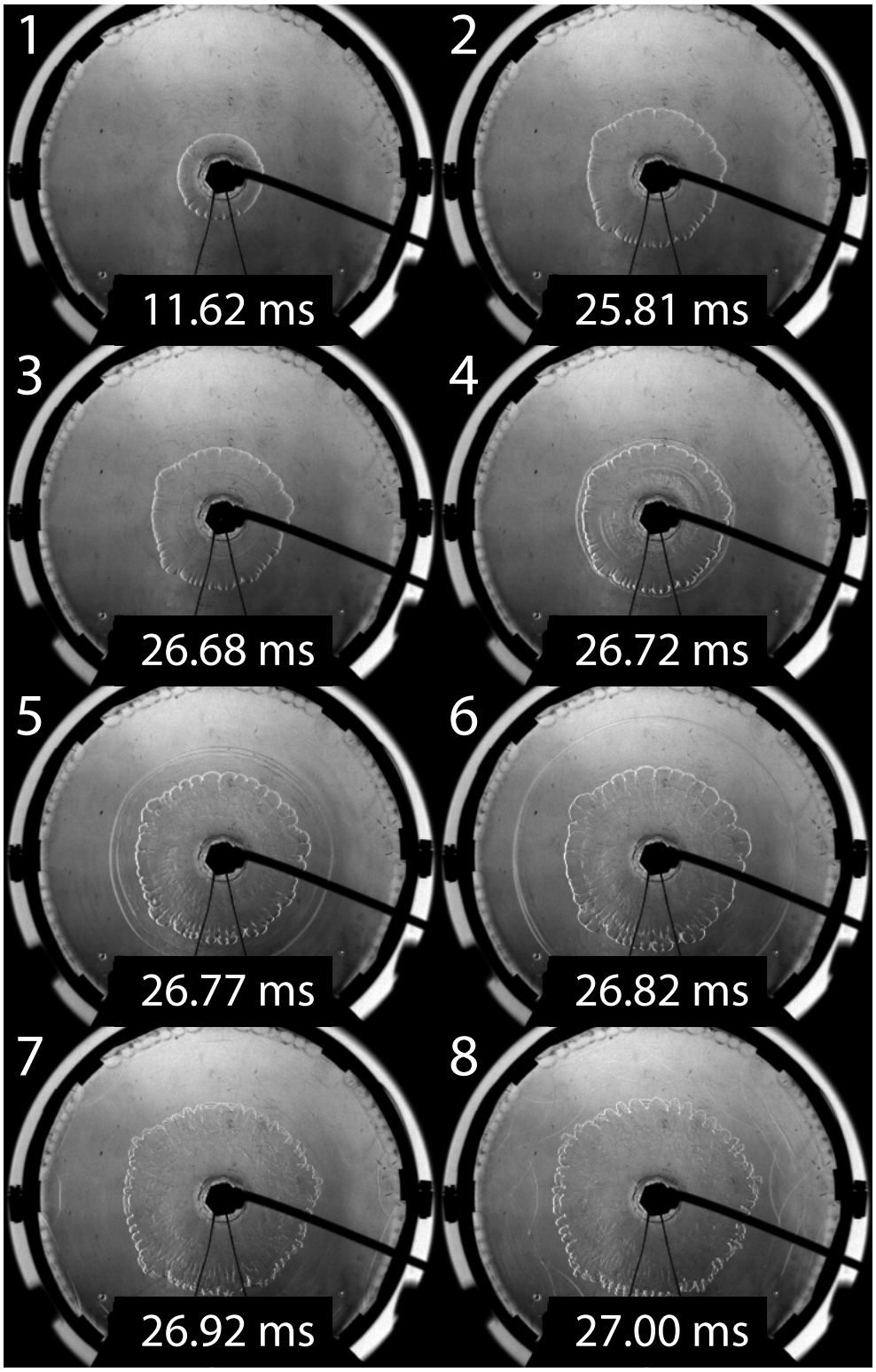

Figure D.31: Schlieren records of detonation-driven shock interacting with a flame in a hydrogen-air mixture at $\phi = 0.3$ propagating in the Hele-Shaw cell. Ambient room conditions. Recorded at 77,481 fps.

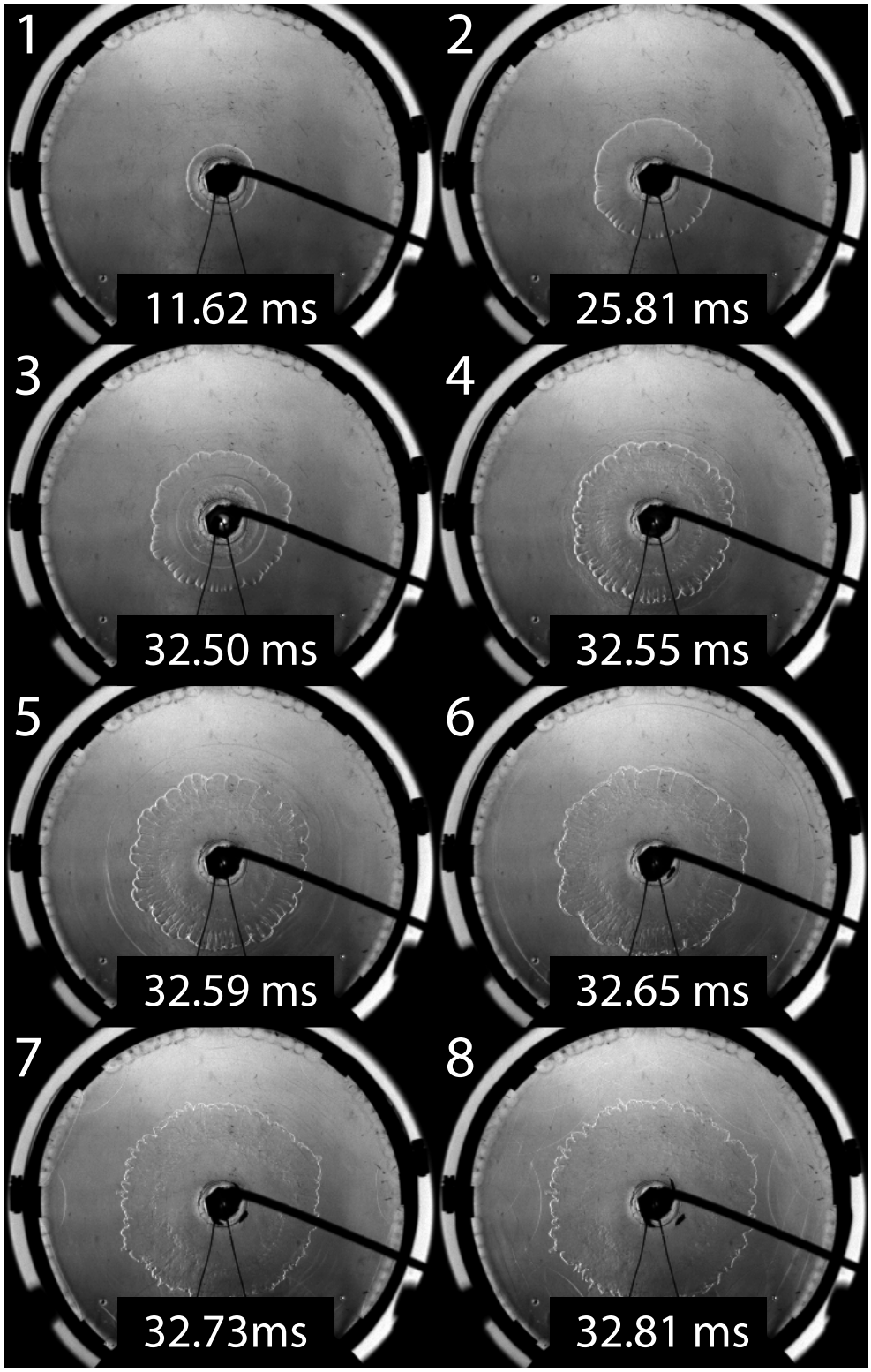

Figure D.32: Schlieren records of detonation-driven shock interacting with a flame in a hydrogen-air mixture at $\phi = 0.3$ propagating in the Hele-Shaw cell. Ambient room conditions. Recorded at 77,481 fps.

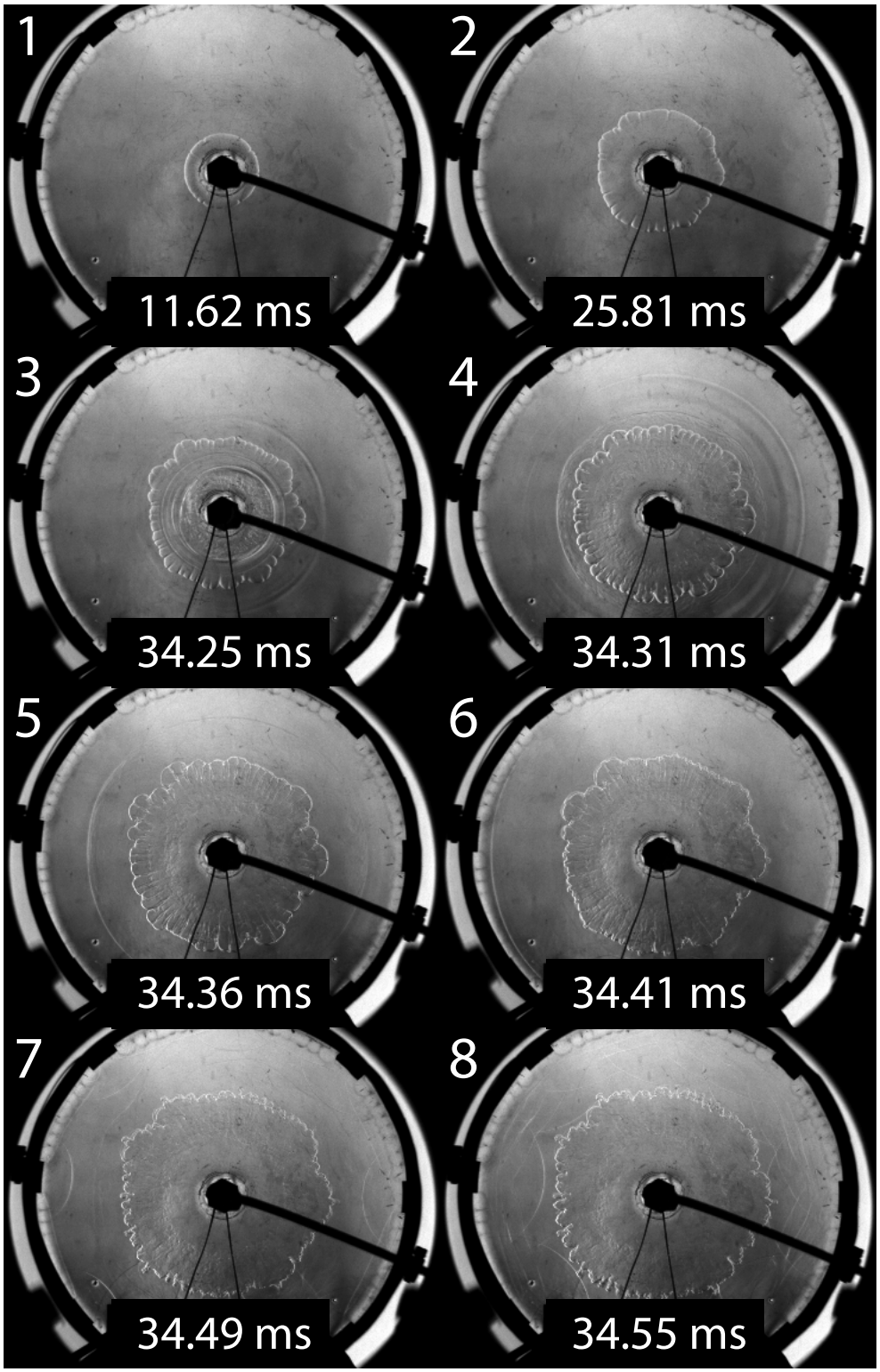

Figure D.33: Schlieren records of detonation-driven shock interacting with a flame in a hydrogen-air mixture at $\phi = 0.3$ propagating in the Hele-Shaw cell. Ambient room conditions. Recorded at 77,481 fps.

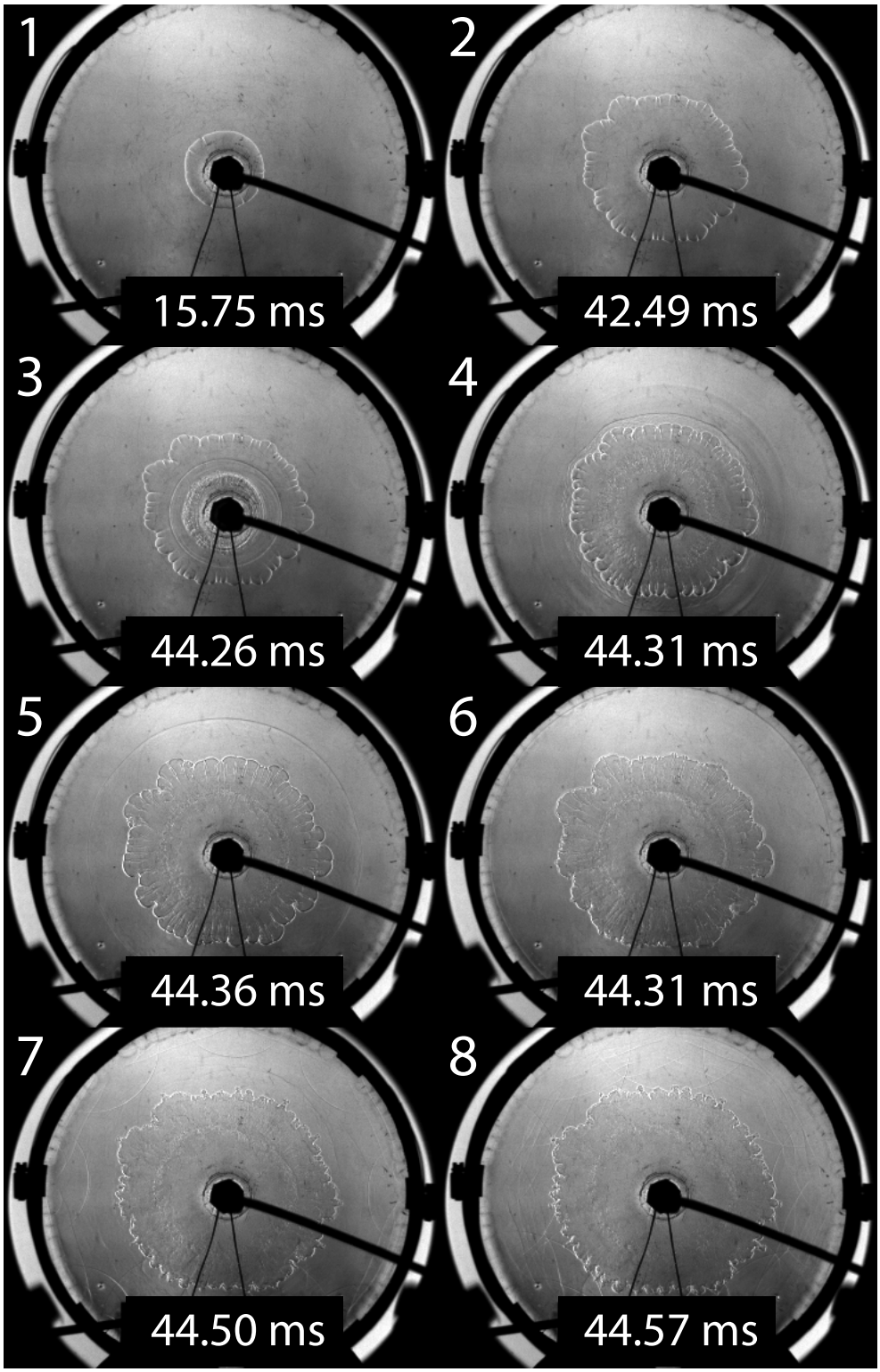

Figure D.34: Schlieren records of detonation-driven shock interacting with a flame in a hydrogen-air mixture at $\phi = 0.3$ propagating in the Hele-Shaw cell. Ambient room conditions. Recorded at 77,481 fps.

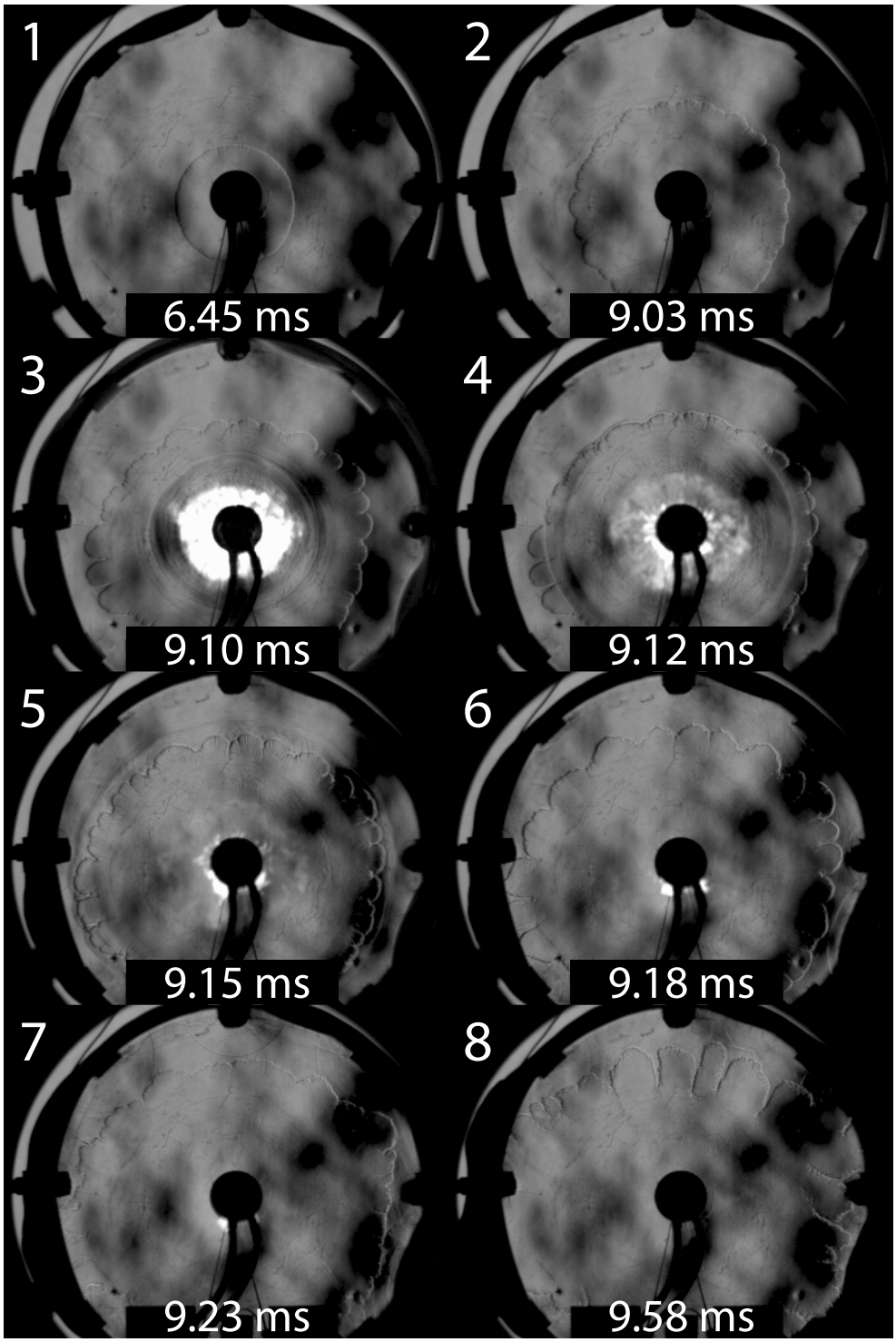

Figure D.35: Schlieren records of HVI-driven shock interacting with a flame in a hydrogen-air mixture at $\phi = 0.6$ propagating in the Hele-Shaw cell. Ambient room conditions. Recorded at 77,481 fps.

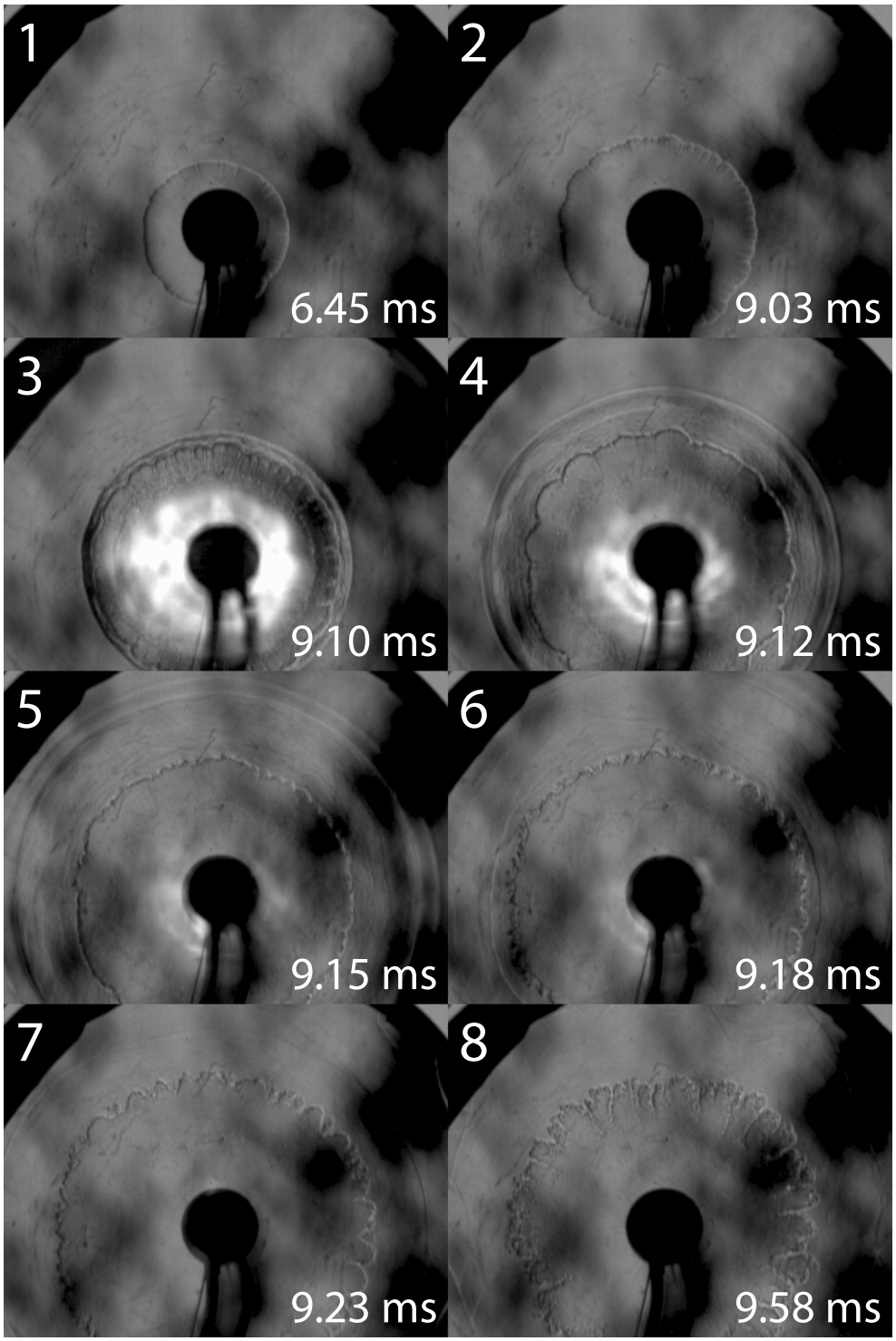

Figure D.36: Schlieren records of HVI-driven shock interacting with a flame in a hydrogen-air mixture at $\phi = 0.6$ propagating in the Hele-Shaw cell. Ambient room conditions. Recorded at 77,481 fps.

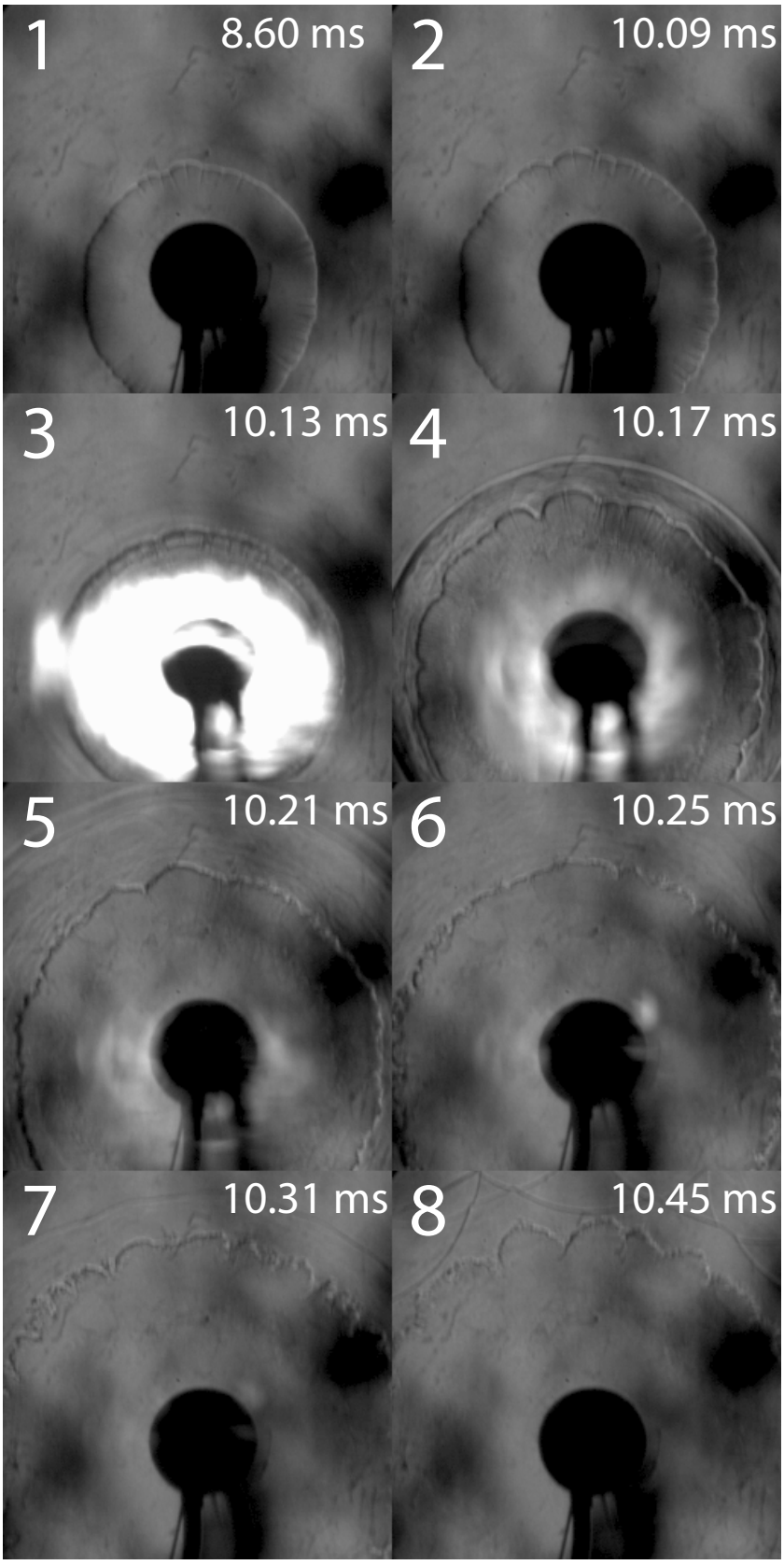

Figure D.37: Schlieren records of HVI-driven shock interacting with a flame in a hydrogen-air mixture at $\phi = 0.6$ propagating in the Hele-Shaw cell. Ambient room conditions. Recorded at 104,918 fps.

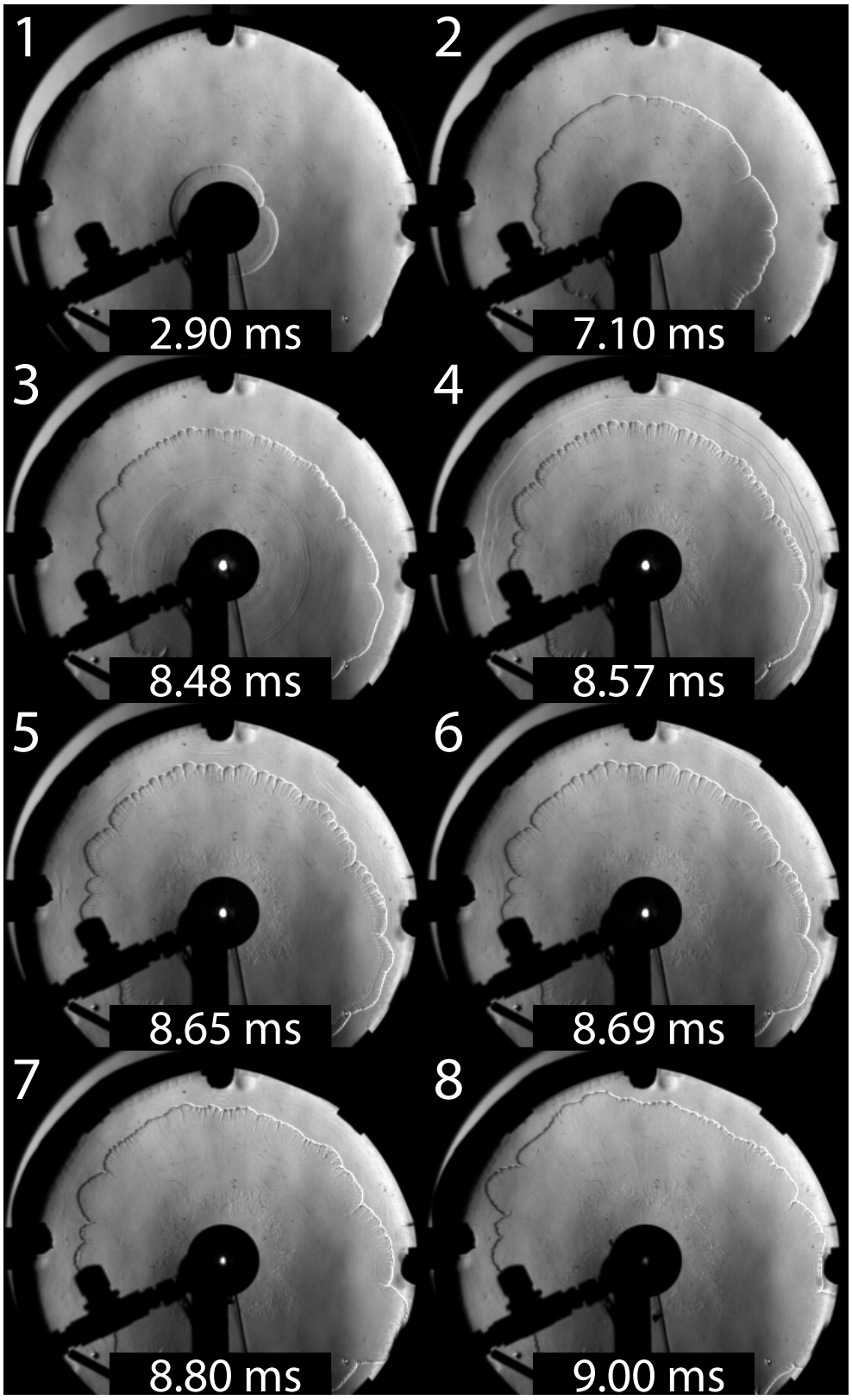

Figure D.38: Schlieren records of detonation-driven shock interacting with a flame in a hydrogen-air mixture at $\phi = 0.6$ propagating in the Hele-Shaw cell. Ambient room conditions. Recorded at 77,481 fps.

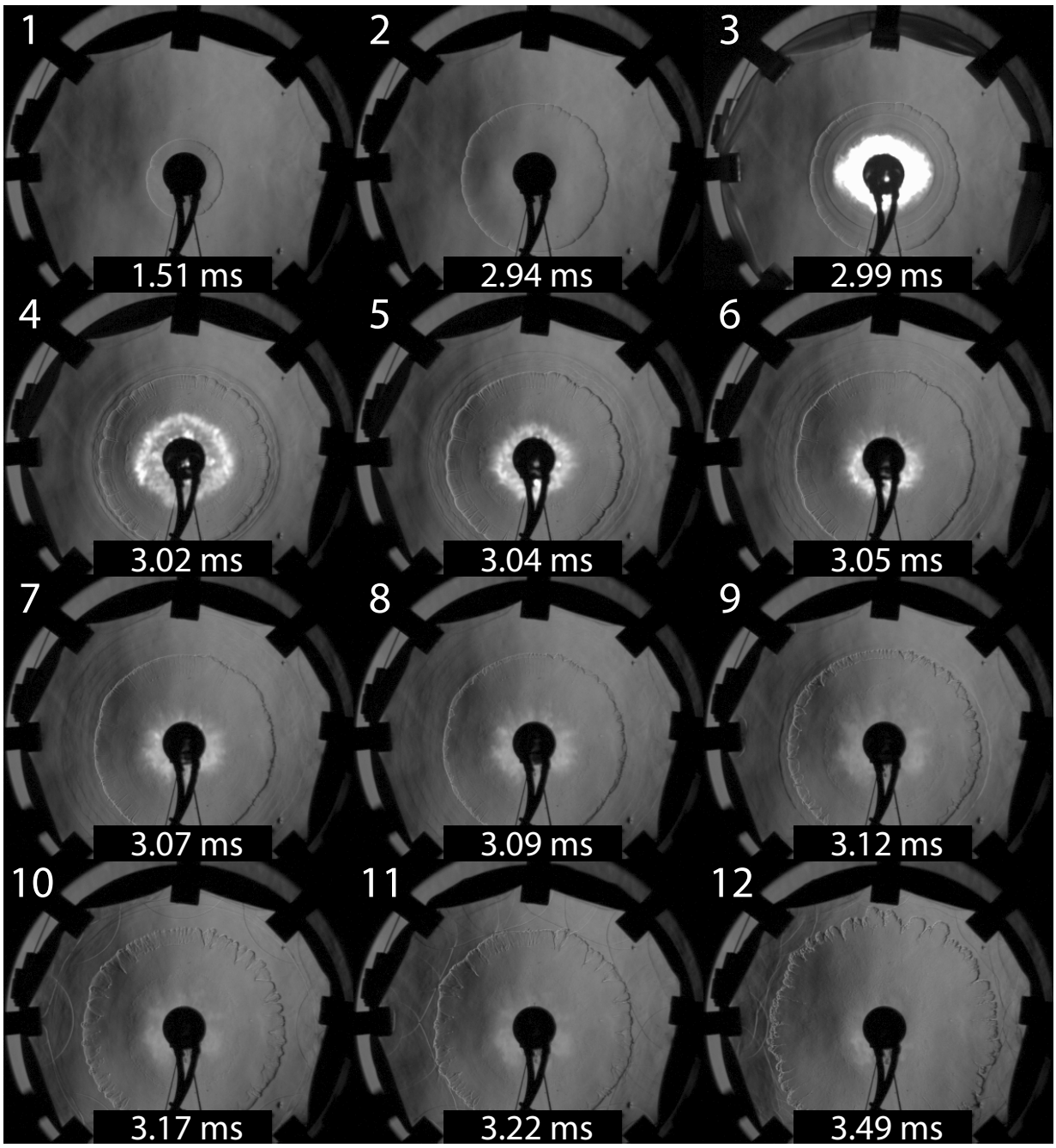

Figure D.39: Schlieren records of HVI-driven shock interacting with a flame in a hydrogen-air mixture at $\phi = 1.0$ propagating in the Hele-Shaw cell. Ambient room conditions. Recorded at 59,590 fps.

D.3 Shock-Flame – Heavy-to-light

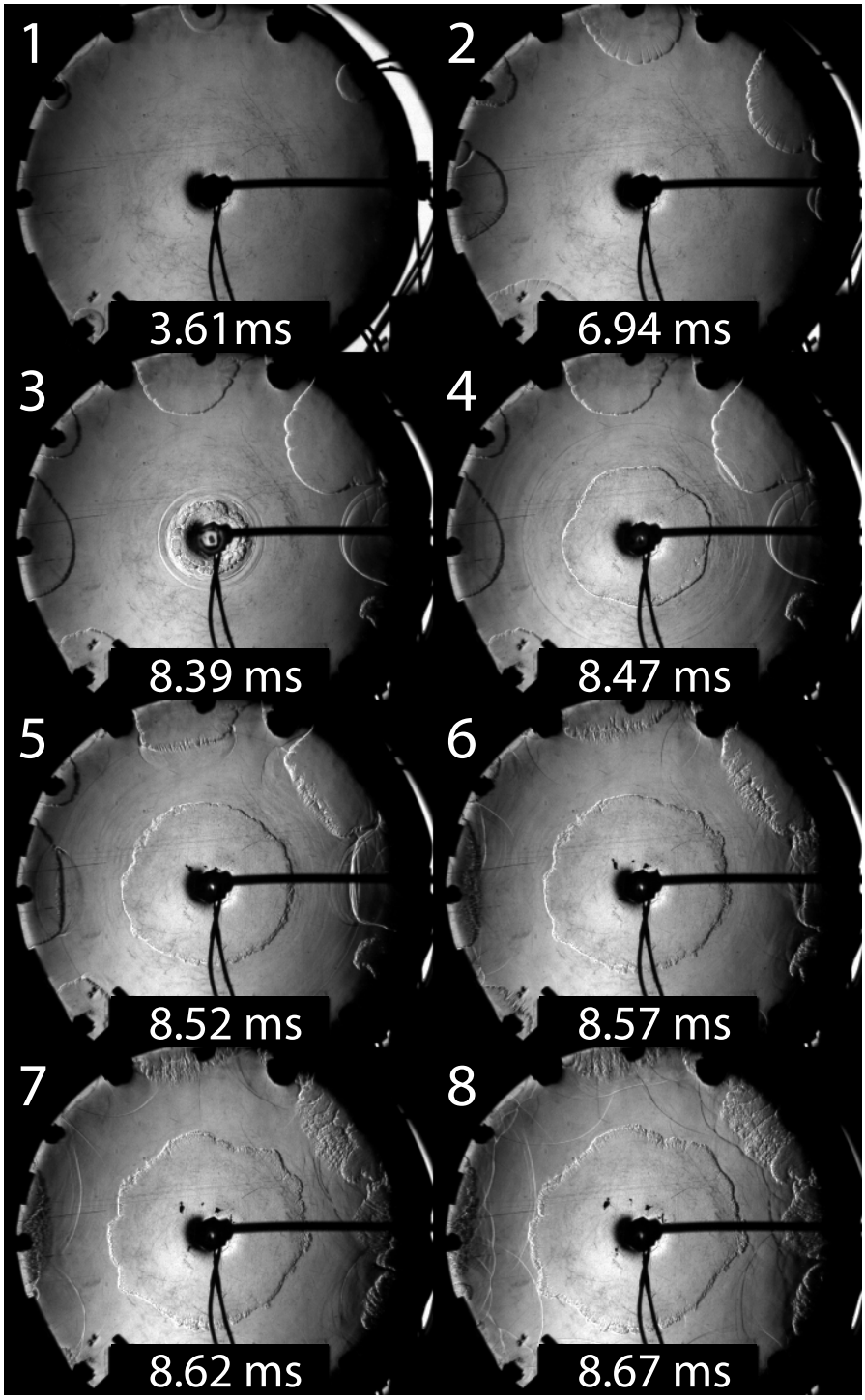

Figure D.40: Schlieren records of detonation-driven shock interacting with a cellular flame front in a hydrogen-air mixture at $\phi = 0.6$ propagating in the Hele-Shaw cell. Ambient room conditions. Recorded at 77,481 fps.

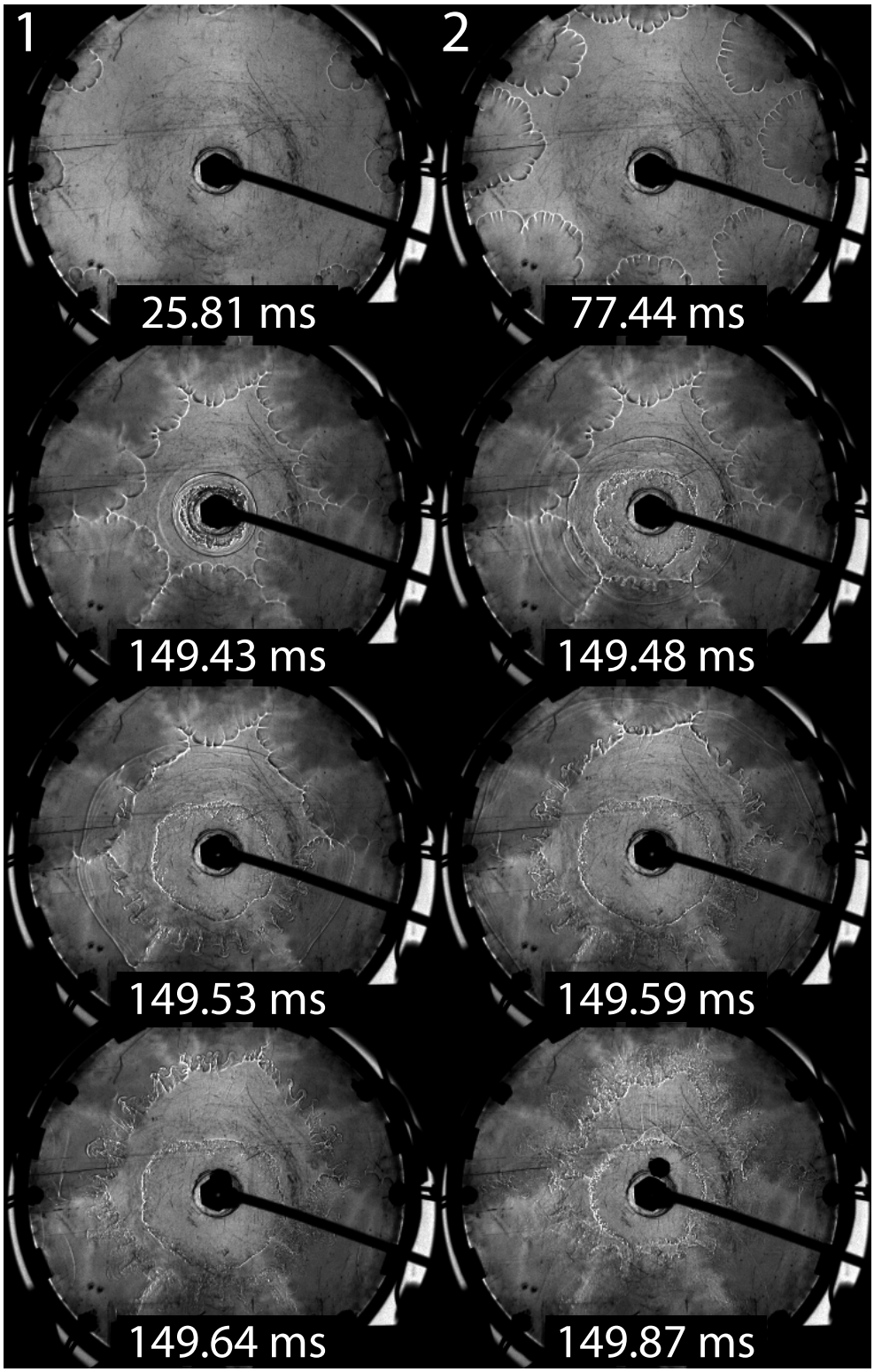

Figure D.41: Schlieren records of detonation-driven shock interacting with a cellular flame front in a hydrogen-air mixture at $\phi = 0.3$ propagating in the Hele-Shaw cell. Ambient room conditions. Recorded at 77,481 fps.

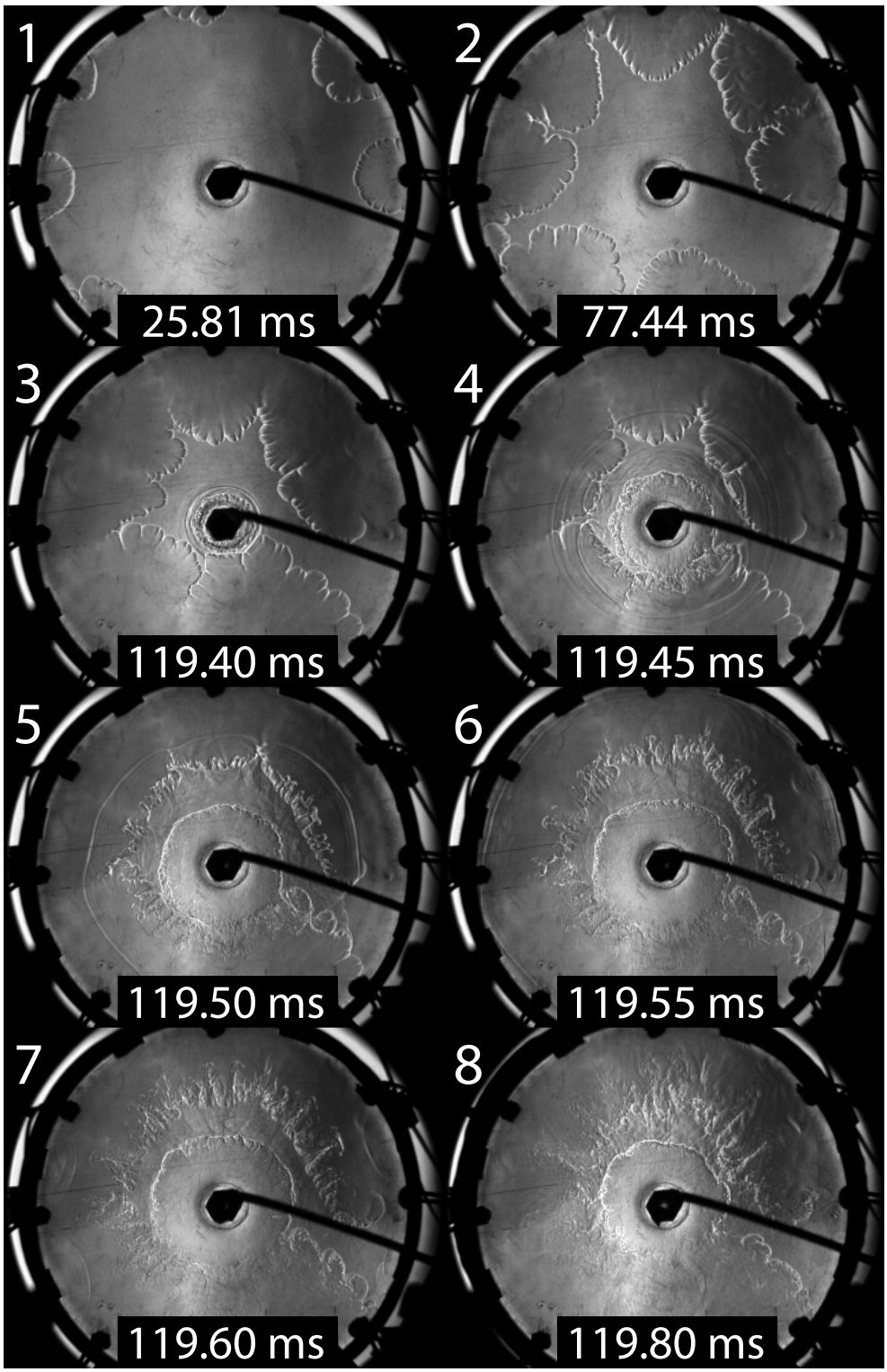

Figure D.42: Schlieren records of detonation-driven shock interacting with a cellular flame front in a hydrogen-air mixture at $\phi = 0.3$ propagating in the Hele-Shaw cell. Ambient room conditions. Recorded at 77,481 fps.

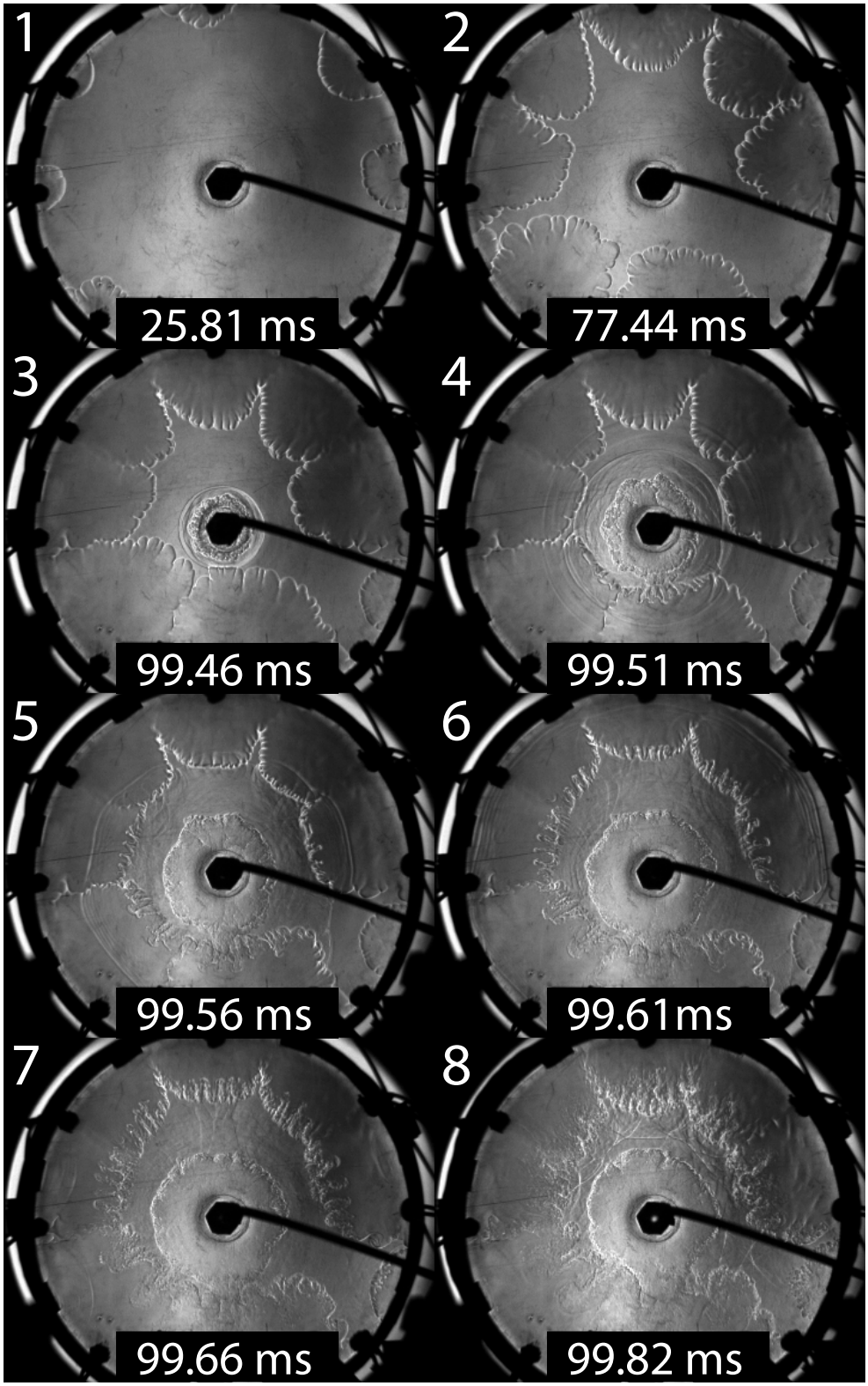

Figure D.43: Schlieren records of detonation-driven shock interacting with a cellular flame front in a hydrogen-air mixture at $\phi = 0.3$ propagating in the Hele-Shaw cell. Ambient room conditions. Recorded at 77,481 fps.

References

[1] E. S. Oran and V. N. Gamezo, "Origins of the deflagration-to-detonation transition in gas-phase combustion," *Combustion and Flame*, vol. 148, no. 1, pp. 4 – 47, 2007.

[2] J. Yang, T. Kubota, and E. E. Zukoski, "Applications of shock-induced mixing to supersonic combustion," *AIAA Journal*, vol. 31, no. 5, pp. 854–862, 1993.

[3] G. H. Markstein, "A shock-tube study of flame front-pressure wave interaction," *Sixth Symposium (International) on Combustion*, vol. 6, no. 1, pp. 387 – 398, 1957.

[4] G. H. Markstein, *Non-steady flame propagation*. Pergamon Press, 1964.

[5] G. Rudinger, "Shock wave and flame interactions," in *Combustion and Propulsion, Third AGARD Colloquium*, p. 153, Pergamon Press London, 1958.

[6] G. Thomas, R. Bambrey, and C. Brown, "Experimental observations of flame acceleration and transition to detonation following shock-flame interaction," *Combustion Theory and Modelling*, vol. 5, no. 4, pp. 573–594, 2001.

[7] J. Picone, E. Oran, J. Boris, and T. Young Jr, "Theory of vorticity generation by shock wave and flame interactions," tech. rep., Naval Research Lab Washington D.C., 1984.

[8] J. M. Picone and J. P. Boris, "Vorticity generation by shock propagation through bubbles in a gas," *Journal of Fluid Mechanics*, vol. 189, no. -1, p. 23, 1988.

[9] A. Khokhlov, E. Oran, A. Chtchelkanova, and J. Wheeler, "Interaction of a shock with a sinusoidally perturbed flame," *Combustion and Flame*, vol. 117, no. 1-2, pp. 99–116, 1999.

[10] L. Massa and P. Jha, "Linear analysis of the Richtmyer-Meshkov instability in shock-flame interactions," *Physics of Fluids*, vol. 24, no. 5, p. 056101, 2012.

[11] N. Attal and P. Ramaprabhu, "Numerical investigation of a single-mode chemically reacting Richtmyer-Meshkov instability," *Shock Waves*, vol. 25, no. 4, pp. 307–328, 2015.

[12] H. Jiang, G. Dong, X. Chen, and B. Li, "A parameterization of the Richtmyer-Meshkov instability on a premixed flame interface induced by the successive passages of shock waves," *Combustion and Flame*, vol. 169, pp. 229–241, 2016.

[13] C. K. Law, *Combustion physics*. Cambridge university press, 2006.

[14] J. Sharif, M. Abid, and P. Ronney, "Premixed-gas flame propagation in Hele-Shaw cells," *Technical report, Spring Technical Meeting, joint U. S. Sections, Combustion Institute, Washington D.C., March 15-17*, 1999.

[15] C. Almarcha, J. Quinard, B. Denet, E. Al-Sarraf, J. M. Laugier, and E. Villermaux, "Experimental two dimensional cellular flames," *Physics of Fluids*, vol. 27, no. 9, p. 091110, 2015.

[16] P. Clavin and G. Searby, *Combustion waves and fronts in flows: flames, shocks, detonations, ablation fronts and explosion of stars*. Cambridge University Press, 2016.

[17] K. Balakrishnan and S. Menon, "On the role of ambient reactive particles in the mixing and afterburn behind explosive blast waves," *Combustion Science and Technology*, vol. 182, no. 2, pp. 186–214, 2010.

[18] D. H. Sharp, "An overview of Rayleigh-Taylor instability," *Physica D: Nonlinear Phenomena*, vol. 12, no. 1-3, pp. 3–18, 1984.

[19] G. Taylor, "The instability of liquid surfaces when accelerated in a direction perpendicular to their planes. I," *Proceedings of the Royal Society of London. Series A. Mathematical and Physical Sciences*, vol. 201, no. 1065, pp. 192–196, 1950.

[20] M. Brouillette, "The Richtmyer-Meshkov instability," *Annual Review of Fluid Mechanics*, vol. 34, no. 1, pp. 445–468, 2002.

[21] C. Bauwens, J. Bergthorson, and S. Dorofeev, "Experimental investigation of spherical-flame acceleration in lean hydrogen-air mixtures," *International Journal of Hydrogen Energy*, vol. 42, no. 11, pp. 7691 – 7697, 2017.

[22] G. S. Settles, *Schlieren and shadowgraph techniques: Visualizing phenomena in transparent media*. Springer-Verlag GmbH, Berlin, Germany, 2001.

[23] R. R. Bhattacharjee, "Experimental investigation of detonation re-initiation mechanisms following a mach reflection of a quenched detonation," Master's thesis, University of Ottawa, 2013.

[24] L. Maley, "On shock reflections in fast flames," Master's thesis, University of Ottawa, 2015.

[25] B. J. McBride and S. Gordon, "Computer program for calculation of complex chemical equilibrium compositions and applications. I: Analysis," vol. 19, 07 1996.

[26] S. A. E. G. Falle and J. R. Giddings, "Body capturing using adaptive cartesian grids," in *Numerical methods for fluid dynamics IV*, pp. 337–343, Oxford University Press, 1993.

[27] J. Li, Z. Zhao, A. Kazakov, and F. L. Dryer, "An updated comprehensive kinetic model of hydrogen combustion," *International Journal of Chemical Kinetics*, vol. 36, no. 10, pp. 566–575, 2004.

[28] G. D. Salamandra, "Interaction between a flame and a shock discontinuity," *ARS Journal*, vol. 30, no. 1, pp. 73–76, 1960.

[29] R. Knystautas, B. H. K. Lee, and J. H. Lee, "Shock-flame interaction in a cylindrical chamber.," *AIAA Journal*, vol. 4, no. 4, pp. 736–737, 1966.

[30] B. Collins and J. Jacobs, "PLIF flow visualization and measurements of the Richtmyer–Meshkov instability of an air/SF-6 interface," *Journal of Fluid Mechanics*, vol. 464, pp. 113–136, 2002.

[31] W. Fickett and W. C. Davis, *Detonation: theory and experiment*. Courier Corporation, 1979.

[32] C. A. Eckett, J. J. Quirk, and J. E. Shepherd, "The role of unsteadiness in direct initiation of gaseous detonations," *Journal of Fluid Mechanics*, vol. 421, pp. 147–183, 2000.